学位論文

Measurement of Cosmic-Ray Muon Spallation Products in Super-Kamiokande with Gadolinium Loaded Water

（ガドリニウム含有水を用いたスーパーカミオカンデにおける
宇宙線ミューオンの核破砕反応による生成物の測定）

2024 年 3 月

篠木 正隆

ABSTRACT

High-energy muons produced by the interactions of cosmic-rays with nuclei in the atmosphere are called cosmic-ray muons. Cosmic-ray muons reaching the surface of the Earth interact with nuclei in materials, producing multiple neutrons and radioactive isotopes. These are the major backgrounds in the rare event searches, including neutrino observations by underground experiments. This thesis describes the results of the measurement of cosmogenic neutrons and ^{9}Li isotopes by analyzing the data from the Super-Kamiokande (SK) detector.

The SK detector is a water Cherenkov detector located 1,000 m underground, with 50,000 tons of ultra-pure water filled in a cylindrical tank. As the upgrade of the detector, gadolinium is loaded in water and the SK-Gd experiment has been started. In the SK-Gd experiment, neutrons are tagged by detecting γ rays emitted after neutron capture reaction on gadolinium. One of the motivations of the SK-Gd experiment is the first observation of neutrinos from past supernovae since the early stage of the universe (supernova relic neutrinos, SRNs). In the SK detector, positrons and neutrons generated by the interactions of electron antineutrinos with protons in water ($\bar{\nu}_e + p \to e^+ + n$) are detected. Comparison of the energy spectrum of SRNs, if it is observed, with theoretical predictions will provide further insight into the frequency and explosion mechanism of supernovae.

In order to detect SRNs in the SK-Gd experiment, it is important to continue stable observations over a long period of time. In this study, the uniformity and stability of gadolinium concentration were confirmed through the detection of neutrons produced by cosmic-ray muons overall the detector. This method established in this study enables monitoring the stability of the detector in parallel with the observations and will lead to the first observation of SRNs in the future. In addition, the production yield of neutrons induced by cosmic-ray muon (cosmogenic neutrons) was measured in this study. Cosmogenic neutrons and recoil nuclei from the neutron scattering are the background for the measurements below the MeV scale. While, it is difficult to accurately reproduce the processes in simulations due to large uncertainty in the hadron production and scattering process. Currently, empirical approaches are ongoing to evaluate the neutron production by the models derived from the measurements, and additional data are required to advance the studies. In this study, neutron yield measurement was measured to be $(2.76 \pm 0.02\,(\text{stat.}) \pm 0.19\,(\text{syst.})) \times 10^{-4}\,\mu^{-1}\text{g}^{-1}\text{cm}^2$. This is the second measurement of neutron yield in water following the SNO experiment. In addition, this measurement was made near the KamLAND detector which measured the neutron yield in carbon. As the muon energy spectrum depends on the depth, this result allows a direct comparison of neutron yields in different targets for the first time. The measurement described in this thesis provides important insights that contribute to advancing a systematic understanding of neutron production by cosmic-ray muons.

This thesis also describes the measurement of the energy spectrum of electrons emitted from β decay of the ^{9}Li. ^{9}Li produced via muon spallation decays with a lifetime of 0.26 s, emitting an electron and a neutron. As electrons and positrons can not be distinguished by the Super-Kamiokande detector, the decay of ^{9}Li is indistinguishable from the interactions of electron antineutrinos ($\bar{\nu}_e + p \to e^+ + n$). Therefore, ^{9}Li is one of the major background sources in the SRN search in low energy region. In this study, β decay of ^{9}Li produced by cosmic-ray muon was selected by requiring the detection of associated neutrons and correlations with the muons. In SK with pure water, the β-spectrum of ^{9}Li was measured above 8 MeV, while, the range of the measurement was extended down to 4.5 MeV using the data acquired with gadolinium-loaded water. Due to the redshift by the expansion of the universe, SRN flux is predicted to be larger in the low energy side. The result of the ^{9}Li spectrum measurement and the analysis method established in this study contribute to improving the sensitivity of the SRN search.

ACKNOWLEDGEMENT

I would like to express my great appreciation to my supervisor Prof. Masaki Ishitsuka. He has guided me with great care daily, and I have been impressed many times by his deep insight into physics. Furthermore, I learned a lot from him, not only about the attitude toward research but also about how to communicate things to others. I would not have been able to complete this research without his support.

The Super-Kamiokande collaborators have taught me much about the low-energy neutrino analysis in Super-Kamiokande, and have given me sound advice on many occasions. In particular, I would like to extend my special thanks to Prof. Yusuke Koshio of Okayama University and Prof. Yasuhiro Nakajima of the University of Tokyo for their extraordinary support since I started this research. I am deeply grateful to them for taking time out of their busy schedules. I am also grateful to Prof. Masayuki Nakahata, Prof. Hiroyuki Sekiya, Dr. Yuuki Nakano, and Dr. Takatomi Yano of the Institute for Cosmic Ray Research at the University of Tokyo, Prof. Yasuo Takeuchi of Kobe University, and Prof. Blair Jamieson of the University of Winnipeg for discussions and important remarks on my research.

I have been got along very well with the members of Okayama University and Tokyo Institute of Technology. Dr. Yota Hino, Dr. Masayuki Harada, Seiya Sakai, Fumi Nakanishi, Tomoaki Tada, Tomohiro Tano, Yuki Shiraishi, Dr. Ryo Matsumoto, and Shota Izumiyama. We not only discussed physics but also went out to eat together many times on business trips. Thanks to them, I was able to enjoy my research life.

I would like to thank all Ishitsuka Lab members including alumni. Without their support, my research life would not have been successful and enjoyable. I hope they will continue to be my good friends.

This work supported by JST SPRING Grant Number JPMJSP2151 and Grant-in-Aid for JSPS Fellows Grant Number 22KJ2809. I thank the financial support.

In closing, I would like to express my sincere gratitude to my family for their support throughout my life.

Contents

List of Figures

List of Tables

Chapter 1

Physics Background

High-energy muons are produced from the interactions of cosmic-rays in the atmosphere and penetrate deep underground. Muons induce electromagnetic showers and hadronic showers, and they interact with nuclei in material to produce secondary particles consisting of nucleons and mesons in chain. Furthermore, the secondary particles induce the neutrons and unstable radioactive isotopes, which are called cosmogenic products. Produced neutrons are captured on nuclei after thermalization, and the γ rays with the energy of several MeV are emitted. While, isotopes emit electrons with MeV-scale via β decay. Therefore, these are background in rare event search in the MeV scale such as neutrino observations. This thesis measured the production of neutrons and ^{9}Li isotopes induced by cosmic-ray muons. This is especially the first measurement of muon-induced neutron yield in SK realized by the upgrade of the detector with Gd loading in ultra-pure water.

This chapter will provide the physics background for this study. The Standard Model of particle physics will be first described, followed by a brief explanation of hadrons and neutrinos. There are various neutrino sources in the universe, and Super-Kamiokande has been observing them. This thesis focuses on neutrinos emitted from past supernovae, supernova relic neutrinos (SRNs). However, SRNs have not been discovered so far, and only the upper limit of flux has been given. This chapter will explain the predictions for the flux and the current status of the searches. Finally, cosmogenic production, which is the subject of this study, will be described and the contributions as the background for SRN searches will be discussed.

1.1 Standard Model of Particle Physics

The Standard Model is the most fundamental theoretical framework describing modern particle physics. In the Standard Model, quarks and leptons make up matter. These fermions interact via gauge bosons such as photons, gluons, and weak bosons. Table 1.1 summarizes the elementary particles included in the Standard Model. There are four basic interactions in nature: strong interaction, electromagnetic interaction, weak interaction, and gravitational interaction. Three of these, other than the gravitational interaction, are treated in the Standard Model. Strong interaction, electromagnetic interaction, and weak interaction are mediated by gluons, photons, and weak bosons, respectively. In addition to the above particles, there are also scalar bosons called Higgs bosons. In the Standard Model, quarks and leptons acquire mass through interaction with the Higgs field.

Quarks and leptons are associated with weak bosons that differ in charge by only one, making each a pair (e.g. up quark and down quark, electron and electron neutrino). There are three types of quarks and leptons that have the same charge but different mass scales, and each of the two types of quarks and two types of leptons constitutes one "generation". For every quark and lepton, there is an antiparticle with the same mass and spin but opposite sign of charges.

The Standard Model has succeeded in describing almost all of the experimental results in the particle physics so far. On the other hand, there are several problems that have not been explained

Table 1.1: Elementary particles in the Standard Model of particle physics

Fermions				Bosons	
Generations	I	II	III	Gauge	Scalar
Quarks	Up (u) Down (d)	Charm (c) Strange (s)	Top (t) Bottom (b)	Photon (γ) Gluon (g) Z^0 $W^{\pm}$	Higgs (H^0)
Leptons	Electron (e) Electron neutrino (ν_e)	Muon (μ) Muon neutrino (ν_μ)	Tau (τ) Tau neutrino (ν_τ)		

Table 1.2: Summary of properties of pion, kaon, proton, and neutron.

Hadron	Symbol	Component	Mass (MeV)	Lifetime (s)
Pion	$\pi^+(\pi^-)$	$u\bar{d}$ $(\bar{u}d)$	139.57	2.6×10^{-8}
	π^0	$(u\bar{u} - d\bar{d})/\sqrt{2}$	134.98	8.4×10^{-17}
Kaon	$K^+(K^-)$	$u\bar{s}$ $(\bar{u}s)$	493.68	1.2×10^{-8}
	K^0_S	$(d\bar{s} - s\bar{d})/\sqrt{2}$	497.61	9.0×10^{-11}
	K^0_L	$(d\bar{s} + s\bar{d})/\sqrt{2}$	497.61	5.2×10^{-8}
Proton	p	uud	938.27	—
Neutron	n	udd	939.57	880

by the Standard Model, such as the origin of neutrino mass, generation structure, and dark matter.

1.2 Hadrons

Quarks (antiquarks) and gluons exist in nature as composite particles called hadrons. Multiple quarks (antiquarks) are bound together via a strong force mediated by gluons and form hadrons. Hadrons are classified into two types according to the number of quarks (antiquarks): mesons and baryons. Mesons consist of quark and antiquark pairs, while baryons contain three quarks. Among various mesons, pion and kaon are the major mesons in nature which are produced by cosmic-ray interacting with nuclei in the Earth's atmosphere. On the other hand, examples of typical baryons are protons and neutrons, which are components of the nucleus. Table 1.2 summarizes properties of pion, kaon, proton, and neutron.

1.3 Neutrinos

Neutrinos are neutral leptons with spin 1/2 that interact only via the weak interaction except for the gravitational interaction. There are three generations (flavors) of neutrinos: electron neutrino ν_e, muon neutrino ν_μ, and tau neutrino ν_τ, corresponding to the charged leptons of electron, muon, and tauon, respectively. There are corresponding antiparticles: electron antineutrino $\bar{\nu}_e$, muon antineutrino, $\bar{\nu}_\mu$, and tau antineutrino $\bar{\nu}_\tau$, corresponding to the charged leptons of positron, positive muon, and positive tauon, respectively.

Neutrinos were predicted by W. E. Pauli in 1930 to explain the conservation of energy in beta decay. The diagram for beta decay of neutron is shown in Figure 1.1. In 1956, the existence of neutrinos was proved by F. Reines and C. Cowan by the observation of electron antineutrinos $\bar{\nu}_e$ produced from a nuclear reactor [1]. In 1962, L. Lederman, M. Schwartz, and J. Steinberger confirmed that ν_e and ν_μ are different elementary particles and that neutrinos have flavors [2]. Subsequently, ν_τ was observed by the DONUT experiment in 2000, and the existence of all three generations of neutrinos were confirmed [3].

Although the Standard Model assumes that neutrinos have no mass, observations of atmospheric neutrinos in Super-Kamiokande experiment led to the discovery of neutrino oscillation phenomena in 1998, which revealed that neutrinos have non-zero mass [4].

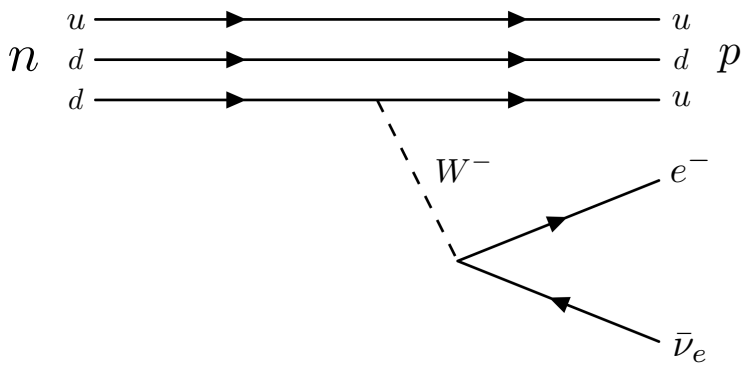

Figure 1.1: Diagram for beta decay of neutron.

1.4 Neutrinos from Supernovae

Massive stars with more than ∼8 times the solar mass reach their end with the explosion. The explosion is called supernova. Supernovae release a large amount of energy, $\sim 10^{51}$ erg (corresponding to 10^{44} J), and more than 99% of the energy is carried out by the emission of neutrinos. Since these neutrinos have information on the explosion mechanism and the supernova rate, neutrino observations are expected to advance our understanding of supernovae. This section describes supernova explosions and neutrino emissions.

1.4.1 Overview of Supernovae

Supernovae are classified into the following categories according to the spectral lines.

- Type I: Supernova without hydrogen spectral line.
  - Type Ia: Supernova with silicon line.
  - Type Ib: Supernova without silicon line but with helium line.
  - Type Ic: Supernova without helium and silicon line.
- Type II: Supernova with hydrogen spectral line.

Type Ia supernovae are called thermonuclear supernovae. In type Ia, the weight of a white dwarf in a binary is increased by the gas absorbed from the other star, and the white dwarf cannot support its own weight at a certain point. Then, a runaway nuclear fusion of the carbon that makes up the core of the white dwarf causes an explosion. The neutrinos emitted from a type Ia supernova have the total energy of $\sim 10^{49}$ erg or less. On the other hand, type Ib, Ic, and II supernovae are called core-collapse supernovae, and the neutrinos emitted by these supernovae have the total energy of $\sim 10^{53}$ erg.

1.4.2 Core-Collapse Supernovae and Neutrino Emission

When supernovae occur, a large amount of neutrinos are emitted. The amount of neutrinos emitted from core-collapse supernovae is greater than thermonuclear supernovae. The mechanism of core-collapse supernovae and neutrino emissions is explained in this section. Figure 1.2 shows a schematic diagram of the process of a core-collapse supernova as explained below.

(1) The core of a star is formed when interstellar gas (mainly hydrogen) in space is collected by gravity.

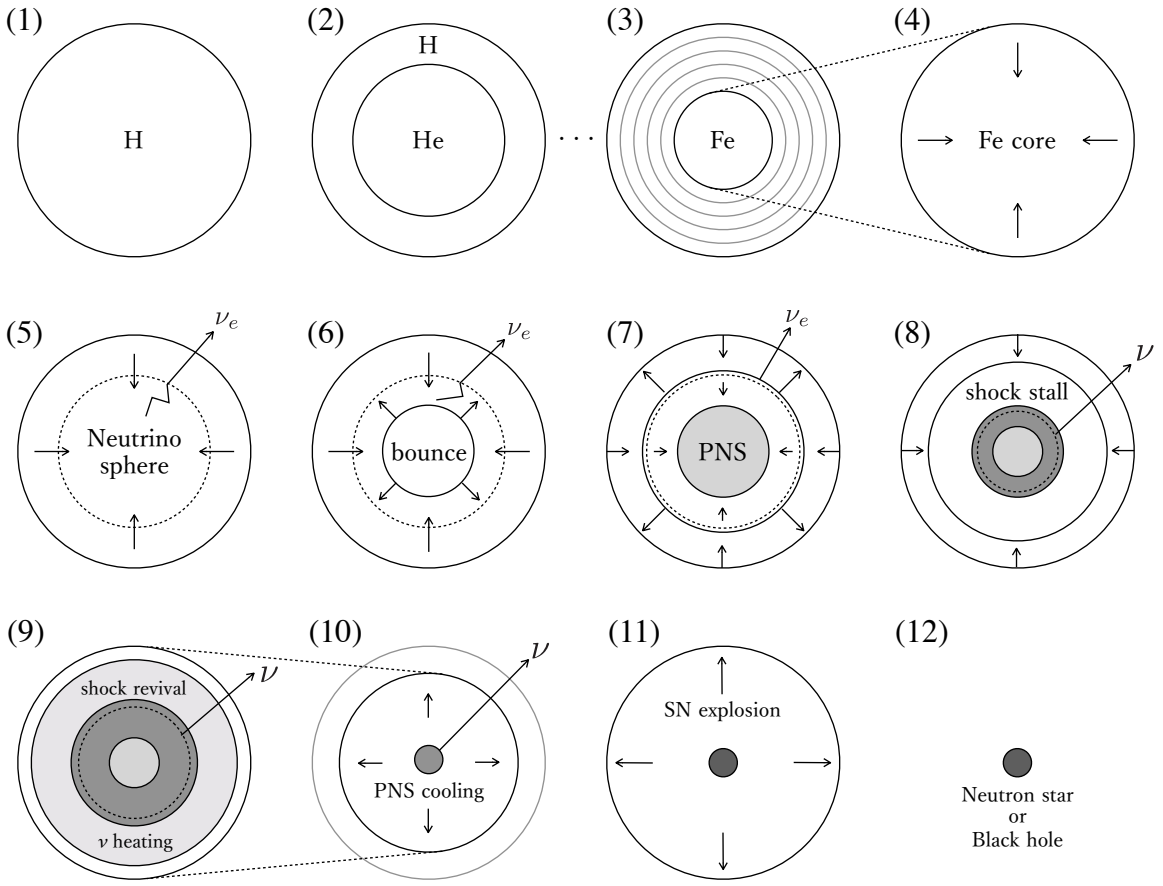

Figure 1.2: Schematic diagram of the process of a core-collapse supernova assuming a neutrino heating mechanism.

(2) As the gas falls toward the center, potential energy is converted into thermal energy, and the center becomes hot and pressurized. When the temperature near the center exceeds 10^7 K, helium is produced through nuclear fusions:

$$4p \rightarrow {}^4\mathrm{He} + 2e^+ + 2\nu_e + 26.73\,\mathrm{MeV}. \tag{1.1}$$

On the other hand, as a nuclear fusion is not occurred by the hydrogen near the surface, a layered structure is formed in the star.

(3) Stars maintain their shape by the balance between self-gravitational contraction and the internal pressure caused by the nuclear fusion. Therefore, when the hydrogen near the center is burned out, gravitational contraction occurs again. This contraction raises the temperature near the center, and when the temperature exceeds 1.5×10^8 K, the nuclear fusion by helium begins. This process is repeated to form multiple layers in the star. The main elements that make up each layer are, in order from the outside: hydrogen, helium, carbon/oxygen, oxygen/neon/magnesium, silicon, and iron. Since iron has the highest binding energy, the nuclear fusions cannot proceed any further.

(4) The internal pressure of the iron core is supported by electron degeneracy pressure and thermal pressure, but when these pressures begin to decrease, the balance between self-gravity and internal pressure is disrupted and core-collapse occurs. When the density of the iron core exceeds $10^9\,\mathrm{g/cm^2}$, electrons are captured by the protons in the iron nucleus and electron neutrinos are emitted:

$$e^- + p \rightarrow \nu_e + n. \tag{1.2}$$

Photodisintegration of iron also occurs when the temperature at the core exceeds $\sim 5 \times 10^9$ K as

$${}^{56}\mathrm{Fe} + \gamma \rightarrow 13\alpha + 4n - 124.4\,\mathrm{MeV}, \tag{1.3}$$

then the core-collapse occurs because the pressure in the core decreases.

(5) In the early stages of the core-collapse, electron neutrinos can escape outward without interacting with surrounding matter. However, when core-collapse proceeds and the core density exceeds $10^{11}\,\mathrm{g/cm^3}$, electron neutrinos cannot escape from the core. The boundary surface where electron neutrinos cannot escape the core is called the neutrino sphere.

(6) When the density of the core near the center reaches $10^{14}\,\mathrm{g/cm^3}$, the repulsive force between approaching nucleons stops core-collapse. However, because material is falling from the outer core at supersonic speeds, shock waves are generated at the boundary between the inner and outer cores. The shock waves propagate outward while breaking up the surrounding nuclei into free nucleons.

(7) Electron neutrinos are produced when the produced free protons capture the surrounding electrons as Eq. (1.2). Electron neutrinos cannot escape while the shock wave propagates inside the neutrino sphere. Then, once the shock wave reaches the outside of the neutrino sphere, electron neutrinos are emitted to the outside. This neutrino emission is called neutronization burst, which occurs within 10 ms from the beginning of core-collapse. The proto-neutron star (PNS) is formed in the innermost part of the star.

(8) During propagation, the shock wave loses energy due to interactions with matter (photodisintegration of nuclei and electron capture by free protons). In this process, neutrinos and antineutrinos of all flavors are produced by the interactions shown in Table 1.3. Due to the electron (positron) capture interactions, the number of ν_e ($\bar{\nu}_e$) is greater than ν_μ and ν_τ ($\bar{\nu}_\mu$ and $\bar{\nu}_\tau$).

Table 1.3: Neutrino process in supernovae and proto-neutron star matter. N means nucleons (neutrons or protons). ν represents neutrinos and antineutrinos of all flavors and ν_x represents ν_μ and ν_τ [5].

Process	Interaction
Electron and ν_e absorption by nuclei	$e^- + (A, Z) \leftrightarrow \nu_e + (A, Z-1)$
Electron and ν_e capture by nucleons	$e^- + p \leftrightarrow \nu_e + n$
Positron and $\bar{\nu}_e$ capture by nucleons	$e^+ + n \leftrightarrow \bar{\nu}_e + p$
Nucleon-nucleon bremsstrahlung	$N + N \leftrightarrow N + N + \nu + \bar{\nu}$
Electron-position pair process	$e^- + e^+ \leftrightarrow \nu + \bar{\nu}$
Plasmon pair-neutrino process	$\gamma^* \leftrightarrow \nu + \bar{\nu}$
Neutrino-pair annihilation	$\nu_e + \bar{\nu}_e \leftrightarrow \nu_x + \bar{\nu}_x$
Neutrino scattering	$\nu_x + \{\nu_e, \bar{\nu}_e\} \leftrightarrow \nu_x + \{\nu_e, \bar{\nu}_e\}$
Neutrino scattering with nuclei	$\nu + (A, Z) \leftrightarrow \nu + (A, Z)$
Neutrino scattering with nucleons	$\nu + N \leftrightarrow \nu + N$
Neutrino scattering with electrons and positrons	$\nu + e^\pm \leftrightarrow \nu + e^\pm$

(9) The produced neutrinos heat the material behind the shock wave, and the stalled shock wave is revived. This phenomenon is called neutrino heating mechanism.

(10) The proto-neutron star is cooled because heat is taken out by the neutrinos.

(11) When the revived shock wave reaches the surface of the star, a supernova explosion occurs, blowing away all the outer layers.

(12) After the explosion, the cooled central proto-neutron star becomes a neutron star or black hole.

The neutrino energy emitted depends on the flavor of the neutrino. Muon neutrino and tau neutrino interact only via neutral current interaction, whereas electron neutrino interacts through both charged and neutral current interactions. As the interaction cross-sections of muon and tau neutrinos are lower than that of electron neutrinos. Muon neutrinos and tau neutrinos can escape from the center where the temperature is higher and therefore they tend to have higher energy than electron neutrinos. Figure 1.3 shows the time evolution of the mean neutrino energy and luminosity obtained from numerical simulations. The results of this numerical simulation predict that the average neutrino energy is about 10–20 MeV.

1.4.3 Observation of Neutrinos from SN1987A

The supernova SN1987A is a type II supernova appeared within the Large Magellanic Cloud. On February 23, 1987, neutrinos from SN1987A were observed in the Kamiokande [7], IMB [8], and Baksan experiments [9]. Figure 1.4 shows the distribution of time and energy of neutrinos from SN1987A in the Kamiokande-II and IMB detectors. These are the first observed neutrinos from outside the solar system, and are the only supernova burst neutrinos observed by humans so far. These observations marked the beginning of neutrino astronomy. Because supernova burst neutrinos hold information to understand the supernovae explosion mechanism, Super-Kamiokande and other detectors around the world are eagerly awaiting the next supernova.

1.5 Supernova Relic Neutrinos

Although supernovae are rare in a galaxy (it is estimated to be about once to a few times every 100 years with some assumptions), the neutrinos emitted by the supernova that have occurred

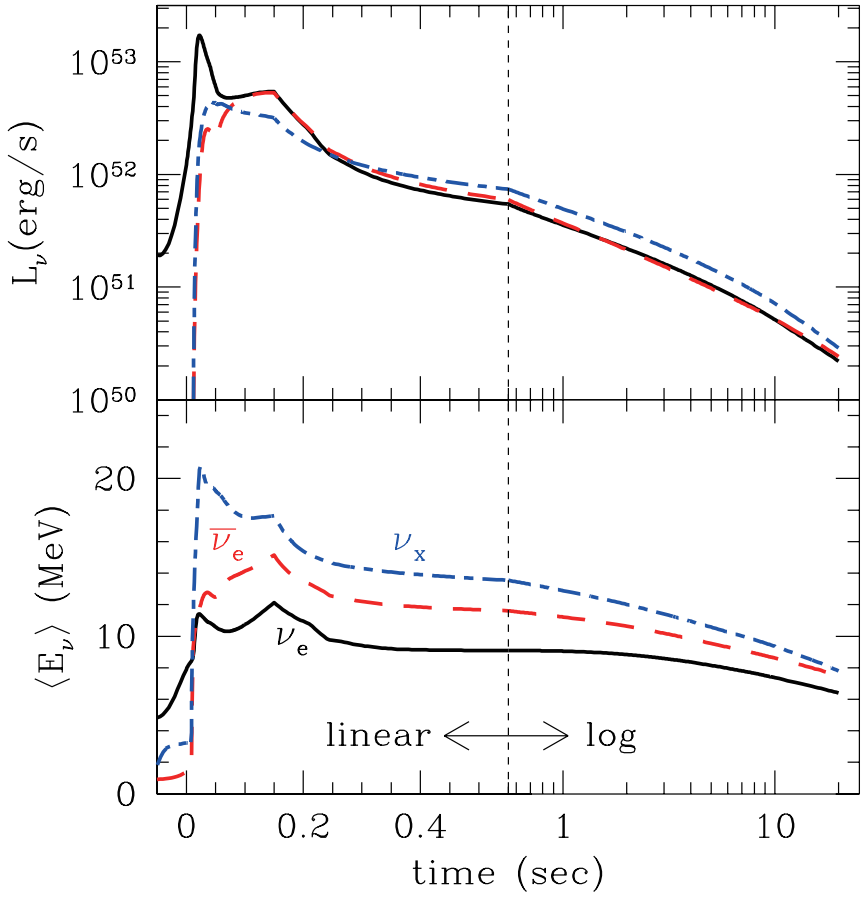

Figure 1.3: Timing distributions of average energy $\langle E_\nu \rangle$ and luminosity L_ν of neutrinos, where $\nu_x = (\nu_\mu + \bar{\nu}_\mu + \nu_\tau + \bar{\nu}_\tau)/4$ [6]. The sharp peak for ν_e with respect to luminosity is due to neutronization bursts.

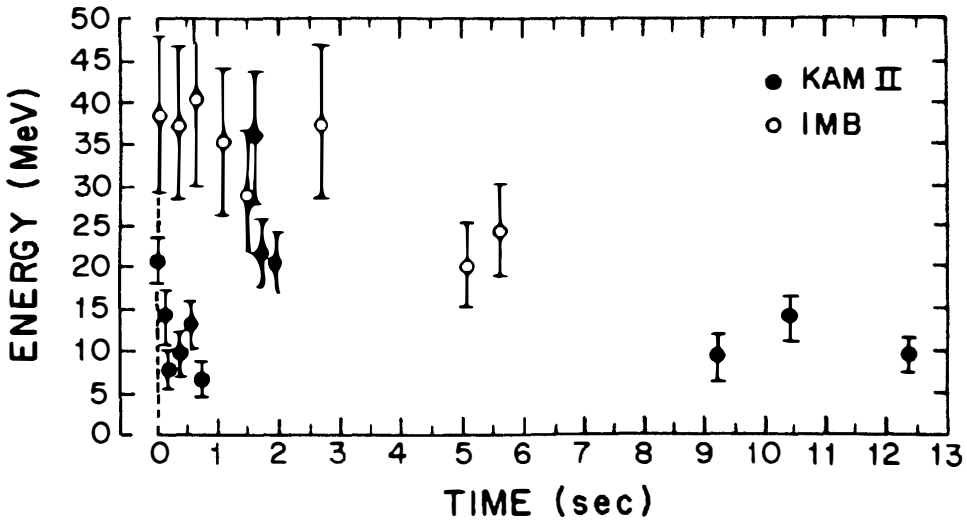

Figure 1.4: Distributions of time and energy of neutrinos from SN1987A, which are observed in the Kamiokande-II (12 events) and the IMB (8 events) experiments [10].

since the beginning of the universe to the present should be uniformly distributed in space. Those neutrinos are called supernova relic neutrinos (SRNs) or diffuse supernova neutrino backgrounds (DSNBs). Although there have been many searches for SRNs, including the Super-Kamiokande experiment, no observations have yet been made. If SRNs are observed and their energy spectra can be compared with the theoretical predictions, it will lead to a better understanding of the supernova explosion mechanism and star formation.

1.5.1 Flux Predictions

The predictions of the current energy spectrum of SRNs are determined by the rate of core-collapse supernovae, the flux of neutrinos emitted in individual supernovae, and the redshift of neutrino energy with the expansion of the universe. Since the amount of neutrinos emitted by a supernova explosion (N_ν) depends on the stellar mass (M) and the metallicity (Z), the neutrino spectrum is written as follows:

$$\frac{dN_\nu(E'_\nu, M, Z)}{dE'_\nu}, \tag{1.4}$$

where E'_ν is the energy of neutrino observed on Earch. The relationship between E'_ν and the energy of neutrino at the time of emission E_ν is expressed as $E_\nu = (1+z)E'_\nu$ using the redshift z. The number density of SRNs at present $dn_\nu(E_\nu)$ is expressed as:

$$\begin{aligned} dn_\nu(E_\nu) &= R_{\rm CC}(z)\frac{dt}{dz}dz\frac{dN(E'_\nu)}{dE'_\nu}dE'_\nu \\ &= R_{\rm CC}(z)\frac{dt}{dz}dz\frac{dN(E'_\nu)}{dE'_\nu}(1+z)dE_\nu, \end{aligned} \tag{1.5}$$

where $R_{\rm CC}(z)$ is the rate of core-collapse supernovae.

SRN is the integral of the neutrinos from supernova emitted so far. The SRN flux at present is expressed as follows:

$$\frac{d\Phi_\nu(E_\nu)}{dE_\nu} = c\int_0^\infty R_{\rm CC}(z)\frac{dt}{dz}\frac{dN(E'_\nu)}{dE'_\nu}(1+z)dz, \tag{1.6}$$

where $d\Phi_\nu(E_\nu)$ represents the flux, $d\Phi_\nu(E_\nu)/dE_\nu$ is the energy spectrum, and c is the speed of light. The relationship between time t and redshift z is also given by the Friedmann equation as follows:

$$\frac{dt}{dz} = \frac{1}{H_0(1+z)\sqrt{\Omega_m(1+z)^3+\Omega_\Lambda}}, \tag{1.7}$$

where H_0 is the Hubble constant, Ω_m is the matter density parameter, and Ω_Λ is the cosmological constant. Therefore, Eq. (1.6) can be transformed as follows:

$$\frac{d\Phi_\nu(E_\nu)}{dE_\nu} = c\int_0^\infty R_{\rm CC}(z)\frac{1}{H_0\sqrt{\Omega_m(1+z)^3+\Omega_\Lambda}}\frac{dN_\nu(E'_\nu)}{dE'_\nu}dz \tag{1.8}$$

As shown in Eq. (1.4), the neutrino number spectrum is a function of the stellar mass M and the metallicity Z. Using the initial mass function $\psi_{\rm IMF}(M)$ and the metallicity distribution function $\psi_{\rm ZF}(z,Z)$, Eq. (1.8) is also expressed as:

$$\begin{aligned} \frac{d\Phi_\nu(E_\nu)}{dE_\nu} &= c\int_0^\infty \frac{dz}{H_0\sqrt{\Omega_m(1+z)^3+\Omega_\Lambda}} \\ &\times \left[R_{\rm CC}(z)\int_0^{Z_{\rm max}}\psi_{\rm ZF}(z,Z)\left\{\int_{M_{\rm min}}^{M_{\rm max}}\psi_{\rm IMF}(M)\frac{dN_\nu(E'_\nu,M,Z)}{dE'_\nu}dM\right\}dZ\right], \end{aligned} \tag{1.9}$$

where $M_{\rm max}$ and $M_{\rm min}$ are the upper and lower limits of the mass of the stars that end with core-collapse. Many theoretical models have been proposed to predict the SRN flux [11–23]. Figure 1.5 shows the predicted energy distribution of the $\bar{\nu}_e$ flux.

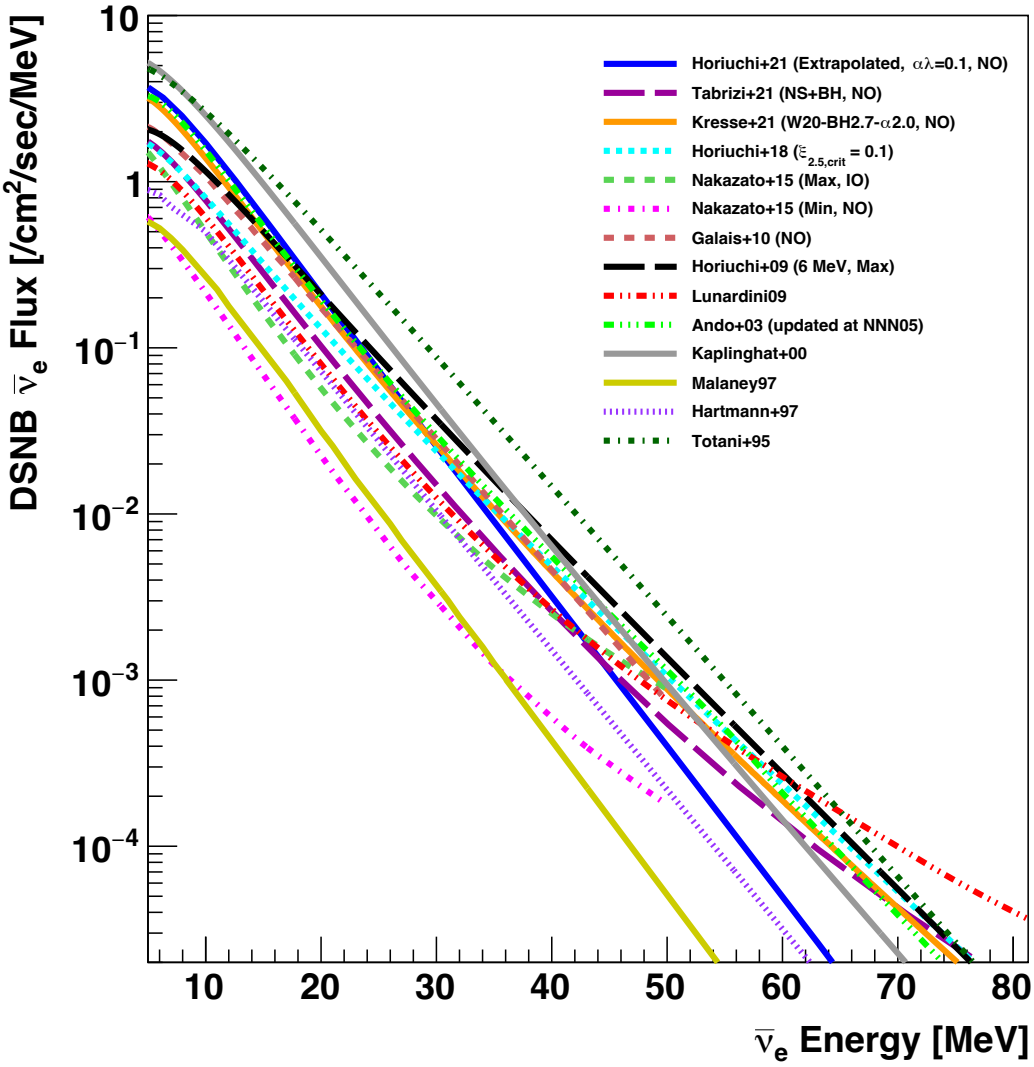

Figure 1.5: SRN $\bar{\nu}_e$ flux predictions from various theoretical models [11–23]. This figure is taken from Ref. [24].

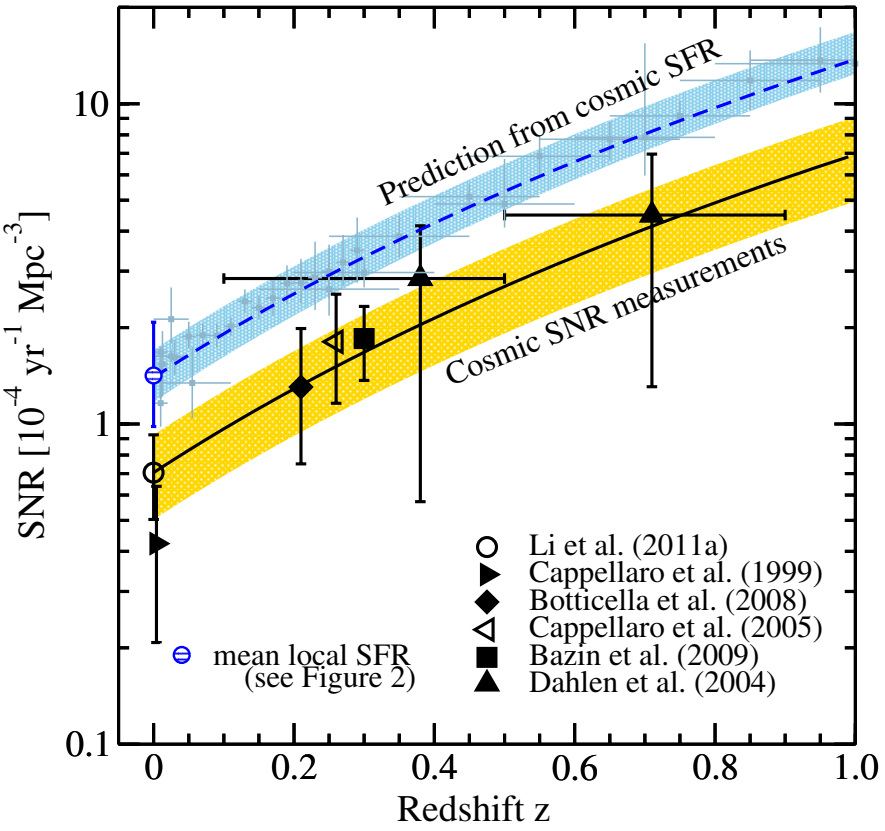

Figure 1.6: Correlation between redshift z and the supernova rate (SNR) [25]. The light blue band represents the SNR expected from the star formation rate (SFR). The yellow band represents the SNR obtained from optical observations.

Figure 1.6 shows the correlation between redshift z and the supernova rate (SNR). Although the observed SNRs are only about half of the predictions, the existence of faint supernovae or light-blocking matter is suggested as a possible explanation. Since neutrinos interact only through the weak interaction besides the gravity, if observations of SRNs can be realized, the frequency of supernova explosions can be confirmed without interference by the absorption or scattering in interstellar medium if observations of SRNs are realized.

1.5.2 Status of SRN Searches

As mentioned in the previous section, SRNs contain important information for understanding the formation rate of massive stars and the mechanism of a supernova explosion. Theoretical predictions of the energy spectrum of SRNs have been made based on various cosmological models and mechanisms of explosion. Until now, experimental searches of SRNs have been made to confirm these predictions but no observation has yet been realized.

All flavors of neutrinos and antineutrinos are emitted from supernovae. In almost all detectors, SRNs are searched for through inverse beta decay (IBD) reactions of electron antineutrinos:

$$\bar{\nu}_e + p \rightarrow e^+ + n, \tag{1.10}$$

because its cross section is by far the largest below ∼20 MeV as shown in Figure 1.7.

Figure 1.8 shows the results of recently reported SRN searches in Super-Kamiokande and KamLAND [24, 26, 27]. In Super-Kamiokande, SRNs are searched for by the coincidence of the prompt signal from the positron produced by the IBD reaction and the delayed signal from γ rays emitted due to the neutron capture on nuclei in water. Cherenkov light is emitted when charged particles

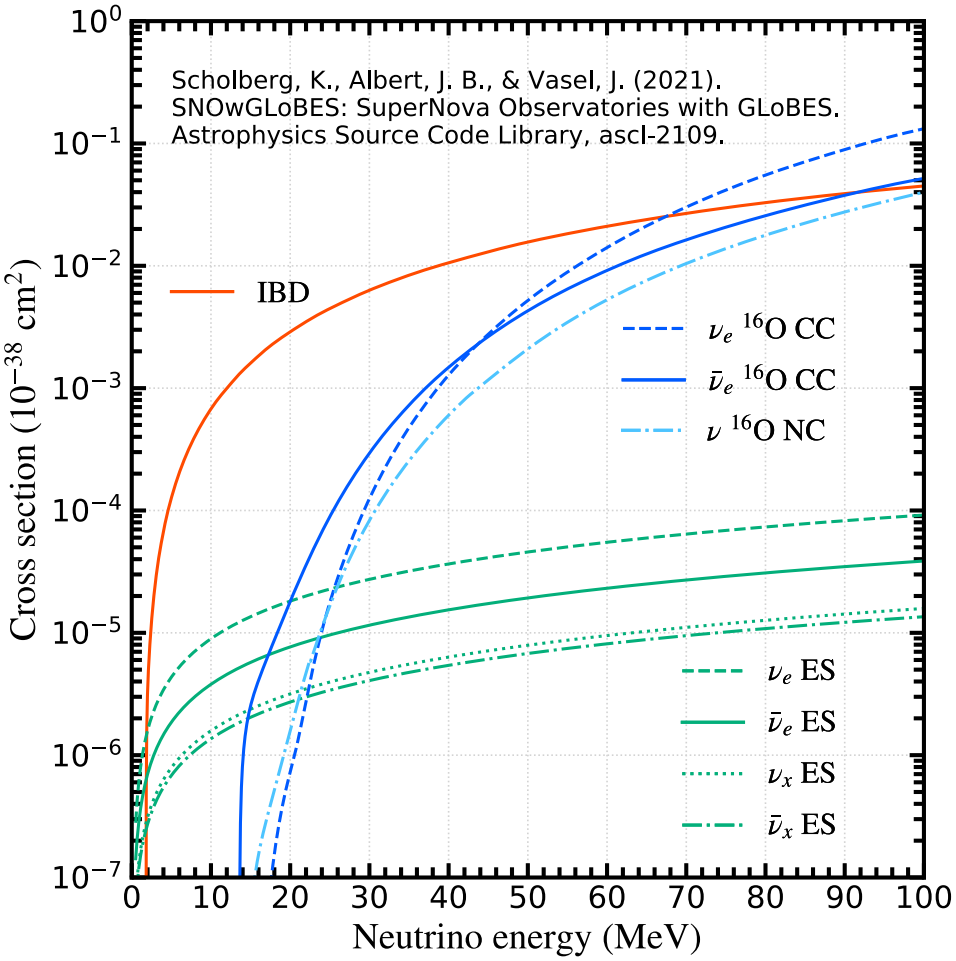

Figure 1.7: Cross sections of neutrino interactions in Super-Kamiokande as a function of neutrino energy. The solid red line represents the inverse beta decay (IBD) reaction. The blue lines represent the neutrino interactions with oxygen nuclei, and the green lines represent elastic scattering of neutrinos.

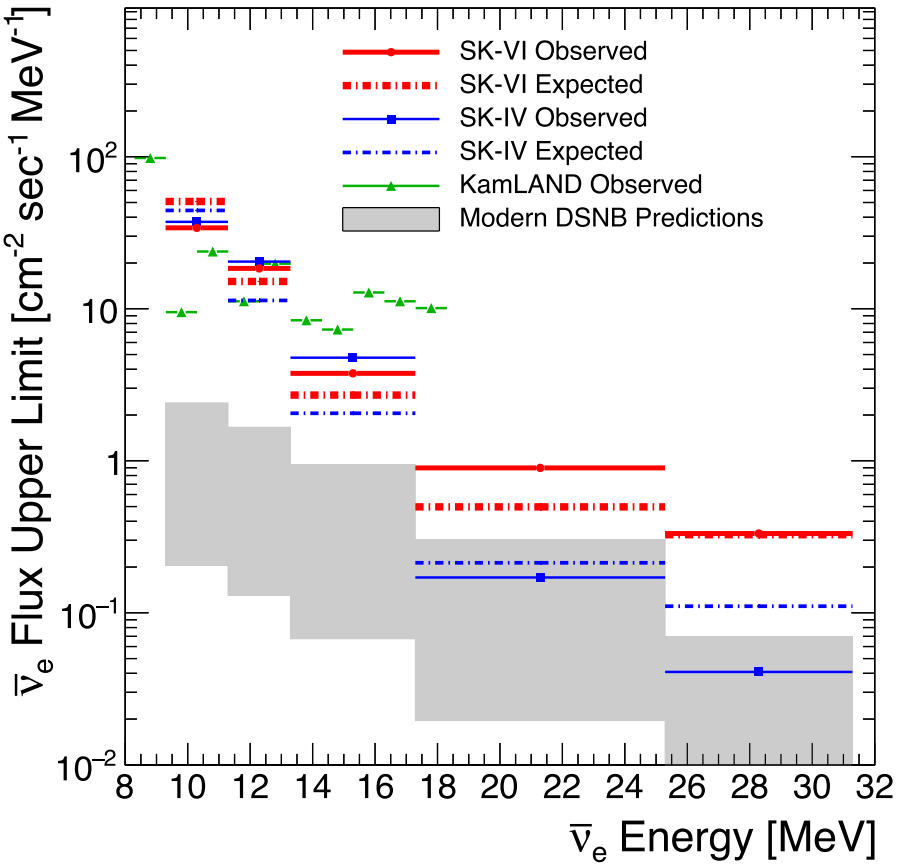

Figure 1.8: Upper limits of the $\bar{\nu}_e$ flux [26]. The red lines show the observed (solid) and expected (dotted-dashed) 90% confidence level (C.L.) upper limit for the period of August 2020 to June 2022 (552 days) in Super-Kamiokande (SK) with 0.01% Gd-loaded water. The blue lines show the observed (solid) and expected (dotted-dashed) 90% C.L. upper limit for the period of September 2008 to May 2018 (2970 days) in SK with ultra-pure water [24]. The green line shows observed 90% C.L. upper limit placed by KamLAND [27]. The gray-shaded region shows the range of the modern theoretical expectation, corresponding to Figure 1.5.

move through water at speeds faster than the speed of light in water. The light is detected by photomultiplier tubes (PMTs) installed on the inner wall of the detector (Chapter 3). The results for two observation periods of SK (SK-IV and SK-VI) are shown in Figure 1.8. Ref. [24] is the result of observations in SK with ultra-pure water for 2,970 days from September 2008 to May 2018 and Ref. [26] is in SK with 0.01% gadolinium (Gd)-loaded water for 552 days from August 2020 to June 2022. In the ultra-pure water period, a neutron is captured by a hydrogen nucleus (proton) after $\sim$200 μs on average, and a single γ ray is emitted with an energy of 2.2 MeV in this process. The neutron detection efficiency was $\sim$20% in SK with ultra-pure water. In 0.01% Gd-loaded water period, neutrons are captured on Gd at a fraction of $\sim$50% within $\sim$110 μs on average. Several γ rays totaling about 8 MeV are emitted after neutron capture on Gd. This can be clearly distinguished from the background consisting of environmental radiation and dark noise of PMTs. Therefore, the neutron-tagging efficiency is significantly improved by loading Gd in water. Ref. [26] is the first result of the SRN search in SK with Gd-loaded water. Despite the fact that the observation period is only about one-fifth of the ultra-pure water period, the sensitivity is comparable to the previous results thanks to high neutron detection efficiency. As the result of the observation in SK with ultra-pure water [24] and Gd-loaded water [26], no significant excess above the expected backgrounds was found, and the limit was set to the SRN $\bar{\nu}_e$ flux above 13.3 MeV.

In KamLAND, SRNs are searched for via the IBD reaction, as was done by SK. The KamLAND detector is filled with liquid scintillator with the volume of about one-twentieth of the SK detector. The scintillation light emitted from charged particles is detected by the PMTs mounted on the wall. The neutron from the IBD reaction is captured on hydrogen in the liquid scintillator and a γ ray is emitted with the energy of 2.2 MeV. Since the light intensity of scintillation emission (in KamLAND) is $\sim 10^3$ times larger than that of Cherenkov emission (in SK), the γ ray from neutron capture on a proton is identified with the efficiency of $\sim$100%. Ref. [27] is the result of observations in KamLAND for 4,528 days from May 2002 to July 2020. No significant excess over background model predictions was found, and a flux upper limit was set for the energy region below $\sim$10 MeV.

1.6 Cosmogenic Productions

The earth is exposed to cosmic-rays, mainly protons with energies widely distributed up to the TeV scale and above. Cosmic-rays interact with nuclei in the atmosphere to produce high-energy muons (cosmic-ray muons). The fraction of those muons reaches the Earth's surface before they decay due to relativistic effects. In experiments that require low background, such as neutrino observations and proton decay searches, the cosmic-ray muons are unavoidable backgrounds. In order to suppress the effects of cosmic-ray muons, those experimental detectors are often constructed deep underground. While, although the thick bedrock reduces the muon flux, cosmic-ray muons with energies above several hundred GeV can reach the detector. These muons interact with the medium in the detector and induce neutrons and unstable radioactive isotopes called cosmogenic products. The γ rays and electrons emitted due to neutrons and isotopes are backgrounds in MeV-scale neutrino observations or dark matter searches. The interaction between muons and nuclei above the several hundred GeV scale is a complex physical process including the hadron scattering with QCD, and reliable simulations have not yet been developed. Therefore, measurements of cosmogenic neutrons and isotopes give an important contribution to understanding the background in neutrino observations and to nuclear physics.

In this section, cosmic-ray muons, their interactions, and the productions of neutrons and radioactive isotopes are explained.

1.6.1 Cosmic-Ray

The Earth's atmosphere is constantly exposed to high-energy particles called "cosmic-rays". Cosmic rays contain $\sim$90% protons, $\sim$9% alpha particles (helium nuclei), and $\sim$1% other particles. The

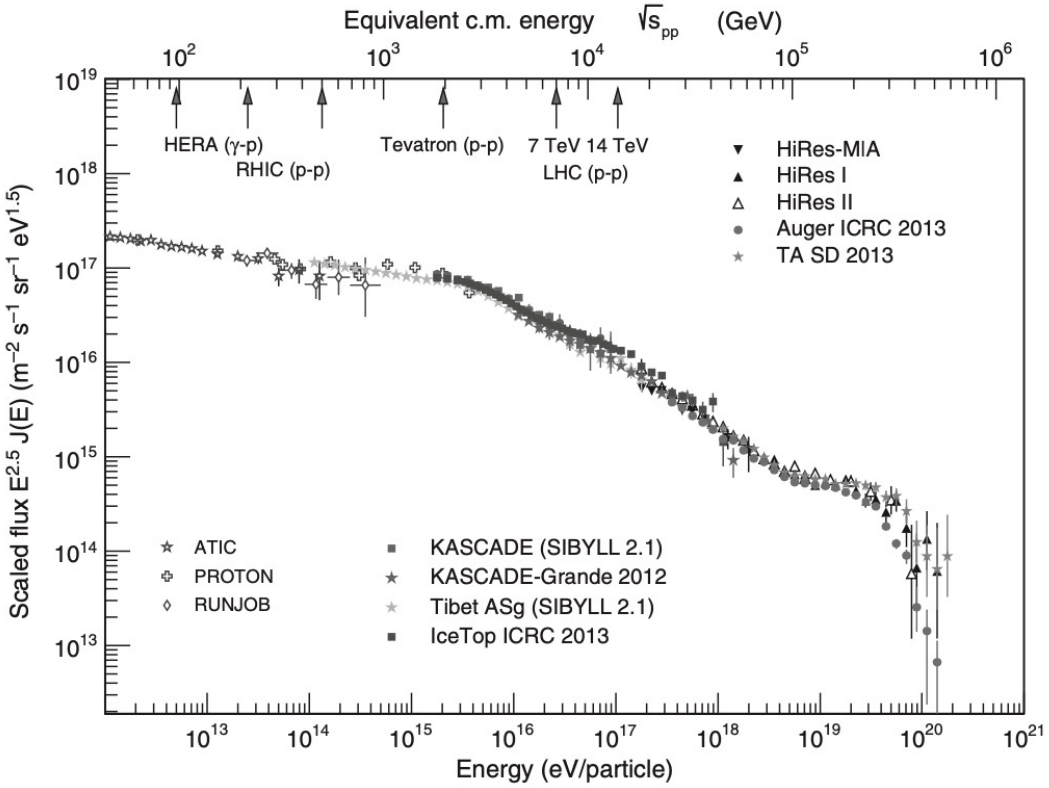

Figure 1.9: Energy spectrum of the primary cosmic-rays [29].

energy spectrum of primary cosmic-rays is shown in Figure 1.9. It shows above 1 GeV, which is relevant to the measurement described in this thesis. The intensity of primary cosmic-ray is approximated as follows:

$$\frac{dN}{dE} \propto E^{-(\gamma+1)}, \tag{1.11}$$

where N is the number of nucleons and E is total energy of nucleons. γ is the integral spectral index determined by observations and depends on the energy regions as follows [28]:

$$\gamma \simeq \begin{cases} 1.7 & (E < 10^6\,\mathrm{GeV}) \\ 2.0 & (10^6 \leq E < 10^9\,\mathrm{GeV}) \\ 1.6 & (E \geq 10^9\,\mathrm{GeV}). \end{cases} \tag{1.12}$$

Cosmic-ray Muon Production

Primary comic-rays interact with nuclei in the atmosphere and produce hadrons. The hadrons produced are mainly pions and kaons. Those pions and kaons have short lifetime and decay to muons and muon neutrinos at ∼15 km above the ground.

$$\pi^{\pm} \to \mu^{\pm} + \nu_{\mu}(\bar{\nu}_{\mu}) \ (\sim 100\%) \tag{1.13}$$

$$K^{\pm} \to \mu^{\pm} + \nu_{\mu}(\bar{\nu}_{\mu}) \ (\sim 64\%) \tag{1.14}$$

These muons are called “cosmic-ray muons”. Figure 1.10 shows the schematic illustration of cosmic-ray muon productions. Muons are the most numerous charged particle at sea level. Muons have a lifetime of 2.2 μs at the rest frame and decay through weak interactions into electrons and neutrinos as follows.

$$\mu^{\pm} \to e^{\pm} + \nu_e(\bar{\nu}_e) + \bar{\nu}_{\mu}(\nu_{\mu}) \tag{1.15}$$

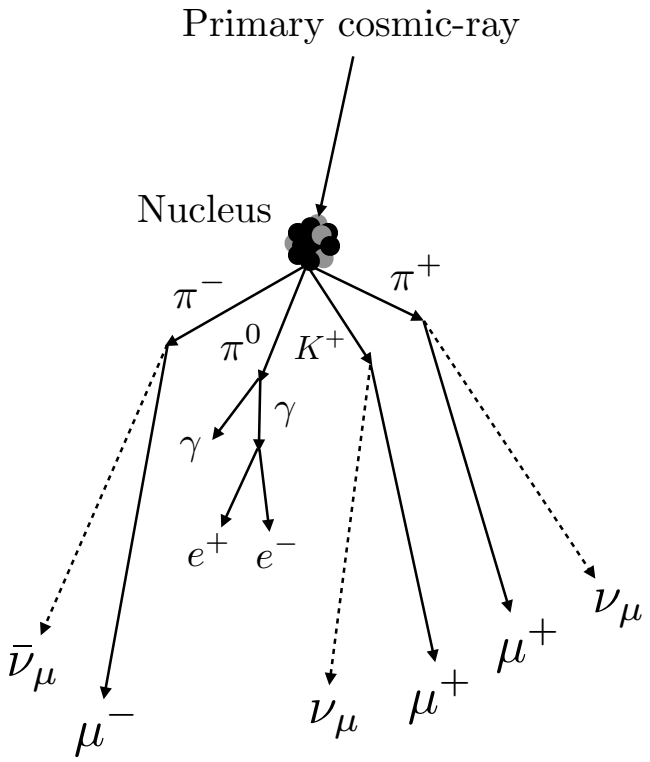

Figure 1.10: Schematic illustration of cosmic-ray muon productions.

Since the muons travel at nearly the speed of light, relativistic effects slow the progress of intrinsic time, allowing them to reach the ground surface if they have sufficiently high energy, typically above GeV scale.

The approximate extrapolation formula of the cosmic-ray muon flux at sea level is introduced by T. Gaisser [30] based on calculations from primary cosmic-ray flux as follows:

$$\frac{dN_\mu}{dE_\mu} = 0.14 \left(\frac{E_\mu}{\mathrm{GeV}}\right)^{-2.7} \left(\frac{1}{1 + \frac{1.1 E_\mu \cos\theta}{115\,\mathrm{GeV}}} + \frac{0.054}{1 + \frac{1.1 E_\mu \cos\theta}{850\,\mathrm{GeV}}} \right), \tag{1.16}$$

where N_μ is the number of muons, E_μ is the muon energy in GeV, and θ is the zenith angle. Here, this formula is valid under the two conditions: (1) muon decay is negligible ($E_\mu > 100/\cos\theta\,\mathrm{GeV}$) and (2) the curvature of the Earth can be neglected ($\theta < 70°$). In the formula, the contributions from charged pions and kaons are considered, while the contributions from charm and heavier particles are negligible below ~10 TeV. Figure 1.11 shows muon spectra at $\theta = 0°$ and 75°, in which compared of the results from Eq. (1.16) and measurements are compared. For the large zenith angle ($\theta > 70°$), the standard Gaisser formula does not reproduce the measurement results. Therefore, the modified Gaisser parametrizations are also proposed in Ref. [31].

Muon Energy Loss

Because the Earth's surface is exposed to cosmic-ray muons, detectors used in experiments for particle physics are often constructed deep underground to avoid the effect of cosmic-ray muons. Magnitude of the suppression will be explained later in this section. Charged particles, including muons, loses the energy in materials through ionization and radiative processes. Figure 1.12 shows the rate of energy loss for positive muons in copper as a function of the momentum.

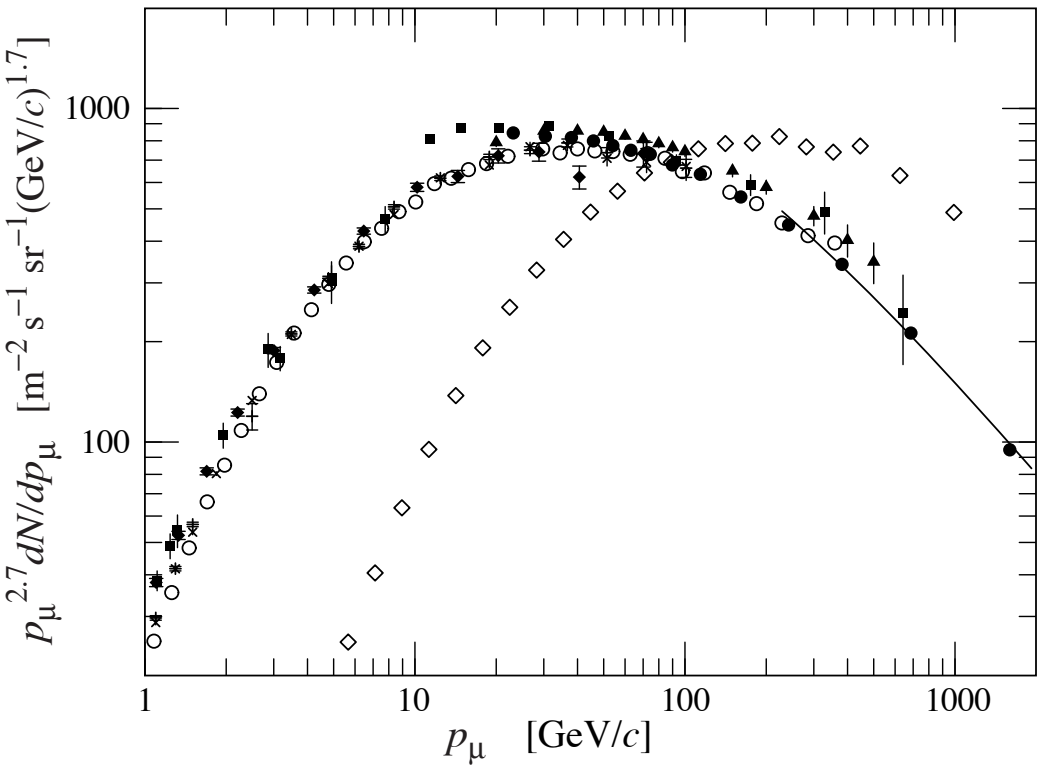

Figure 1.11: Spectrum of muons at zenith angle $\theta = 0°$ (points other than white rhombuses) and $\theta = 75°$ (white rhombuses) at sea level. The solid line is the result from Eq. (1.16) at $\theta = 0°$ [32].

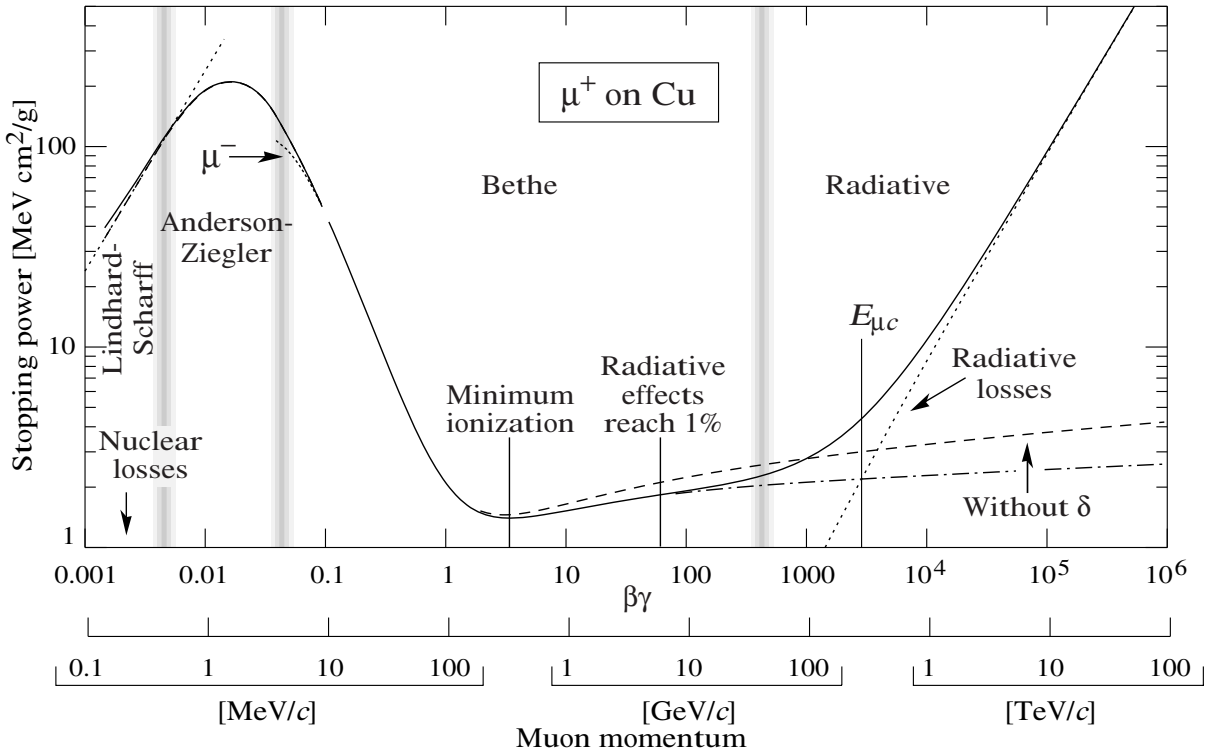

Figure 1.12: The rate of energy loss for positive muons in copper as a function of momentum [32]. The solid line is the total energy losses.

Table 1.4: Summary of variables used in the Bethe formula.

Variable	Definition	Units or Value
E	Incident particle energy	MeV
x	Travel length	cm
v	Speed of particle from a stationary system	
c	Speed of light	$2.998 \times 10^8\,\mathrm{m\,s^{-1}}$
β	v/c	
γ	Lorentz factor $1/\sqrt{1-\beta^2}$	
m_e	Electron mass	$0.511\,\mathrm{MeV}/c^2$
r_e	Classical electron radius	2.82 fm
N_A	Avogadro's number	$6.02 \times 10^{23}\,\mathrm{mol^{-1}}$
ze	Charge of incident particle	
Z	Atomic number	
A	Atomic mass	$\mathrm{g\,mol^{-1}}$
K/A	$4\pi N_A r_e^2 m_e c^2/A$	$0.307\,\mathrm{MeV\,g^{-1}\,cm^2}$ for $A = 1\,\mathrm{g\,mol^{-1}}$
$T_{\max}$	Maximum energy transfer possible in a single collision	MeV
I	Mean excitation energy	eV
$\delta(\beta\gamma)$	Density effect correction to ionization energy loss	

Ionization process The ionization processes are dominant below ∼100 GeV, corresponding to the "Bethe" region of Figure 1.12. When charged particles pass through materials, the electric field of the charged particles causes to ionize or excite the atoms in the materials. If an electron in the atom or molecule receives energy from charged particles and the energy received is greater than the binding energy of electrons, the electron is ejected from the atom or molecule. On the other hand, if the energy received is less than the binding energy of the electron, the atom or molecule are excited. The mean rate of energy loss for charged particles is described by the Bethe formula,

$$-\frac{dE}{dx} = Kz^2\frac{Z}{A}\frac{1}{\beta^2}\left[\frac{1}{2}\ln\frac{2m_e c^2\beta^2\gamma^2 T_{\max}}{I^2} - \beta^2 - \frac{\delta(\beta\gamma)}{2}\right]. \tag{1.17}$$

The variables used in the Bethe formula are summarized in Table 1.4. When charged particles travel through matter at speeds greater than ∼96% of the speed of light (corresponding to "Minimum ionization" threshold of Figure 1.12), the energy loss of the particles becomes a nearly constant value, $\sim 2\,\mathrm{MeV\,g^{-1}\,cm^2}$. Charged particles with the energy loss in matter close to the possible minimum value are called minimum ionization particles (MIPs). Cosmic-ray muons in GeV scale are known as typical particle in this category.

Radiative process The radiative processes are more important than ionization above ∼100 GeV, corresponding to the "Radiative" region of Figure 1.12. In this process, muons induces photons, electromagnetic showers, and hadronic showers via the electromagnetic and strong interactions in materials. The average rate of energy loss is written as

$$-\frac{dE}{dx} = a(E) + b(E)E, \tag{1.18}$$

where $a(E)$ is the energy loss by the ionization processes given by Eq. (1.17) and $b(E)E$ is the radiative contributions. The radiative process consists of the three contributions; bremsstrahlung, direct e^+e^- pair production, and photonuclear reaction. When a muon is suddenly slowed or its path is bent in electric fields in materials, photons are radiated. This radiation is called bremsstrahlung. In the e^+e^- pair production, a muon emit a virtual photon, which produces a pair of electrons

and positrons in the Coulomb field of the nucleus. In the photonuclear reaction (photodisintegration), a muon interacts with a nucleus via a virtual photon, and then hadrons are emitted. Figure 1.13 shows $b(E)$ as a function of the muon energy E and the contributions for each radiative process in the $b(E)$. In the region of $E \gtrsim 100\,\mathrm{GeV}$, the term $b(E)E$ is dominant because of $a(E) \simeq 2\,\mathrm{MeV\,g^{-1}\,cm^2}$.

Muon Flux Underground

If the detector is located deep underground, cosmic-ray muons lose energy in rock before they reach the detector due to the above interactions. Therefore, the flux underground is suppressed compared to the surface. The muon intensity is described as a function of a slant depth as

$$I(h) = I_1 e^{-h/\lambda_1} + I_2 e^{-h/\lambda_2}, \tag{1.19}$$

where $I(h)$ is the muon intensity at the slant depth, h [34]. The parameters in Eq. (1.19) are determined using the experimental data in Figure 1.14, $I_1 = (8.60 \pm 0.53) \times 10^{-6}\,\mathrm{cm^{-2}\,s^{-1}\,sr^{-1}}$, $I_2 = (0.44 \pm 0.06) \times 10^{-6}\,\mathrm{cm^{-2}\,s^{-1}\,sr^{-1}}$, $\lambda_1 = 0.45 \pm 0.01\,\mathrm{km.w.e.}$, and $\lambda_2 = 0.87 \pm 0.02\,\mathrm{km.w.e.}$ Here, the unit km.w.e. (kilo-meter water equivalent) is the conversion of general depth to water depth. As a well-known guide, cosmic-ray muons fall at a frequency of $\sim 1\,\mathrm{s^{-1}}$ on a palm-sized area ($\sim 100\,\mathrm{cm^2}$) at the Earth's surface. The flux of cosmic-ray muons is suppressed to 10^{-5} of the ground surface at 1,000 m underground (2,700 m.w.e.) where the Super-Kamiokande detector is located. As a result, about two muons per second enter the SK detector although the surface area on the top of the detector is $\sim 10^7\,\mathrm{cm^2}$. Not only the muon flux but also the average muon energy correlates with the depth from the surface. The deeper underground, the higher the energy required to reach that depth. Figure 1.15 shows the muon energy spectra in various underground sites with several km.w.e. overburden. For each site, The spectrum extends to above 10^3 GeV and the average muon energy is several hundred GeV.

1.6.2 Cosmogenic Neutrons

Neutron Production Process

Cosmogenic neutrons (muon-induced neutrons), the target of this study, refer to neutrons produced by cosmic-ray muons and the secondary particles caused by them. The production processes are described as follows.

(a) Muon spallation:
Muons directly interact with nuclei via the exchanging of a virtual photon or Z-boson. Nucleons and mesons (e.g. neutrons and pions) are emitted subsequently. The diagram of muon spallation is shown in Figure 1.16.

(b) Photonuclear reaction:
As described in Section 1.6.1, the radiation loss is dominant in the energy region above $\sim 100\,\mathrm{GeV}$. When a muon passes through materials, the muon direction is bent due to the Coulomb field created by the nucleus. Then muons lose the energy and photons are emitted by bremsstrahlung. These photons interact with electrons in matter via the photoelectric effect, Compton scattering, and e^+e^- pair production. These processes produce electromagnetic showers, which are composed of electrons, positrons, and photons. Among those, high-energy photons are often absorbed by nuclei via the photonuclear reactions, and then nucleons and mesons are produced. The diagram of photonuclear reaction is shown in Figure 1.17.

(c) Hadron spallation:
High-energy pions produced in the process (a) and (b) interact with the nucleus via pion absorption and pion-nuclear scattering, emitting a large number of high-energy nucleons and

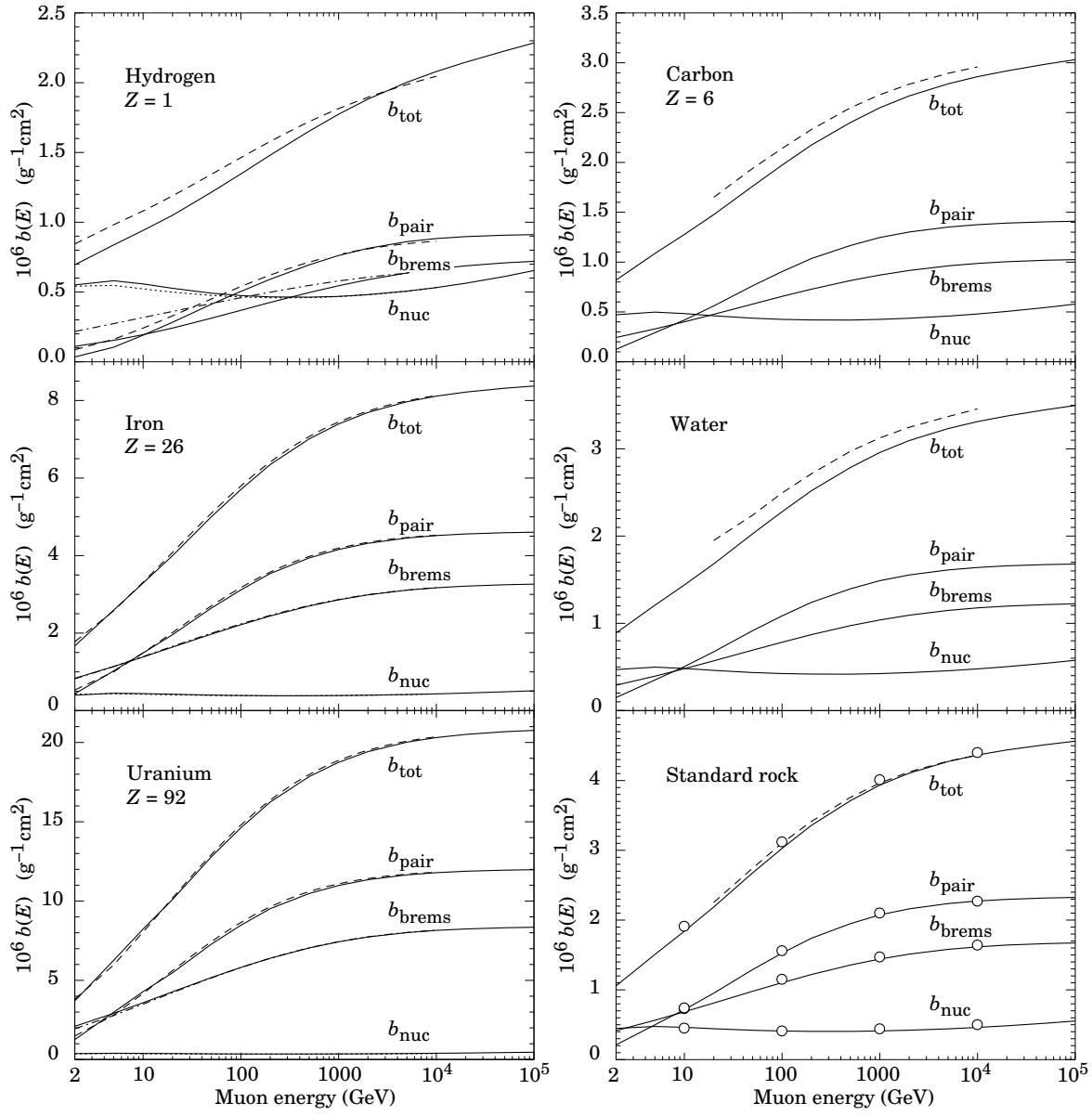

Figure 1.13: $b(E)$ as a function of the muon energy E and each contribution for bremsstrahlung (b_{brems}), e^+e^- pair production (b_{pair}), and photonuclear reaction (b_{nuc}) in some materials [33].

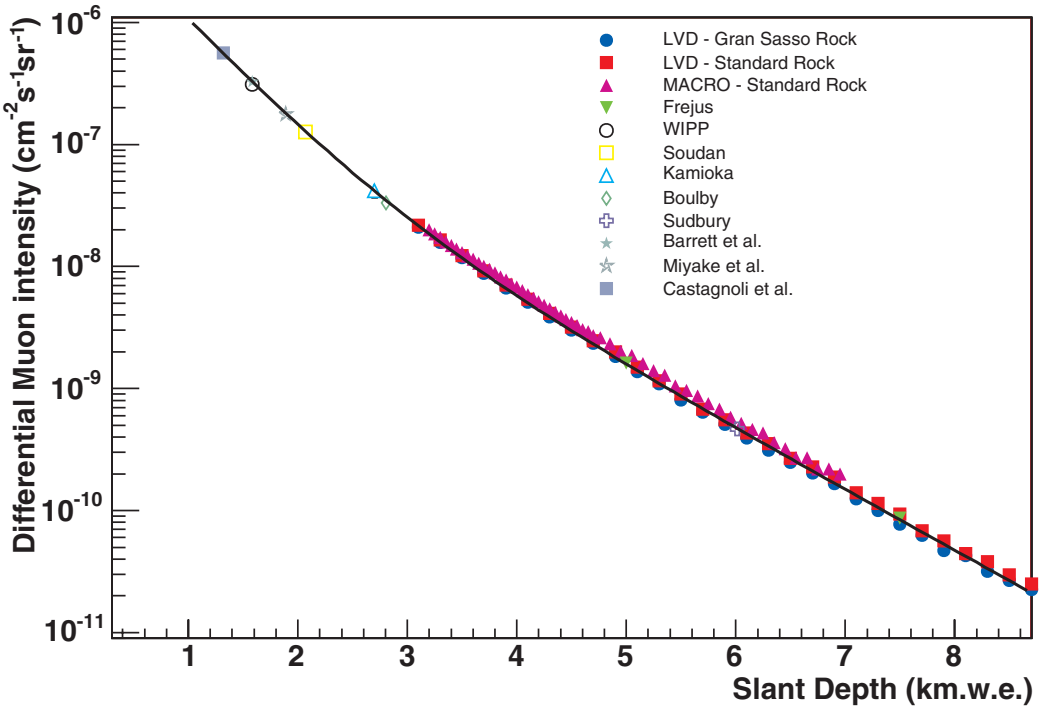

Figure 1.14: Correlation between intensity of cosmic-ray muons and the slant depth for different underground sites [34]. The points are experimental data and the solid line is Eq. (1.19).

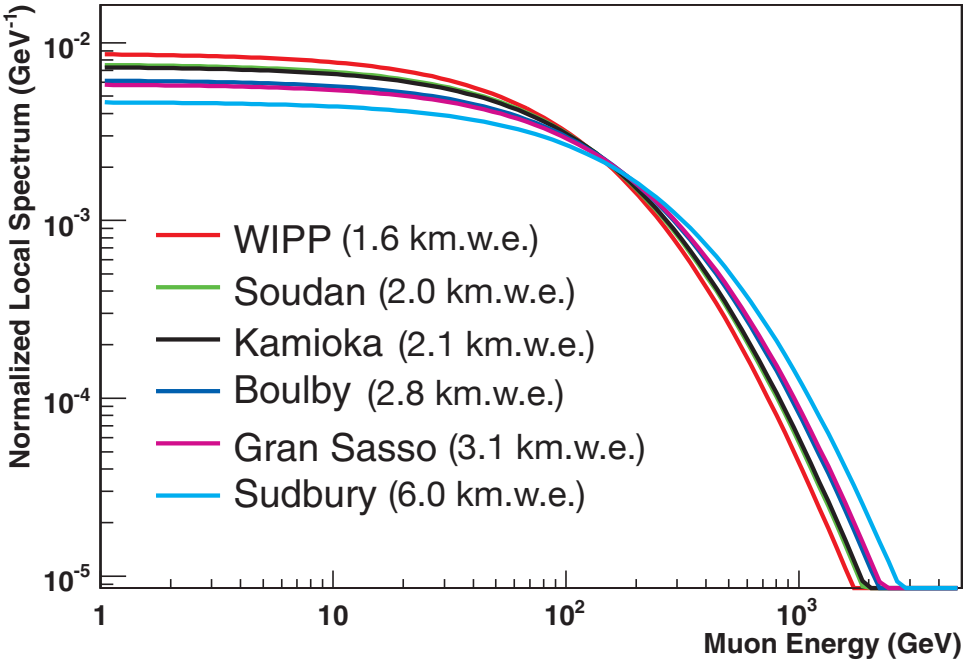

Figure 1.15: Energy spectra of cosmic-ray muons reach various underground sites [34]. The equivalent vertical depth relative to a flat overburden for each site are added as Ref. [34].

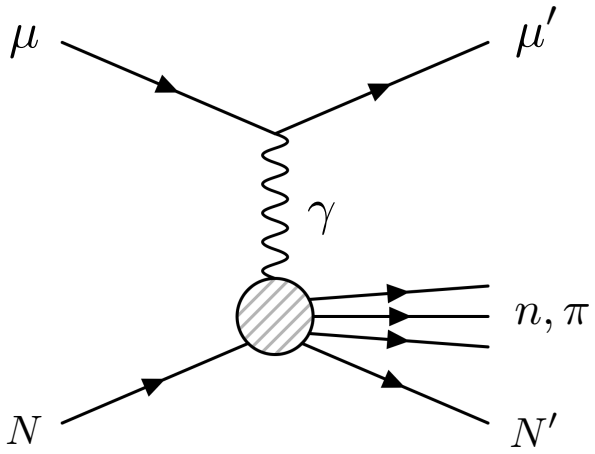

Figure 1.16: Diagram of muon spallation [35].

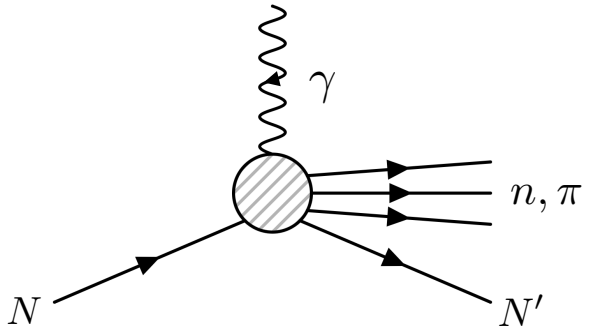

Figure 1.17: Diagram of photonuclear reaction [35].

pions. These secondary particles interact with other nuclei, repeating the same process, and the number of nucleons and mesons increase accordingly. These cross sections are not well understood and this process makes it difficult to evaluate neutron production by simulation.

(d) Muon capture:
When a negative muon is slowed down in materials, the muon is captured by a proton in a nucleus via a W-boson. The proton is transferred into the neutron and a muon neutrino is produced as

$$\mu^- + p \rightarrow \nu_\mu + n. \tag{1.20}$$

The diagram of muon capture is shown in Figure 1.18. In case nucleus is excited, a de-excitation γ ray is emitted.

Figure 1.19 shows the simulated energy spectrum of neutrons induced in C_nH_{2n} by 280 GeV muons. The spectrum extends to ~1 GeV. The photonuclear reaction of γ ray and nucleon is dominant below the neutron energy of ~40 MeV, while the pion spallation is dominant above that energy.

Neutrons induced by cosmic-ray muons lose the energy in material via the interaction with nuclei, and finally they are captured by nuclei. Various types of nuclear interaction occur in material, depending on the type of nucleus and the energy of the neutrons. Above several tens of MeV, the initial energy of muon-induced neutrons, neutrons knock out nucleons and nuclei via the inelastic scattering. In particular, when a neutron imparts significant energy to a nucleus, multiple neutrons, protons, and alpha particles are released. Neutrons further lose the energy through multiple scatterings and reach thermal equilibrium with the thermal motion of the atom.

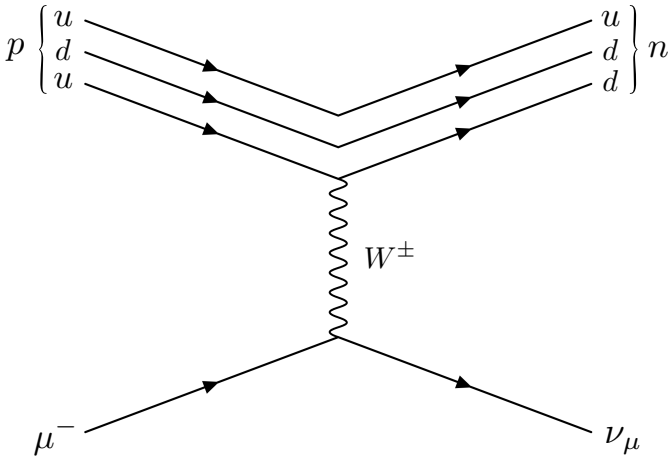

Figure 1.18: Diagram of muon capture.

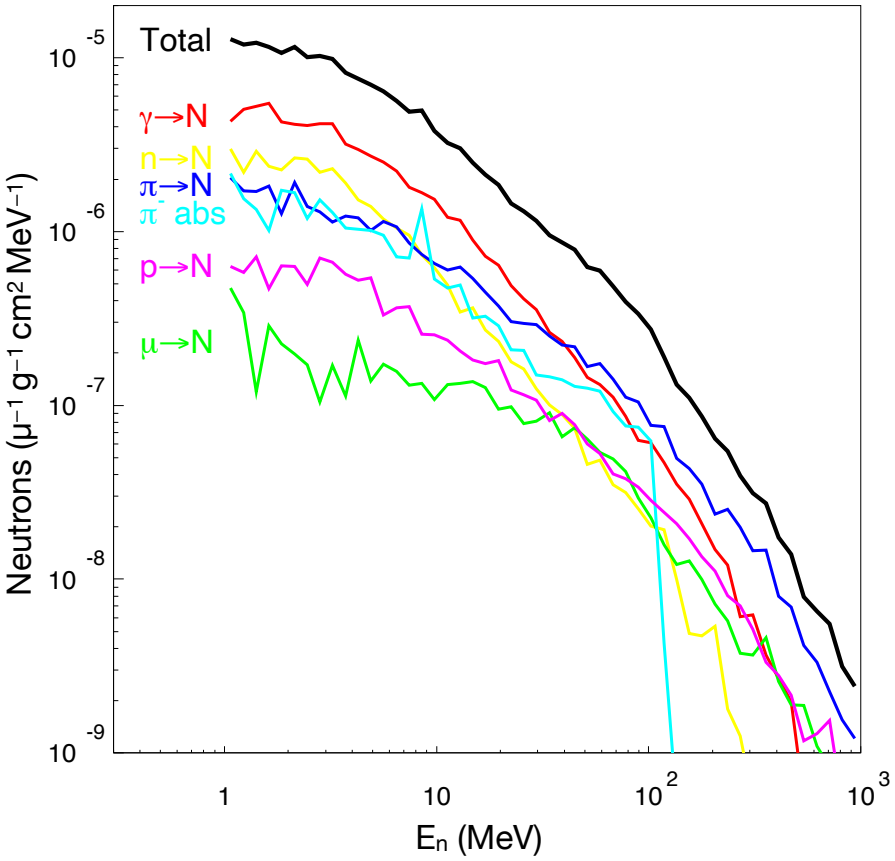

Figure 1.19: Simulated energy spectrum neutrons induced in C_nH_{2n} by 280 GeV muons [36], which is shown as the black line. The contributions of the neutron production processes are also shown: photonuclear reaction ($\gamma \rightarrow N$), neutron scattering ($n \rightarrow N$), pion spallation ($\pi \rightarrow N$), pion absorption (π^- abs), proton spallation ($p \rightarrow N$), and muon spallation ($\mu \rightarrow N$).

Table 1.5: Measurements of the neutron yield Y_n in different experiments. $\langle E_\mu \rangle$ is average of muon energy at the detector. LS represents organic liquid scintillator.

Experiment	Target	Depth (m.w.e.)	$\langle E_\mu \rangle$ (GeV)	Y_n (μ^{-1}g^{-1}cm^2)
Hertenberger [37]	LS	20	13	$(2 \pm 0.7) \times 10^{-5}$
Bezrukov [38]	LS	25	14.7	$(4.7 \pm 0.5) \times 10^{-5}$
Boehm [39]	LS	32	16.5	$(3.6 \pm 0.3) \times 10^{-5}$
Bezrukov [38]	LS	316	55	$(1.21 \pm 0.12) \times 10^{-4}$
Aberdeen [40]	LS	611	90	$(1.19 \pm 0.22) \times 10^{-4}$
Enikeev [41]	LS	750	120	$(2.15 \pm 0.15) \times 10^{-4}$
Daya Bay [42]	LS	860	143	$(1.70 \pm 0.12) \times 10^{-4}$
KamLAND [43]	LS	2700	260	$(2.8 \pm 0.3) \times 10^{-4}$
LVD [44]	LS	3100	270	$(4.5 \pm 1.2) \times 10^{-4}$
Borexino [45]	LS	3800	283	$(3.1 \pm 0.1) \times 10^{-4}$
SNO [46]	D_2O	5890	363	$(7.28^{+1.59}_{-1.12}) \times 10^{-4}$

These neutrons are called thermal neutrons. The thermal energy of the nucleus is $k_B T$, where k_B represents the Boltzmann constant, 8.6×10^{-5} eV/K, and T is the thermodynamic temperature. The typical kinetic energy of thermal neutrons is about 25 meV at room temperature ($T \sim 300$ K). When thermalized neutrons are captured by nuclei in the materials, the nuclei are excited, and then γ rays are emitted when the excited nuclei transition to the ground state. In this study, neutron capture interactions on gadolinium are observed as described in Section 3.7.

Cosmogenic Neutron Yield

Neutrons produced via the muon spallation and following inelastic scattering have been measured in several experiments. In practice, γ rays emitted from neutron capture are detected by liquid scintillator and water Cherenkov detectors constructed underground. The amount of cosmogenic neutrons is evaluated using the neutron yield. Neutron yield Y_n is defined as the number of neutrons produced per muon, per unit muon path length, and per density of the target material:

$$Y_n = \frac{N_n}{N_\mu L_\mu \rho}, \tag{1.21}$$

where N_n is the amount of neutrons captured by nuclei in the detector. N_μ is the number of muons entering the detector, L_μ is the average track length of the muons, and ρ is the density of the medium. The unit of the neutron yield is expressed as follows:

$$\frac{\text{neutrons}}{\text{muons} \times \text{cm} \times \text{g/cm}^3} = \mu^{-1}\text{g}^{-1}\text{cm}^2, \tag{1.22}$$

where μ^{-1} represents "per muon". The measurements of the neutron yield are listed in Table 1.5. Several experiments have measured cosmogenic neutron production yields at various depths with different muon energies. Most of these measurements were made with organic liquid scintillator, which contains mostly carbon and hydrogen. Among those, the majority of neutrons are produced via cosmic-ray muon spallation interactions with carbon nuclei. While, the measurement in water is limited and SNO is the only experiment that measured the neutron yield using heavy water (D_2O) [46]. In a water-based detector, the neutrons are produced via the muon spallation interactions with oxygen nuclei. Figure 1.20 shows the measurement results from various experiments shown in Table 1.5. The overlaid dashed lines are the models assumed in the FLUKA-based simulations for cosmogenic neutron productions and propagation [47, 48], in which the neutron yield is calculated as $Y_n = aE_\mu^b$ with the parameter to reproduce experiment results. The FLUKA-based simulations are developed for the precise estimation of the cosmogenic neutron background in rare

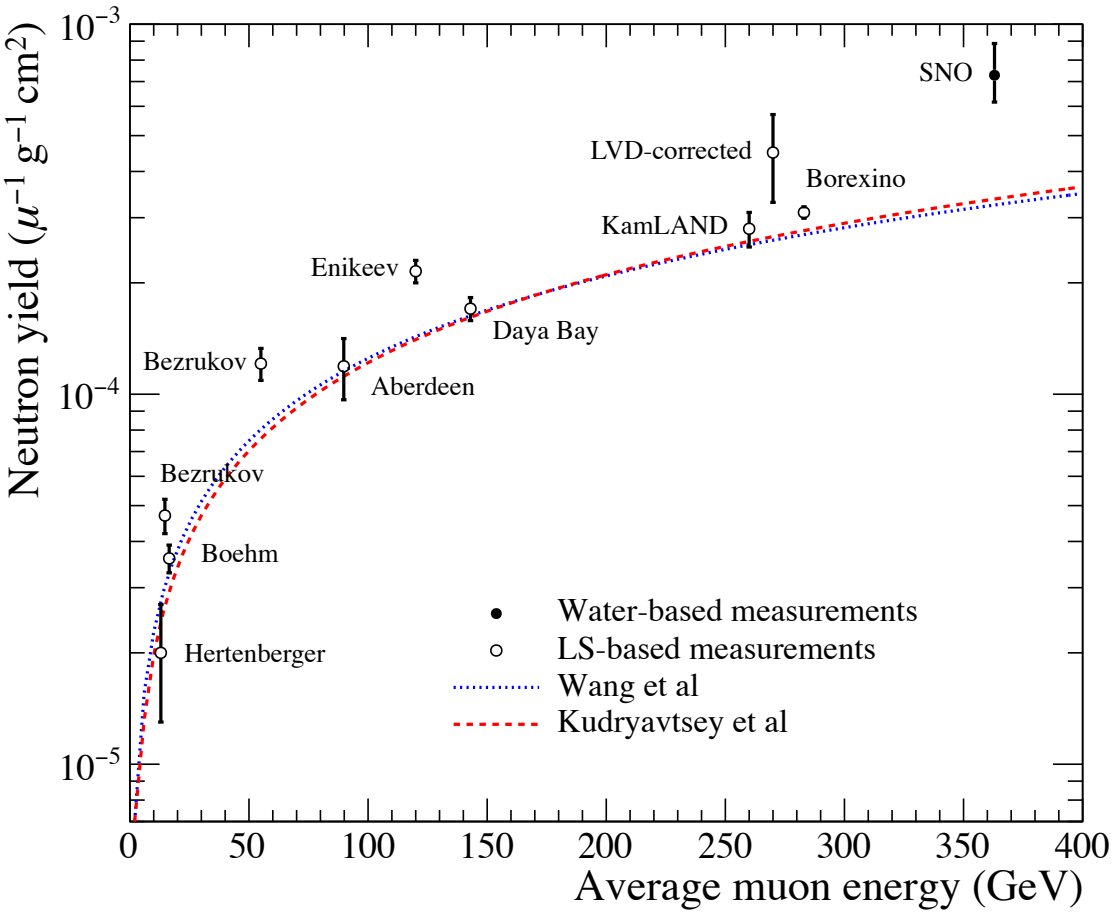

Figure 1.20: Comparison between the previous measurement results [37–46] and predictions for liquid scintillator with FLUKA-based simulations calculated by Wang et al [47] (blue dotted line) and Kudryavtsey et al [48] (red dashed line). The open circles represent the liquid scintillator-based (LS-based) results and the filled circles represent the water-based results.

event searches such as neutrino observation and dark matter search. Therefore, additional experimental data will lead to improving the FLUKA-based simulation and more reliable estimation of the cosmogenic neutron background.

In this study, neutron yield in water is measured using the Super-Kamiokande detector. This measurement can be compared with that from the SNO experiment which measured the neutron yield in heavy water at the different depth with different muon energy. In addition, this measurement can be also compared with that from the KamLAND detector which measured the neutron yield in liquid scintillator at the same depth as the SK detector.

1.6.3 Cosmogenic Isotopes

Isotopes Produced in Water

Cosmic-ray muons induce not only neutrons but also various radioactive isotopes through the interactions with oxygen nuclei. The isotopes produced in water are predicted using FLUKA-simulation by Ref. [49] and summarized in Table 1.6. Figure 1.21 shows the half-lives and predicted yield above 3.5 MeV (corresponding to the energy threshold of SK). Isotopes that emit electrons with neutrons via β decay are especially indicated in Figure 1.21 (red circles); ^{8}He, ^{9}Li, ^{11}Li, and ^{16}C. The $\beta + n$ decay of those isotopes cannot be distinguished from inverse beta decay (IBD) reaction by $\bar{\nu}_e$ ($\bar{\nu}_e + p \rightarrow e^+ + n$). Therefore, those isotopes are major background sources for SRN

Table 1.6: Radioactive isotopes induced by cosmic-ray muon spallation; the fourth column is the end point kinetic energy of the emitted electrons (or positrons) [49, 50].

Isotope	Life time (s)	Decay mode	Q-value (MeV)	Production process
^{11}Be	19.9	β^- (55%)	11.51	$^{16}\mathrm{O}(n, \alpha + 2p)^{11}\mathrm{Be}$
		$\beta^-\gamma$ (31%)	$9.41 + 2.10(\gamma)$	
^{16}N	10.3	β^- (66%)	10.44	$^{16}\mathrm{O}(n, p)^{16}\mathrm{N}$
		$\beta^-\gamma$ (28%)	$4.27 + 6.13(\gamma)$	
^{15}C	3.53	β^- (63%)	9.77	$^{16}\mathrm{O}(n, 2p)^{15}\mathrm{C}$
		$\beta^-\gamma$ (37%)	$4.51 + 5.30(\gamma)$	
^{8}Li	1.21	β^-	~13.0	$^{16}\mathrm{O}(\pi^-, \alpha + {}^2\mathrm{H} + p + n)^{8}\mathrm{Li}$
^{8}B	1.11	β^+	~13.9	$^{16}\mathrm{O}(\pi^+, \alpha + 2p + 2n)^{8}\mathrm{B}$
^{16}C	1.08	$\beta^- + n$	~4	$^{18}\mathrm{O}(\pi^-, n + p)^{16}\mathrm{C}$
^{9}Li	0.26	β^- (49%)	13.6	$^{16}\mathrm{O}(\pi^-, \alpha + 2p + n)^{9}\mathrm{Li}$
		$\beta^- + n$ (51%)	~10	
^{9}C	0.18	$\beta^- + p$	3–15	$^{16}\mathrm{O}(n, \alpha + 4n)^{9}\mathrm{C}$
^{8}He	0.17	$\beta^-\gamma$ (84%)	$9.67 + 0.98(\gamma)$	$^{16}\mathrm{O}(\pi^-, {}^3\mathrm{H} + 4p + n)^{8}\mathrm{He}$
		$\beta^- + n$ (16%)		
^{12}Be	0.034	β^-	11.71	$^{18}\mathrm{O}(\pi^-, \alpha + p + n)^{12}\mathrm{Be}$
^{12}B	0.029	β^-	13.37	$^{16}\mathrm{O}(n, \alpha + p)^{12}\mathrm{B}$
^{13}B	0.025	β^-	13.44	$^{16}\mathrm{O}(\pi^-, 2p + n)^{13}\mathrm{B}$
^{14}B	0.020	$\beta^-\gamma$	$14.55 + 6.09(\gamma)$	$^{16}\mathrm{O}(n, 3p)^{14}\mathrm{B}$
^{12}N	0.016	β^+	16.38	$^{16}\mathrm{O}(\pi^+, 2p + 2n)^{12}\mathrm{N}$
^{13}O	0.013	$\beta^+ + p$	8–14	$^{16}\mathrm{O}(\mu^-, \mu^- + p + 2n + \pi^-)^{13}\mathrm{O}$
^{11}Li	0.012	β^- (6%)	20.62	$^{16}\mathrm{O}(\pi^+, 5p + \pi^0 + \pi^+)^{11}\mathrm{Li}$
		$\beta^- + n$ (86%)	~16	

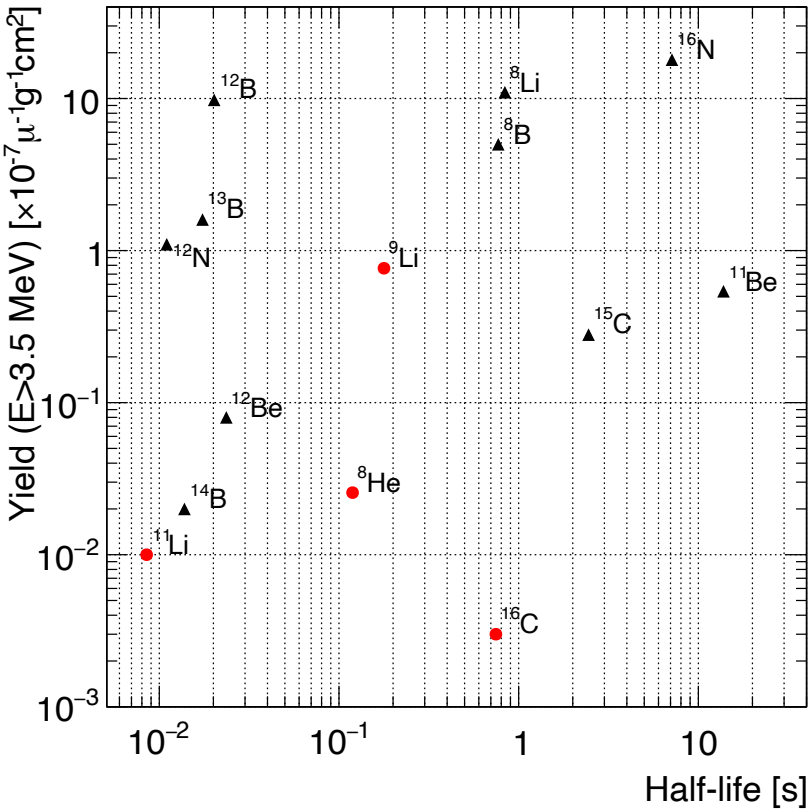

Figure 1.21: Half-lives and predicted yield above 3.5 MeV [51]. The yields for each isotope are predicted by Ref. [49]. The red circles represent isotopes which emit electron with neutron. The black triangles represent isotopes which emit only electron.

search. Among those, ^{9}Li has a relatively large yield, a high branching ratio of $\beta + n$ decay, and a long lifetime which makes it difficult to reject using the time correlation with muon. On the other hand, ^{8}He yield is less than one-tenth of ^{9}Li yield, and ^{8}He has a lower branching ratio of $\beta + n$ decay ($\sim$16%). ^{11}Li has a short lifetime and strong timing correlation with the cosmic-ray muons. The yield of ^{16}C is much less than those of other isotopes. Therefore, ^{9}Li is the major background source among those isotopes.

Lithium-9 Background for SRN Searches

Figure 1.22 shows the comparison of SRN signal and ^{9}Li decay. The SK-Gd experiment observes SRNs through the coincidence of the IBD reaction of $\bar{\nu}_e$ and the neutron capture reaction on Gd. Several γ rays with a total energy of about 8 MeV are emitted after neutron capture on Gd. On the other hand, the ^{9}Li emits an electron and a neutron via β decay at a branching ratio of 50.8% (^{9}Li $\beta + n$ decay event) as shown in Figure 1.23. These ^{9}Li $\beta + n$ decay event cannot be distinguished from the IBD signal. For the SRN search in SK, the muon-induced isotopes are eliminated using the distance between the muon track and decay positions of isotopes. However, a certain rate of isotopes remain and become the major background in SRN search below $\sim$15 MeV as shown in Figure 1.24.

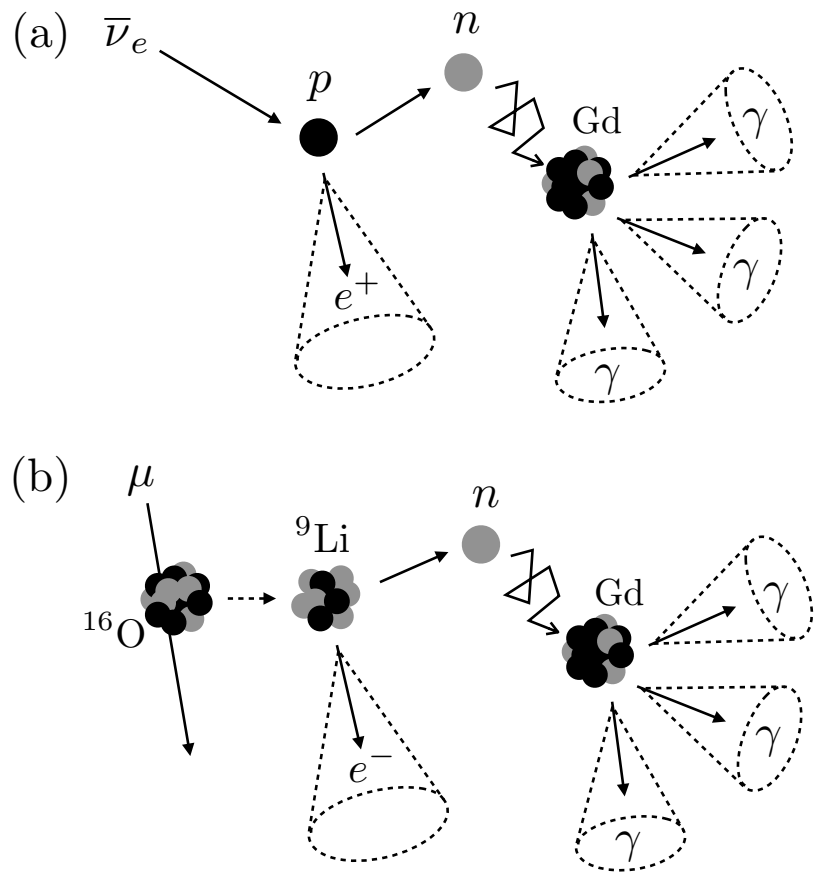

Figure 1.22: Schematic illustration of (a) the IBD event of SRN ($\bar{\nu}_e$) and (b) the ^{9}Li $\beta + n$ decay event.

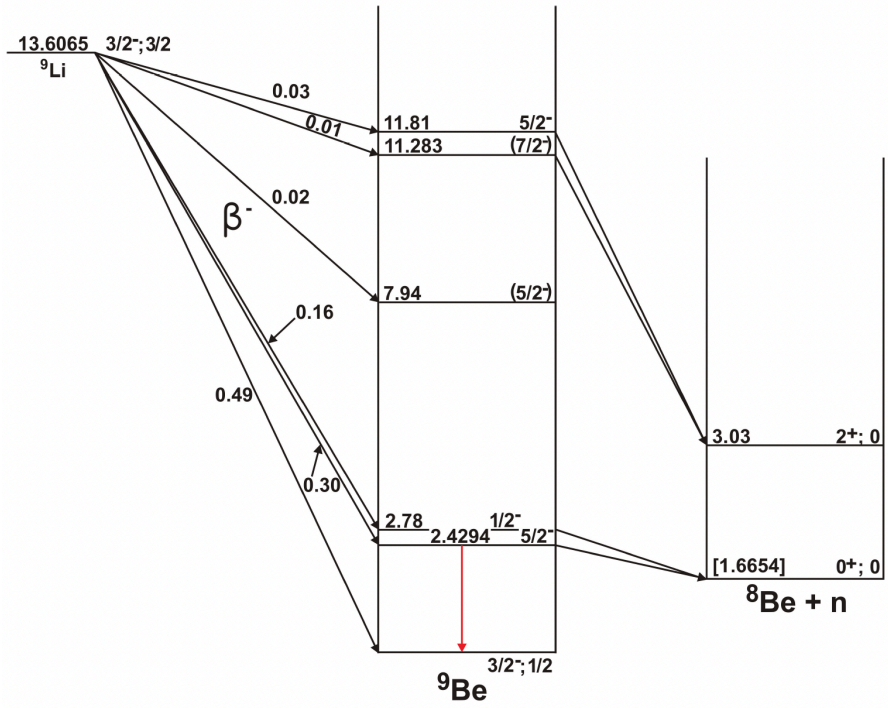

Figure 1.23: Decay scheme of ^{9}Li based on Particle Data Group [52].

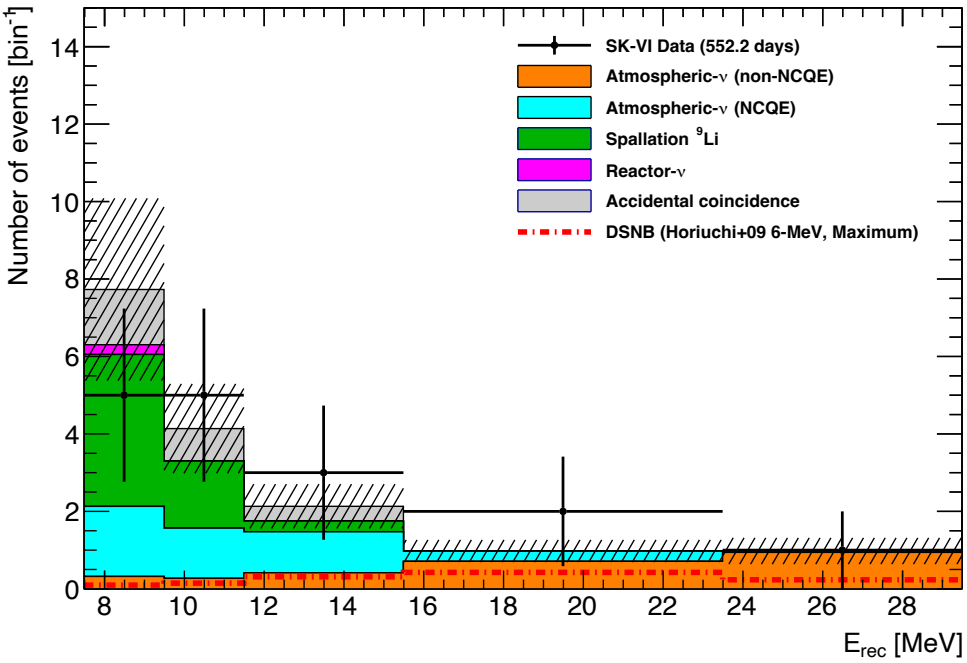

Figure 1.24: Reconstructed kinetic energy spectrum of the observed data and the expected background for the SRN searches in SK with 0.01% Gd-loaded water [51]. The green component in the histogram shows muon-induced ^{9}Li background expected from the ^{9}Li yield measured in SK with ultra-pure water.

Chapter 2

Motivation

Since July 2020, gadolinium (Gd) has been loaded in ultra-pure water of the Super-Kamiokande (SK) detector aiming for the first observation of neutrinos from past supernovae (supernova relic neutrinos, SRNs). The new phase of the experiment with Gd-loaded water is named SK-Gd. The detection efficiency of neutrons and the background rejection are significantly improved by the introduction of Gd. The SK-Gd experiment was operated with a Gd mass concentration of 0.01% from August 2020 to May 2022, and this study was performed with the data acquired during the period. This thesis describes the following three studies in Chapter 6, 7, and 8.

1. The stability and uniformity of the Gd concentration in the detector were verified by measuring neutrons induced by cosmic-ray muon spallation (Chapter 6).

2. Extending the above study, the yield of the neutron from the muon spallation in water was measured (Chapter 7).

3. The energy spectrum of β decay with neutrons of ^{9}Li, the major background in the low energy region in the SRN search, was measured (Chapter 8).

1. Evaluation of stability and uniformity of Gd concentration

The expected number of SRN interactions in SK depends on the models but it is typically a few events per year in the energy region of 10–30 MeV. Therefore, rare signals must be searched for in a large amount of the background for more than 10 years to observe the signals with more than 3σ significance. Thus, in order to detect SRN in the SK-Gd experiment, it is necessary to monitor the stability of the detector including the uniformity of the Gd concentration and continue stable observations over a long period. Indeed, the introduction of Gd into a large detector is challenging as the unexpected chemical reaction of Gd solute with the detector material may cause degradation of the Gd-loaded water such as precipitation although soak tests have been performed carefully before the installation. In this study, the stability and uniformity of the Gd concentration in the detector were evaluated with neutrons induced by cosmic-ray muons. The result for the first six months of data is reported in Ref. [53], which is extended to the entire observation period with 0.01% concentration in this thesis.

2. Measurement of cosmogenic neutron production

The production yield of neutrons induced by cosmic-ray muons was measured in this study. Neutrons and the recoil nuclei produced by their scattering cause the background in the search for rare events at the MeV scale, such as the recoil nuclei by dark matter, by the underground experiments. While, it is difficult to precisely calculate the processes with simulation due to the large uncertainties in the calculations of hadron production and scattering processes. Previous experimental results suggest that there is a relationship of $Y_n \propto (E_\mu)^a$ between the average energy of cosmic-ray muons arriving at the detector E_μ and the neutron production yield Y_n. The FLUKA simulation

reproduces the measurement of $Y_n \propto (E_\mu)^a$ in the organic liquid scintillator but it still underestimates the neutron yield by about 10–30% [34, 47, 48]. GEANT4-based simulation reported even lower estimation of neutron yield by ∼30% than that from FLUKA above 100 GeV of muon energy [54]. Therefore, it is important to experimentally measure the neutron production yield at different conditions in order to better understand and model the physics processes. Most previous experiments have used organic liquid scintillator (carbon target) to measure neutron yield, while the neutron yield in water was measured in this study using the SK detector. This is the second case after the SNO experiment [46] which measured at much deeper underground than SK, corresponding to higher muon energy. The comparison of the two measurements provides information on the energy dependence for the water target. Furthermore, as the SK detector is located near the KamLAND detector which is a liquid scintillator detector, this study enables a comparison of neutron yield measurements with different targets at the same depth (same muon energy) for the first time. For these reasons, this study provides a further understanding of neutron production and secondary interactions and helps establish a reliable simulation of muon spallation. The result of this study is reported in Ref. [55].

3. Measurement of cosmogenic ^{9}Li production

The energy spectrum of electrons from β decay of ^{9}Li was measured in this study. ^{9}Li is one of the cosmogenic isotopes produced in water by cosmic-ray muon. ^{9}Li is an unstable nucleus with a lifetime of 0.26 s and emits an electron and a neutron, which are indistinguishable from the SRN signals, $\bar{\nu}_e + p \rightarrow e^+ + n$. In previous analysis in SK, SRNs have been searched in the energy region above 8 MeV. Correspondingly, ^{9}Li has been measured in the region above 8 MeV with ultra-pure water [50]. In this study, data from SK with 0.01% Gd-loaded water were analyzed by a newly developed method to measure the β spectrum of ^{9}Li down to 4.5 MeV. Theoretical prediction of the SRN flux depends on the number of supernovae in the history of the universe, and this depends on the number of stars formed in the universe and the fraction of stars massive enough to cause core-collapse supernovae. The uncertainty regarding the history of star formation increases as it is older. As neutrinos produced from supernovae in the earlier stage of the universe have lower energy due to the effect of redshift, it is important for experiments to measure the SRN flux at lower energy. This study measured the energy spectrum of electrons from ^{9}Li decay, which is the major background at low energy below 10 MeV. In addition, the analysis method developed in this study can be applied in the future SRN search by the SK-Gd experiment to extend the energy range at the lower side and improve the sensitivity of the observation.

Chapter 3

Super-Kamiokande

This study was performed using the data observed by the Super-Kamiokande detector. This chapter describes the details of the configurations of the Super-Kamiokande detector and then describes the upgrade with gadolinium loading, the SK-Gd experiment, which has been started since August 2020.

3.1 Detection Principle

Charged particles generated in the Super-Kamiokande (SK) detector are observed by the detection of the Cherenkov light in water as shown in Figure 3.1. Cherenkov light is emitted when charged particles travel faster than the speed of propagation of light in a medium. The light is emitted in a conical shape at an angle θ_c with respect to the direction of travel of the charged particle, which satisfies the following equation

$$\cos\theta_c = \frac{1}{n\beta}, \tag{3.1}$$

where n represents the refractive index of the medium and β $(= v/c)$ is the ratio of the velocity v of a charged particle in vacuum to the speed of light c. Since the refractive index of pure water is 1.34, θ_c is about 42° for a charged particle traveling at nearly the speed of light ($\beta \simeq 1$).

Since Cherenkov light is not emitted unless the velocity of the charged particle exceeds the speed of propagation of light in the medium, there is a threshold for the energy of a charged particle that

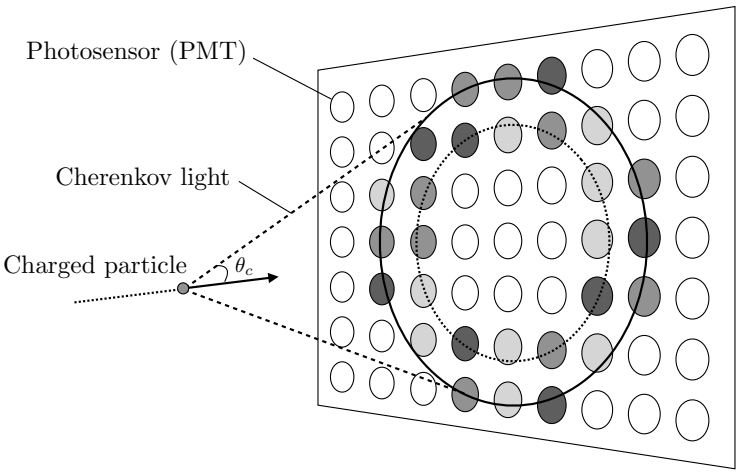

Figure 3.1: Schematic illustration of Cherenkov detection.

Table 3.1: Energy thresholds to emit Cherenkov light in water.

Charged particle	Mass m (MeV/c^2)	Energy threshold E_{th} (MeV)
Electron	0.511	0.768
Muon	106	159
Pion	140	210
Kaon	494	742
Proton	938	1,410

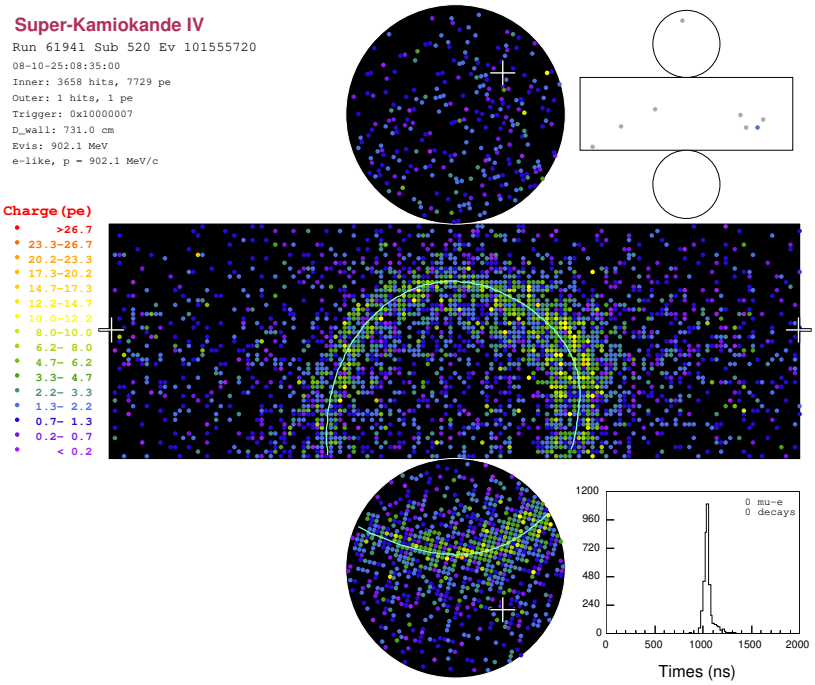

Figure 3.2: Example of an event display for an electron. Points correspond to PMTs on the inner wall and the color scale represents the observed electric charge of each PMT.

can emit Cherenkov light, given by the following equation:

$$E \geq \frac{mc^2}{\sqrt{1-1/n^2}} \equiv E_{\mathrm{th}}. \tag{3.2}$$

The threshold E_{th} for each charged particle is summarized in Table 3.1.

The number of photons dN emitted as Cherenkov light while an electron travels a small distance dx at a velocity β in a medium with refractive index n is given by

$$\frac{d^2N}{dxd\lambda} = \frac{2\pi\alpha}{\lambda^2}\left(1-\frac{1}{n^2\beta^2}\right), \tag{3.3}$$

where λ is the wavelength of the photon and α is the fine-structure constant.

Cherenkov photons are detected by photosensors (photomultiplier tubes, PMTs) mounted on the inner wall of the detector. Figure 3.2 shows an example of an event display for an electron. Electron generated or scattered in water emits Cherenkov photons until the momentum is decreased below the Cherenkov threshold due to the energy loss in water. Vertex (position where the charged particle is generated), direction, and kinetic energy are measured by the amount of the detected photons, timing of the detection, and the location of the hit-PMTs (ring pattern).

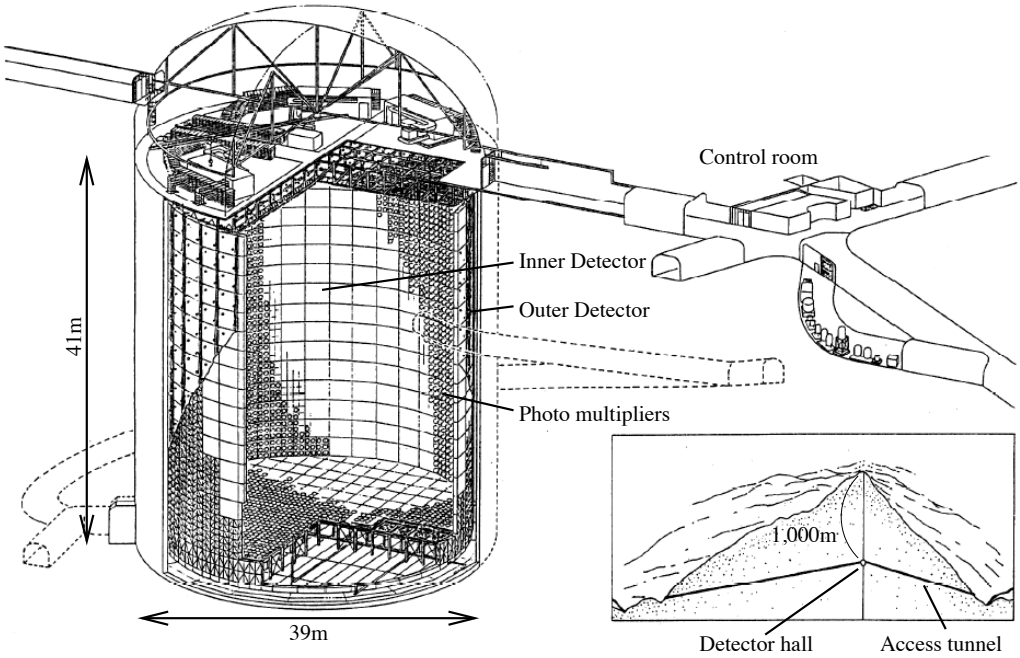

Figure 3.3: The Super-Kamiokande detector [56].

3.2 Overview of Super-Kamiokande

The SK detector is a large water Cherenkov detector located 1,000 m underground, corresponding to 2,700 m-water-equivalent overburden, at the Kamioka mine in Hida City, Gifu Prefecture, Japan (Figure 3.3). The detector is a cylindrical tank, 39.3 m in diameter and 41.4 m high, filled with 50 kton of ultra-pure water. PMTs are equipped on its inner wall. When neutrinos enter the SK detector and interact with electrons or nuclei in the water or γ rays scattered in the water, charged particles are generated. The neutrinos can be observed by detecting the Cherenkov light emitted by the charged particles as they travel through the water. Although cosmic-ray muons are the major background for the observation, the flux of cosmic-ray muons is suppressed to $\sim 10^{-5}$ of that at the ground surface thanks to the detector being located 1,000 m underground.

3.3 Detector Structure

3.3.1 Water Tank

The SK detector is divided into two concentric regions: the inner detector (ID) and the outer detector (OD) as shown in the left of Figure 3.4. The ID and OD are optionally separated.

The ID is a cylindrical volume, 33.8 m in diameter and 36.2 m high, filled with 32.5 kton of ultra-pure water. 20-inch PMTs facing inward are mounted on the walls. The number of PMTs installed varies depending on the observation period. In the period after the introduction of gadolinium, 11,129 PMTs were attached to the wall, covering $\sim$40% of the surface area of the inner wall with the photocathode. The 3×4 PMTs are laid out on the wall as one set (super module) as shown in the right of Figure 3.4. The area outside the photocathode is covered with a black sheet to prevent light from reflecting off the wall.

The OD is the volume surrounds the ID with a thickness of 2.05 m on the top and bottom and 2.2 m on the sides. The walls of the OD are equipped with 1,885 outward-facing 8-inch PMTs. The main purpose of the OD is to identify cosmic-ray muons and to attenuate γ-rays and neutrons generated in the surrounding rock. When neutrinos incident on the detector interact in the ID and Cherenkov light is emitted by the charged particles produced, the light is detected only by

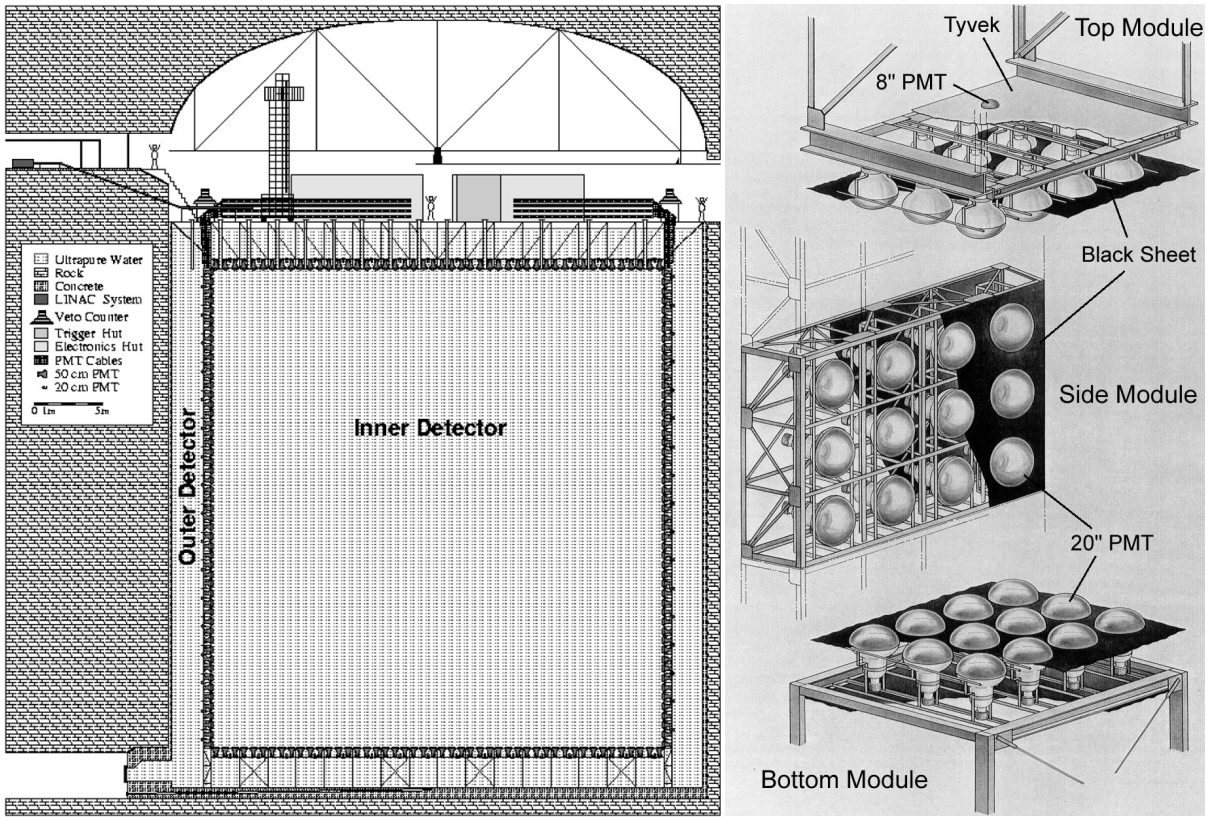

Figure 3.4: Cross section of the SK detector (left) and the support structure for PMTs (right) [56].

the 20-inch PMTs in the ID and not by the 8-inch PMTs in the OD. On the other hand, as the cosmic-ray muons are charged particles, Cherenkov light is detected by both the PMT in the OD and the PMT in the ID when the muons enter the detector. Thus, neutrinos and cosmic-ray muons are distinguished by checking the reaction of the PMTs in the OD. The schematic diagram is shown in Figure 3.5.

In the ID, the wall surfaces other than photocathode of PMTs are covered with black sheets as written before, whereas the wall of the OD are covered with white reflective sheets called Tyvek sheets to improve the light collection efficiency of PMTs.

3.3.2 Photomultiplier Tube

PMTs are sensitive photosensors which consists of photocathode to convert photons into electrons (photoelectrons, p.e.) by the photoelectric effect and dynodes to multiply the electrons and extract them as electrical signals. PMTs detect photons by the following process as illustrated in Figure 3.6.

1. A photon incidents the photocathode of the PMT and excites an electron in the photocathode (external photoelectric effect), causing the photoelectron to strike out.

2. Photoelectron is accelerated and led to the first dynode by the focusing electrode. Multiple secondary electrons are emitted when it strikes the first dynode.

3. The secondary electrons are accelerated by the electric field created by the potential difference between adjacent dynodes and collide with the second dynode. Multiple electrons are emitted for each incident electron.

4. Electrons multiplied by repeated collisions at the dynode reach the anode and are extracted as electric current.

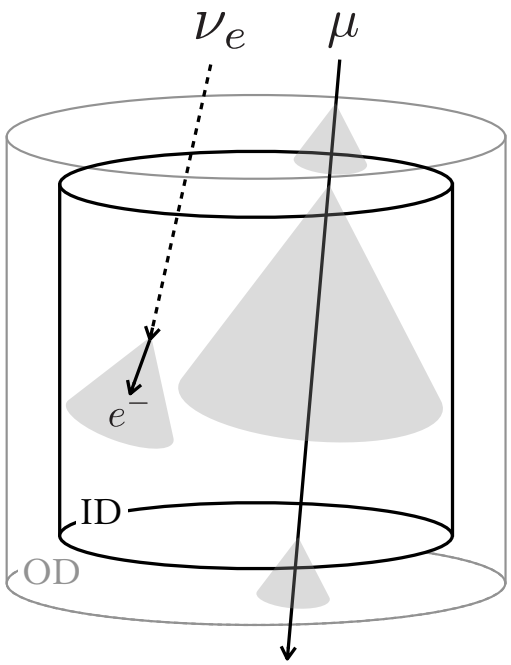

Figure 3.5: Schematic illustration of an electron neutrino and a cosmic-ray muon arriving at the SK detector.

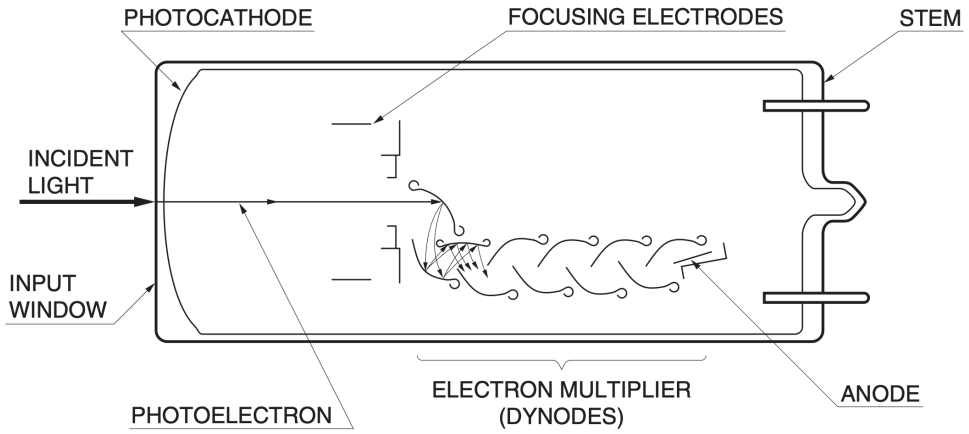

Figure 3.6: Schematic illustration of the detection principle of PMT [57].

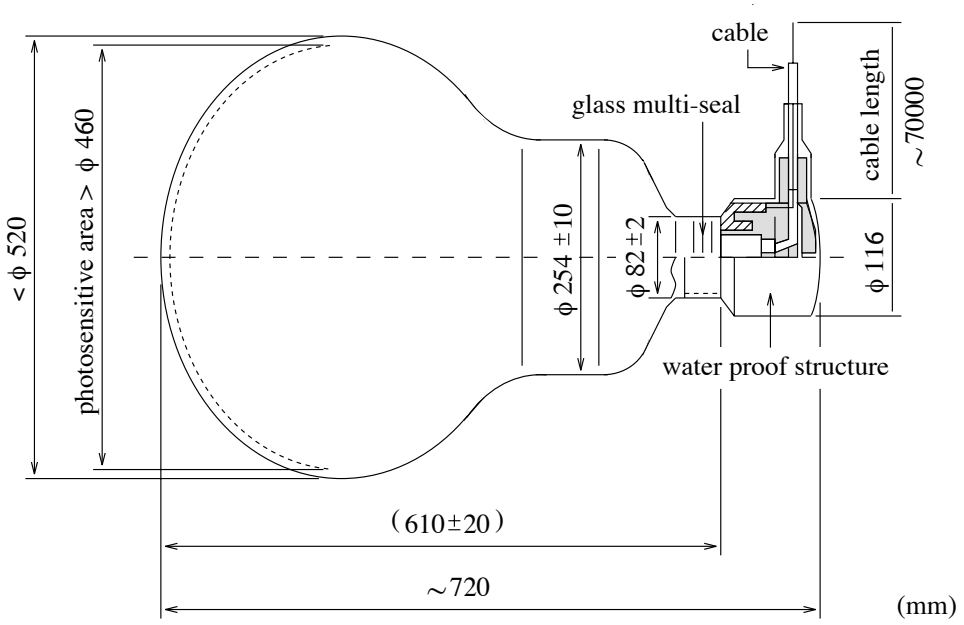

Figure 3.7: Schematic illustration of 20-inch PMT installed the SK detector [56].

Table 3.2: Characteristics of the 20-inch PMT.

Model number	Hamamatsu R3600
Photocathode area	50 cm in diameter
Weight	13 kg
Pressure tolerance	6 kg/cm^2
Photocathode material	Bialkali (Sb-K-Cs)
Quantum efficiency	22% at wavelength of 390 nm
Dynode	Venetian blind type (11 stages)
Gain	10^7 at ~2 kV
Dark current	200 nA at 10^7 gain
Dark noise rate	3 kHz at 10^7 gain
Transit time	90 ns at 10^7 gain
Transit time spread	2.2 ns (1σ)

The 20-inch PMTs (Hamamatsu R3600) are equipped in the inner detector of SK (Figure 3.7). The photocathode of PMT is made of bialkali (Sb-K-Cs) and a sensitive to the wavelength of 280–660 nm, which matches the typical wavelength of Cherenkov light in SK, ~390 nm. The probability that a photon is converted to a photoelectron at the photocathode is called the quantum efficiency. The quantum efficiency reaches a maximum at a wavelength of 390 nm with a value of 22% (Figure 3.8). The dynote has 11-stage Venetian blind type. High-voltage (HV) of ~2 kV are applied to the PMTs to give the gains of ~10^7 where the gain represents the amplification ratio of the number of electrons in the output signal to the number of photoelectrons. Table 3.2 summarizes the characteristics of the 20-inch PMT.

Since the interior of the PMT is in a vacuum to improve photoelectron collection efficiency and prevent internal discharges, an implosion occurs if the glass of the PMT is broken. SK experienced a serious accident in 2001 in which about half of the PMTs were damaged by an implosion of one PMT. Since then, all PMTs have been equipped with shock-wave protection cases to prevent chain implosion. The photosensitive area of the PMT is covered with a 12 mm thick acrylic cover, and the back side is covered with fiberglass-reinforced plastic. Holes are drilled in the case to allow outside water to flow in, and the gap between the case and the PMT is filled with water. The acrylic cover

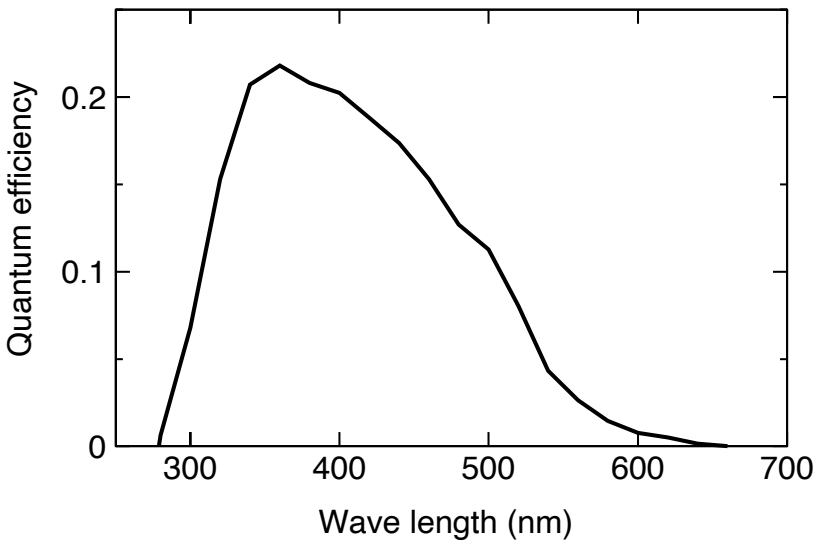

Figure 3.8: Wavelength dependence of quantum efficiency of the 20-inch PMT [56].

of the photosensitive area has a transmittance of more than 96% for a photon of 350 nm wavelength and has only a small impact on the detection of Cherenkov photons.

Photoelectrons generated inside the PMT may not reach the dynode if there is a geomagnetic field; a 100 mG magnetic field parallel to the dynode reduces the light collection efficiency by about 10% [58]. There is a geomagnetic field of about 450 mG around the SK detector site. Therefore, 26 Helmholtz coils are wound around the detector to reduce the influence of the geomagnetic field. These coils reduce the influence of the geomagnetic field on the detection efficiency of the PMT to 2% [58].

3.3.3 Observation Phases

The SK experiment started the observation in April 1996. The observation period of SK has been divided into seven phases. Table 3.3 summarizes the detector configuration in each phase.

SK-I

The period from the start of the observations in April 1996 to July 2001 is referred to as SK-I. In July 2001, the water inside the detector was drained and the defective PMTs were replaced. However, in November 2001, while pouring water into the detector after the replacement work was completed, the PMT breakage accident described above occurred. As a result of this accident, 6,779 ID PMTs and 1,017 OD PMTs were lost.

SK-II

After the accident, 5,182 ID PMTs were reloceted to cover the inner wall uniformly and the observation was resumed in October 2002, and the data acquisition continued until October 2005. This period is called SK-II. The PMTs are equipped with shock-wave protection cases from the SK-II period to prevent chain breakage of the PMTs.

SK-III

In June 2006, the water tank was opened again and new PMTs were installed to fill the missing locations due to the accident. This installation brought the total number of ID PMTs to 11,129, and observation was conducted from July 2006 to August 2008. This period is referred to as SK-III.

Table 3.3: Observation phases of SK. This analysis used the data acquired during SK-VI.

Phase	Start	End	ID PMTs (coverage)	OD PMTs	Gd concentration (%)
SK-I	Apr. 1996	Jul. 2001	11,146 (40%)	1,885	—
SK-II	Oct. 2002	Oct. 2005	5,182 (19%)	1,885	—
SK-III	Jul. 2006	Aug. 2008	11,129 (40%)	1,885	—
SK-IV	Sep. 2008	May 2018	11,129 (40%)	1,885	—
SK-V	Feb. 2019	Jul. 2020	11,129 (40%)	1,885	—
SK-VI	Jul. 2020	May 2022	11,129 (40%)	1,885	0.01
SK-VII	Jul. 2022	—	11,129 (40%)	1,885	0.03

SK-IV

A new electronics module, QBEE, was introduced in August 2008 to record the low energy signals a specific condition for neutron search (Section 3.4.1). The data acquisition took place from September 2008 through May 2018. This period is referred to as SK-IV. At present, SK-IV has the longest observation period.

SK-V

In preparation for the installation of gadolinium (Gd) in ultra-pure water, modifications of the detector were made from July 2018 to January 2019. The modification includes water seals to prevent a leak of Gd-loaded water, improvement of piping in the tank, and replacement of defective PMTs. The data acquisition period from the end of January 2019, after the completion of the refurbishment work, to June 2020, when the Gd-loading work begins, is referred to as SK-V. SK-V is the last phase for the observation using ultra-pure water.

SK-VI

In July 2020, 13 tons of gadolinium sulfate octahydrate $Gd_2(SO_4)_3 \cdot 8H_2O$ were introduced to ultra-pure water in the detector, corresponding to 0.01% of Gd mass concentration. The experiment using the Gd-loaded water in the SK detector is specially named the SK-Gd experiment. The Gd-loading work was completed in August 2020 and the SK-VI period has been started. In this study, the data acquired during this period was used to evaluate the performance of neutron detection and the stability and measure the cosmogenic productions.

SK-VII

In July 2022, 26 tons of $Gd_2(SO_4)_3 \cdot 8H_2O$ were added to Gd-loaded water in the detector. The Gd mass concentration has reached to 0.03% and the SK-VII data-taking period has been started.

3.4 Data Acquisition System

3.4.1 Front-End Electronics

The analog signal from each PMT is sent via a 70 m cable to the electronics hat on top of the tank. The analog signal is then digitized by a front-end electronics module, and the timing of photo-detection and the integrated charge of the signal, which is nearly proportional to the number of observed photons, are sent to a computer for data storage. The data from all hit PMTs are sorted in time order, collected as an event, and stored on disk if one of the trigger conditions described in the next sections is satisfied.

Table 3.4: Trigger condition for SK.

Trigger type	Trigger condition	Time window (μs)
SLE	$N_{200} \geq 34$	$[-0.5, +1.0]$
LE	$N_{200} \geq 47$	$[-5, +35]$
HE	$N_{200} \geq 52$	$[-5, +35]$
SHE	$N_{200} \geq 60$	$[-5, +35]$
AFT	SHE trigger is issued.	$[+35, +535]$
OD	$N_{200} \geq 22$	$[-5, +35]$

Since the beginning of the SK-IV data-taking period, data acquisition has been upgraded with a new front-end electronics module, QTC-Based Electronics with Ethernet (QBEE). In the Super-Kamiokande detector, the event rate is higher at lower energy due to environmental radiation and random coincidence of PMT dark noise. Therefore, the energy threshold (corresponds to the number of hit-PMTs) is determined by the upper limit of the rate handled by the electronics and data acquisition system. The high-speed data process with QBEE enabled the observation of low-energy events that could not be recorded with simple hardware triggers. One of the major analyses that benefited from this update is the SRN search with neutron tagging. A positron and a neutron are generated through the IBD reaction of an electron antineutrino, in which the background is largely suppressed by detecting a delayed coincidence: the signals of the positron and γ rays from the neutron capture on the nucleus. During the SK-IV phase with ultra-pure water, the neutron is captured on a proton (hydrogen nucleus) in the water after $\sim$200 μs on average and a 2.2 MeV γ ray is emitted. It was not possible to observe 2.2 MeV γ rays with only $\sim$6 hit-PMTs because the trigger threshold could not be lowered. With the introduction of QBEE, all PMT signals, including PMT dark noise, can be sent from the electronics to the merger PC for event selection later by software.

3.4.2 Trigger System

The data of events are stored if they satisfy one of the conditions set by the trigger. When the total number of coincidence ID PMT hits within 200 ns, N_{200}, exceeds a certain threshold, a trigger is issued, and hit information surrounding the trigger timing is recorded. There are four levels of primary triggers in SK with different thresholds: trigger types are super low energy (SLE), low energy (LE), high energy (HE), and super high energy (SHE) as summarized in Table 3.4. In addition to these, the AFT trigger is issued after the SHE trigger without OD since SK-IV after the upgrade of the electrons as explained in the previous section. Since SK-VI, the AFT trigger is issued after the SHE trigger regardless of whether the OD trigger is issued or not. All PMT signals are stored for 500 μs after the AFT trigger is issued. These data are used mainly for the detection of neutron captures as described in this thesis. The time window is the range for taking the data around the timing when N_{200} exceeds the threshold.

For example, the SHE trigger has been used for SRN search. If N_{200} exceeds 60, the SHE trigger is issued and opens a 40 μs time window (from 5 μs before to 35 μs after the trigger timing). Furthermore, the AFT trigger is also issued and data of all PMT signals in a 500 μs time window (from 35 μs to 535 μs after the SHE trigger timing) is stored. For the IBD event ($\bar{\nu}_e + p \rightarrow e^+ + n$) by an electron antineutrino, the prompt positron event is searched from SHE-triggered events, and the delayed neutron capture event is searched from PMT signals in SHE+AFT time window.

For the measurement of the cosmogenic neutron production discussed in Chapter 6 and 7, neutron capture events are searched for in the time window after a cosmic-ray muon event. The SHE and OD triggers are issued simultaneously for a cosmic-ray muon event and the AFT trigger window is opened after the muon event. The neutron capture events are searched in the AFT window.

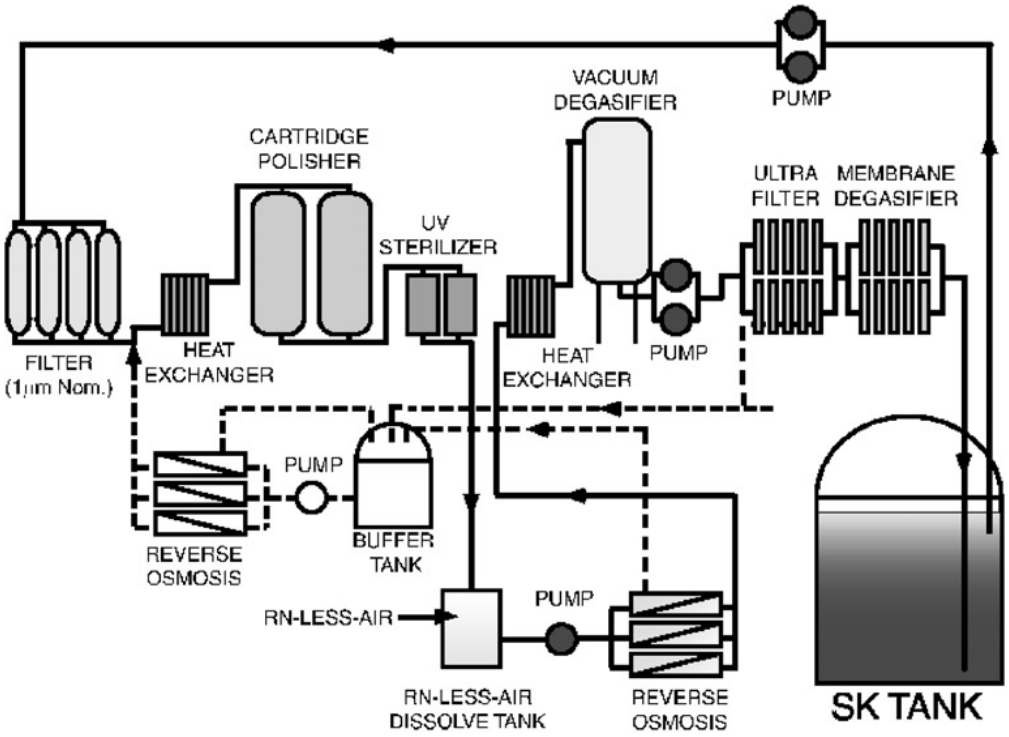

Figure 3.9: Schematic illustration of water purification system [56].

3.5 Water Purification System

The ultra-pure water for the SK detector is produced by purifying groundwater in the Kamioka mine. Groundwater contains impurities such as particulates, metal ions, bacteria, and radioactive materials. Particulates, metal ions, and bacteria scatter or absorb Cherenkov light, reducing the water transmittance, and radioactive materials dissolved in water can cause background events for neutrino observations. In particular, bismuth-214 (^{214}Bi), a daughter nuclide of radon-222 (^{222}Rn), emits an electron with energies below 3.26 MeV through β decay. This is the major background source around the energy threshold (∼3.5 MeV) for the SK analysis at MeV scale such as an observation of solar neutrinos. Therefore, water purification is essential to improve measurement accuracy.

To maintain high purity, water is constantly circulated through the detector and purified at a flow rate of 60 tons/h. Water collected from the top of the detector is purified through a purifier and then flows into the detector from the bottom. This purification system suppresses the radon concentration from 9.1 mBq/m^3 to 1.7 mBq/m^3 [59] and keep the water attenuation length to be ∼100 m. However, as the purified water flows in from the bottom of the detector and is collected from the top as written above, the water circulation system causes a vertical asymmetry in water quality. The water is clearer at the bottom than at the top. This is avoidable by making convection in the detector but it mixes the Rn contaminated water close to the wall with the water in the central region with lower Rn contamination and eventually increase the background in the fiducial volume for the analysis. Therefore, water convection in the detector is intentionally suppressed by controlling the temperature, flow rate, and location of water supply and drainage. The temperature of the water in the tank is maintained at about 14 °C and is constantly monitored with an accuracy of 0.01 °C. This prevents water convection, suppress the bacteria growth, and keeps the temperature-dependent PMT performance stable. The schematic illustration of water purification system is shown in Figure 3.9. The water is purified by the following steps [56].

1. 1 μm mesh filter:

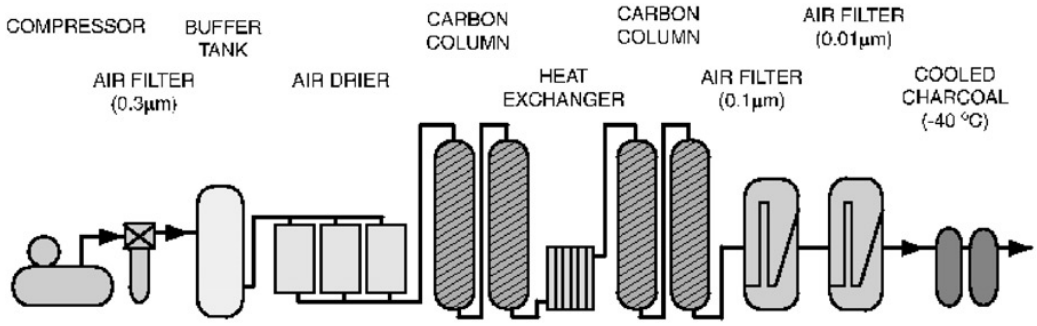

Figure 3.10: Schematic illustration of air purification system [56].

To remove particulates larger than 1 μm.

2. Heat exchanger:
   To keep the water temperature at 14 °C. The pumps used for water circulation and the PMTs are the major heat sources in the water.

3. Ion exchanger:
   To remove ions (Fe^{2+}, Ni^{2+}, Co^{2+}, $CO_3{}^{2-}$, etc.) from water.

4. Ultraviolet sterilizer:
   To kill bacteria.

5. Rn-less-air dissolving system:
   To improve the efficiency of radon gas removal during purification in a vacuum deaerator, radon-removed air is dissolved in pure water.

6. Reverse osmosis filter:
   To perform filtration using osmosis and remove organic compounds with molecular weights greater than 1,000.

7. Cartridge ion exchanger:
   To removes 99% of ions dissolved in water.

8. Ultra filter:
   To remove particulates of a few nm in size.

9. Membrane degasifier:
   To remove radon and oxygen dissolved in the water.

3.6 Air Purification System

Radon concentrations are higher in the Kamioka mine than outdoors because radon is produced by uranium in the rock. There is a gap of about 60 cm between the water surface in the detector and the top cap of the detector. To prevent radon in that air from dissolving into the water, the Rn free air is fed into the gap. The schematic illustration of air purification system is shown in Figure 3.10. The air is purified by the following steps [56].

1. Compressor:
   To compress air to 7.0–8.5 bar.

2. Air filter:
   To remove dust from compressed air.

Table 3.5: Thermal neutron capture cross sections for each gadolinium isotope, hydrogen, oxigen, and sulfur [60]. The unit of cross section b corresponds to $10^{-24}\,\mathrm{cm}^2$.

Isotope	Natural abundance (%)	Cross section (b)
^{152}Gd	0.20	740
^{154}Gd	2.18	85.8
^{155}Gd	14.80	61,100
^{156}Gd	20.47	1.81
^{157}Gd	15.65	254,000
^{158}Gd	24.84	2.22
^{160}Gd	21.86	1.42
^{1}H	99.99	0.33
^{16}O	99.76	0.0002
^{32}S	94.85	0.53

3. Air drier:
   To remove water and CO_2 in the air to improve the efficiency of radon removal.

4. Carbon column:
   To absorb radon using activated carbon.

5. Cooled charcoal:
   To absorb radon using activated carbon cooled to $-60\,^{\circ}\mathrm{C}$.

3.7 The SK-Gd Experiment

3.7.1 Gadolinium Loading

Gadolinium (Gd) is a rare earth element with atomic number 64. It has the largest thermal neutron capture cross-section of any natural elements. Table 3.5 shows the thermal neutron capture cross sections for each Gd isotope.

The ^{157}Gd (^{155}Gd) captures a neutron and is excited to a resonance state of ^{158}Gd (^{156}Gd). It then transitions to the ground state of ^{158}Gd (^{156}Gd) through multiple energy levels, emitting several γ rays. Several γ rays with a total energy of 7.9 MeV are emitted from ^{157}Gd,

$$n + {}^{157}\mathrm{Gd} \rightarrow {}^{158}\mathrm{Gd}^{*} \rightarrow {}^{158}\mathrm{Gd} + \gamma\text{'s (7.9 MeV in total)}, \tag{3.4}$$

and several γ rays with a total energy of 8.5 MeV are emitted for ^{155}Gd,

$$n + {}^{155}\mathrm{Gd} \rightarrow {}^{156}\mathrm{Gd}^{*} \rightarrow {}^{156}\mathrm{Gd} + \gamma\text{'s (8.5 MeV in total)}. \tag{3.5}$$

When Gd is introduced to water at a mass concentration of 0.01%, ∼50% of neutrons are captured on Gd (the right of Figure 3.11) and the remaining 50% is captured on protons (hydrogen nuclei). Furthermore, the Gd concentration correlates with the time it takes for neutrons to be captured on Gd, Δt. Δt follows an exponential function $\exp(-\Delta t/\tau)$, where τ is called the capture time constant. Dense Gd concentrations shorten the time it takes for neutrons to be captured on Gd. The left-hand plot of Figure 3.11 shows the correlation between the capture time constant and the Gd mass concentration.

The first Gd loading began on July 14, 2020, and was completed on August 17, 2020. In this period, 13.2 tons of Gd sulfate octahydrate $Gd_2(SO_4)_3 \cdot 8H_2O$ was dissolved in 50 ktons of water, resulting in a Gd sulfate mass concentration of 0.026% which corresponds to 0.01% mass concentration of Gd. In order to make the Gd concentration uniform, Gd-loaded water was injected from the bottom of the tank and pure water was drained from the top of the tank, as shown in

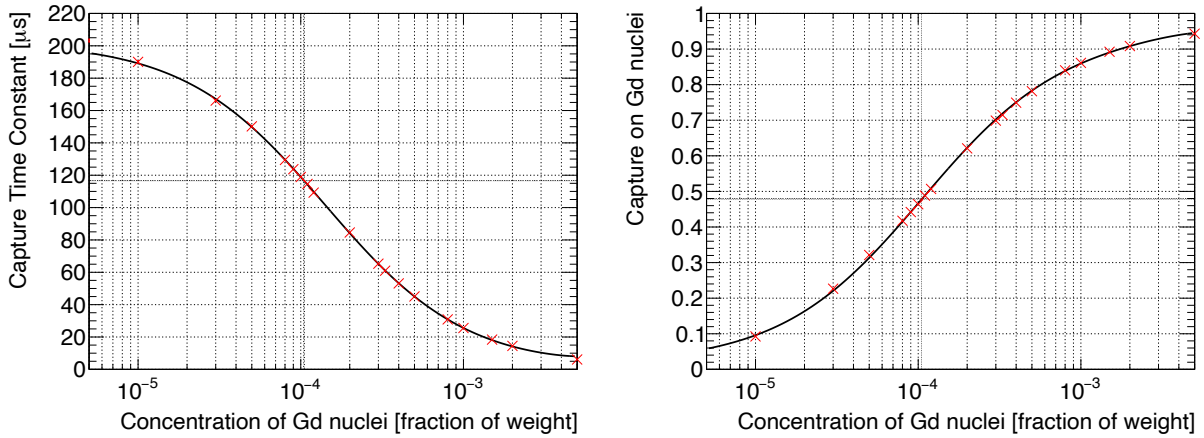

Figure 3.11: Correlation between the time constant and Gd mass concentration (left), and between neutron capture fraction on Gd and Gd mass concentration (right) [51].

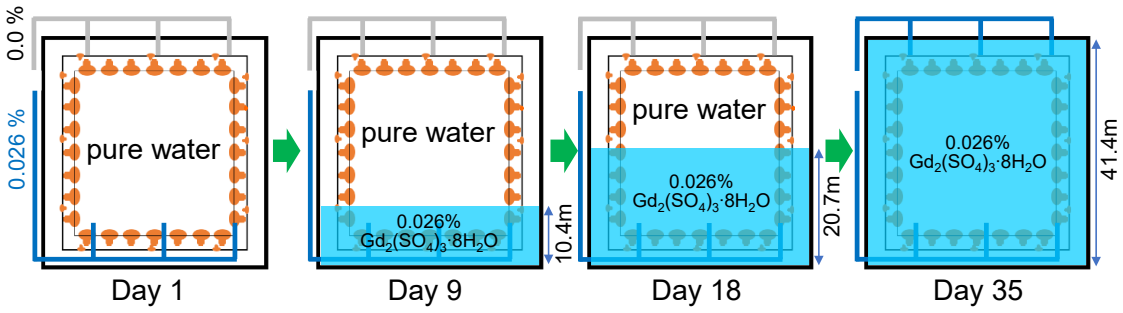

Figure 3.12: Schematic illustration of Gd loading [60].

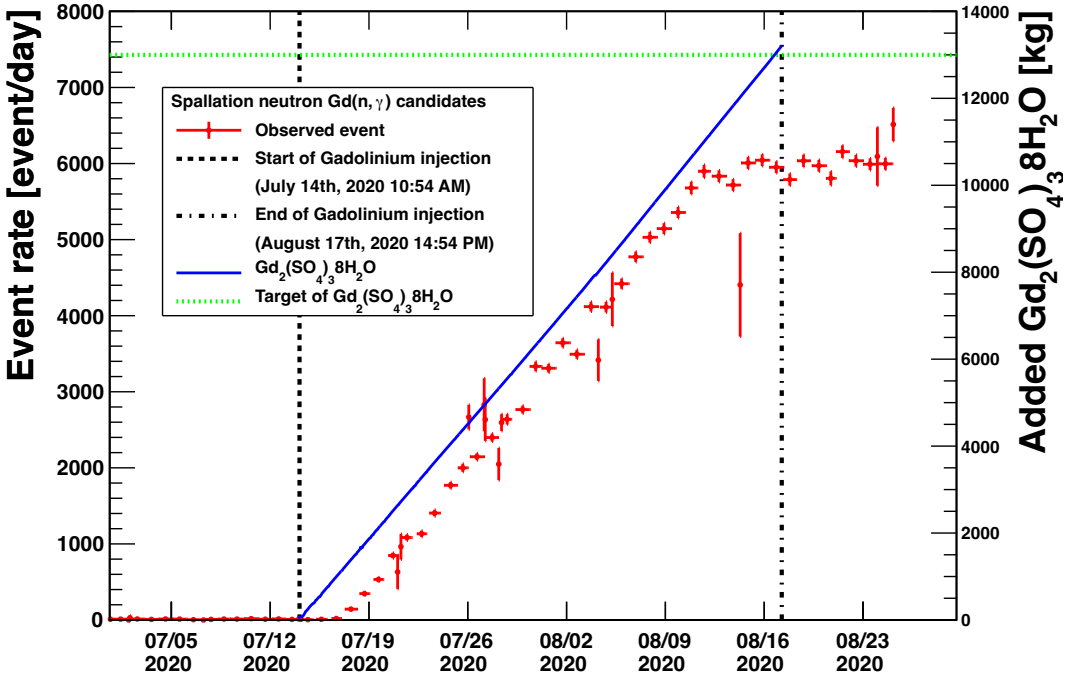

Figure 3.13: The time variations of the amount of Gd sulfate octahydrate added to the water and the event rate of neutron capture events on Gd. The red points represent the event rate of muon-induced neutrons captured on Gd, and the blue line represents the amount of Gd sulfate octahydrate doped in the water.

Figure 3.12. Gd-loaded water supplied at lower temperature than that in the tank so that the pure water was efficiently drained from the top. Figure 3.13 shows the time variations of the amount of Gd sulfate octahydrate added to the water and the event rate of neutron capture events on Gd for the neutrons induced by the cosmic-ray muon spallation and captured on Gd in the fiducial volume (the region more than 2 m from the ID wall). The reason for the gap between the start of Gd loading and the rise of the event rate is that it took time for the Gd sulfate solution to reach the fiducial volume. Similarly, the reason for the gap between the time when the event rate became constant and the end of Gd loading is that the Gd sulfate solution filled the fiducial volume at 2 m below the top. Figure 3.14 shows the time variation of the vertex distribution for events that muon-induced neutrons are captured on Gd. It was confirmed by the vertex distributions that the Gd is loaded gradually upward from the bottom.

3.7.2 SK-Gd Water System

In the water circulation system of SK-Gd, the bacteria and particulates removal system used is still in operation. On the other hand, since it is necessary to circulate water while retaining gadolinium (Gd^{3+}) and sulfate (SO_4^{2-}) ions, an ion exchange resin was newly developed to remove only ions other than Gd^{3+} and SO_4^{2-}. A schematic illustration of the SK-Gd water system is shown in Figure 3.15, and the main purification process is described below [60].

1. Gd-dissolving system:

   The $Gd_2(SO_4)_3 \cdot 8H_2O$ powder delivered by the hopper is weighed and dissolved into water in a buffer tank via a circle feeder. The solution is sent to the solution tank and pretreatment system.

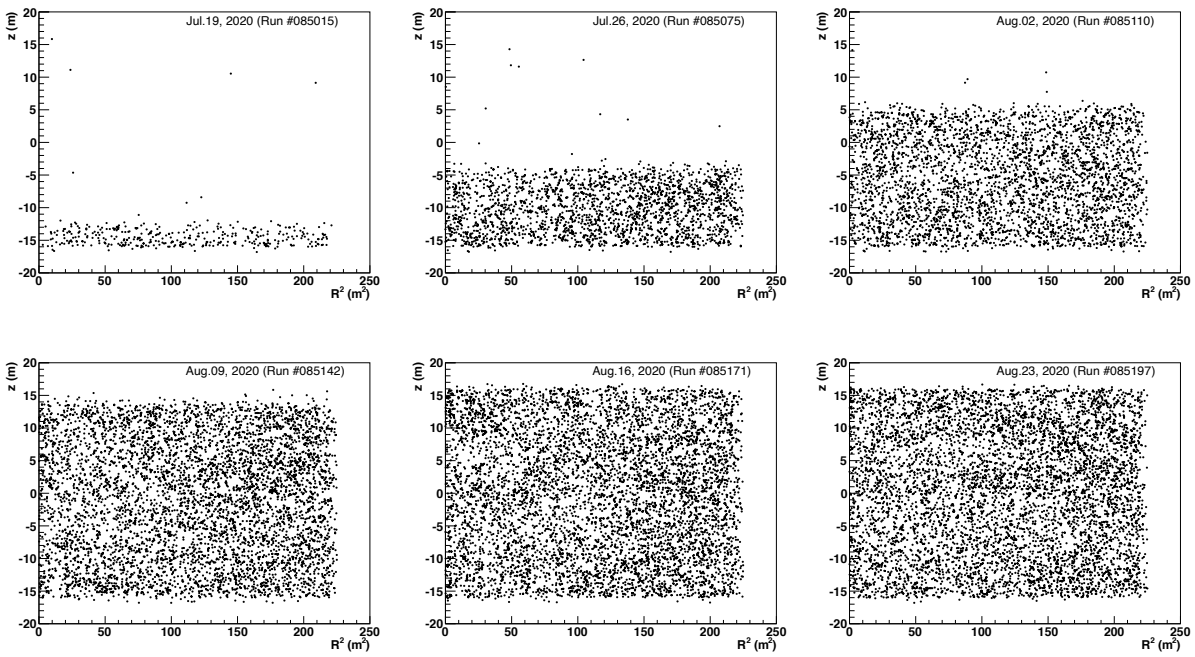

Figure 3.14: Distributions of event vertex where cosmic-ray muon-induced neutrons were captured on Gd. The horizontal axis represents the square of the detector radius, and the vertical axis represents the height. From July 19 to August 23, 2020, changes in the event vertex distribution were checked on a weekly basis.

2. Pretreatment system:

   Ions other than Gd^{3+} and SO_4^{2-} are removed by a cation exchange resin inert to Gd^{3+} and an anion exchange resin inert to SO_4^{2-}, and an ultraviolet total organic carbon reduction lamp (TOC lamp) decomposes organic impurities. As in the purification system for pure water, ultraviolet radiation and ultrafilters are also used in the pretreatment section to kill bacteria and remove microscopic dust particles.

3. Purification system:

   After merging with pure water, the gadolinium sulfate solution is purified by the TOC lamps, heat-exchange units (HE), ion exchange resins, ultraviolet sterilizer, and ultrafiltration modules (UF). These units are arranged in two parallel systems, circulating at $60\,m^3/h$ each for a total flow rate of $120\,m^3/h$.

In the Gd loading process, pure water was drained from the top of the detector to the dissolution device to dissolve Gd^{3+} and SO_4^{2-}, which was then introduced into the detector from the bottom. In this process, the water temperature inside the detector was raised by about $0.3\,°C$ higher than that of the Gd-loaded water introduced from the bottom so that the Gd-loaded water was introduced by piling up from the bottom of the detector as explained Section 3.7.1. That situation is shown in Figure 3.12, 3.13, and 3.14.

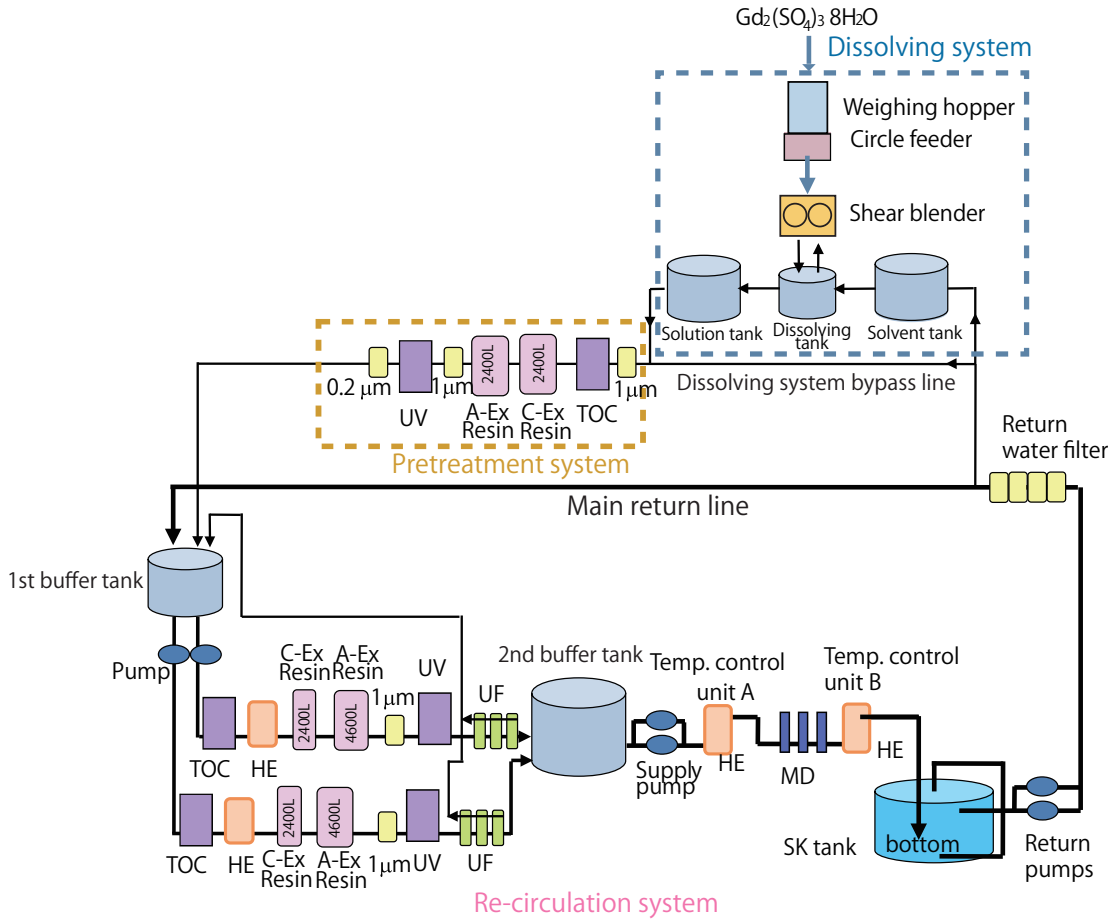

Figure 3.15: Schematic illustration of SK-Gd water system [60].

Chapter 4

Detector Calibration

This chapter describes the calibration method for the Super-Kamiokande (SK) detector. The SK detector is filled with 50 kton of gadolinium-loaded water and 11,129 20-inch PMTs are mounted on the inner wall. In order to realize the precise measurement with stable conditions, it is important to understand the detector response and monitor it from time to time by the detector calibration. The target of the calibration includes the fundamental properties such as the characteristics of PMTs and the individual difference, absorption, and scattering of photons in water, as well as the physics measurement such as the energy scale and neutron detection. Monte Carlo (MC) simulation is developed based on the measurement by the calibration with some corrections to reproduce the time variations of the observed data.

4.1 PMT Calibration

In the SK detector, Cherenkov photons emitted by charged particles are observed by PMTs mounted on the wall, and the number of photons and the detected time are used for the data analysis. Three calibration methods are described in this section: the calibration of the quantum efficiency, which is the probability that an incident photon is converted into a photoelectron at the PMT photocathode, the gain, which is the amplification rate of photoelectrons at the PMT, and the time to acquire the signal.

4.1.1 Quantum Efficiency

As explained in Section 3.3.2, a photon incident on the photocathode of a PMT excites electrons and emits photoelectrons due to the photoelectric effect. The probability that a photon is converted into a photoelectron is called the quantum efficiency (QE) which is typically ∼20%. There are individual differences in the QE of PMTs attached to the inner detector (ID), which can be a source of systematic uncertainty in the energy reconstruction. Therefore, it is necessary to accurately measure the QE of individual PMTs.

The NiCf source (Figure 4.1) is used to measure the QE. The NiCf source is a γ ray source that contains californium-252 (^{252}Cf), a neutron source, in a spherical polyethylene resin mixed with nickel oxide (NiO) powder. Californium is an actinide element with atomic number 98, and ^{252}Cf is one of its isotopes. The ^{252}Cf has the half-life of 2.65 years, and it decays with emission of an α particle at a branching ratio of 96.9% or by spontaneous fission with a probability of 3.1%. During spontaneous fission, an average of 3.76 neutrons with the energies of ∼2 MeV and an average of 10.8 γ rays with a total energy of 8.2 MeV are emitted. The intensity of the Cf source currently used in SK is 0.3 MBq.

The neutrons emitted by spontaneous fission lose energy through elastic scattering with protons in the polyethylene and be thermalized. The thermalized neutrons are captured by the Ni nucleus and a γ ray with 6–9 MeV is emitted. Because the source is spherical, γ rays are emitted isotropi-

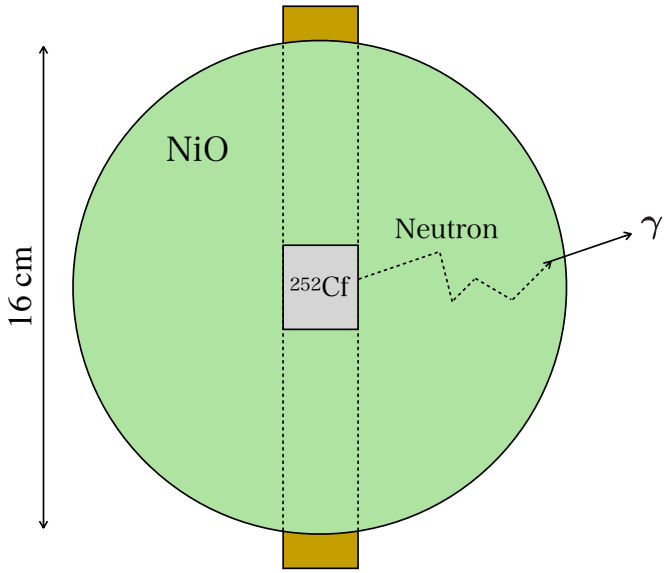

Figure 4.1: Schematic illustration of the NiCf source.

cally. The emitted γ rays produce or scatter electrons in water and the photons are emitted from Cherenkov radiation. Since the amount of light is not large and only zero or one photon incident on each PMT in most cases, the NiCf source is suitable for measuring QE.

The hit rate for each PMT is calculated for both the data and the MC simulation, and the ratio is taken to obtain the value of the relative QE for each PMT. Figure 4.2 summarizes the PMT hit rates for each PMT location (barrel, top, and bottom of the detector). In order to suppress the positional dependence of water quality, the water condition is made uniform in the detector by convecting the water in the detector, and the data is acquired by measurement using a NiCf source placed near the center of the detector. MC simulations are generated assuming that QE of all PMTs are equal. The obtained relative QE of each PMT are stored as a "QE table" and used for energy reconstruction.

4.1.2 PMT Gain

When a photon is incident on the photocathode of a PMT, photoelectrons are emitted by the photoelectric effect. The photoelectrons are accelerated by the electric field applied inside the PMT, and several secondary electrons are emitted when they hit the dynode. After photoelectrons are amplified by multiple dynodes, they are extracted as electrical signals. The amplification factor for a single photoelectron is called gain. The expected value of the output charge is expressed as:

$$Q_i = N_i \times QE_i \times G_i, \tag{4.1}$$

where Q_i represents the output charge and the unit is pC. N_i represents the number of incident photons to the i-th PMT, QE_i represents the quantum efficiency, and G_i is the gain of the i-th PMT. Therefore, the unit of the gain G_i is pC/p.e. G_i is defined in SK by two components of the absolute gain G_{abs} and the relative gain $G_{\mathrm{rel},i}$:

$$G_i \equiv G_{\mathrm{abs}} \times G_{\mathrm{rel},i}. \tag{4.2}$$

The absolute gain G_{abs} was determined from average of output charge distribution for single photoelectron to be 2.46 pC/p.e. using the NiCf calibration. $G_{\mathrm{rel},i}$ is a relative gain of each PMT measured using an N_2 laser. The ratio of the amount of charge Q_i to the number of photoelectrons N_i observed at the i-th PMT is proportional to $G_{\mathrm{rel},i}$ because $Q_i \propto QE_i \times G_{\mathrm{rel},i}$ and $N_i \propto QE_i$:

$$G_{\mathrm{rel},i} \propto \frac{Q_i}{N_i} \tag{4.3}$$

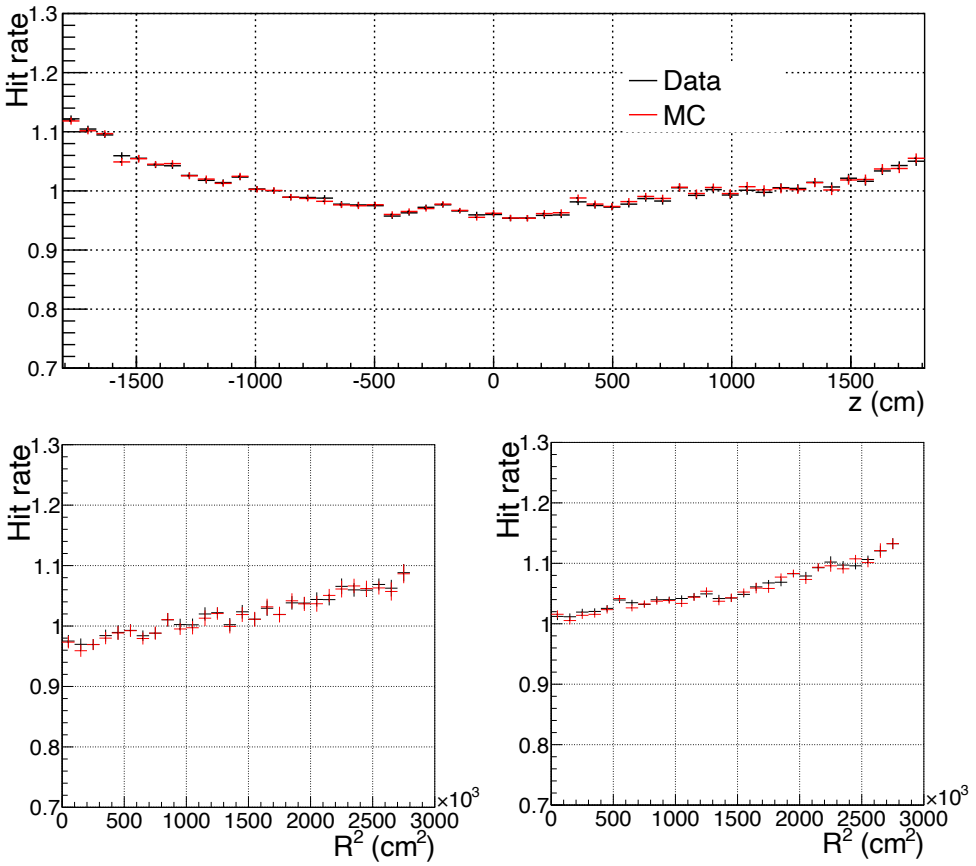

Figure 4.2: Positional dependence of PMT hit rate for the barrel (top), the top (bottom left), and the bottom (bottom right). For the top figure, the horizontal axis shows height (z). For the bottom two figures, the horizontal axes show the radius squared ($R^2 = x^2 + y^2$). The black and red point shows the data and MC, respectively. The plots are normalized so that the hit rate averages one overall the detector. The larger PMT hit rate at the edge of the detector, where $|z|$ and R^2 are large, is due to the effect of reflection.

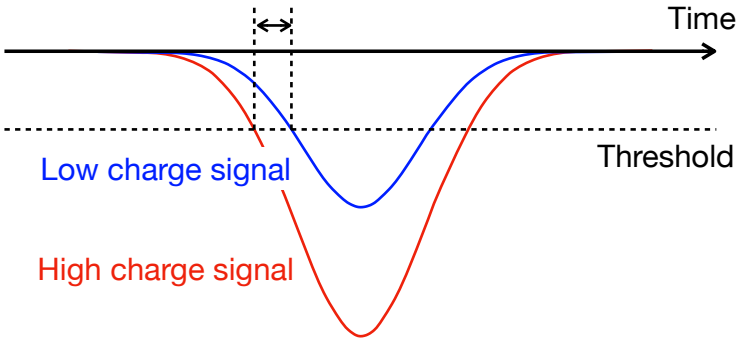

Figure 4.3: Schematic illustration of time-walk.

Since $G_{\mathrm{rel},i}$ is a relative value, it is normalized so that the average is one. The observed charge in each PMT is converted into the number of photoelectrons (equivalent to number of detected photons) from $G_{\mathrm{rel},i}$ and G_{abs} obtained above.

4.1.3 Timing Calibration

For low-energy events below several tens of MeV, it is assumed that at most one photon is detected by each PMT, and the reconstruction for the event vertex is performed using the information of the signal detection time by hit-PMTs. Assuming that all photons are emitted from a single vertex at the same time, the time difference of the time t at which the signal from each PMT is detected and the time of flight t_{tof} of the photon to reach the PMT, $t - t_{\mathrm{tof}}$ are ideally identical for all hit-PMTs. The purpose of timing calibration is to correct for the variations of each PMT due to differences in cable lengths and the response of the electronic device.. In addition, a signal with a large amount of charge has a higher pulse, resulting in a faster signal rise compared to a signal with a smaller amount of charge. This is called "time-walk" and shown in Figure 4.3. Therefore, the time to read out the signal depends on the amount of the charge. To correct for this effects, the correlations between time and charge for all PMTs are measured beforehand using an N_2 laser with a short pulse width and stored in the database (called "TQ-map"). The correction is applied from the TQ-map to the detection time for the time shift. Figure 4.4 shows an example of TQ-map for a PMT. The TQ-map are prepared for all 11,129 PMTs.

4.2 Measurement of Water Transparency

4.2.1 Laser Calibration

The intensity of the light attenuates exponentially with the distance traveled in the water as:

$$I(\lambda) = I_0(\lambda) \exp\left(-\frac{r}{L(\lambda)}\right), \tag{4.4}$$

where λ is wavelength of light, $I_0(\lambda)$ is initial value of light intensity, r is light travel distance, and $L(\lambda)$ is an attenuation length in water. As light travels through water, it is either absorbed or scattered. Scattering effects can be divided into symmetric scattering (Rayleigh scattering and symmetric Mie scattering) and asymmetric scattering (forward Mie scattering). The water attenuation length $L(\lambda)$ in the MC simulation is introduced with those contributions as:

$$L(\lambda) = \frac{1}{\alpha_{\mathrm{abs}}(\lambda) + \alpha_{\mathrm{sca,sym}}(\lambda) + \alpha_{\mathrm{sca,asy}}(\lambda)}, \tag{4.5}$$

where $\alpha_{\mathrm{abs}}(\lambda)$, $\alpha_{\mathrm{sca,sym}}(\lambda)$, and $\alpha_{\mathrm{sca,asy}}(\lambda)$ are water quality parameters representing absorption, symmetric scattering, and asymmetric scattering, respectively. These parameters are determined by laser calibration.

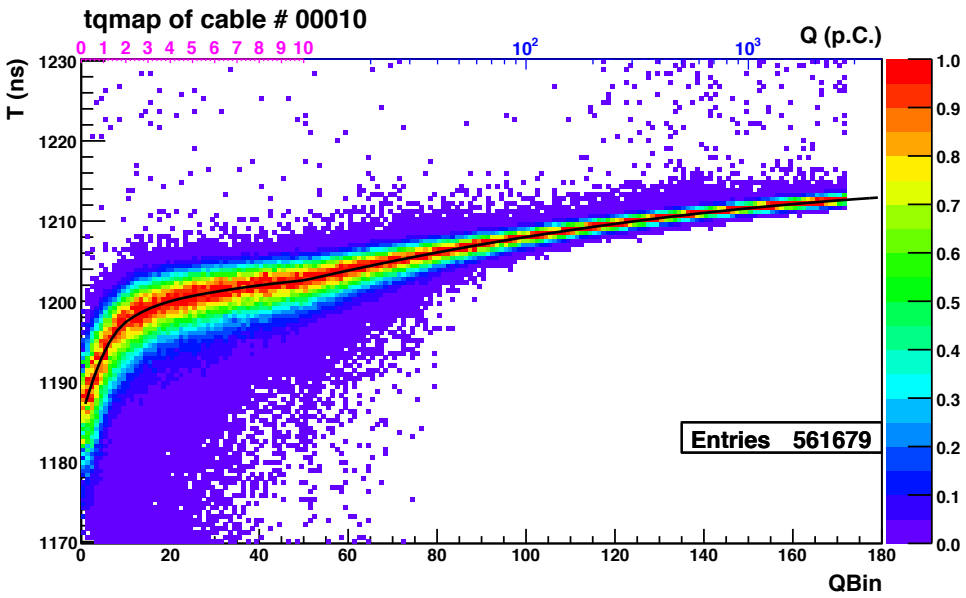

Figure 4.4: Example of TQ-map for a PMT. The vertical axis corresponds to the detection time of the signal, with a larger value indicating a faster detection time. The horizontal axis corresponds to the detected charge.

The PMT hit rates are monitored in various wavelength regions using laser dinode with wavelengths of 337, 375, 405, 445, and 473 nm. The measurement flow is as follows.

1. To measure the effect of scattering at different angles, the inner wall of the detector is divided into six regions: one top and five side (B1–B5) regions (Figure 4.5).

2. For each PMT in each region, the number of hit PMTs ($N_{\rm hit}$) and the total observed photoelectrons ($Q_{\rm tot}$) are measured, and the ratio ($N_{\rm hit}/Q_{\rm tot}$) is obtained.

3. MC simulations corresponding to this measurement are generated while varying water quality parameters and the $N_{\rm hit}/Q_{\rm tot}$ values are compared to the data.

4. Water quality parameters are determined to reproduce the data by minimum χ^2 method, i.e. minimizing the difference between the data and MC.

From the above measurements, the water quality parameters $\alpha_{\rm abs}(\lambda)$, $\alpha_{\rm sca,sym}(\lambda)$, and $\alpha_{\rm sca,asy}(\lambda)$ were obtained as a function of light wavelength as follows:

$$\alpha_{\rm abs}(\lambda) = \begin{cases} P_0 \times \dfrac{P_1}{\lambda^4} + P_0 \times P_2 \times \left(\dfrac{\lambda}{500}\right)^{P_3} & (\lambda \leq \lambda_{\rm thr}) \\ P_0 \times \dfrac{P_1}{\lambda^4} + {\rm Popefry}(\lambda) & (\lambda > \lambda_{\rm thr}) \end{cases} \tag{4.6}$$

$$\alpha_{\rm sca,sym}(\lambda) = \frac{P_4}{\lambda^4} \times \left(1.0 + \frac{P_5}{\lambda^2}\right) \tag{4.7}$$

$$\alpha_{\rm sca,asy}(\lambda) = P_6 \times \left(1.0 + \frac{P_7}{\lambda^4} \times (\lambda - P_8)^2\right). \tag{4.8}$$

The additional function Popefry(λ) of $\alpha_{\rm abs}(\lambda)$ for $\lambda > \lambda_{\rm thr}$ is defined by the absorption coefficient calculated theoretically by R. M. Pope and E. S. Fry [61].

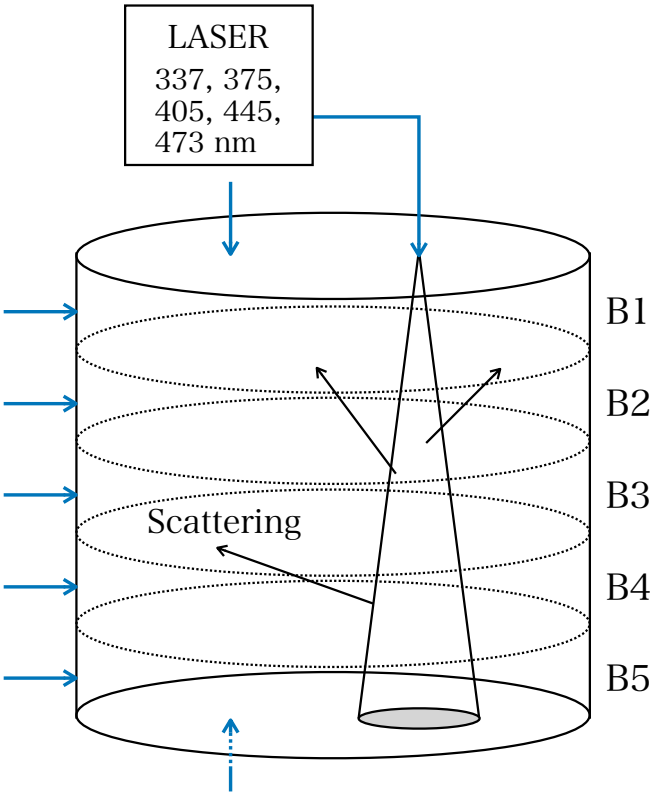

Figure 4.5: Schematic illustration of the laser calibration for measuring water quality parameters. The blue arrows indicate the position of the laser incidence.

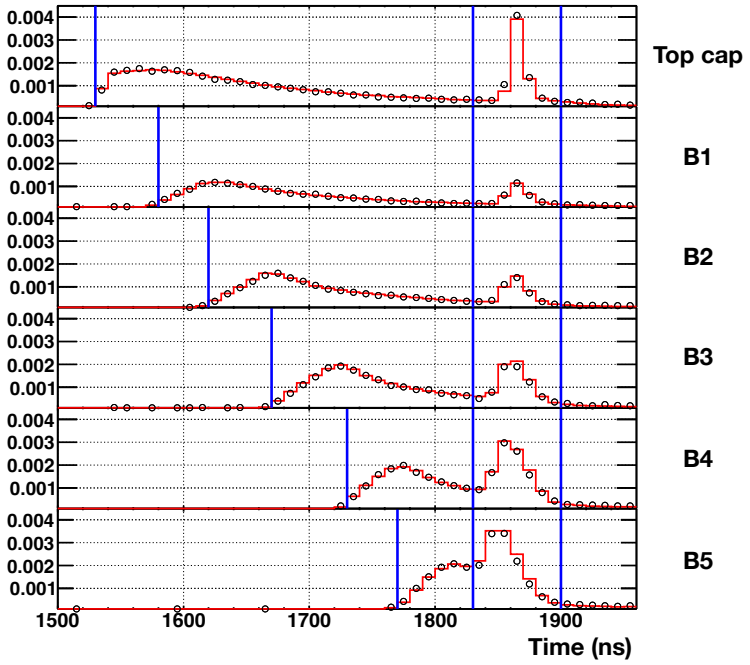

Figure 4.6: Time distribution of the ratio of the number of hit PMTs N_{hit} to the total charge Q_{tot} [58]. Distributions are shown in order from top to bottom. The horizontal axis is the time that the PMT detects the light after subtraction of the time of flight of the light, in ns. The vertical axis is the ratio $N_{\mathrm{hit}}/Q_{\mathrm{tot}}$. Black circles represent the data and red lines represent the MC simulations. The gradual peaks on the left-hand side are due to hits from light scattered in water. The peak on the right-hand side is derived from light reflected at the bottom of the detector.

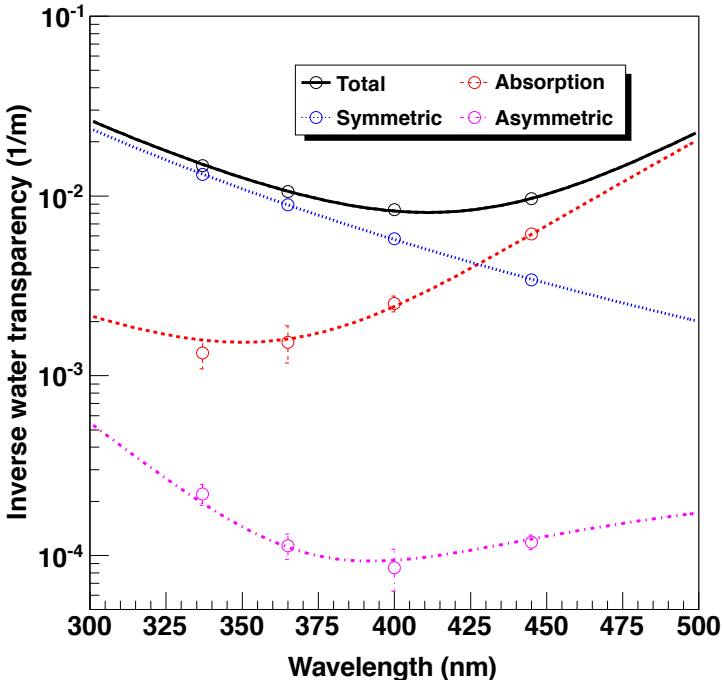

Figure 4.7: Wavelength dependence of water quality parameters [58]. Red dashed line shows $\alpha_{\mathrm{abs}}(\lambda)$, blue dotted line shows $\alpha_{\mathrm{sca,sym}}(\lambda)$, and magenta dashed-dotted line shows $\alpha_{\mathrm{sca,asy}}(\lambda)$, respectively.

4.2.2 Top-Bottom Asymmetry of Water Quality

The top-bottom asymmetry of the water transmission in the SK detector is also measured by the hit rates with the NiCf source. As described in Section 3.5, it has been confirmed that there is a vertical asymmetry in the transmittance of the water in the SK detector due to the water circulation system. Top-bottom asymmetry is defined using the average PMT hit rate R_{top} on the top cap, the average PMT hit rate R_{bot} on the bottom cap, and the average PMT hit rate R_{bar} on the barrel.

$$\alpha_{\mathrm{TBA}} = \frac{R_{\mathrm{top}} - R_{\mathrm{bot}}}{R_{\mathrm{bar}}} \times 100\ (\%) \tag{4.9}$$

Figure 4.8 shows the time variation of α_{TBA} measured using the NiCf source from December 2008 to September 2022.

4.3 Energy Calibration

In the SK experiment, the energy is calibrated using the linear accelerator (LINAC) and Deuterium-Tritium neutron (DT) generator. Below $\mathcal{O}(10)$ MeV, the total energy of the charged particle is reconstructed using the effective number of hit PMTs, N_{eff}, corrected for the light attenuation, acceptance anf the other effects (see Chapter 5).

4.3.1 LINAC

The LINAC is located around the top of the SK tank as shown in Figure 4.9 and used to inject a mono-energetic electron with 5–18 MeV downward into the detector from various positions. The energy of the injected electrons is measured beforehand with an accuracy within ±20 keV by a germanium detector. The absolute value of the energy scale is calibrated by a comparison of the reconstructed N_{eff} value and the energy of the injected electron. The resulting function is

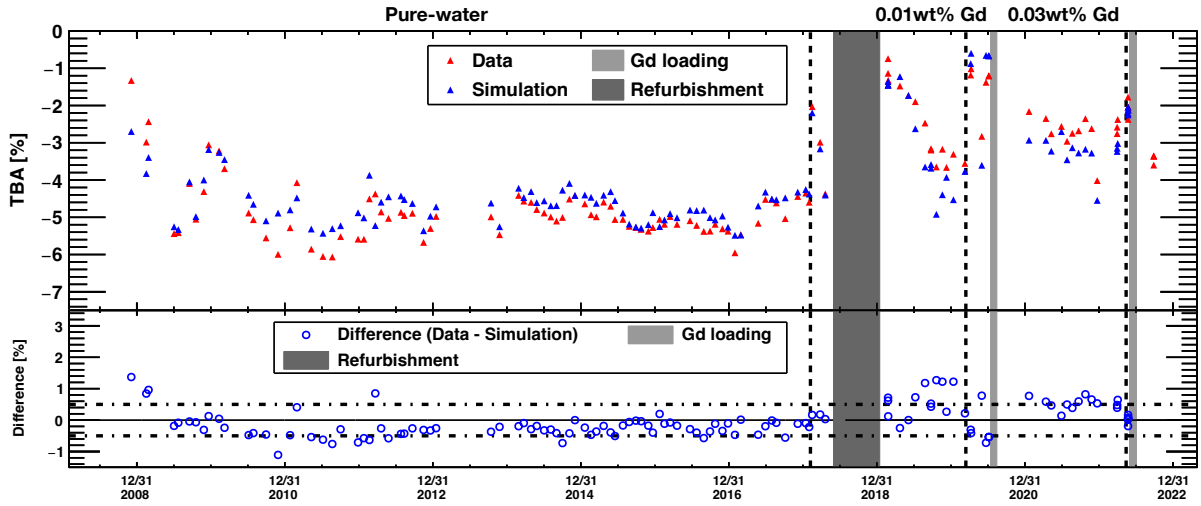

Figure 4.8: Time variation of top-bottom asymmetry measured using the NiCf source from December 2008 to September 2022. The red and blue triangle show the TBA value of the data and the MC, respectively. The blue open circle shows the difference between the data and the MC. The vertical dashed line shows the convection period to suppress TBA. This figure is taken from Ref. [62].

described in Section 5.2. The data obtained from the LINAC calibrations at several positions in the SK detector are compared with the corresponding MC simulations to check the position dependence of the energy scale and evaluate the systematic uncertainties.

4.3.2 DT Generator

The energy scale determined by LINAC is verified using the DT generator which produces electrons isotropically emitted from β decay of ^{16}N. Since electrons are produced isotropically by the DT generator, unlike the LINAC which injected electrons only downward, it is possible to check the directional dependence of the energy reconstruction.

DT generator is a neutron source that emits neutrons from helium and deuterium in the following reaction:

$$^{3}\mathrm{He} + {}^{2}\mathrm{H} \rightarrow {}^{4}\mathrm{He} + n \tag{4.10}$$

The neutron has an energy of 14.2 MeV, which are captured by ^{16}O in the water, in addition to hydrogen and Gd, and subsequently ^{16}N and a proton are produced.

$$^{16}\mathrm{O} + n \rightarrow {}^{16}\mathrm{N} + p \tag{4.11}$$

The ^{16}N has the lifetime of 10.3 s and it emits an electron (< 4.3 MeV) and γ (6.1 MeV) at the branching ratio of 66% or only an electron (< 10.4 MeV) at 28%:

$$^{16}\mathrm{N} \rightarrow {}^{16}\mathrm{O} + e^{-} + \nu_e \tag{4.12}$$

The DT generator is not suitable for calibration of the absolute energy scales, but the systematic uncertainty on the directional dependence of the energy reconstruction can be estimated using the isotropic emission of decay electrons and γ rays. The procedure of DT calibration is shown below and also illustrated in Figure 4.10:

1. The DT generator attached is submerged in the water in the detector using a crane. When the DT generator reaches a predetermined position, it stops and the DT generator is activated.

2. The DT generator produces $\sim 3 \times 10^6$ neutrons. About 1% of these neutrons are captured by ^{16}O, which undergoes the reaction described above to produce ^{16}N.

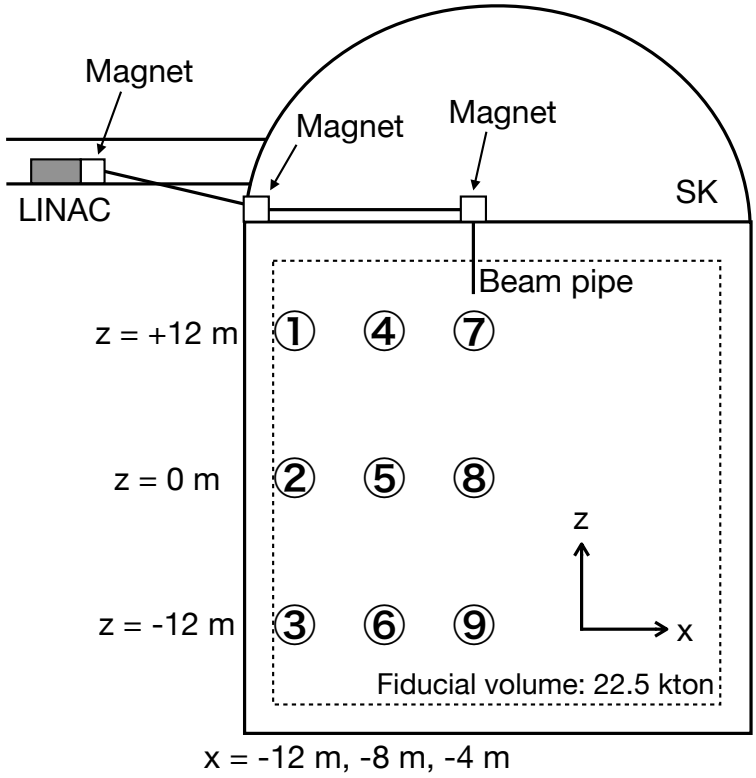

Figure 4.9: Schematic illustration of LINAC calibration.

3. To avoid shadowing of the DT generator itself, the DT generator was pulled up by 2 m. The data of electrons and γ rays generated by the decay of ^{16}N are then acquired.

4.4 Measurement of Gadolinium Concentration

In August 2020, the dissolution of gadolinium sulfate octahydrate $Gd_2(SO_4)_3 \cdot 8H_2O$ into the ultra-pure water in the SK detector was completed and the SK-Gd experiment has been started. The Gd mass concentration in the water was 0.01% from August 2020 to May 2022 (SK-VI) and was increased to 0.03% from July 2022 (SK-VII). In order to ensure Gd is dissolved in water without unexpected chemical reactions, it is necessary to periodically measure the Gd concentration in the detector. For this purpose, measurement of Gd concentration is conducted about once every a few weeks using the Americium/Beryllium (Am/Be) source.

A neutron and a γ ray are emitted from an Am/Be source through the following reactions:

$$^{241}\mathrm{Am} \rightarrow {}^{237}\mathrm{Np} + \alpha \tag{4.13}$$

$$^{9}\mathrm{Be} + \alpha \rightarrow {}^{12}\mathrm{C}^{*} + n \tag{4.14}$$

$$^{12}\mathrm{C}^{*} \rightarrow {}^{12}\mathrm{C} + \gamma\ (4.4\,\mathrm{MeV}). \tag{4.15}$$

As shown in Figure 4.11, the Am/Be source is surrounded by eight BGO scintillators. The calibration source is submerged in water in the detector for 30 minutes and the data is acquired. Once a 4.4 MeV γ ray is generated by the AmBe source, it produces electrons in the BGO scintillator through interactions such as photoelectric absorption, Compton scattering, and electron pair production. Then, scintillation light is emitted as the electrons pass through the BGO scintillator. This process occurs on a time scale of ns. Since it takes $\sim$100 μs for neutrons to be thermalized in water and captured on Gd or hydrogen, the neutron capture event occurs after the scintillation emission.

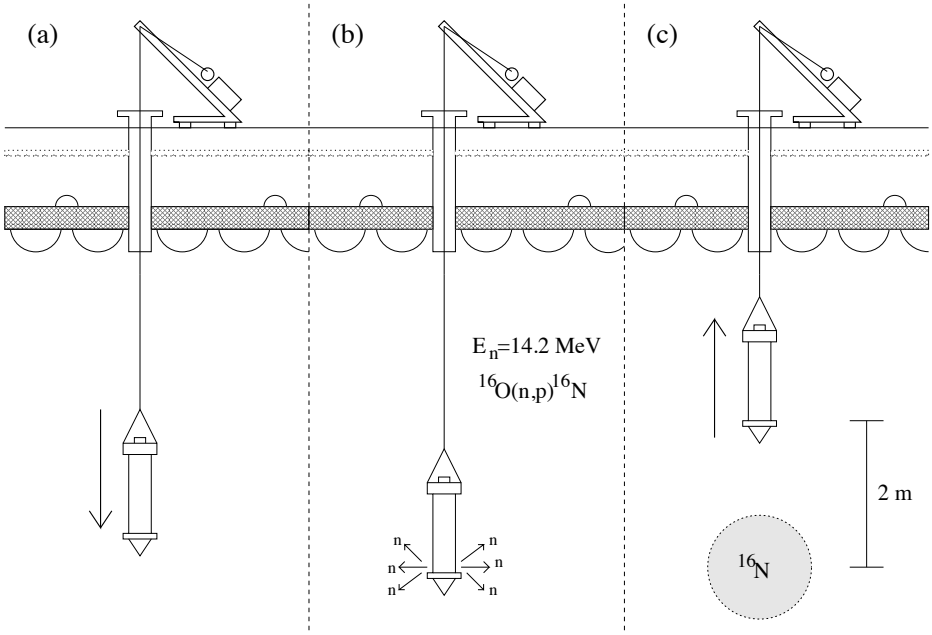

Figure 4.10: Schematic illustration of DT calibration.

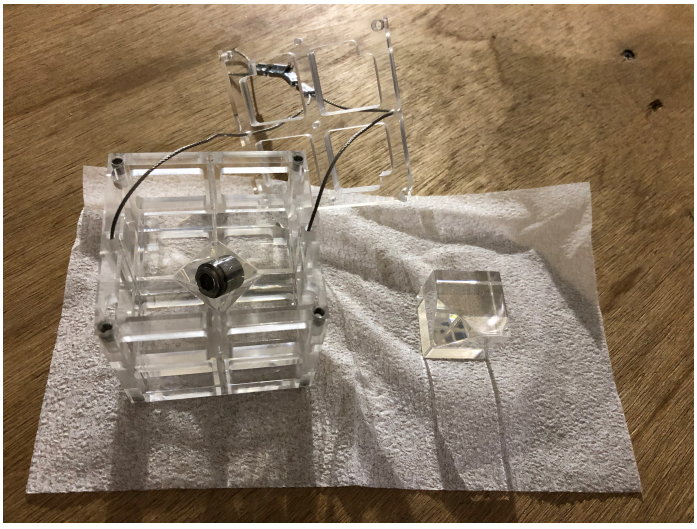

Figure 4.11: Am/Be source and BGO scintillators. The cylindrical source in the center on the left is the AmBe source. The source is surrounded by BGO scintillators. One of the eight pieces is shown on the right.

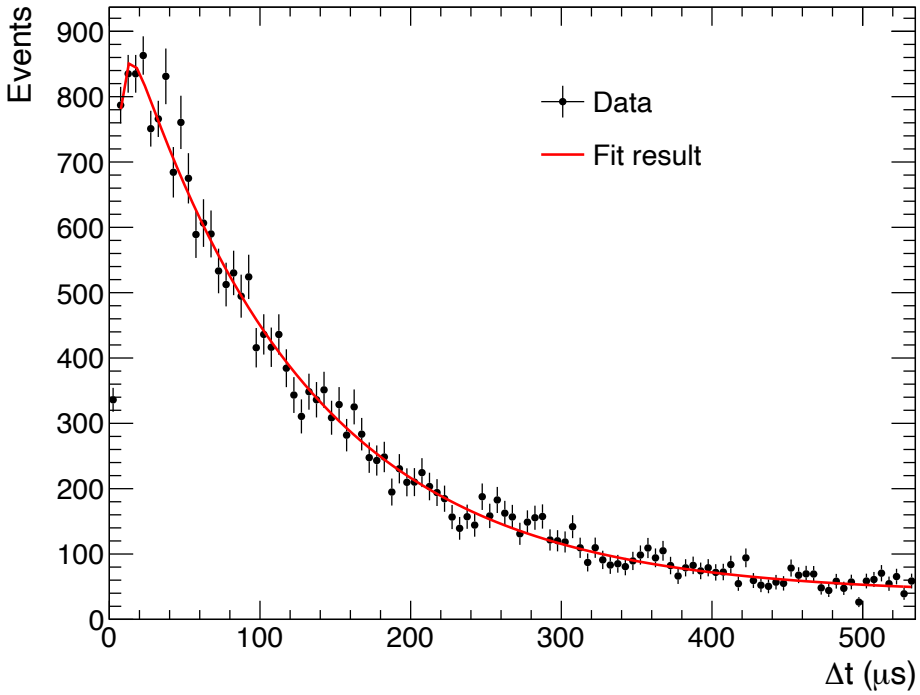

Figure 4.12: The distribution of the time difference Δt between the prompt and delayed events. The points are the data and the solid line is the fit result with Eq. 4.16.

The scintillation signal is called the prompt signal and the following neutron capture signal is called the delayed signal. The neutrons are identified by delayed coincidence measurement.

When the 4.4 MeV γ rays lose all their energy inside the BGO, a scintillation emission of $\sim$1,000 p.e. is detected (amount of scintillation light emission is larger than Cherenkov light emission for the same energy deposition by approximately one order of magnitude). This is sufficient to satisfy the SHE trigger (>60 ID hit-PMTs within 200 ns time window) to be issued. Once an SHE trigger is issued, all PMT hit information is stored up to the following 535 μs, and the delayed signal is searched in the time window. The time constant of neutron capture on Gd is determined by the time difference between the prompt and delayed signals, and the Gd concentration in the water is indirectly measured using the correlation between the capture time constant and the Gd concentration (Figure 3.11).

Figure 4.12 shows the distribution of the time difference Δt between the prompt and delayed events. The Δt distribution is fitted by the following function:

$$f(\Delta t) = a\left(1 - \exp\left(-\frac{\Delta t}{\tau_{\rm th}}\right)\right)\exp\left(-\frac{\Delta t}{\tau}\right) + b. \tag{4.16}$$

The fit determines a, b, and τ, where a and b are normalization constants corresponding to the number of signal and background events, respectively, and τ is the capture time constant on Gd. $\tau_{\rm th}$ represents the thermalization time constant, which is set to 4.3 μs [60]. Figure 4.13 shows the neutron capture time constants obtained from the Am/Be source calibrations performed in the latter half of 2020, as an example. The average of τ measured by the Am/Be source is 116.5 ± 0.2 μs overall the observation period with the Gd mass concentration of 0.01% (SK-VI).

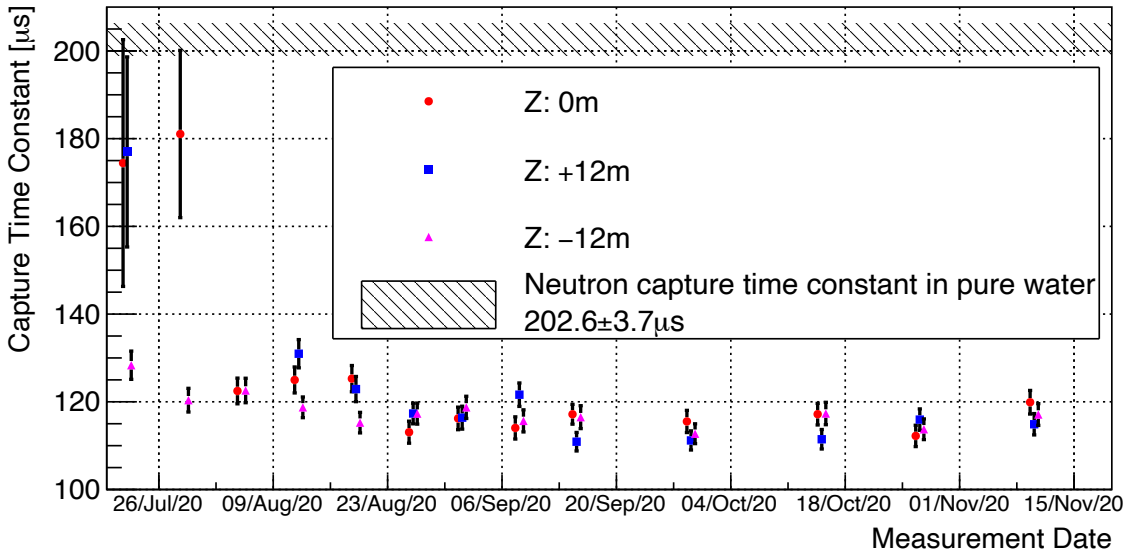

Figure 4.13: The neutron capture time constants obtained from the Am/Be source calibrations performed in the latter half of 2020 [60].

Chapter 5

Event Reconstruction

As shown in Chapter 6, 7, and 8, the signal and background are identified by the distance between the muon track and the vertex of neutron capture and electron events. This chapter will describe the overview of the algorithm to reconstruct the MeV scale events and muon events. Vertex positions and muon track are reconstructed from the signal (integral charge proportional to light intensity and timing information) of each PMT detected by Super-Kamiokande.

5.1 Vertex and Direction Reconstruction

Figure 5.1 shows the event displays of the Super-Kamiokande (SK) detector for electrons with the reconstructed energies of 16 MeV and 310 MeV for example. No clear rings can be seen at the MeV scale energies. As a guide, at 10 MeV electrons, the signal is detected in ∼60 PMTs. In most PMTs, a single photon (actually a single electron produced by the photoelectric effect of a single photon) is detected. Hereafter, the signal generated when a single photon is detected at a PMT is referred to as 1 p.e.

The reconstruction is performed by an algorithm called BONSAI (Branch Optimization Navigating Successive Annealing Iterations) [63]. In the vertex reconstruction of the low-energy region (typically between a few MeV to a few tens of MeV in SK), the trajectory of a charged particle is assumed to be a point, i.e. all Cherenkov photons are emitted from a point source. An electron with energy of 20 MeV can travel a distance of about 10 cm in pure water, which is small enough for the size of the detector (about 40 m), so this assumption is valid for the MeV scale. Among the many PMTs placed in the detector, the PMT that detects photons is called the "hit-PMT". The time information of the hit-PMTs is used to reconstruct the event vertex position. For each hit-PMT, the residual time $t - t_{\mathrm{tof}} - t_0$ is defined. where t is the time when the photon was detected at the PMT (hit time), t_{tof} is the time it took for the photon to reach the hit-PMT from the event vertex position (the subscript "tof" represents "time of flight".), and t_0 is the time when the Cherenkov light is emitted from the charged particle in the detector. Using this residual time, the likelihood function $\mathcal{L}(\boldsymbol{x}, t_0)$ is defined for each position $\boldsymbol{x}$ of the event candidate as

$$\mathcal{L}(\boldsymbol{x}, t_0) = \sum_{i=1}^{N_{\mathrm{hit}}} \ln P(t_i - t_{\mathrm{tof},i} - t_0), \tag{5.1}$$

where $P(t_i - t_{\mathrm{tof},i} - t_0)$ is the probability density function of the residual time determined from the LINAC calibration (see Chapter 4), as shown in Figure 5.2. The likelihood function $\mathcal{L}(\boldsymbol{x}, t_0)$ is calculated at each point in the detector as $\boldsymbol{x}$ is changed, and the location with the largest value is determined as the reconstructed vertex position. The number of emitted Cherenkov photons depends on the energy of the generated charged particles, and the total number of hit-PMTs changes. Therefore the accuracy of the event reconstruction depends on the energy. Figure 5.3 shows the energy dependence of the vertex resolution in event reconstruction. The vertex resolution

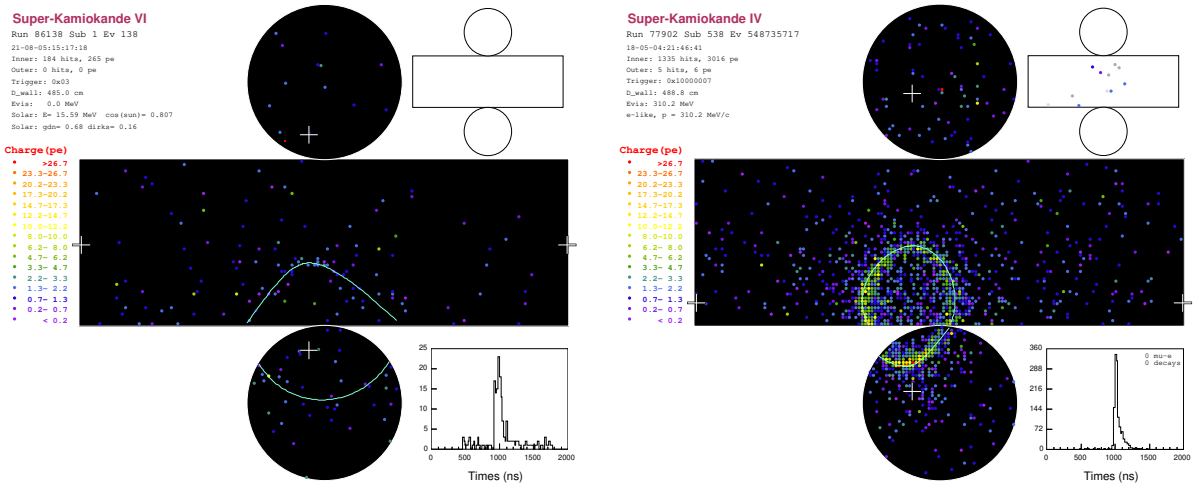

Figure 5.1: Event displays of the Super-Kamiokande detector for electrons with reconstructed energies of 15.6 MeV (left) and 310 MeV (right) for the data. The center developed view shows the inner detector and the upper right shows the outer detetor. The color points shows PMTs and the color scale represents the total number of detected photoelectrons by each PMT. The light green rings in the event displays are the reconstructed rings.

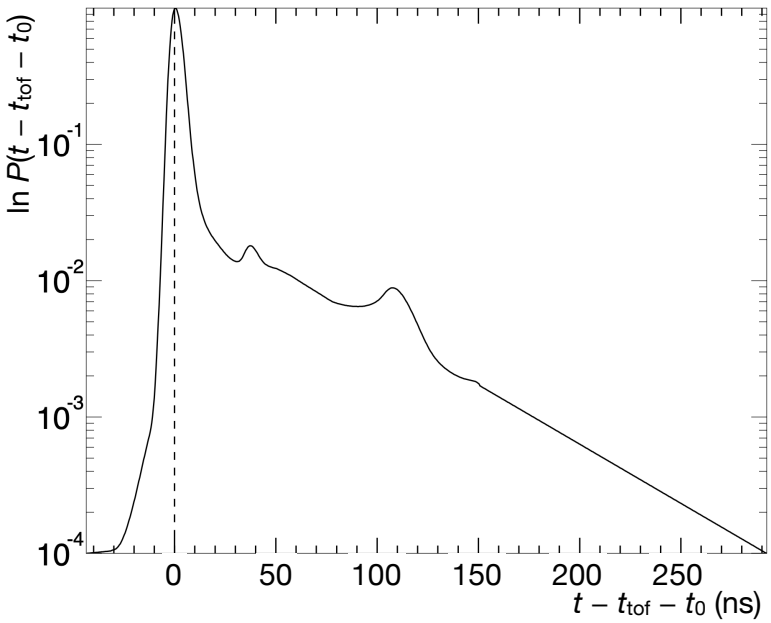

Figure 5.2: Probability density function of the residual time used to reconstruct the event vertex position. The second and third peaks are those seen due to the PMT afterpulses.

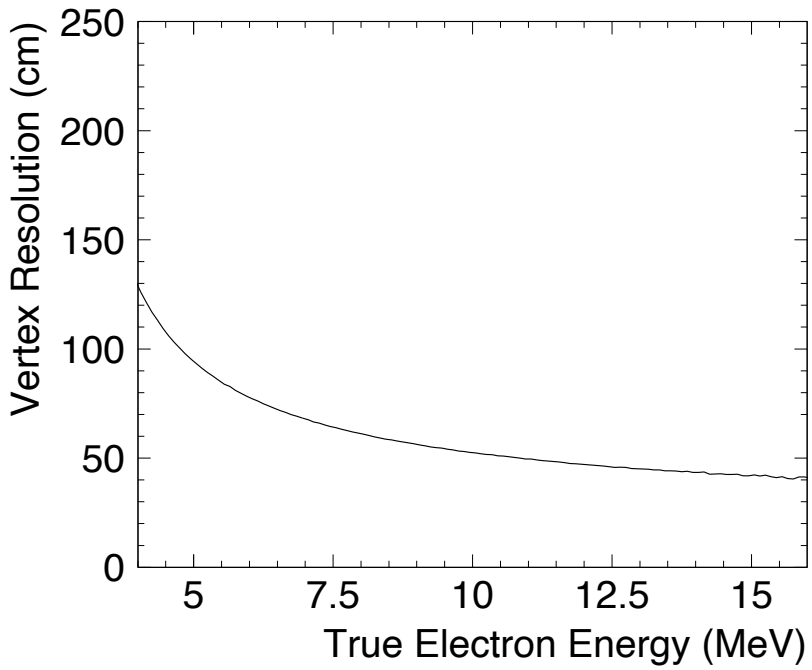

Figure 5.3: Vertex resolution as a function of total energy of an electron. This figure is taken from Ref. [64].

(1σ) is defined as the range of distances between the true and reconstructed vertex that includes 68.3% of the true event vertex position (Figure 5.4). The resolution decreases with the energy of electron from ~130 cm at 4 MeV to less than 60 cm above 10 MeV.

As the next step, direction of the charged particle is reconstructed. The Cherenkov light ring pattern is used for direction reconstruction as the center of the ring corresponds to the direction of the charged particle. The maximum likelihood method is used to determine the direction. The likelihood function is defined as

$$\mathcal{L}(\boldsymbol{d}) = \sum_{i=1}^{N_{20}} \left(\ln f(\cos\Theta_i, E) \times \frac{\cos\theta_i}{F(\theta_i)} \right), \tag{5.2}$$

where $\boldsymbol{d}$ is the direction of the charged particle and N_{20} is the number of hit-PMTs that detected the photon within 20 ns around the time of the event. $f(\cos\Theta_i, E)$ is the distribution function of the angle Θ_i between the direction of the charged particle and the direction from the vertex position (where Cherenkov photons are emitted) to the location of the i-th PMT which observes the photon. It also depends on the energy E due to multiple scattering in water by the electromagnetic field (Coulomb scattering). $\cos\theta_i / F(\theta_i)$ is the correction term for the solid angle of each PMT viewed from the vertex position. The definition of the angle is shown in Figure 5.5. $F(\theta)$ represents the PMT acceptance given by

$$F(\theta) = 0.205 + 0.524\cos\theta + 0.390\cos^2\theta - 0.132\cos^3\theta. \tag{5.3}$$

The parameters g_{vtx} and g_{dir} are defined to indicate the certainty of event point and direction reconstruction. The parameter g_{vtx}, which represents the degree of certainty of the vertex

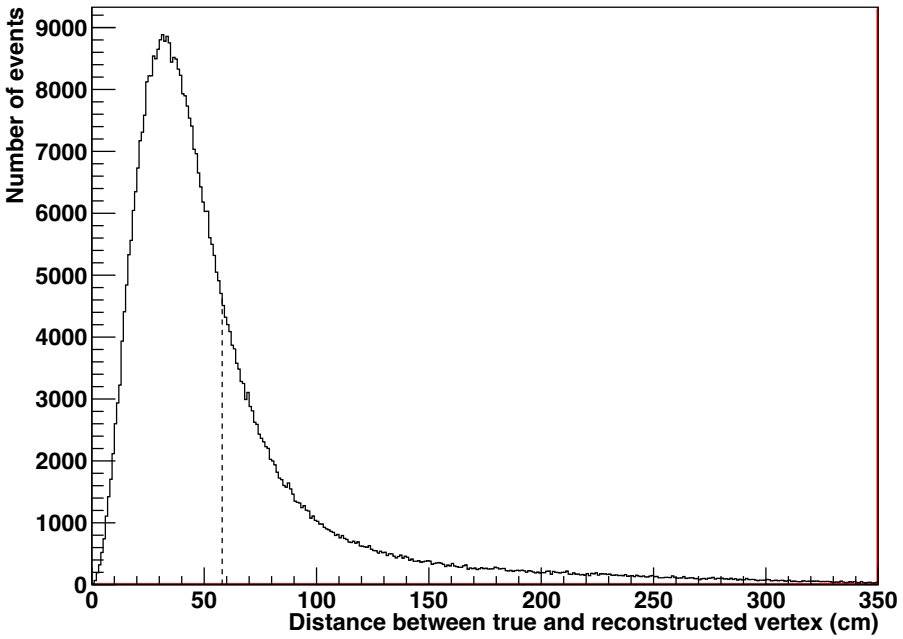

Figure 5.4: Distribution of the distance between the true and reconstructed vertex for a Monte Carlo (MC) simulation with 10 MeV electrons generated uniformly in the detector. Since the range from 0 cm to the dotted line (58 cm) contains 68.3% of the total, 58 cm is the resolution of the vertex reconstruction.

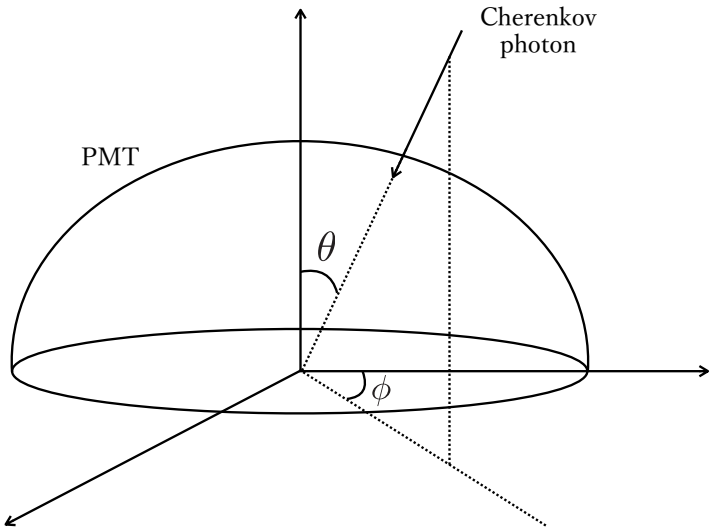

Figure 5.5: Definition of incident angle (θ, ϕ) of photon to PMT surface.

reconstruction, is defined as

$$g_{\mathrm{vtx}} = \frac{\sum_i \exp\left[-\frac{1}{2}\left(\frac{\Delta\tau_i}{\omega}\right)^2\right] \exp\left[-\frac{1}{2}\left(\frac{\Delta\tau_i}{\sigma}\right)^2\right]}{\sum_i \exp\left[-\frac{1}{2}\left(\frac{\Delta\tau_i}{\omega}\right)^2\right]}, \tag{5.4}$$

where $\Delta\tau_i \equiv t_i - t_{\mathrm{tof},i} - t_0$. ω gives the weight to suppress the dark noise and σ is the time resolution of the PMT for a single photoelectron signal, which are set to 60 ns and 5 ns, respectively. g_{vtx} takes values in the range from zero to one. The closer to one, the more certain the reconstruction is.

The certainty of direction reconstruction, g_{dir}, is evaluated by the uniformity of the hit-PMTs based on the Kolmogorov-Smirnov test as follows

$$g_{\mathrm{dir}} = \frac{\max\{\Phi_{\mathrm{uni},i} - \Phi_{\mathrm{data},i}\} - \min\{\Phi_{\mathrm{uni},i} - \Phi_{\mathrm{data},i}\}}{2\pi}, \tag{5.5}$$

where $\Phi_{\mathrm{uni},i}$ is the direction angle of the i-th hit-PMT when PMT hits are assumed to be uniformly distributed around the ideal Cherenkov ring, and $\Phi_{\mathrm{data},i}$ is the angle formed by the direction of the reconstructed charged particle and the direction from the vertex position to the location of the i-th hit-PMT. g_{dir} takes values in the range from zero to one, with the value closer to zero for more certain reconstruction.

Using the two parameters g_{vtx} and g_{dir}, the parameter Δg^2 is defined to represent the certainty of the event reconstruction[1].

$$\Delta g^2 \equiv g_{\mathrm{vtx}}^2 - g_{\mathrm{dir}}^2 \tag{5.6}$$

The Δg^2 takes values in the range from -1 to $+1$, with larger value for more accurate event reconstruction.

5.2 Energy Reconstruction

In the energy region below a few tens of MeV, the number of hit-PMTs is used for the energy reconstruction. For the energy scale with small number of emitted photons, most hit-PMTs detect only one photoelectron although same PMTs close to the vertex position may detect multiple photoelectrons. The number of hit-PMTs is used instead of using the total number of photoelectrons because the resolution of PMTs is not sufficiently high to accurately count the number of photoelectrons in the signal. Firstly, the number of PMTs that detected light within 50 ns around the event time, N_{50}, is counted for energy reconstruction. It is known that if N_{50} is used as is, the reconstructed energy will differ depending on the event vertex positions. Therefore, the effective number of hit-PMTs with some corrections, N_{eff}, is usedfor the energy reconstruction. The N_{eff} is calculated from N_{50} with some corrections as

$$N_{\mathrm{eff}} = \sum_{i=1}^{N_{50}} \left[(X_i - \epsilon_i^{\mathrm{tail}} - \epsilon_i^{\mathrm{dark}}) \times \frac{N_{\mathrm{all}}}{N_{\mathrm{alive}}} \times \frac{S(0,0)}{S(\theta_i,\phi_i)} \times \exp\left(\frac{r_i}{L_i^{\mathrm{eff}}}\right) \times \frac{1}{QE_i(1 + C \cdot G_i(t))} \right]. \tag{5.7}$$

Below is an explanation of each correction term in Eq. (5.7).

- Occupancy X_i:

  If an event occurs at the edge of the fiducial volume and Cherenkov photons are emitted toward the detector wall, multiple photons may be detected in one PMT. In this case, it is likely that photons are also detected by the surrounding PMTs. Thus, the expected number

[1] The Δg^2 is internally called as "ovaQ" (One dimensional variable of Vertex and Angular reconstruction Quality).

of photons detected by a PMT is estimated by the number of hit-PMTs surrounding the PMT. Using the ratio x_i ($= n_i/N_i$) of the number of PMTs N_i surrounding the i-th hit-PMT and the number of hit-PMTs n_i among them, X_i is expressed as

$$X_i = \begin{cases} \dfrac{-\log(1-x_i)}{x_i} & (x_i < 1) \\ 3.0 & (x_i = 1) \end{cases}$$

- Correction for delayed hits ϵ_i^{tail}:

  Fraction of hits leaks out of the 50 ns time window due to scattering in water or reflection on the detector wall or surface of the PMT before the photons are detected. The ϵ_i^{tail} is introduced to compensates the leak of the delayed hits. The definition is

$$\epsilon_i^{\text{tail}} = \frac{N_{100} - N_{50}}{N_{50}} - R_{\text{dark}}^{\text{ave}} \times 50\,\text{ns} \times \frac{N_{\text{alive}}}{N_{50}}, \tag{5.8}$$

  where N_{alive} is the total number of properly working PMTs and $R_{\text{dark}}^{\text{ave}}$ is the average dark rate of all PMTs.

- Correction for PMT dark hit ϵ_i^{dark}:

  Even in the absence of light irradiation, single photoelectron is often detected by PMT due to thermionic emission and Cherenkov light emitted by radioactive isotopes contained in the glass of PMT. This signal is called dark noise, and the rate is called dark rate. Averaged dark noise rate of all PMTs in the inner detector of SK is 3 kHz depending on the obsevation priod. As 11,129 PMTs are equipped in the SK detector, ∼2 PMT output the dark noise in 50 ns in average. For the event below 10 MeV, the effect of dark noise cannot be ignored because the amount of light observed is small, typically ∼60 photons at 10 MeV. The expected value of dark noise is subtracted in the measurement of the energy. Since the dark rate varies with time, it must be corrected according to the observation period.

  The correction for hit-PMTs due to dark noise is defined as

$$\epsilon_i^{\text{dark}} = R_{\text{dark}}^{\text{ave}} \times 50\,\text{ns} \times \frac{N_{\text{alive}}}{N_{50}} \times \frac{r_j^{\text{dark}}}{\sum_j^{N_{50}} \frac{r_j^{\text{dark}}}{N_{50}}}, \tag{5.9}$$

  where r_{dark}^i is the measured dark rate for the i-th hit-PMT. The expected number of dark hits in a time width of 50 ns is calculated from the average dark rate of the hit-PMTs.

- Correction for fraction of properly working PMTs $N_{\text{all}}/N_{\text{alive}}$:

  N_{all} is the total number of PMTs installed in the inner detector, which was 11,129 during the data taking period from August 2020 to May 2022 (SK-VI). About 1% of the installed PMTs were not in operation due to malfunction in that period. N_{50} is normalized by $N_{\text{all}}/N_{\text{alive}}$ to correct the time variation, where The number of PMTs in normal operation, N_{alive}, varies depending on the observation period.

- Correction for photon incident angle $S(\theta, \phi)$:

  The PMTs protrude from the inner wall of the detector. Therefore, the effective photocathode coverage depends on the angle of incidence of photons. To correct for this, a function $S(\theta, \phi)$ is introduced. The definitions of the photon incident angles θ and ϕ are shown in Figure 5.5.

  $S(\theta, \phi)$ was obtained by a simulation with the cylindrical structure using a Geant4 and generating photons at random positions and directions in the detector. The definition of $S(\theta, \phi)$ is

$$S(\theta, \phi) = \frac{N_{\text{obs}}(\theta, \phi)}{N_{\text{inc}}(\theta, \phi)}, \tag{5.10}$$

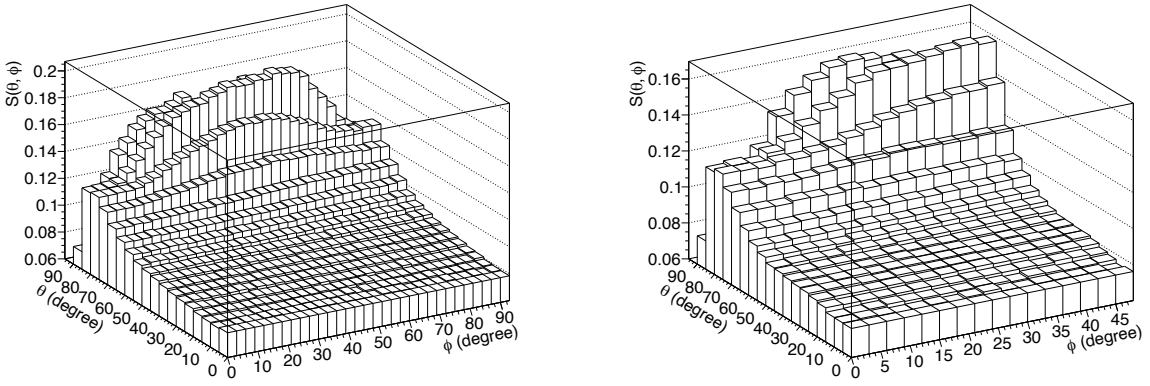

(a) Correction function $S(\theta, \phi)$ for barrel PMTs.

(b) Correction function $S(\theta, \phi)$ for cap PMTs.

Figure 5.6: Correction function for photocathode coverage $S(\theta, \phi)$

where $N_{\text{gen}}(\theta, \phi)$ is the total number of photons incident on the PMT at angle (θ, ϕ), and $N_{\text{inc}}(\theta, \phi)$ is the total number of photoelectrons produced by the photoelectric effect from photons incident on the PMT at angle (θ, ϕ). Figure 5.6 shows the shape of the function $S(\theta, \phi)$. Note that the PMTs attached to the side wall of the detector (barrel PMTs) and those attached to the top and bottom of the detector (cap PMTs) have different ranges of angles at which photons can incident the PMT surface, so they are defined separately.

- Correction for water attenuation effects $\exp(r_i/L_i^{\text{eff}})$:

  Cherenkov light is attenuated from the emission point to the PMT due to scattering and absorption in water. The attenuation rate is expressed as $\exp(-r_i/L_i^{\text{eff}})$, where r_i is the distance from the event vertex position to the i-th PMT and L_i^{eff} is the effective water transmission length from the event vertex position to the i-th PMT, taking into account the position dependence and time variation of water quality. As described in Section 4.2.2, it has been confirmed that there is a position dependence of the transmission length L of water in the detector along the vertical axis due to the effect of water circulation system. The position dependence is modeled as follows with the first-order dependence in the height (z-axis):

$$L(\lambda, z) = \begin{cases} \dfrac{1}{\alpha_{\text{abs}}(\lambda) \times (1 + \beta z) + \alpha_{\text{sca}}(\lambda)} & (z > -12\,\text{m}) \\ \dfrac{1}{\alpha_{\text{abs}}(\lambda) \times (1 - \beta \cdot 12\,\text{m}) + \alpha_{\text{sca}}(\lambda)} & (z \leq -12\,\text{m}) \end{cases} \tag{5.11}$$

  where λ is the wavelength of the photon. When the photon travels a distance r_i in water, the reaction cross section $\sigma_i(\lambda)$ is expressed as

$$\sigma_i(\lambda) = \alpha_{\text{abs}}(\lambda) \left[1 + \beta \left(z + \frac{1}{2} r_i \cdot dz_i\right)\right] + C_{\text{sca}} \cdot \alpha_{\text{sca}}(\lambda), \tag{5.12}$$

  where dz_i is the z component of the unit direction of the photon. The C_{sca} is a constant introduced to account for the effect of photon scattering. Since it is difficult to accurately estimate the contribution of scattering of photons in water, the position dependence of N_{eff} is compared by changing the value of C_{sca}, and the value with the smallest magnitude is used for event reconstruction. In this case, the probability p_i of a photon arriving at the i-th PMT from the event point is expressed as

$$p_i = \int_{\lambda_{\text{min}}}^{\lambda_{\text{max}}} w_0(\lambda) \exp(-\sigma_i(\lambda) \cdot r_i) d\lambda, \tag{5.13}$$

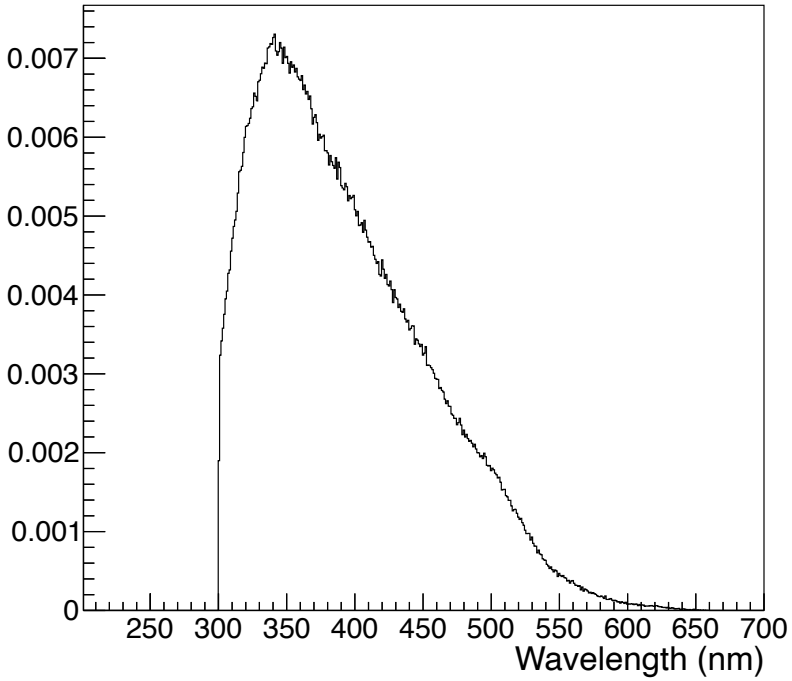

Figure 5.7: Probability density distribution of Cherenkov photon wavelengths $w_0(\lambda)$.

where $w_0(\lambda)$ is the probability density distribution of Cherenkov photon wavelengths, as shown in Figure 5.7. It is integrated with the weight for attenuation effects from $\lambda_{\mathrm{min}} = 300\,\mathrm{nm}$ to $\lambda_{\mathrm{max}} = 650\,\mathrm{nm}$. The probability p_i can also be expressed using the effective water transmission length L_i^{eff} as

$$p_i = \exp\left(-\frac{r_i}{L_i^{\mathrm{eff}}}\right). \tag{5.14}$$

From the comparison of Eq. (5.13) and (5.14), the effective water transmission length L_i^{eff} can be expressed as follows:

$$L_i^{\mathrm{eff}} = -\frac{r_i}{\ln\left(\int_{\lambda_{\mathrm{min}}}^{\lambda_{\mathrm{max}}} w_0(\lambda)\exp(-\sigma_i(\lambda)\cdot r_i)d\lambda\right)} \tag{5.15}$$

L_i^{eff} is uniquely determined from the distance between the event vertex and the i-th hit-PMT.

- Correction for PMT quantum efficiency and PMT gain variation $[QE_i(1 + C \cdot G_i(t))]^{-1}$:

  Since the quantum efficiency is different for each PMT, the non-uniformity is corrected. QE_i is the relative quantum efficiency of the i-th PMT, which is evaluated using the data taken with a NiCf source (see Section 4.1.1). $G_i(t)$ is relative gain of i-th hit-PMT. C is a constant calculated based on the assumption that the correlation between the time variation of PMT gain and the time variation of hit rate is linear.

From the above corrections, the effective number of hit-PMTs, N_{eff}, is determined. The energy of the charged particles is reconstructed from N_{eff} using the following relationship between N_{eff}

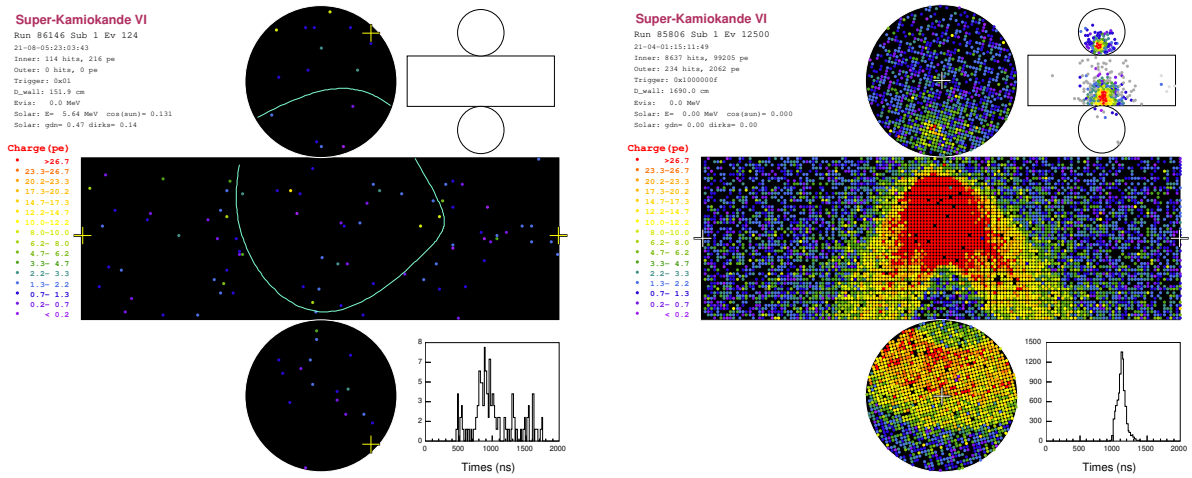

Figure 5.8: Comparison of eventdisplays for an electron with a few MeV (left) and a cosmic-ray muon (right).

and the reconstructed total energy $E_{\rm rec}$.

$$E_{\rm rec} = \begin{cases} \sum_{i=1}^{6} P_i (N_{\rm eff})^{i-1} & (N_{\rm eff} < N_{\rm thr}) \\ \sum_{i=1}^{6} P_i (N_{\rm thr})^{i-1} + (N_{\rm eff} - N_{\rm thr}) \sum_{i=2}^{6} (i-1) P_i (N_{\rm thr})^{i-2} & (N_{\rm eff} \geq N_{\rm thr}) \end{cases} \tag{5.16}$$

where $N_{\rm thr} = 331.7$. The parameters P_i are determined by a fit to the calibration data using LINAC by which electrons with known energies are generated inside the detector (Section 4.3.1). $P_1 = 0.74$, $P_2 = -0.13$, $P_3 = -1.07 \times 10^{-4}$, $P_4 = 9.68 \times 10^{-7}$, $P_5 = -3.04 \times 10^{-9}$, $P_6 = 3.31 \times 10^{-12}$.

5.3 Muon Event Reconstruction

Cosmic-ray muon events are by far more energetic than the MeV-scale electron-like events discussed in the previous sections, resulting in much higher PMT hits and charges observed in SK as shown in Figure 5.8. In addition, the trajectories of cosmic-ray muon events are track-like unlike MeV-scale electron-like events which can be treated as a point source in the SK detector. This section provides an overview of the algorithm that identifies muons and reconstructs their directions and trajectories. Further details are described in Ref. [65, 66].

Before the muon reconstruction, the ID hit-PMTs used in the reconstruction are selected with the observed charged in each ID hit-PMT (first cleaning cut). The criteria of the ID hit-PMT selection are classified by the total number of ID hit-PMTs, as shown in Table 5.1.

Table 5.1: Selection criteria of the ID hit-PMT.

Number of ID hit-PMTs	Observed charge of ID hit-PMT
$< 8{,}000$	≥ 2.0 p.e.
8,000–10,000	≥ 2.5 p.e.
$> 10{,}000$	≥ 3.0 p.e.

After the first cleaning cut, the number of hit-PMTs contained in the eight PMTs surrounding a hit-PMT within 10 ns window, $N_{\rm nn}$, is calculated. $N_{\rm nn}$ is called the nearest neighbor hits and Figure 5.9 shows an example for $N_{\rm nn} = 4$. Only the ID hit-PMTs which have more than certain

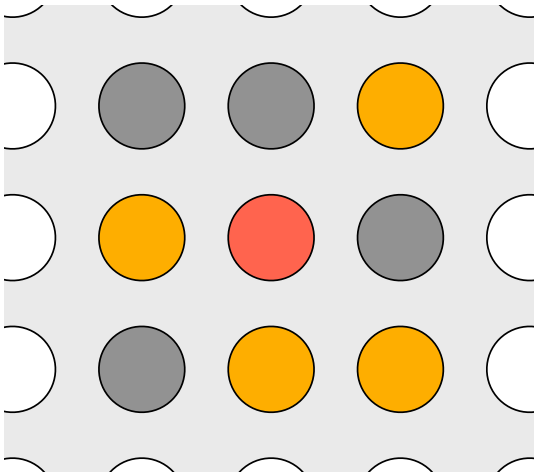

Figure 5.9: Schematic illustration of the case of $N_{\mathrm{nn}} = 4$. The central red circle shows the standard hit-PMT. In the surrounding eight PMTs, the orange circles show hit-PMTs and the gray circles show the unhit-PMTs.

number of N_{nn} are used for the muon reconstruction. The conditions for N_{nn} are shown in Table 5.2.

Table 5.2: Requirements for N_{nn} corresponding to the number of ID hit-PMTs after the first cleaning cut.

Number of ID hit-PMTs after the first cleaning	N_{nn} threshold
< 500	1
500–2,500	2
2,500–5,000	3
5,000–7,500	4
$> 7{,}500$	5

After the PMT hit cleaning above, the entrance position of the cosmic-ray muons to the ID and the timing are estimated as the location and hit timing of the earliest hit-PMT with $N_{\mathrm{nn}} \geq 3$. If there is no hit-PMT with $N_{\mathrm{nn}} \geq 3$, the threshold is reduced until an entrance position candidate is found.

Next, the direction is reconstructed. Hit-PMTs used for the direction reconstruction are restricted by the hit timing. Considering a fact that velocity of muons at GeV-scale is faster than the speed of light propagation in water, Cherenkov light from the muon can not reach a PMT earlier than the travel time of the muon:

$$T_{\mathrm{early}} = T_{\mathrm{entry}} + \frac{D}{v_1}, \tag{5.17}$$

where T_{entry} represents the PMT hit timing at the entrance position, D represents the distance between the entrance position and the location of each hit-PMT, and v_1 is set to be 3.4×10^8 m/s which is slightly faster than the speed of light to accommodate fluctuations of PMT hit timing. In addition, Cherenkov light from the muon also can not reach a PMT later than the travel time of the photons in the water:

$$T_{\mathrm{later}} = T_{\mathrm{entry}} + \frac{D}{v_2}, \tag{5.18}$$

where v_2 is set to be 1.8×10^8 m/s which is slightly slower than the speed of propagation of light in the water by the same reason as written above. The direction reconstruction is performed using the hit-PMTs with the hit timing from T_{early} to T_{later}. Then, the direction is estimated to maximize

goodness G, defined as follows:

$$G = F(f_{\text{cone}}) \sum_{i=1}^{N} g(\delta t_i), \tag{5.19}$$

where f_{cone} represents the ratio of the number of PMTs in the Cherenkov cone to the total number of the selected hit-PMTs. The direction from the entry point to the PMT hit should be within the Cherenkov cone. Therefore, the relationship between muons and hit-PMTs should satisfy at least one of the following two conditions:

- $\boldsymbol{d} \cdot \boldsymbol{r} > 0.74$, where $\boldsymbol{d}$ represents a unit vector from the muon entrance position to hit-PMT and $\boldsymbol{r}$ represents the muon direction.
- $D < 2\,\text{m}$.

The latter condition is used to collect hit-PMTs close to the entrance position. After f_{cone} is evaluated, $F(f_{\text{cone}})$ is calculated based on the following form:

$$F(f_{\text{cone}}) = \begin{cases} \dfrac{0.9}{C_{\text{cut}}} f_{\text{cone}} & (f_{\text{cone}} < 0.75) \\ \dfrac{0.1 f_{\text{cone}} + 0.9 - C_{\text{cut}}}{1 - C_{\text{cut}}} & (f_{\text{cone}} > 0.75) \end{cases}, \tag{5.20}$$

where $C_{\text{cut}} = 0.74$. δt_i represents the time difference between the measured hit timing of the i-th hit-PMT and the expected timing given by the muon track assumed in the iteration. $g(\delta t_i)$ is defined as follows:

$$g(\delta t_i) = \begin{cases} \exp\left(-\dfrac{\delta t_i}{\lambda(q_i)}\right) & (\delta t_i < 0) \\ \exp\left(-\dfrac{(\delta t_i - t_{\text{mean}}(q_i))^2}{2(\sigma(q_i))^2}\right) & (\delta t_i > 0 \text{ or } q_i > 30\,\text{p.e.}) \end{cases}, \tag{5.21}$$

where q_i represents the observed charge of i-th hit-PMT. $t_{\text{mean}}(q)$, $\sigma(q)$, and $\lambda(q)$ were determined by timing distributions from the data as follows:

$$t_{\text{mean}}(q) = 2.563 - 0.029 \times q \tag{5.22}$$

$$\sigma(q) = 1.690 + 2.514 \exp\left(-\frac{q}{2.453}\right) \tag{5.23}$$

$$\lambda(q) = 1.254 + 14.863 \exp\left(-\frac{q}{2.316}\right). \tag{5.24}$$

Chapter 6

Evaluation of Stability and Uniformity of Neutron Detection

In order to observe supernova relic neutrinos (SRNs) in Super-Kamiokande (SK) with Gd-loaded water (SK-Gd), it is important to continue stable observations for a long period of time. It takes more than 10 years to achieve the observation with modern theoretical expectations. The key of the SK-Gd experiment is the detection of neutron capture on Gd in the water. Electron antineutrinos in SRN interact with free protons (hydrogen nuclei) in the entire volume of the detector to produce positrons and neutrons ($\bar{\nu}_e + p \rightarrow e^+ + n$). Therefore, it is important to confirm the Gd concentration is uniform in the detector and monitor the stability during the observation period. In this study, a method was established to evaluate the stability and uniformity of the neutron detection by the SK-Gd detector using neutrons induced by cosmic-ray muons. This chapter describes the evaluation method and the stability in the period from September 2020 to June 2022 after gadolinium loading.

6.1 Overview

As described in Chapter 1, cosmic-ray muons and muon-induced showers interact with oxygen nuclei in water to produce neutrons, which are called muon-induced neutrons or cosmogenic neutrons. These neutrons are thermalized in water within $\sim$5 μs and then captured on hydrogen or Gd. If a neutron is captured on hydrogen, a 2.2 MeV γ ray is emitted. On the other hand, if a neutron is captured on Gd, multiple γ rays totaling $\sim$8 MeV are emitted. Among those, the selection criteria of the data analysis were set to collect neutron captures on Gd to suppress background at low energy region. The time from neutron production to capture by hydrogen or Gd and the fraction of Gd capture depend on the concentration of Gd dissolved in water. 13 tons of Gd sulfate octahydrate ($Gd_2(SO_4)_3 \cdot 8H_2O$) were dissolved in 50 kton of ultra-pure water during the first SK-Gd phase (SK-VI), which has been started since August 2020. This corresponds to a Gd mass concentration of 0.01%, at which concentration neutrons are captured on hydrogen or Gd in $\sim$116 μs on average. $\sim$50% of neutrons are captured on Gd with this Gd concentration.

The calibration with the Am/Be neutron source (Section 4.4) is performed about once every a few weeks to confirm the stability of Gd concentrations in the water. The Am/Be source is submerged in the detector along the center axis using a wire and data are acquired at three positions: bottom ($-$12 m), center, and top ($+$12 m) for 30 minutes each. The calibration source allows precise measurement of the neutron detection efficiency, while there are a few limitations: (1) neutron detection efficiency off the counter axis of the cylindrical detector can not be measured; (2) variations between the calibrations can not be monitored. In order to compensate for the limitations and to measure the uniformity and stability of Gd concentration in the detector, a new method using cosmogenic neutrons was proposed and established in this study. As the cosmic-ray muons are reaching SK at a frequency of $\sim$2 s^{-1}, the muon-induced neutrons allow monitoring of Gd concentration in parallel to the neutrino observation. Furthermore, as the spallation interaction

Table 6.1: The features of the neutrons from Am/Be source and cosmic-ray muons.

Neutron source	Am/Be	Cosmic-ray muon
Frequency	Every a few weeks	Continuous ($\sim 2\,s^{-1}$)
Position	Specific (3 positions)	Uniform
Multiplicity	1	0 to $\mathcal{O}(10^2)$

occurs overall the detector, it is possible to confirm the uniformity of Gd concentration with muon-induced neutrons. Table 6.1 shows the features of the neutrons from the Am/Be source and cosmic-ray muon spallation.

6.2 Analysis Flow

After cosmic-ray muons enter the SK detector and produce neutrons via the spallation interaction, those neutrons are thermalized and captured on hydrogen or Gd. Among those, neutrons captured on Gd are selected in the analysis as written above. Neutrons are identified by detecting γ rays emitted immediately after the neutrons are captured on Gd. Figure 6.1 shows the schematic illustration of the muon-induced neutron observation in SK. The analysis flow is shown as follows.

1. A cosmic-ray muon enters the SK detector. The muon is selected by the signals in the outer detector and the total number of observed photons in the inner detector.

2. Neutrons are often produced by the muon or the secondary shower interacting with ^{16}O as explained in Section 1.6.2. Those neutrons are thermalized in water and then captured on hydrogen or Gd after $\sim 116\,\mu s$ on average in Gd-loaded water with 0.01% Gd mass concentration. Once a neutron is captured on Gd, several γ rays of $\sim 8\,MeV$ in total are emitted. Signals from neutron capture on Gd are searched in the time after the time of cosmic-ray muon arrival.

3. In order to distinguish the neutron capture signals from the background mainly due to radioactivity, the event selections are applied. Neutron capture candidates are selected using the event quality (based on the PMT hit pattern and hit timing), the total number of hit-PMTs, and the distance between the muon track and the vertex of neutron capture events.

4. Distributions of the time differences between the muon arrivals and neutron capture events are fitted by exponential functions to evaluate the neutron capture time constant for each region in the detector. The Gd concentration in water can be checked from the neutron capture time constant referring to their correlations.

6.3 Cosmic-Ray Muons

Figure 6.2 shows the event display when a cosmic-ray muon entered the SK detector from the top and passed through it while losing energy in the water. Signals of cosmic-ray muons are recorded in both inner detector (ID) and outer detector (OD) (Section 3.4.2 for trigger system). In this analysis, muon candidates are selected by requiring the total number of observed photons (equivalent to the number of observed photoelectrons) of the ID PMTs to be greater than 1,000 p.e., which corresponds to $\sim 140\,MeV$, and the tracks are reconstructed with the muon fitter.

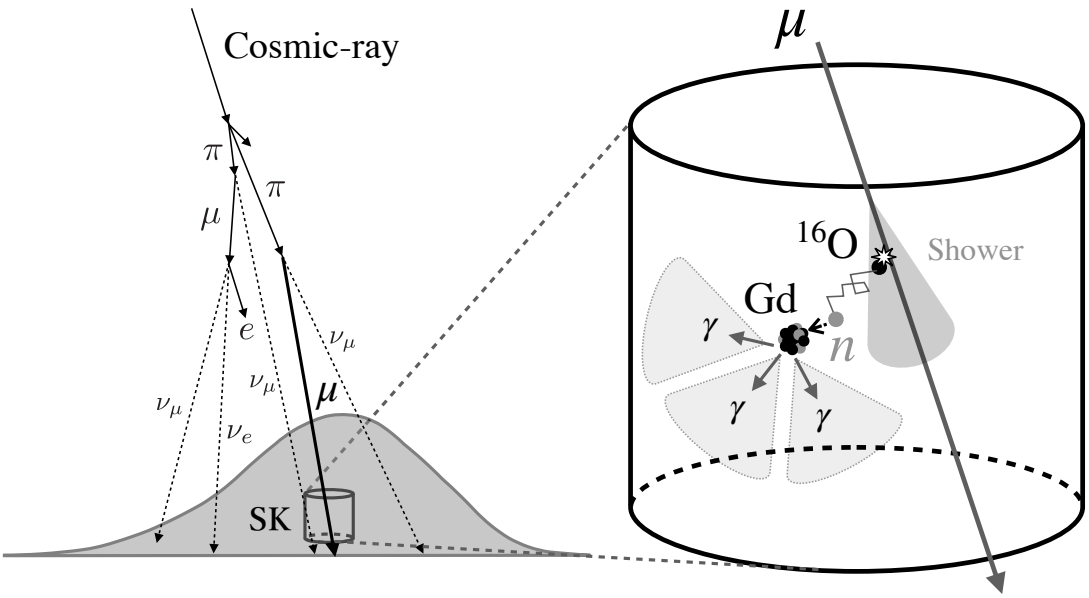

Figure 6.1: Overview of cosmogenic neutron obsevation in SK.

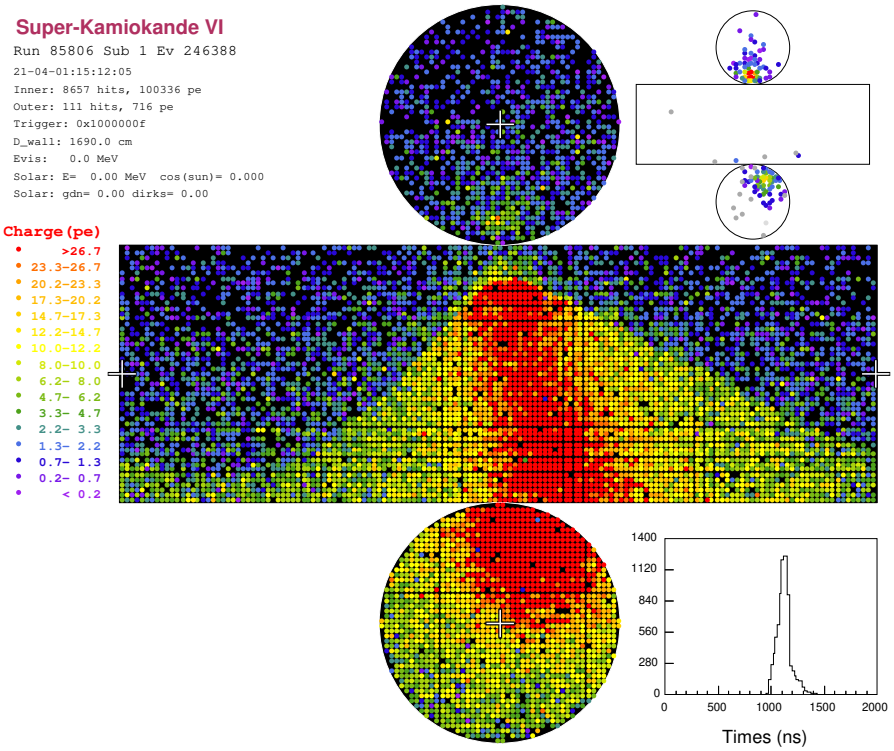

Figure 6.2: Distribution of PMTs that detected photons when a cosmic-ray muon penetrates the SK detector (event display). The center developed view shows the ID PMTs and the upper right shows the OD PMTs. The color of each point indicates the total charge of PMT signal which corresponds to the number of photons detected by the PMT.

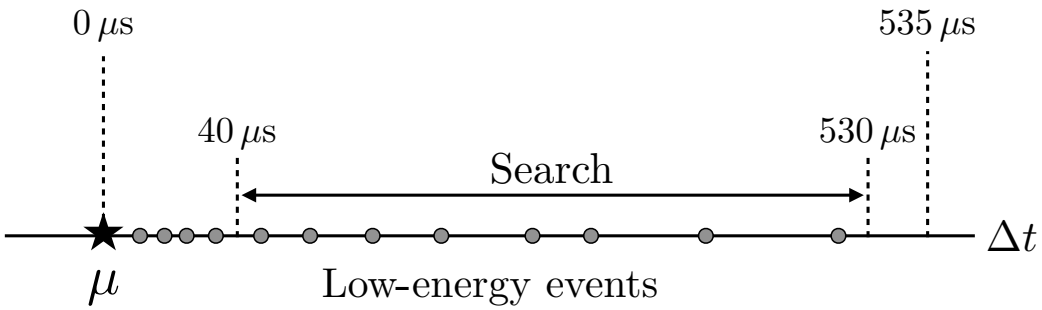

Figure 6.3: Schematic illustration of cosmogenic neutron searches.

6.4 Neutron Capture Event Selection

6.4.1 Overview of Neutron Search

As explained in Section 3.4.2, not all PMT hit information is stored due to the limitation of the data transfer and the storage size, while the hit information is stored for specific conditions with the triggers. Once the ID and OD triggers are issued due to cosmic-ray muon, all PMT hit information for up to 535 μs following the muon event is stored. Event candidates are searched for in the stored data, and event reconstruction (Section 5) is applied to the event candidates. These delayed events at the MeV scale following the muon are called "low-energy events" in this analysis. In order to select neutron captures on Gd against the background events, several cuts are applied to the low-energy events following the muon. In this section, the data acquired in the 24-hour of September 11–12, 2020, will be presented as an example. The rest of the data were available in the same way to check the stability of the neutron detection. The schematic illustration of cosmogenic neutron searches is shown in Figure 6.3.

6.4.2 Preselection

Neutron capture candidates are searched within the time window $40\,\mu\text{s} \leq \Delta t \leq 530\,\mu\text{s}$, where Δt represents the time interval from the muon arrival. The events with $\Delta t < 40\,\mu$s are not used to avoid the contamination of the electron from a muon decay and fake signals from PMT called after-pulses. After the large signals of PMTs by cosmic-ray muons, fake signals are often generated by the same PMTs. This is due to the ionization of the residual gas in the PMT by the photoelectrons. The ionized gas is led to the photocathode by the electric field and further photoelectrons are emitted when it hits the photocathode. It is known that PMTs installed in SK generate after-pulses approximately 10–20 μs after the first signal (main pulse).

In order to exclude the background due to radioactivity near the ID wall [59], a fiducial volume cut is applied based on the reconstructed vertex position. Typical SK analysis uses the data in the fiducial volume defined with the boundary 2 m away from the ID wall, corresponding to 22.5 kton (full volume of the ID is 32.5 kton). Therefore, in this study, the Gd concentration was evaluated in the fiducial volume.

6.4.3 Event Quality

Unlike signal events, which have a peaked timing distribution and a ring pattern, the time and location of hit-PMTs for the background due to PMT dark noise are randomly distributed. Such distributions are deviated from the expectation by the Cherenkov light emitted from a point-like source. These backgrounds can be reduced by evaluating the goodness of event reconstruction, which is described in Section 5.1. Figure 6.5 shows the distributions of g_{vtx} and g_{dir} of the data after all cuts except for the quality cut are applied. In this analysis, events with $g_{\text{vtx}} > 0.4$ and $g_{\text{dir}} < 0.4$ are retained as signal candidates.

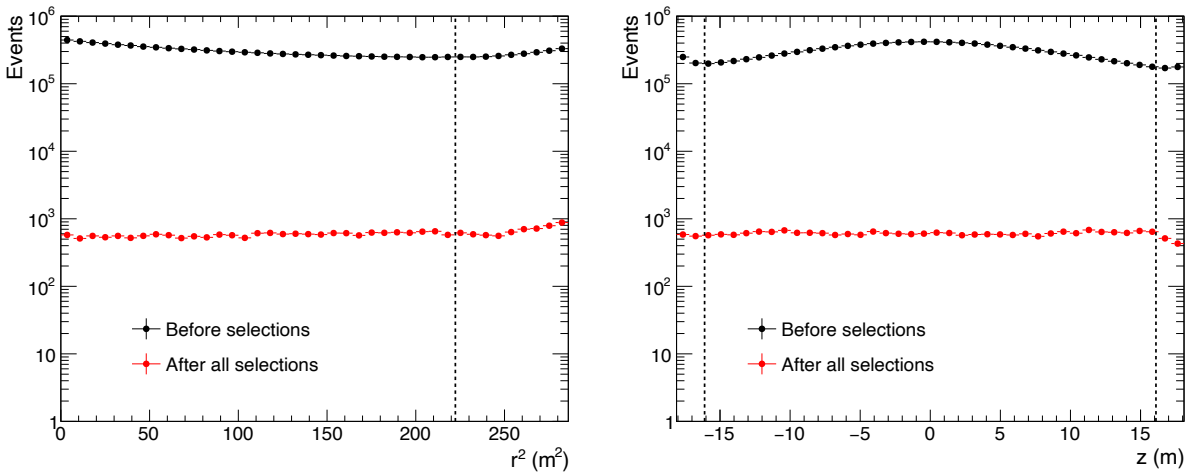

Figure 6.4: Distributions of the radial (left) and central axial (right) positions (r and z) for the data (September 11, 2020) before (black) and after (red) the event selections. Events are rejected if the distance from the ID wall is less than 2 m. The dashed lines correspond to the boundary of the fiducial volume. A large number of events are found around the center of the detector before the event selections, which are caused by the background events due to random coincidence of PMT dark hits.

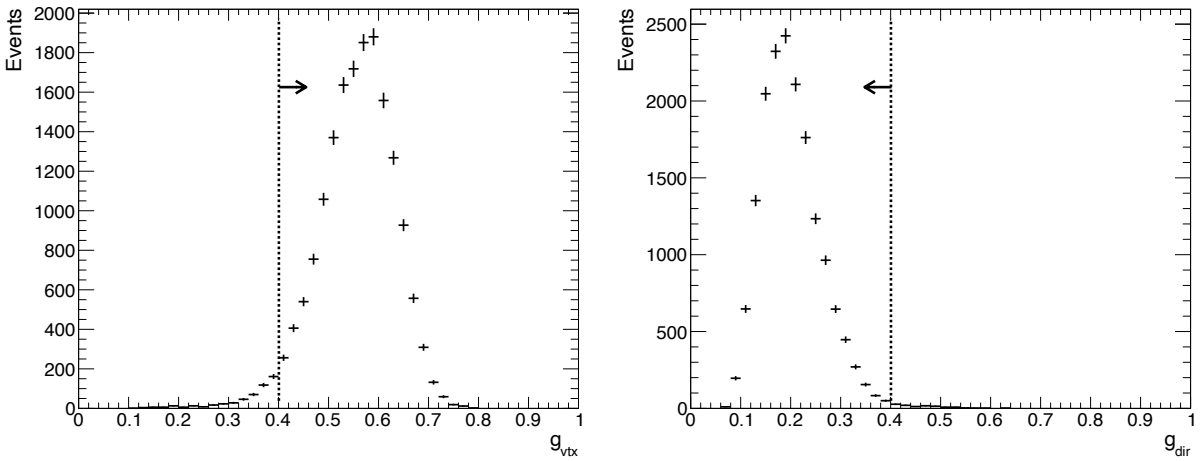

Figure 6.5: Distributions of g_{vtx} (left) and g_{dir} (right) for the data (September 11, 2020) after all cuts except for the quality cut are applied. The points show the data and the dotted lines show the cut conditions to select the signals from neutron captures on Gd.

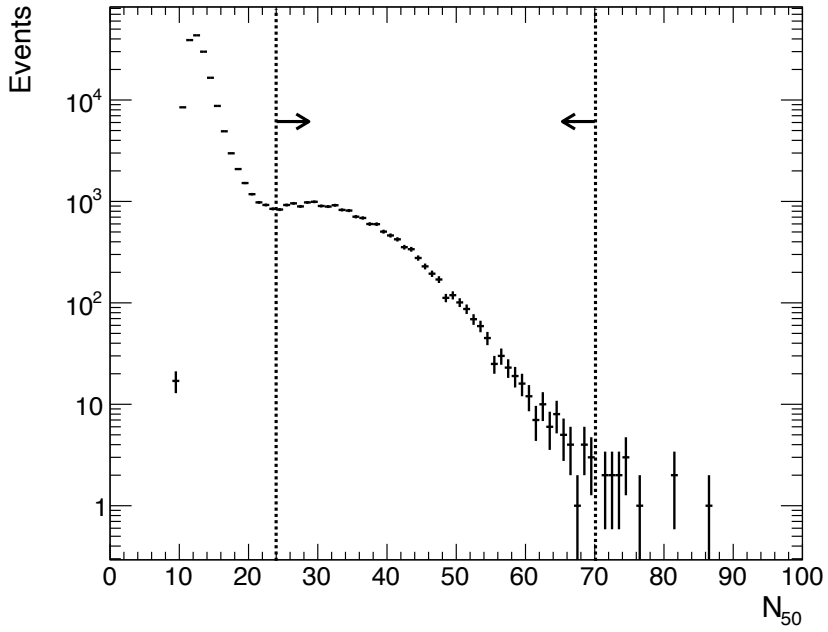

Figure 6.6: Distributions of N_{50} for the data (September 11, 2020) after all cuts except for the N_{50} cut are applied. The points show the data and the dotted lines show the range to select the signals from neutron captures on Gd.

6.4.4 Number of Hit-PMTs

The energy is determined from the number of hit-PMTs with some corrections as explained in Section 5.2, which is nearly equivalent to the number of observed photons as most of the hit-PMTs detect only one photon. Since radioactive isotopes are primarily present up to ∼4 MeV which is below the signal from neutron capture on Gd, event selection is applied by the number of hit-PMTs. In order to suppress the contamination of the background, the number of hit-PMTs within a 50-ns time window (N_{50}) is counted after the time of flight of photon from the reconstructed vertex to the hit-PMTs is subtracted from the PMT hit time. Figure 7.4 shows the distribution of N_{50} of the data after all cuts except for the N_{50} cut are applied. The selection criterion is set as $24 \leq N_{50} \leq 70$.

6.4.5 Transverse Distance from Muon Track

As the neutrons produced from muons are thermalized typically within a few meters and captured on Gd, it is effective to use the transverse distance between the muon track and the reconstructed vertex to identify muon-induced neutrons. The definition of the transverse distance L_t is outlined in Figure 6.7. L_t exhibits a correlation with the distance traversed by secondary particles produced within the muon-induced hadronic shower in water. In cases of multiple muons entering the detector at the same timing, L_t is defined as the distance from the reconstructed vertex to the nearest muon track. Figure 6.8 shows the distribution of L_t of the data after all cuts except for the L_t cut are applied. For this analysis, the selection criterion is set as $L_t < 500$ cm.

6.5 Measurement of Neutron Capture Time Constant

The time difference from the preceding muon, Δt, is calculated for every low-energy event. The reduction of low-energy events after each selection is shown in Figure 6.9 for the Δt distribution. The time constant for neutron capture on Gd is evaluated with the Δt distribution after the event selections (the red line in Figure 6.9). Since the time difference between neutron production and

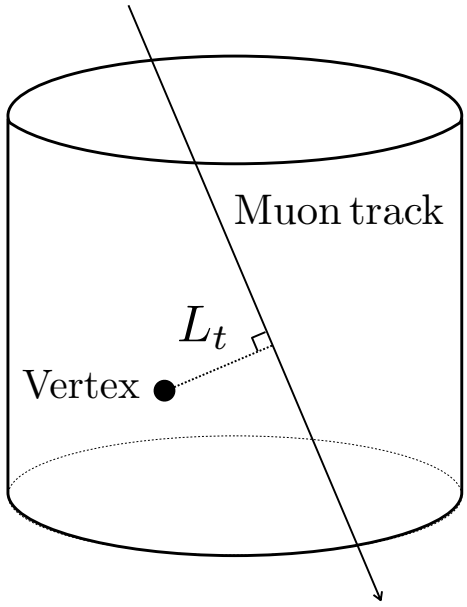

Figure 6.7: Definition of transverse distance (L_t) between the muon track and the reconstructed vertex.

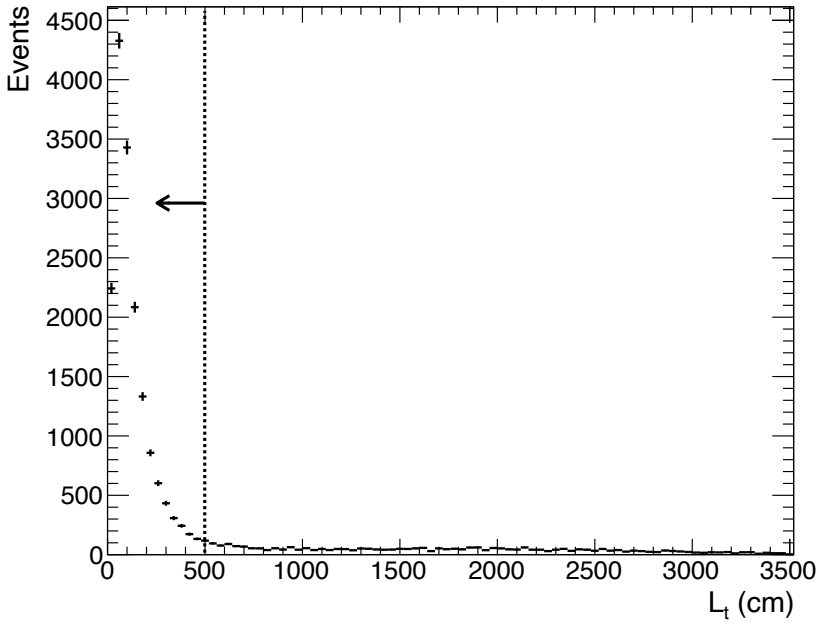

Figure 6.8: Distributions of L_t for the data (September 11, 2020) after all cuts except for the L_t cut are applied. The points show the data and the dotted lines show the criterion to select the signals from neutron captures on Gd.

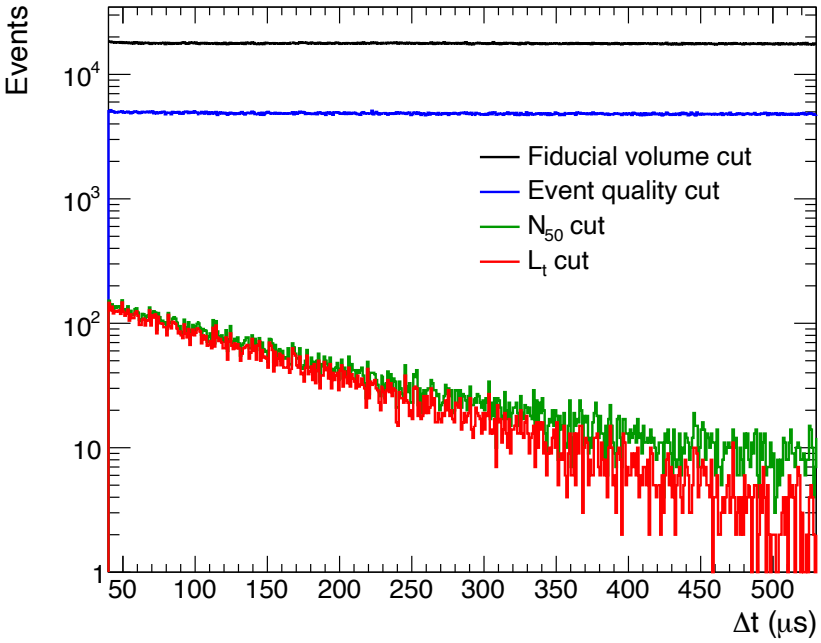

Figure 6.9: Distributions of Δt for the data (September 11, 2020) applied event reductions in sequence.

capture on Gd follows an exponential distribution, the Δt distribution is fitted by the following function:

$$f(\Delta t) = A \exp\left(-\frac{\Delta t}{\tau}\right) + B, \tag{6.1}$$

where A represents the normalization of neutron events and B represents background events. τ represents the time constant of the neutron capture. τ is correlated with the Gd concentration in the water, and the stability of τ corresponds to the stability of the Gd-loaded water and detector response. The average of τ measured with the Am/Be source (Section 4.4) is $116.5 \pm 0.2\,\mu$s during the entire observation period in SK with 0.01% Gd-loaded water (SK-VI phase). Figure 6.10 shows the fit result of the Δt distribution for the data after the event selections (corresponding to the red line in Figure 6.9). As a result of the fit, τ is evaluated to be $126.1 \pm 2.3\,\mu$s, which is significantly different from the result from Am/Be calibration.

One of the differences between the measurements with the Am/Be sources and cosmic-ray muons is the number of simultaneously produced neutrons (neutron multiplicity). In the measurements with Am/Be source, only one neutron is produced at a time. Therefore, at most one neutron capture event on Gd is detected following the prompt signal. While, in the measurements with cosmic-ray muon, multiple neutrons may be produced through the spallation interaction. In such cases, there may be multiple neutron capture events on Gd following a prompt signal due to a cosmic-ray muon. Figure 6.11 shows the number of neutron capture candidates following a muon after the event selections, M. The distribution expands to $M \sim 100$. The true neutron multiplicity is even larger because some of the neutrons, such as the neutrons captured on hydrogen, are missed due to the event selection. As the probability of neutron capture follows exponential function, neutron capture occurs more frequently in shorter time intervals in case multiple neutrons are produced by the muon spallation. Neutron capture candidates are searched with sliding time windows and the PMT hits within the $1.3\,\mu$s time window are collected as a single event. If there are multiple neutron captures within $1.3\,\mu$s, only one of them is selected as a signal candidate as illustrated in Figure 6.12 and the missing neutrons in the dead time cause inefficiency depending on the neutron multiplicity and Δt. Thus, a large neutron multiplicity makes the efficiency in the short Δt region

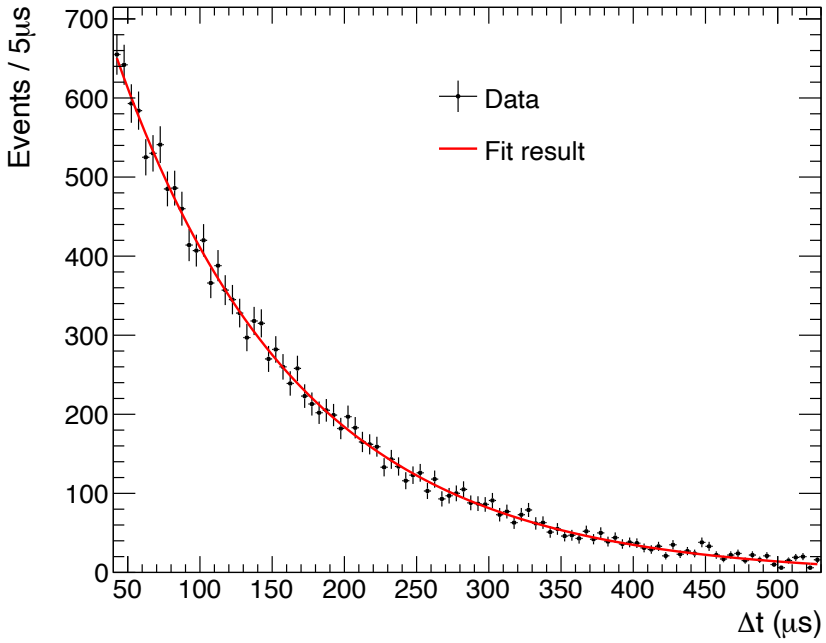

Figure 6.10: Distribution of the time difference between the muon and the followiing neutron capture candidates, Δt, for the data (September 11, 2020). The points are the data and the solid line is the fit result.

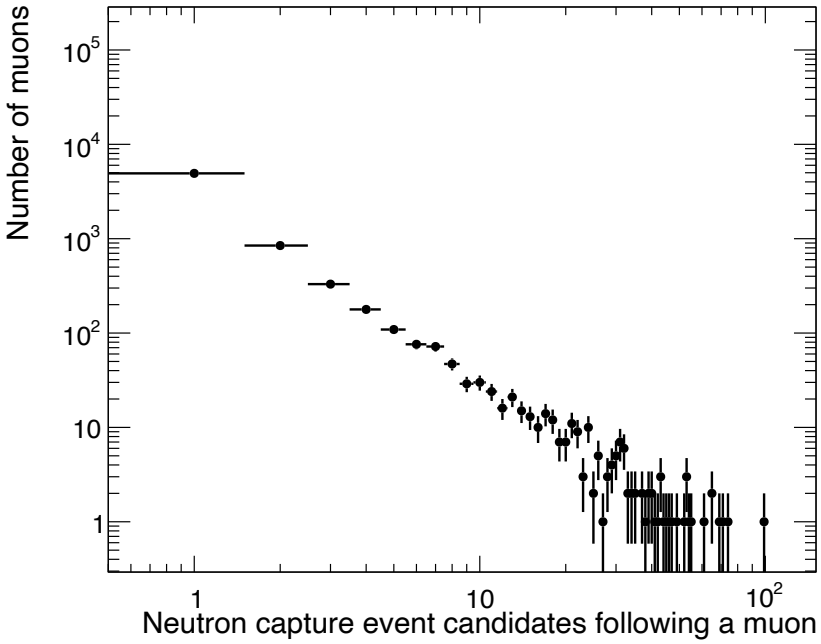

Figure 6.11: Distribution of the number of neutron candidates following a muon that remain after the event selections.

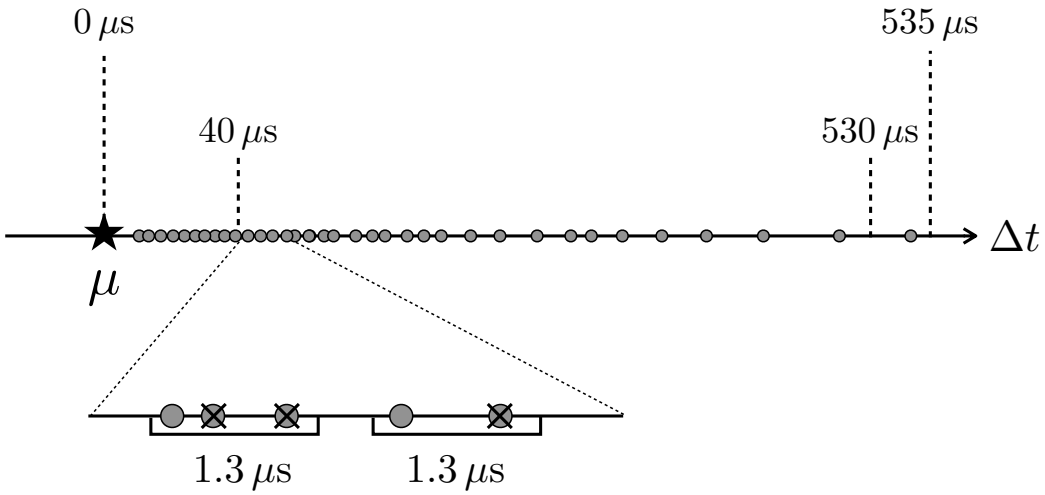

Figure 6.12: Schematic illustration of the dead time effect in the short Δt region. The gray circles represent neutron capture events.

lower. As a result, the capture time constant is biased to a larger value.

Based on the above considerations, only muons with $M = 1$ are selected, and the capture time constant τ is obtained from the Δt distribution. The Δt distribution and the fit result for the data are shown in Figure 6.13, where τ is fitted to be $116.1 \pm 3.6\,\mu$s. This value is consistent with the time constant $116.5 \pm 0.2\,\mu$s measured with the Am/Be source.

6.6 Evaluation of the Stability and Uniformity

This section describes the evaluation of the stability and uniformity of the neutron detection using neutrons induced by cosmic-ray muons. As the time constant for the neutron capture depends on the Gd concentration (shown in Figure 3.11 of Section 3.7), the stability and uniformity of Gd-loaded water can be checked by this measurement. Here, the stability and uniformity of the neutron capture time constant are evaluated during the observation period in SK with 0.01% Gd-loaded water. The period from September 10, 2020, to June 1, 2022, is divided into 42 periods with 15 days for each period, and the neutron capture time constant is evaluated for each period.

Figure 6.14 shows the time variation of the neutron capture time constant as a function of time. Neutron capture conditions ($M = 1$) in the entire fiducial volume were used for this plot. The variation of the time constant was obtained by fitting the values obtained at each time period with a Gaussian function as shown in Figure 6.15. The mean and standard deviation are found to be $116.3 \pm 0.2\,\mu$s and $1.1 \pm 0.1\,\mu$s, respectively. As a result, the neutron capture time is found to be stable within 0.9%. This corresponds to the stability of Gd concentration to be 2.3% and fraction of Gd capture to be 1.1% referring to Figure 3.11.

In addition, the fiducial volume is divided into nine regions to confirm the uniformity of Gd-loaded water in the fiducial volume and the stability. Figure 6.16 shows the vertex positions of neutron capture events for $M = 1$ on the period 0 (shown in Figure 6.14). Dashed lines in the plot show the boundary of nine regions. The position dependence of the time constant for the neutron capture on Gd is confirmed from the Δt distributions for events in each region. As an example, Figure 6.17 shows the Δt distributions in each region at the period 0 and the values of the time constants obtained by fitting the distributions. This analysis is performed for the entire period, and Figure 6.18 shows the stability of the capture time constant in each region. The variation of the time constant for each period and each region is obtained by Gaussian fit as shown in Figure 6.19. The mean and standard deviation are found to be $116.4 \pm 0.2\,\mu$s and $3.0 \pm 0.1\,\mu$s, respectively. As

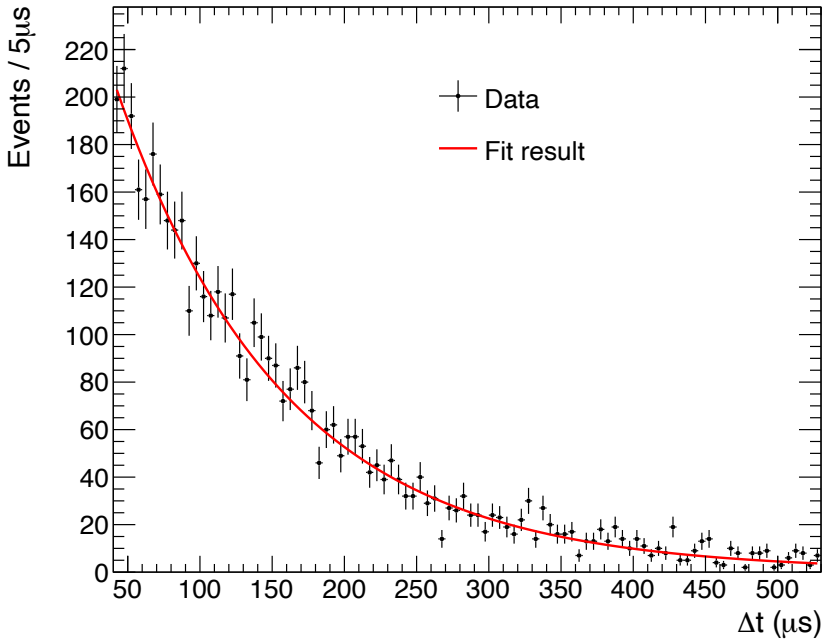

Figure 6.13: Distribution of the time difference between the muon and the followiing neutron capture candidates, Δt, for the data (September 11, 2020). Only the events with one neutron ($M = 1$) are plotted. The points are the data and the solid line is the fit result.

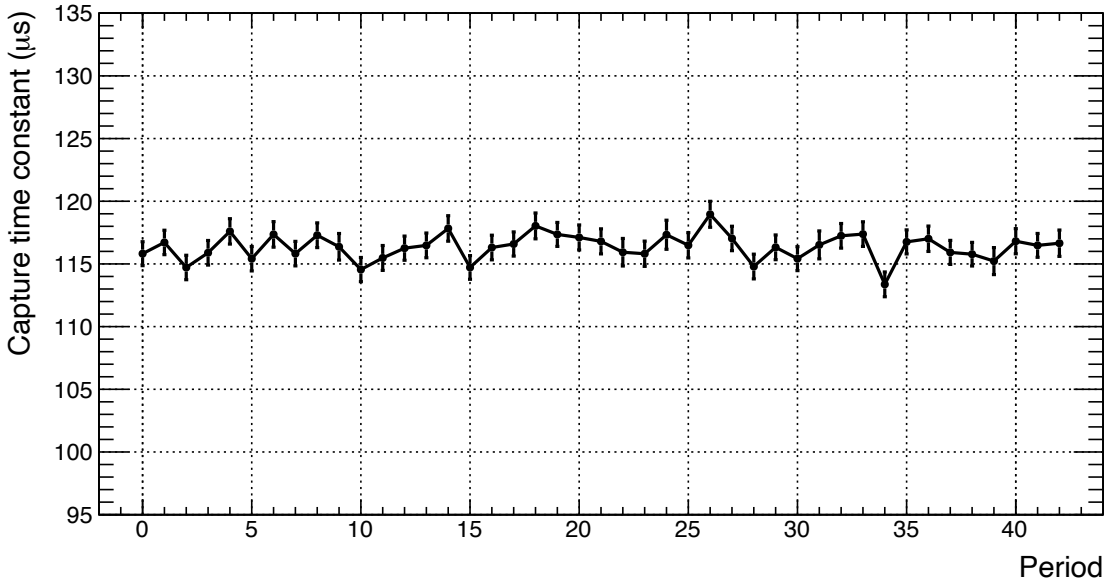

Figure 6.14: Stability of the neutron capture time constant for events in the fiducial volume of the detector. The period from September 10, 2020 to June 1, 2022 is divided into 42 periods each with 15 days.

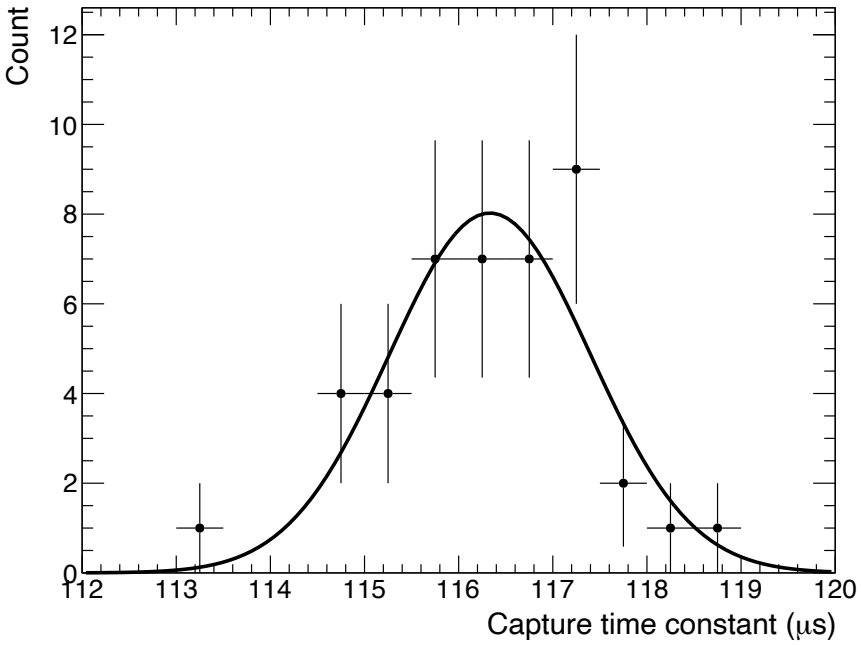

Figure 6.15: Distribution of capture time constant in each 15 days period. Solid line shows the Gaussian fit with mean value of $116.3 \pm 0.2\,\mu$s and sigma of $1.1 \pm 0.1\,\mu$s.

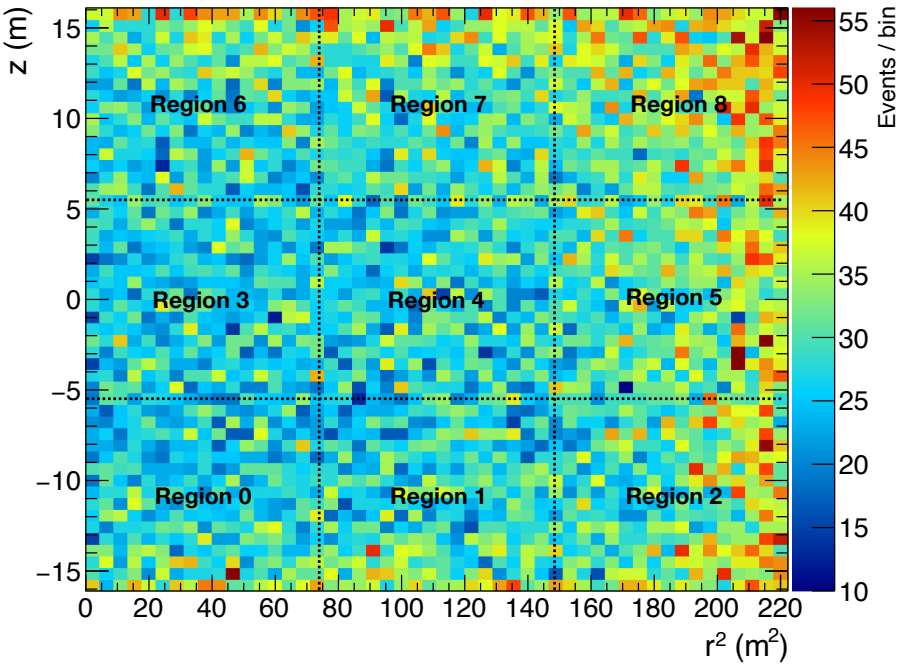

Figure 6.16: The vertex positions of neutron capture events for $M = 1$ on the period 0. The horizontal axis represents the square of the detector radius, the vertical axis represents the height, and the color scale shows the number of events per bin. Dashed lines show the boundaries of nine regions.

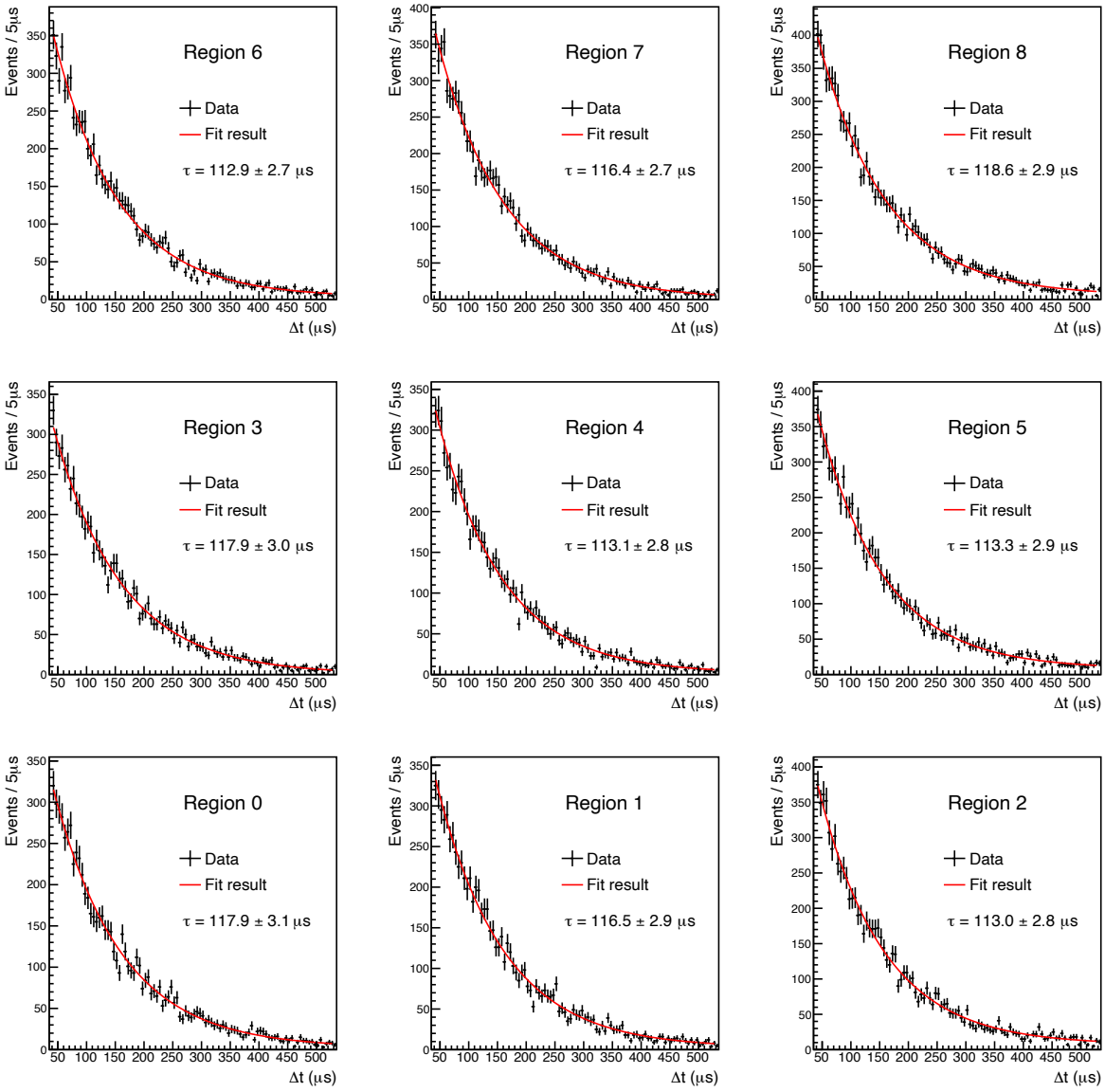

Figure 6.17: The Δt distributions in each region at the period 0. The points are the data and the solid lines are fit results. Time constants obtained by the fits are also shown in each plot.

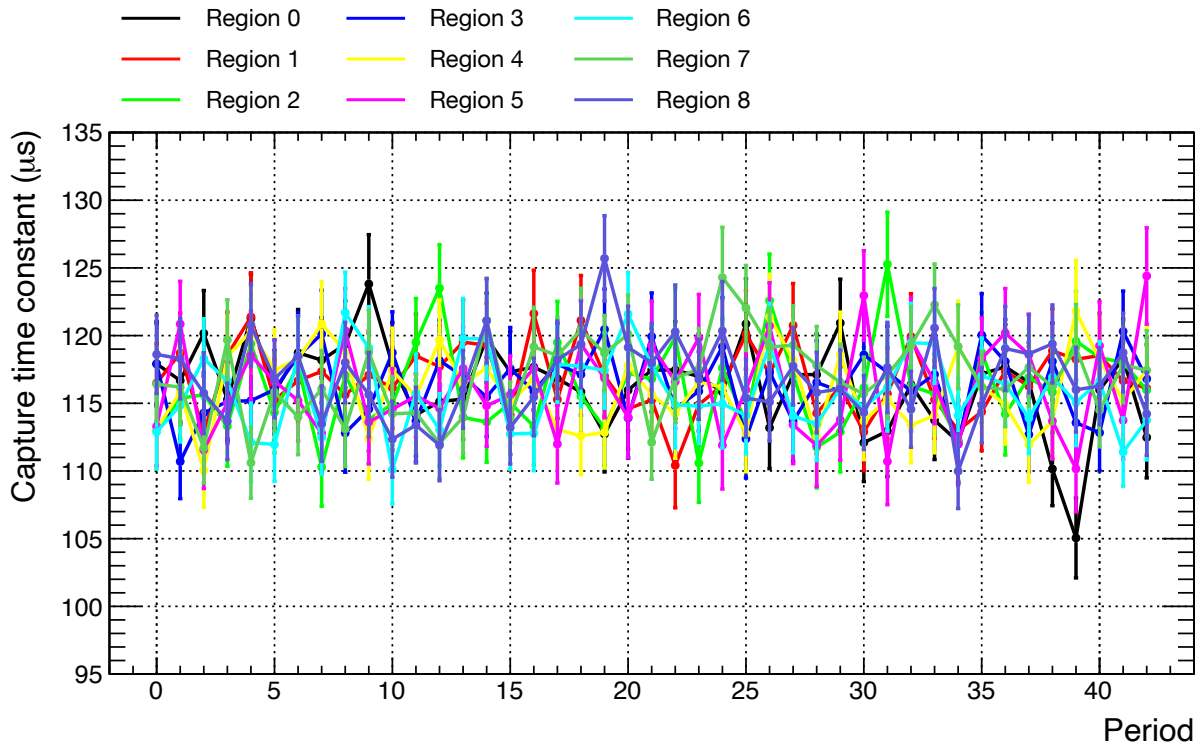

Figure 6.18: Stability of the neutron capture time constant in each region. The period from September 10, 2020 to June 1, 2022 is divided into 15 days. The color of each point represents the region in the detector defined in Figure 6.16.

a result, stability and uniformity of the neutron time constant were confirmed within 2.6%. This corresponds to the stability and uniformity of Gd concentration to be 6.3% and the fraction of Gd capture to be 3.1% referring to Figure 3.11.

SRN search is performed by the comparison of the reconstructed energy spectra for the observed data and the expected background as shown in Figure 1.24. Therefore, in order to conclude the existence of the SRN signals from the data, it is important to estimate the expected background and suppress the uncertainties. As the major background events, atmospheric neutrinos, ^{9}Li, and reactor neutrinos consist of the prompt signal and the neutron capture events, any systematic biases in the neutron detection efficiency, such as due to time variation or position dependence of Gd capture fraction, result in the underestimation or overestimation of the background rate. According to the study described in this thesis, the stability and uniformity of the Gd capture fraction were confirmed within $\pm$3.1% for the data taken from September 2020 to June 2022 (SK-IV period). This value is negligible compared to the current estimation of the systematic uncertainties from the other sources ($\sim$30%). This method using the neutrons induced by comic-ray muons can be also applied to the observed data in the future to monitor the stability and uniformity of Gd concentration or detect the unexpected problems in the water quality at the early stage, which are essential to collect reliable data for long time period realize the first observation of SRN signal.

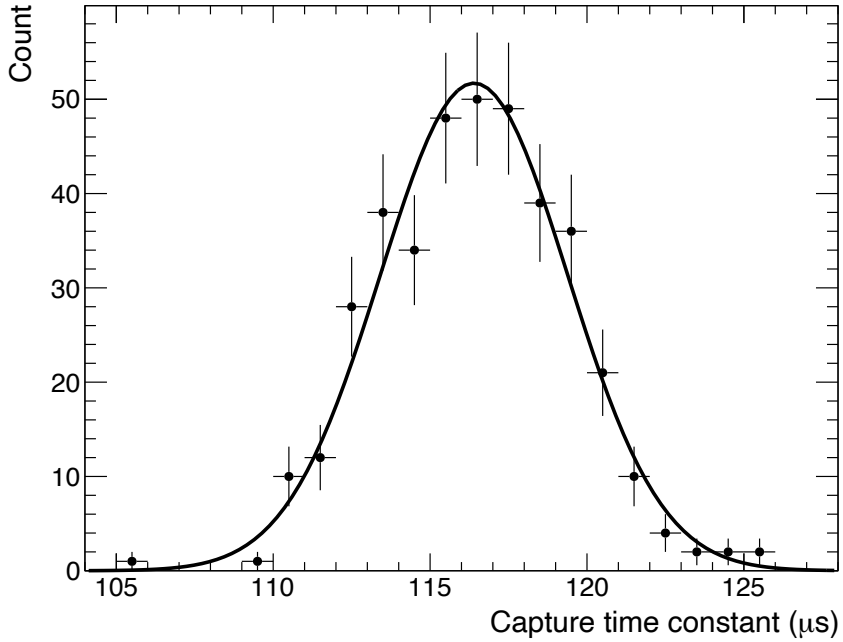

Figure 6.19: Distribution of capture time constant in each 15 days period and each region. Solid line shows the Gaussian fit with mean value of $116.4 \pm 0.2\,\mu$s and sigma of $3.0 \pm 0.1\,\mu$s.

Chapter 7

Measurement of Cosmogenic Neutron Production

Neutrons produced by the cosmic-ray muon spallation are a major background source for underground neutrino experiments. Cosmogenic neutron production yields have already been measured in underground neutrino experiments using liquid scintillators, such as KamLAND [43] and Daya Bay [42], while neutron production yield in the water Cherenkov detector has so far been measured only by SNO [46] with D_2O. Since the accuracy of theoretical prediction to cosmogenic neutron production is limited due to the complicated process in the nucleus and secondary hadron scattering, estimation of the neutron yield heavily relies on the experimental data. Therefore, it is important to accumulate the measurements at differential depths (corresponding to different muon energy) and detector medium. As explained in Section 3.7, gadolinium (Gd) was introduced to the Super-Kamiokande detector in 2020 to improve the detection efficiency of neutrons and started the operation of SK-Gd. This enabled us to measure the cosmogenic neutron production in water with high precision. In this study, the neutron production yield was measured using 283.2 days of data taken by the Super-Kamiokande detector with Gd-loaded water from September 2020 to September 2021 (called SK-VI data-taking period to distinguish from the other configurations). This study is the first physics measurement by the Super-Kamiokande detector with Gd-loaded water and therefore it is important as a confirmation of the detector performance in detecting neutrons. The results of this study are reported in Ref. [55].

7.1 Overview of the Analysis

In this study, the amount of neutrons produced by cosmic-ray muons was measured. The search method for neutron capture events on Gd is almost the same as that described in the previous chapter.

1. The method of the neutron capture event selection following the cosmic-ray muon is the same as described in Section 6.2. In addition, this chapter will discuss selection efficiencies because it is necessary to correct the number of neutron capture events missed due to event selections (Section 7.4).

2. The number of neutron capture events is estimated from the distribution of the time difference between the cosmic-ray muon and the remaining neutron candidates after the selections are applied (Section 7.5).

3. The neutron yield is obtained from the sum of muon track lengths and the number of neutron capture events with the corrections for the selection efficiencies. Systematic uncertainties on the measurements are estimated for each source of the uncertainty (Section 7.6). Finally, the results are presented in Section 7.7.

Table 7.1: Detector configurations and the number of events during the analysis period.

Detector	Phase	SK-VI
	Gd concentration	0.01%
Period	Start date	Sep. 10, 2020
	End date	Sep. 26, 2021
	Livetime	283.2 days
Triggers	ID (SHE)	60 PMTs/200 ns
	OD	22 PMTs/200 ns
	AFT sub	20 PMTs/200 ns
Muons	Events	49,495,584 (174,773 /day)
	Events (corrected)	47,677,780 (168,354 /day)
Low-energy events	Events	1,825,281,155 (6,445,202 /day)

7.2 Detector Configuration and Data Set

Table 7.1 summarizes the detector configurations during the period. This analysis used 283.2 days of data taken in the SK detector with Gd-loaded water from September 10th, 2020 to September 26th, 2021. As described in Section 7.1, a muon is first observed, and then neutron capture events are searched for in the time window following the muon. Since Cherenkov light is detected in the inner detector (ID) and outer detector (OD) for muons entering the SK detector. Events taken with both ID (SHE trigger, Section 3.4.2) and OD triggers are stored as cosmic-ray muon events. Once a SHE trigger is issued, all PMT hits for 500 μs following the SHE-triggered event are stored (AFT trigger, Section 3.4.2). Low-energy events are searched from the PMT hits recorded by the AFT trigger in the analysis as the candidates for neutron capture events (AFT sub-trigger search).

The following description is about the trigger problem found in the data set and its correction. It was found that the AFT trigger rate was limited to once every 21 ms during the data acquisition period of this analysis, and therefore the AFT trigger was not always issued following the SHE trigger. This causes an underestimation of the number of muon-induced neutrons after muons due to missing low-energy events. The discrepancy between SHE and AFT trigger rate was evaluated to be 3.7% and the number of muons was scaled by 0.963 ($= 1 - 0.037$) to correct for this.

7.3 Cosmic-Ray Muons

As explained in the previous chapter, cosmic-ray muons are recorded by both the ID and OD triggers. Muon candidates are selected by requiring the total number of observed photons of the ID PMTs to be greater than 1,000, which corresponds to ~140 MeV, and the tracks are reconstructed with the muon fitter. The cosmic-ray muons are classified into following four types:

- Single through-going muon: A single muon penetrates the ID.
- Stopping muon: A single muon loses energy and stops inside the ID.
- Multiple muons: Multiple muons (muon bundles) pass through the ID. These muons are produced by the same cosmic-ray within the atmosphere. Therefore, the directions of all muons are assumed to be the same (muon tracks are in parallel) in the track reconstruction algorithm.
- Corner-clipping muon: A single muon gazes the edge of the ID.

The total number of muons used in this analysis, N_μ, is counted as $N_\mu = 47{,}677{,}780 \simeq 4.77 \times 10^7$ for 283.2 days of exposure.

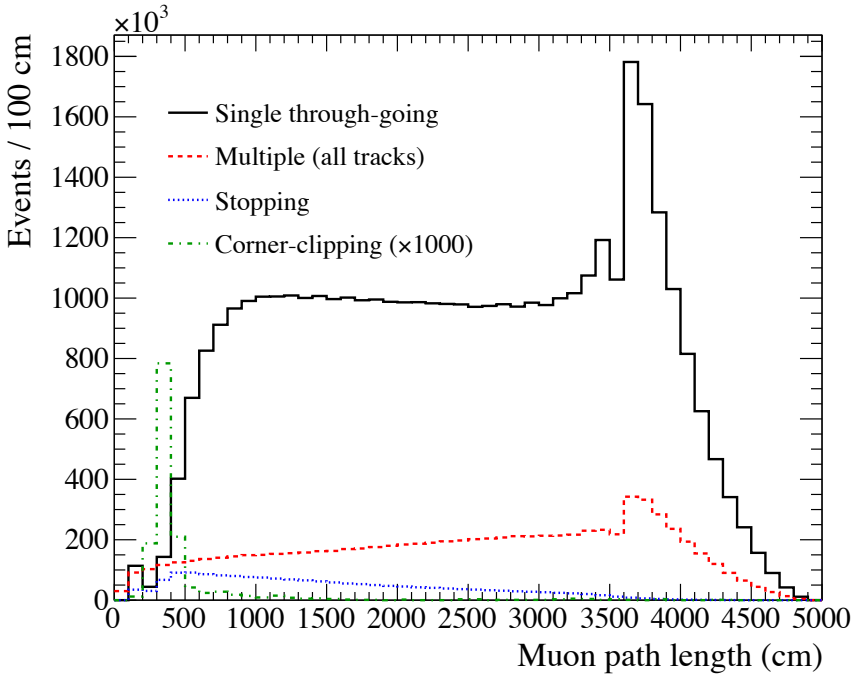

Figure 7.1: Distributions of path length L_μ for single through-going (solid), multiple (dashed), stopping (dotted), and corner-clipping (dot-dashed) muons. The distribution of corner-clipping muons is scaled by a factor of 1,000.

Figure 7.1 shows the distributions of the measured track lengths of muons in the detector. The peak of the track length distribution at around 3,700 cm corresponds to muons that penetrate the detector from the top to the bottom. The average path length L_μ was obtained to be $L_\mu = 2{,}427$ cm.

The average number of neutrons produced in muon spallation depends on the energy of the muon. The energy of cosmic-ray muons at the SK site is estimated using the simulation. The muon flux at sea level is modeled by modifying Gaisser's parametrization [30] according to Ref. [31]. The MUSIC code [67] is used to simulate muon propagation in the rock. The simulations account for the topography of Mount Ikenoyama surrounding the SK area [43, 68] and the rock models of standard [33, 69] and Ikenoyama [31]. The density of the rock is assumed to be in the range of 2.65–2.75 g/cm^3. The average muon energy incident on the SK detector $\overline{E}_\mu$ is estimated to be $\overline{E}_\mu = 259 \pm 9$ GeV with the calculation method from Ref. [43], where the uncertainty was estimated by varying the rock model and density. Figure 7.2 shows the cosine of the zenith angle and azimuthal angle of muons at the SK site. The muon flux from the MUSIC code is overlaid with the reconstructed directions of the data. The MUSIC simulation reproduces the ϕ dependence of the muon flux as the topography of Mount Ikenoyama is implemented in the simulation. Muon flux is higher for $\phi \sim 170°$ and $\phi \sim 280°$ where the overburden of the rock is thinner than the other directions. Small discrepancy tells the mismodeling of the topography due to the limitation of the modeling for the detailed structure of the topography and rock density. The discrepancy of the $\cos\theta$ distribution around $\cos\theta \sim 1$, which corresponds to vertically entering muons, is not yet understood. Possible causes are the mismodeling of the primary cosmic-ray flux, atmosphere, and geomagnetic field around the experimental site. The cut off energy of primary cosmic-ray and the trajectory of muons depend on the magnetic field. In order to evaluate the impact of the discrepancy in $\cos\theta$ distribution, the averaged energy of muons entering the detector was calculated with the weight as a function of $\cos\theta$ to reproduce the data. The variation of the averaged energy was found to be ± 0.17 GeV which is negligible compared to the other uncertainties.

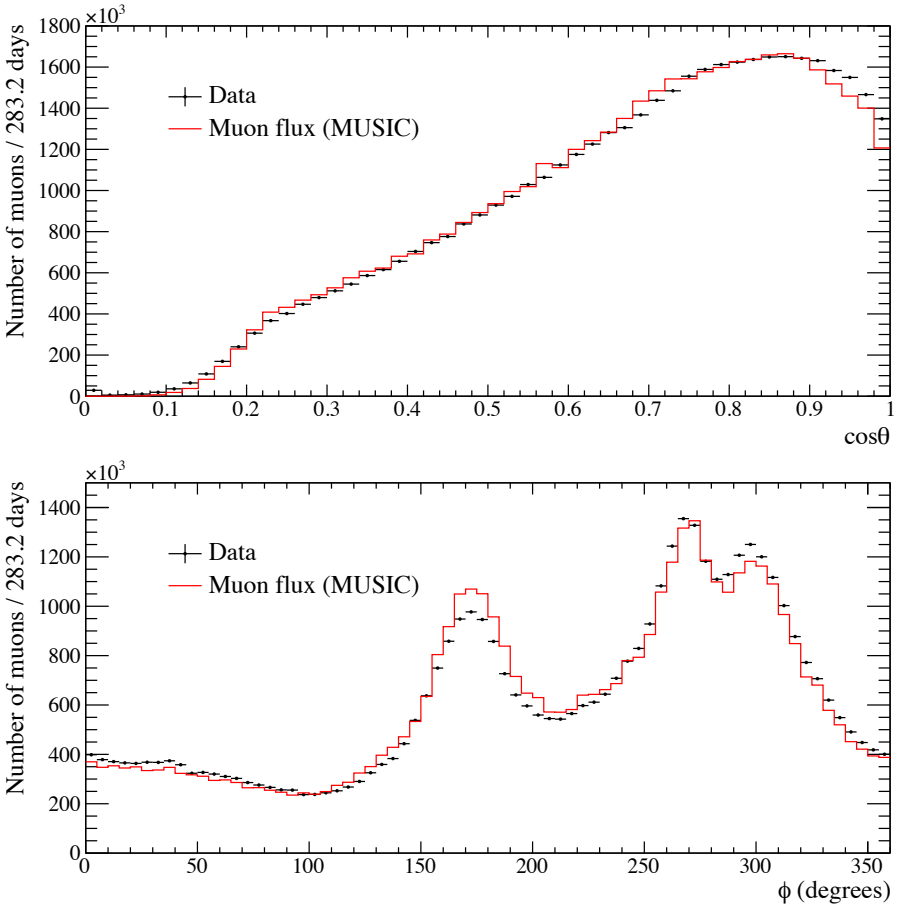

Figure 7.2: Zenith (θ) and azimuthal (ϕ) dependence of the muon rate at the SK site. Reconstructed directions of the muons from the data (black points) are overlaid with the muon flux at the SK site calculated by the MUSIC code (red lines). Muon flux distributions are normalized to the data. $\phi = 0$ corresponds to the direction from east to west.

7.4 Neutron Capture Event Selection

The method of the neutron capture event selection is almost the same as the method described in the previous chapter. Once the ID and OD triggers are issued due to a muon arrival, the data for the 535 μs following the muon event are also stored. Event candidates of neutron capture on Gd are searched for in that time window. The objective here, however, is to count the number of neutrons produced by cosmic-ray muons. Therefore, a more detailed analysis is also performed to estimate the selection efficiency for the events of neutron capture on Gd and systematic uncertainties.

7.4.1 Preselection

The time difference between the muon and the following low-energy events is defined as Δt. Neutron capture candidates are searched within the time window $40 \leq \Delta t \leq 530\,\mu$s. The events with $\Delta t < 40\,\mu$s are not used to avoid the contamination of the electron from a muon decay and fake signals from PMT after-pulses (Section 6.4.2).

In order to exclude the background due to radioactivity near the ID wall [59] and neutrons entering from the surrounding rock, a fiducial volume cut is applied based on the reconstructed vertex position. The fiducial volume of this analysis is defined with the boundary 4 m away from the ID wall corresponding to 14.7 kton. As shown in the latter section, neutron yield is measured for the total volume of the inner detector with the correction for the signal efficiency of the volume cut given by the ratio of the fiducial volume to the total volume of the ID. In order to accurately calculate the number of neutrons produced in the fiducial volume (neutron yield), the propagation of neutrons, i.e. number of neutrons entering the fiducial volume and those exiting the fiducial volume, should be taken into account. If neutrons produced by muons in the fiducial volume leak out of the fiducial volume, the number of neutrons is underestimated. On the other hand, if neutrons produced in the bedrock surrounding the detector or outside the fiducial volume leak in the fiducial volume, the number of neutrons is overestimated. They are not perfectly cancelled each other due to entering neutrons generated by the muons outside of the detector. The fiducial volume is smaller than the other analysis in SK [24] in order to suppress the systematic uncertainty associated with the leak-in/-out of neutrons as shown in Section 7.6.5, while the statistical uncertainty is still smaller than the systematic uncertainty[1].

7.4.2 Event Quality

In order to reduce the background due to PMT dark noise, the goodness of event reconstruction is evaluated as described in Section 5.1. The distribution of $g_{\rm vtx}$ and $g_{\rm dir}$ for neutron capture on Gd in the Monte Carlo simulation (MC) is shown in Figure 7.3. In this analysis, events with $g_{\rm vtx} > 0.4$ and $g_{\rm dir} < 0.4$ are retained as signal candidates. The signal efficiency for the event quality cut is evaluated with the MC as $(92.62 \pm 0.29)\%$ with the MC statistical uncertainty.

7.4.3 Number of Hit-PMTs

In order to reject the background due to the radioactivity, the event selection is applied by setting a criterion for the number of hit-PMTs in a 50-ns time window, N_{50}. The distributions of N_{50} for the data are shown in Figure 7.4, where the data is divided into the sample of $40\,\mu$s $\leq \Delta t \leq 240\,\mu$s (on-time) and the sample of $430\,\mu$s $\leq \Delta t \leq 530\,\mu$s (off-time). Since neutrons of $\sim$98% are captured within 430 μs, the background component is dominant in the off-time window. The schematic illustration of Δt distribution and on-/off-time is shown in Figure 7.5. Background events from accidental coincidences are assessed using the off-time sample and subsequently subtracted from the on-time sample. The resulting distributions of N_{50} for the data are compared with the MC as shown in Figure 7.6, in which the discrepancy between the data and MC is due to the overlap

[1] The standard fiducial volume is defined with boundary 2 m away from the ID wall, corresponding to 22.5 kton.

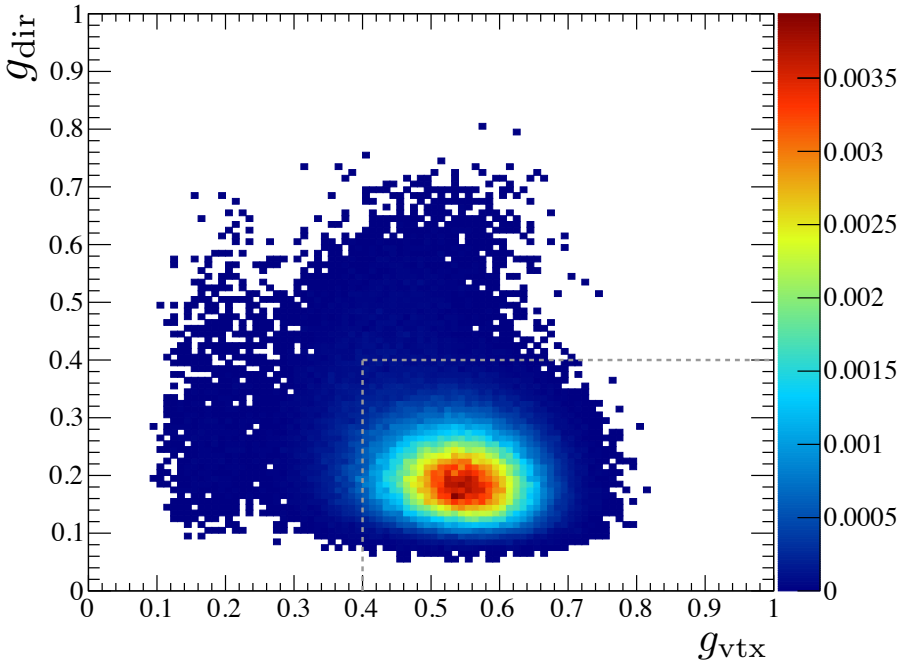

Figure 7.3: Distribution of g_{vtx} and g_{dir} for neutron capture on Gd in the MC. The color scale is the number of events normalized by area. The gray dashed lines are the cut thresholds.

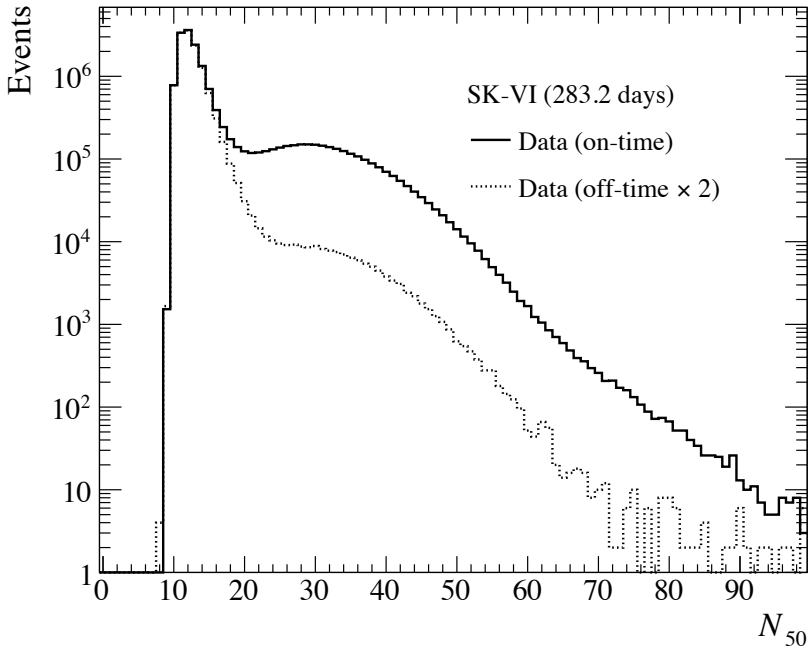

Figure 7.4: Distributions of N_{50} for the data in on-time ($40\,\mu\mathrm{s} \leq \Delta t \leq 240\,\mu\mathrm{s}$) window (solid line) and off-time ($430\,\mu\mathrm{s} \leq \Delta t \leq 530\,\mu\mathrm{s}$) window (dotted line).

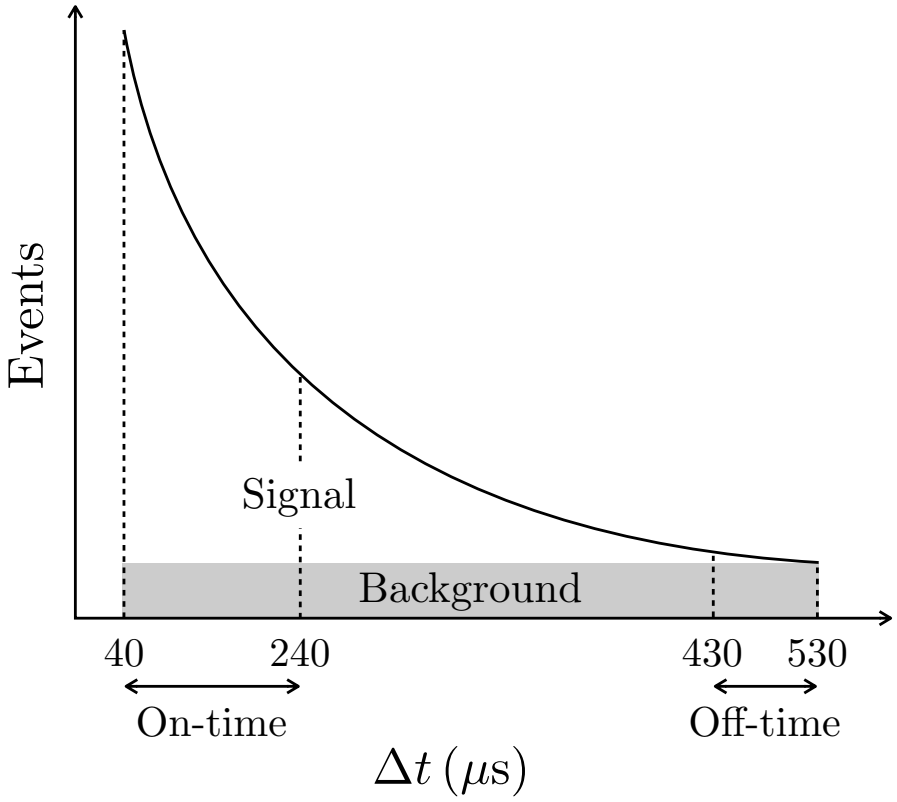

Figure 7.5: Schematic illustration of Δt distribution and on-/off-time windows.

of multiple neutrons as explained in Section 7.6. To suppress the contamination of the events of a single γ ray with 2.2 MeV from neutron capture on hydrogen, the threshold criterion is set as $24 \leq N_{50} \leq 70$. The signal efficiency resulting from the N_{50} cut is estimated as $(80.22 \pm 0.27)\%$, utilizing the distribution of neutron captures in the MC. The uncertainty is attributed to MC statistics. Details of systematic uncertainties are explained in Section 7.6.4.

7.4.4 Transverse Distance from Muon Track

In order to select events that are correlated with muons, it is effective to use the transverse distance between the muon track and the reconstructed vertex. The definition of the transverse distance L_t is shown in Figure 6.7 in Section 6.4.5. Figure 7.7 shows the distribution of L_t of the data after all cuts except for the L_t cut are applied. For this analysis, the selection criterion is set as $L_t < 500$ cm. The signal efficiency is calculated as $(97.25 \pm 0.10)\%$ from the data after background subtraction.

7.5 Number of Neutrons

Number of events after each selection criterion is summarized in Table 7.2. Because the background events remain after all event selections, the number of signals for neutron capture on Gd is estimated from the distribution of the time difference between the muon and the following neutron candidates, Δt. Figure 7.8 shows Δt for the data after all selection criteria are applied. The Δt distribution follows an exponential function with a small flat component due to the background events. The total number of neutron capture signals is extracted by a fit to the Δt distribution. The capture time of neutrons in SK is measured using the Am/Be source as $116.4 \pm 0.3\,\mu$s for a single neutron emitted from the Am/Be source. While, the multiple neutron production by the cosmic-ray muons causes the missing of neutrons due to the data acquisition described in Section 6.5. Therefore,

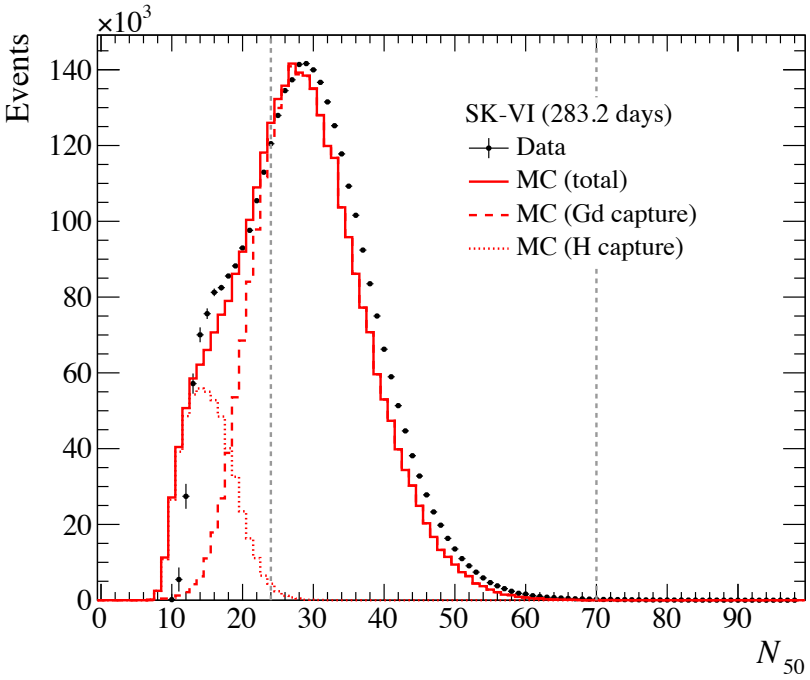

Figure 7.6: Distribution of N_{50} for data (black points, background subtracted) and MC (red lines). Contributions of the Gd capture (dashed line) and hydrogen capture (dotted line) are also plotted. All cuts except for the N_{50} cut are applied for the data and the remaining background is evaluated from off-time ($430\,\mu\text{s} \leq \Delta t \leq 530\,\mu\text{s}$) and subtracted from on-time ($40\,\mu\text{s} \leq \Delta t \leq 240\,\mu\text{s}$). Only the event quality cut is applied for MC and the entries of the total MC distribution are normalized to the data by the height of the peak. The gray dashed lines are N_{50} cut thresholds.

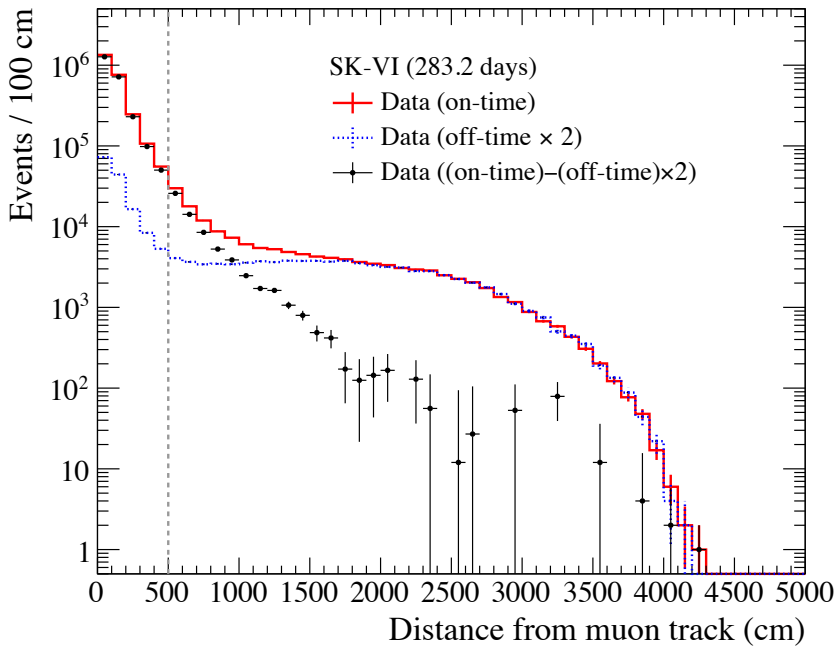

Figure 7.7: Distribution of transverse distance (L_t) between the muon track and the reconstructed vertex for data (black points). The background is evaluated from off-time ($430\,\mu\text{s} \leq \Delta t \leq 530\,\mu\text{s}$, dotted line) and subtracted from on-time ($40\,\mu\text{s} \leq \Delta t \leq 240\,\mu\text{s}$, solid line). Since neutrons are captured on Gd after $\sim$100 μs on average, events also occur in the off-time range and a peak is seen within 500 cm. The dashed line is the L_t cut threshold.

Table 7.2: Number of observed events after each selection

Event selection	Number of events
Analysis volume	1,825,281,155
Event quality	478,986,895
Number of hit-PMTs N_{50}	3,363,430
Transverse distance L_t	3,084,524

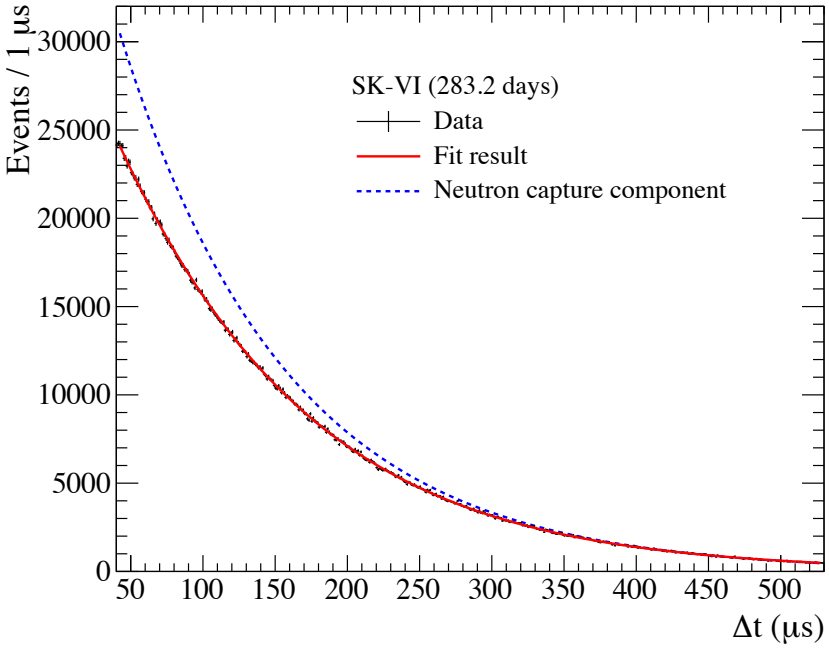

Figure 7.8: Distribution of the time difference between the muon and the following neutron capture candidates. The data are shown by filled circles. The solid red line is the fit result with Eq. (7.1). The dashed blue line is the neutron capture component. The reduced χ^2 is found to be $\chi^2/\text{d.o.f.} = 500.6/487$ as the fitting result, corresponding to a p-value of 32.5%.

variation of the effective capture time should be taken into account for several neutrons emitted from muon spallation. Since the Δt dependence of the inefficiency follows an exponential function, the Δt distribution is fitted with the function:

$$f(\Delta t) = \left(A \exp\left(-\frac{\Delta t}{\tau_n} \right) + B \right) \left(1 - C \exp\left(-\frac{\Delta t}{\tau_\mathrm{d}} \right) \right), \tag{7.1}$$

in which A, C, and τ_d are parameters determined by a fit. The first part of Eq. (7.1) corresponds to the neutron capture components and the second part represents the inefficiency due to the dead time effect. τ_n is the neutron capture time constant obtained from measurements of Am/Be calibration as $\tau_n = 116.4 \pm 0.3\,\mu$s and A represents the normalization of neutron events. B represents the background rate which was estimated to be 27.80 ± 1.57 using the data obtained with random triggers. B is fixed in the fit at the central value and the uncertainty on the background estimation is accounted as the systematic uncertainty. The second term absorbs the effect of dead time with the time constant τ_d and the normalization parameter C. The dead time effect is more significant at small Δt where the neutron captures are more frequent and it is gradually moderated with Δt. The best-fit parameters are $A = (4.39 \pm 0.02) \times 10^4$, $C = 0.256 \pm 0.003$, and $\tau_\mathrm{d} = 216.6 \pm 10.0\,\mu$s. It is confirmed with a toy MC for different neutron multiplicities that the time dependence and magnitude of the dead time effect are reasonable. The total number of detected neutron capture

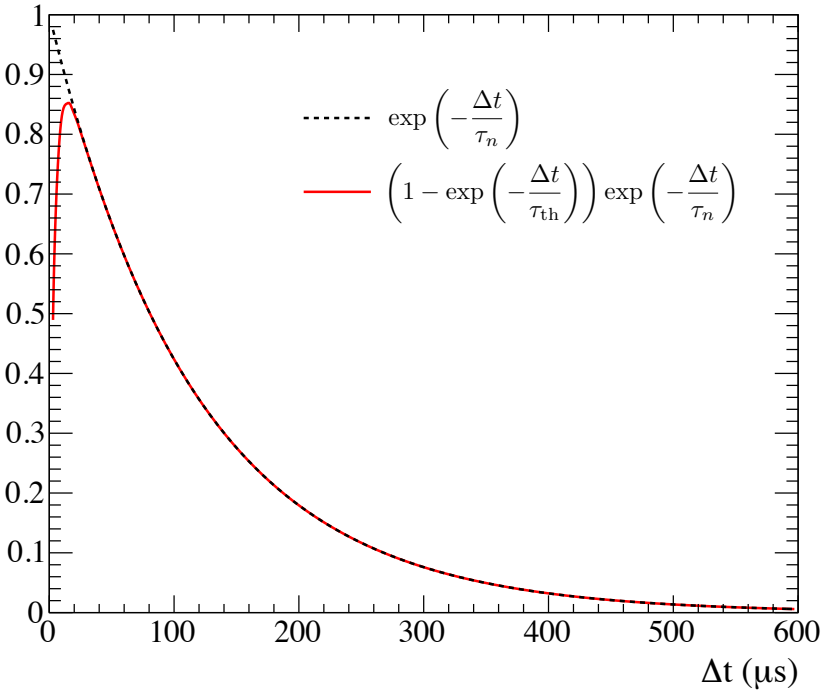

Figure 7.9: Shapes of the normal exponential function and the exponential function considered neutron thermalization. τ_n and $\tau_{\rm th}$ represent the time constants for neutron capture on Gd and thermalization of neutron in water, $\tau_n = 116.4\,\mu$s and $\tau_{\rm th} = 4.3\,\mu$s, respectively.

signals, S_n is obtained as $S_n = (3.57 \pm 0.02) \times 10^6$ using the integral:

$$S_n = \int_{40\,\mu\rm s}^{530\,\mu\rm s} A \exp\left(-\frac{\Delta t}{\tau_n}\right) d(\Delta t). \tag{7.2}$$

The signal efficiency for the time window ϵ_t is obtained by dividing S_n by the integral from zero to infinity for the function $f(\Delta t)$. Here, it should be taken into account that neutrons are thermalized before being absorbed by Gd and that thermalization takes several μs. Therefore, in the short Δt region, the functional form deviates from the exponential function. The time for the neutrons to thermalize in water is taken into account in the following function:

$$f_{\rm th}(\Delta t) = A\left(1 - \exp\left(-\frac{\Delta t}{\tau_{\rm th}}\right)\right)\exp\left(-\frac{\Delta t}{\tau_n}\right), \tag{7.3}$$

where $\tau_{\rm th}$ is the time constant for thermalization of neutrons in water, $\tau_{\rm th} = 4.3\,\mu$s [60]. The shape of the function is shown in Figure 7.9. ϵ_t is evaluated from the ratio of integrals from 40 to 530 μs to integrals from zero to infinity for the function $f_{\rm th}(\Delta t)$ as follows:

$$\epsilon_t = \frac{S_n}{\displaystyle\int_0^\infty f_{\rm th}(\Delta t)\; d(\Delta t)} \tag{7.4}$$

As the result, the signal efficiency for the time window ϵ_t is evaluated to be $(72.45 \pm 0.39)\%$.

The total number of neutrons produced by the muons can be obtained by correcting S_n for the signal efficiency:

$$N_n = \frac{S_n}{\epsilon}, \tag{7.5}$$

where N_n is the total number of neutrons and ϵ is the signal efficiency given by a product of the efficiencies for each event selection summarized in Table 7.3. The neutron capture fraction on Gd

Table 7.3: Summary of the signal efficiencies for each event selection. The efficiency for the volume cut is calculated by the ratio of the analysis volume to the full volume. The Gd capture fraction and the uncertainty are estimated from the neutron capture time constant by the Am/Be calibration (Section 4.4) based on the correlation given by the GEANT4-based simulation. The other uncertainties are statistical.

Event selection	Efficiency (%)
Analysis volume	45.39
Gd capture fraction	47 ± 1
Event quality	92.62 ± 0.29
Number of hits N_{50}	80.22 ± 0.27
Transverse distance L_t	97.25 ± 0.10
Time window	72.45 ± 0.39
Total	11.17 ± 0.08

Table 7.4: Summary of the systematic uncertainties on the measurement of neutron yield.

Source	Uncertainty (%)
Number of muons	2.0
Muon path length	1.3
Gd capture fraction	2.2
Gd capture time	1.2
Neutron thermalization	2.2
Signal efficiency for L_t cut	0.6
Signal efficiency for N_{50} cut	4.7
Contamination of hydrogen capture	0.4
Leak-in/-out of neutrons	2.2
Background estimation	0.3
Total	6.7

depends on the Gd concentration in water and the neutron capture time constant. The Gd capture fraction is estimated to be 47% from the correlation with the neutron capture time constant given by the GEANT4-based simulation with the uncertainty estimated to be 1%, which corresponds to a systematic uncertainty of 2.2% for N_n. Total signal efficiency was obtained as (11.17 ± 0.08)%.

7.6 Systematic Uncertainties

The systematic uncertainties on the measurement of neutron yield are described in this section. The systematic uncertainties are summarized in Table 7.4. The total systematic uncertainty is estimated to be 6.7% by adding all in quadrature.

7.6.1 Muon Tracks

The uncertainties associated with the count of muons and the path length originate from the performance of the muon fitter. In the case of multiple muons, simultaneously incident muons are counted up to ten muons, and the reconstruction assumes their parallel traversal through the detector. To validate the accuracy of the counting by the muon fitter, the number of muon tracks is counted by eyes from the event display by identifying the entry and exit points of muons. The examples of event displays for well-/mis-reconstructed events are shown in Figure 7.10. A discrepancy of 2.0% is found in the comparison of the results for 2,000 events by eye-scan and the

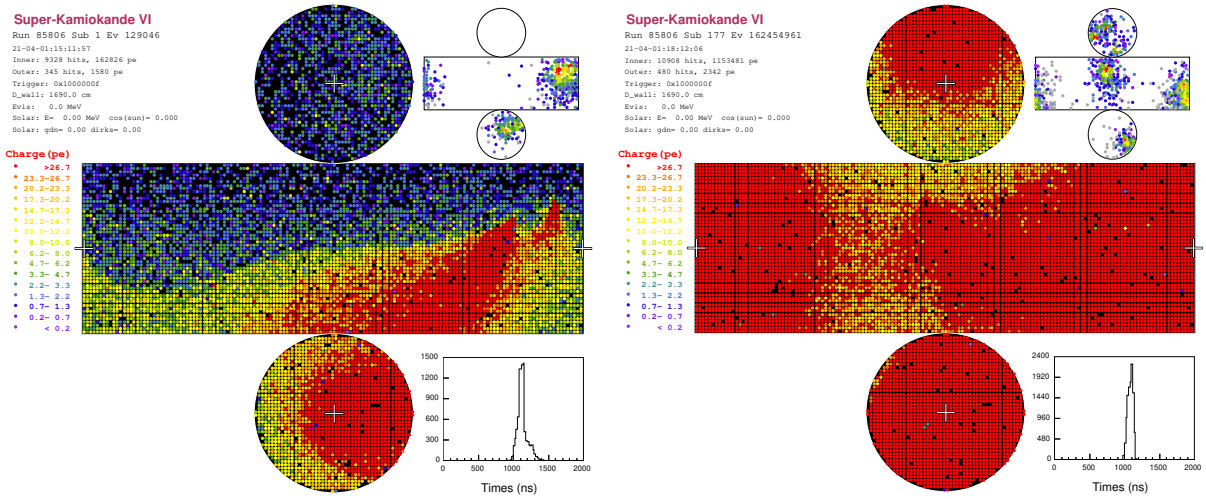

Figure 7.10: The example of event displays for a well-reconstructed event (left) and a mis-reconstructed event (right) for multiple muons. For the well-reconstructed event, two tracks are recognized by both the eye-scann and reconstruction by muon fitter. For the mis-reconstructed event, four tracks are recognized by the eye-scan from the entering and exit points while the reconstructed number of tracks is six.

muon fitter. This value is factored in as the systematic uncertainty associated with N_μ, stemming from the accuracy of the muon fitter.

The accuracy of the path length reconstruction has been estimated to be 30 cm for each track. This is caused by the granularity of the PMTs on the wall which are arranged with ∼50 cm intervals. The systematic uncertainty on the neutron yield due to the measurement of L_μ is estimated to be 1.3%.

7.6.2 Neutron Capture

The systematic uncertainty associated with the Gd capture time is assessed at 1.2%, taking into account the uncertainty on τ_n. Although the cut on N_{50}, $24 \leq N_{50} \leq 70$, is designed to select neutron captures on Gd, a small fraction of neutron captures on hydrogen is contaminated in the final neutron capture candidates (as shown in Figure 7.6). According to the MC, the proportion of neutron capture on hydrogen nuclei is 0.4%. This value is accounted for as the systematic uncertainty.

Uncertainty on the Gd capture fraction is mainly due to the modeling of the neutron thermalization process. As the ratio of neutron capture cross sections for hydrogen to Gd is higher at higher energy, a fraction of Gd capture becomes smaller for a slower thermalization process. A Geant3-based [70] detector simulation is used in Super-Kamiokande (SKDetSim) including this study. However, a high precision transport model for neutrons is not implemented in Geant3. Since the physics processes of neutrons become more important in SK-Gd, Geant4-based [71] detector simulation (SKG4) is being developed. SKG4 can describe the physics process of neutrons more accurately. In order to estimate the uncertainty on the neutron thermalization, Gd capture fractions are compared with SKDetSim and SKG4 while changing the neutron kinetic energy from 1 MeV to 100 MeV. The maximum deviation between SKDetSim and SKG4 is found to be 1%. The systematic uncertainty on the neutron yield measurement stemming from the 1% uncertainty on the Gd capture fraction from the neutron thermalization model is estimated to be 2.2% from the difference.

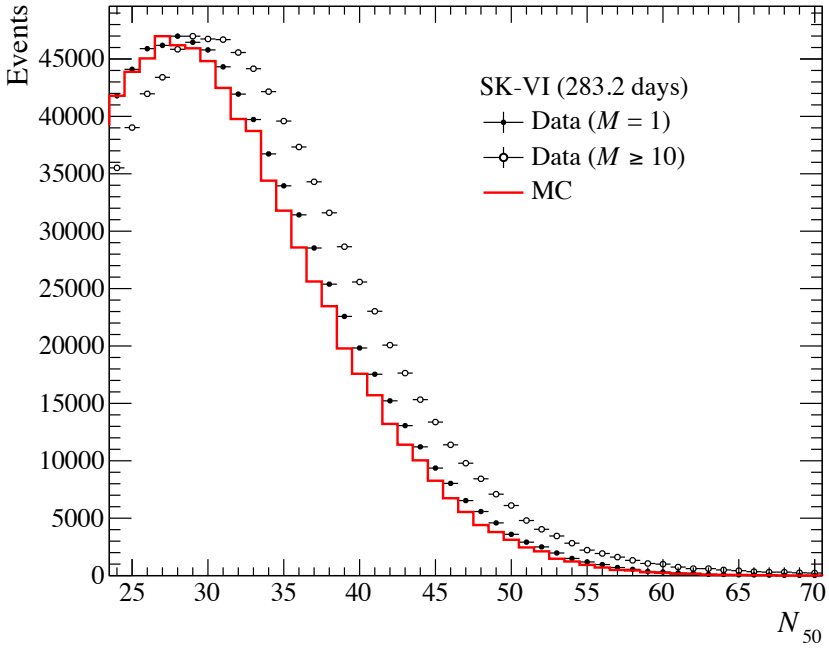

Figure 7.11: Comparison of N_{50} distributions for MC (solid red line) with data for $M = 1$ (filled circles) and $M \geq 10$ (open circles), where M is the number of neutron capture candidates following a muon that remain after the event selections.

7.6.3 Transverse Distance

The systematic uncertainty of the L_t cut is evaluated by applying different L_t cuts with thresholds ranging from 400 to 600 cm. The resolution on the muon entrance position is ∼50 cm. The vertex resolution for neutron capture on Gd was measured by the calibration with AmBe source to be ∼100 cm. Therefore, the threshold 500 cm for L_t cut is sufficiently larger than the resolutions of event reconstructions. The variation of neutron yield was checked by changing the cut threshold by ±100 cm, which is a comparable size to the resolutions of event reconstructions. The relative variation is below 0.6%, which is assigned as the systematic uncertainty.

7.6.4 Number of Hit-PMTs

The primary source of systematic uncertainty lies in the signal efficiency related to the N_{50} cut. As explained in Section 7.5, N_{50} represents the number of hit-PMTs within a 50 ns time window, which is strongly correlated with the total energy of γ rays generated in the detector. In the N_{50} distribution shown in Figure 7.6, a 4.1% disparity in the N_{50} scale is observed between the data and the MC. This value is estimated by scaling the MC distribution to fit the data in the range $24 \leq N_{50} \leq 70$. While neutrons are generated uniformly in the ID one at a time in the MC, several neutrons are produced at once from muon spallation and multiple neutron captures can occur simultaneously within the same time window. Inefficiency is caused by this feature as explained in Section 7.5, and in addition, N_{50} from the data tends to be larger due to overlaps of hit-PMTs in the same time window. The correlation between the number of neutron capture events following a muon and the N_{50} distributions is shown in Figure 7.11 in which MC is generated with single neutrons. For candidates with single neutron capture, the discrepancy is 1.6%, while it is 7.9% for events with greater than or equal to ten neutron captures. As the number of neutron candidates increases, the discrepancy increases due to the pile-up effect. This pile-up effect is also confirmed in the MC with multiple neutrons generated simultaneously as shown in Figure 7.11. As there is no reliable model to predict the number of neutrons produced by the cosmic-ray muon spallation

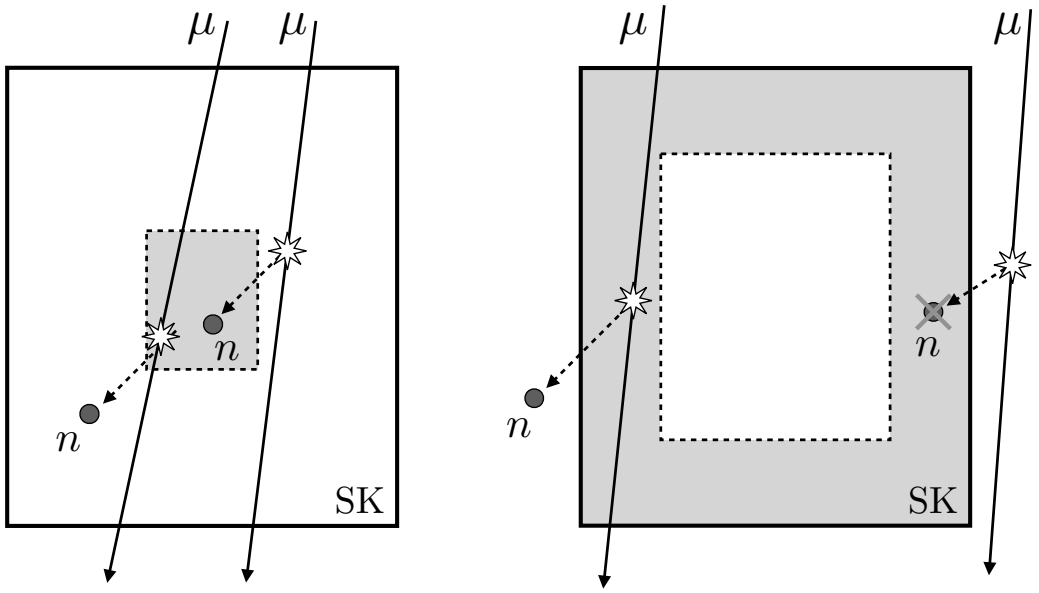

Figure 7.12: Schematic illustrations of leak-in/-out of neutrons around the detector center (left) and near the detector wall (right). As shown in the left hand figure, the event rate around the center of the neutron capture is expected to be uniform as the numbers of neutrons that leak-in and leak-out are likely balanced. While, in the right hand figure, the event rate near the wall is expected to be lower than that around the center because the muon correlation is not taken.

at the underground detector, the systematic uncertainty of 4.7% is assigned to account for the variation in the N_{50} scale. The uncertainty on the signal efficiency for the N_{50} cut is estimated to be 4.7% from the variation when the N_{50} distribution is scaled by 4.1%.

7.6.5 Leak-In and Leak-Out of Neutrons

Leak-in/-out of neutrons is one of the main sources of systematic uncertainty in other experiments, such as KamLAND [43] and Daya Bay [42]. The fraction of leak-in and leak-out neutrons to the total neutron captures depends on the ratio of surface area to volume of the detector ($\sim 1/r$). Since SK has a larger volume than the other detectors listed above, a fraction of leak-in/-out neutrons should be smaller. The event rate of neutron capture around the center of the ID is expected to be uniform as the numbers of neutrons that leak in and out are likely balanced. On the other hand, the event rate near the ID wall is expected to be lower than that around the center. This is because when muons penetrate the surrounding rock or the OD, neutrons from their spallation are not counted even if they are reconstructed in the ID because the parent muons are not tagged in this analysis. The schematic illustrations described in the above are shown in Figure 7.12. A systematic uncertainty of 2.2% is assigned to account for the leak-in/-out by changing the boundary of the fiducial volume from 5 to 7 m from the ID wall.

7.6.6 Background Estimation

The uncertainty on the background estimation was evaluated to be 5.7% from the statistical uncertainty of the random trigger sample. Systematic uncertainty on the neutron yield measurement is evaluated from this value to be 0.3% by fitting the Δt distribution shown in Figure 7.8 varying the parameter B in Eq. (7.1).

Table 7.5: Average muon energy and neutron yield for each azimuthal angle of incident muons. The units of the neutron yield are $10^{-4}\,\mu^{-1}\mathrm{g}^{-1}\mathrm{cm}^2$. The error is statistical only.

Azimuthal angle	Fraction (%)	$\overline{E}_\mu$ (GeV)	Y_n
315°–45°	19.4	265	2.81 ± 0.05
45°–135°	11.5	272	2.88 ± 0.06
135°–225°	27.1	257	2.77 ± 0.04
225°–315°	42.0	253	2.67 ± 0.03

7.7 Results

The neutron yield Y_n is defined as the neutron production rate per unit muon track length and per unit density, which can be calculated as

$$Y_n = \frac{N_n}{N_\mu L_\mu \rho} = \frac{S_n}{\epsilon N_\mu L_\mu \rho}, \tag{7.6}$$

where ρ is the density of the Gd-loaded water, $\rho = 1.000\,\mathrm{g/cm}^3$ with 0.026% concentration of $Gd_2(SO_4)_3 \cdot 8H_2O$. The uncertainty of the density is less than 0.1% and negligible compared to be other uncertainties. The other parameters are as previously described: $S_n = (3.57 \pm 0.02) \times 10^6$, $\epsilon = 11.17 \pm 0.08\%$, $N_\mu = 4.77 \times 10^7$, and $L_\mu = 2{,}427\,\mathrm{cm}$. Definitions of these parameters are explained in the previous sections. It should be noted that the neutron yield includes both primary neutrons from muon spallation and secondary neutrons from hadronic interactions. The neutron yield is measured to be $(2.76 \pm 0.02\,(\mathrm{stat.}) \pm 0.19\,(\mathrm{syst.})) \times 10^{-4}\,\mu^{-1}\mathrm{g}^{-1}\mathrm{cm}^2$.

Figure 7.13 shows the comparisons with other experiments. Most of those yields were measured using liquid scintillators except for the SNO experiment which measured the yield in heavy water. Super-Kamiokande is the first experiment to measure the yield in light water. The KamLAND detector is located in the same mountain as the SK detector at almost the same depth. Although the target material in the SK detector is water and different from the KamLAND detector, the measured neutron yields are consistent within the uncertainties.

In addition, neutron yields are calculated for each muon direction. Due to the shape of the mountains surrounding SK, the flux and average energy of muons from each azimuthal angle at the detector site are different. The azimuthal dependence of the muon flux is shown in Figure 7.2. The azimuthal distribution is divided into four parts of 90° each, and the muon energy and neutron yield are estimated for each region. The results shown in Table 7.5 show that the higher the muon energy, the greater the neutron yield, as expected.

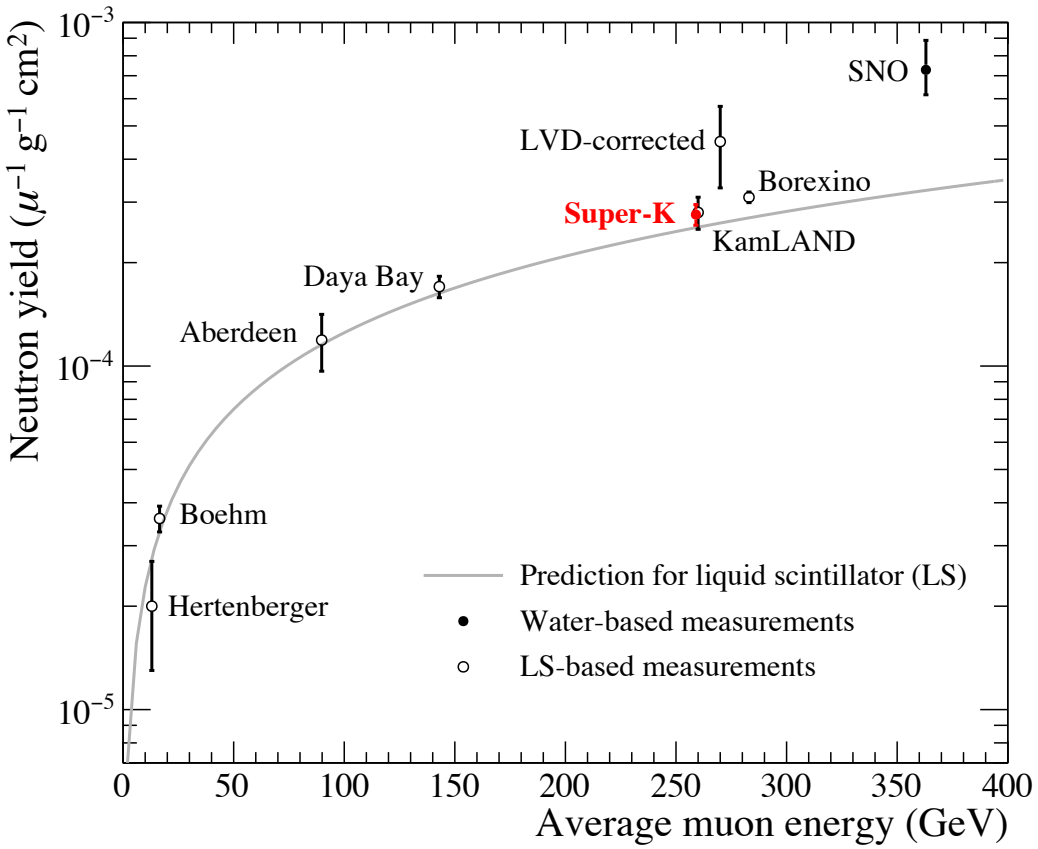

Figure 7.13: Correlations between neutron yields and muon energies in various experiments. The muon energy corresponds to the depth at which the detector is located. The filled circles represent the water-based results [46]; in particular, the red one shows the result of this analysis. The open circles represent the measurements with liquid scintillator (LS) detector [37, 39, 40, 42–45]. The gray solid line shows predictions for LS using FLUKA [47].

Chapter 8

Measurement of Cosmogenic Lithium-9 Production

Cosmic-ray muons induce the secondary showers in water, which interact with ^{16}O and produce neutrons and various radioactive isotopes. Of those isotopes, ^{9}Li is one of the major background sources in the search for SRNs below ∼14 MeV. ^{9}Li emits an electron and a neutron via β decay at a branching ratio of 50.8% (^{9}Li $\beta+n$ decay, $^{9}\mathrm{Li} \rightarrow {}^{8}\mathrm{Be} + e^- + \bar{\nu}_e + n$). The ^{9}Li $\beta+n$ decay can fake the inverse beta decay of SRNs ($\bar{\nu}_e + p \rightarrow e^+ + n$) as e^+ and e^- can not be distinguished by the SK detector. The ^{9}Li decays with a lifetime of 0.257 s and a Q-value of 13.6 MeV. This lifetime is larger than the veto time after muons which is set to 1 ms with $2\,\mathrm{s}^{-1}$ muon rate. The SRN analysis in SK uses correlations between the muon and electron events such as the time difference from the muon to the electron event and the distance from the muon track to the vertex position of the electron event to reduce the background. While, a fraction of the ^{9}Li $\beta+n$ decay events remains after event reduction and becomes the background for the SRN search. Therefore, it is important to measure the energy spectrum of ^{9}Li in advance in order to estimate the amount of the ^{9}Li background in the SRN search. The previous ^{9}Li analysis was performed above 8 MeV, the same energy range as the SRN search with the data in SK with ultra-pure water [50], while the energy range of the SRN search will be expanded to the low-energy side below 8 MeV in SK with Gd-loaded water to increase the statistics of the data and improve the sensitivity. In this study, the analysis method was newly developed for the data taken with Gd-loaded water, and the ^{9}Li energy spectrum was measured down to 4.5 MeV for the first time in the SK detector.

8.1 Overview of ^{9}Li $\beta + n$ Decay Event Search

The ^{9}Li events were selected by searching for pairs of electron events and neutron capture on Gd (n-Gd capture) events following cosmic-ray muon events. Figure 8.1 is the schematic illustration of the time correlations of these three events. In this analysis, the pair of the electron and n-Gd capture event was searched first, and then the parent muon of the ^{9}Li isotope was searched within the previous one second. Hereafter, an electron event and a neutron capture event are called "prompt event" and "delayed event", respectively. The analysis flow is as follows.

1. An electron and a neutron are emitted from ^{9}Li decay. The signal from the electron should be observed first (prompt event), and then the neutron is thermalized in water, and γ rays are emitted after the thermalized neutron is captured on the surrounding hydrogen or Gd (delayed event). The selection criteria are set to collect n-Gd capture events in this analysis in the time window from 35 μs to 535 μs after the prompt events. The pairs are selected using the information of the reconstructed energy and the distance between the prompt and delayed events.

2. The presence of a ^{9}Li $\beta + n$ decay event means that there should be a cosmic-ray muon that

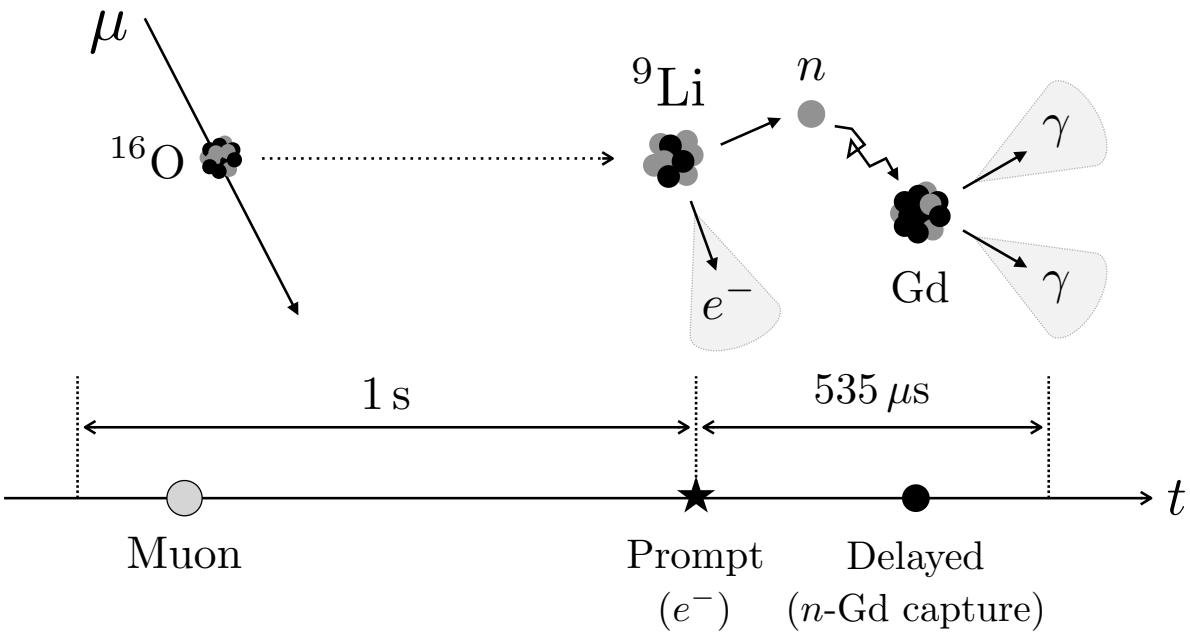

Figure 8.1: Overview of cosmogenic ^{9}Li analysis in SK.

induced the ^{9}Li at the time preceding the ^{9}Li $\beta + n$ decay event. In this analysis, if the pair of prompt and delayed events is found in Step 1, the muon is searched within 1 s before the prompt event. As there are more than one muons within 1 s in general with the muon rate of $2\,\mathrm{s}^{-1}$ in the SK detector, the candidate muon is selected using the likelihood which is defined by the variables for the features of muons with large energy deposit in the detector due to the spallation interaction and the spacial relationship between the muon track and the prompt event vertex. If there are muons within 1 ms immediately before the prompt event, the prompt and delayed events are not selected as ^{9}Li candidate because these events are likely caused by muon-induced neutrons.

3. If the triple coincidence of muon, prompt, and delayed event is found, the time difference between the muon and prompt events (Δt_{pd}) is calculated. Δt_{pd} is used to evaluate the number of the ^{9}Li $\beta + n$ decay events by fitting the distribution. The fit is applied for each energy region of prompt events to extract the number of ^{9}Li $\beta + n$ decay in each energy, and the β spectrum of the ^{9}Li $\beta + n$ decay is obtained.

8.2 Selection of Prompt and Delayed Event Pair

8.2.1 Preselection

Cherenkov photons are emitted due to the environmental radiations from the rock surrounding the detector or PMTs mounted on the wall. To eliminate such backgrounds, the events are selected with the distance between the vertex position and the inner detector (ID) wall, d_{wall}. Events with $d_{\mathrm{wall}} > 2\,\mathrm{m}$ are used in the analysis. The region corresponds to the volume of 22.5 kton. Furthermore, the directions of the background events occurring near the ID wall are mostly inward. Therefore, in addition to the selection criteria for the distance between the event vertex position and the ID wall, the distance to the wall along the direction of the particle (Cherenkov ring) is used as a selection criterion. Such distance is called effective distance d_{eff}, which is defined by the reconstructed vertex and direction as the distance from the reconstructed vertex to the ID wall back along the reconstructed direction. A schematic illustration is shown in Figure 8.2. Because

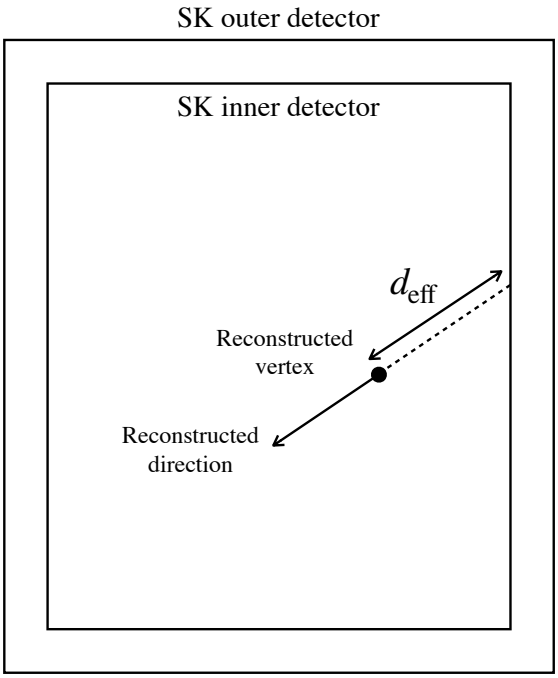

Figure 8.2: The definition of the effective distance from the ID wall d_{eff}.

the energy of environmental radiation is distributed mostly below a few MeV, the selection criteria are set separately for the region of reconstructed energy E_{rec}: $d_{\mathrm{eff}} > 650\,\mathrm{cm}$ for $E_{\mathrm{rec}} < 5\,\mathrm{MeV}$ and $d_{\mathrm{eff}} > 400\,\mathrm{cm}$ for $E_{\mathrm{rec}} \geq 5\,\mathrm{MeV}$. A tighter cut is applied for lower energy events to suppress the contamination of the background due to environmental radiation. Note that this cut already has been applied as part of data acquisition (real-time process) to reduce the data storage. In the real-time process, the cuts for event quality and reconstructed energy have been also applied: $\Delta g^2 \geq 0.10$ and $E_{\mathrm{rec}} \geq 3.0\,\mathrm{MeV}$.

Since prompt and delayed event pairs will be searched, prompt event candidates are removed if there are no other events within the following $535\,\mu\mathrm{s}$.

8.2.2 Event Quality Cut

In order to reject the background event due to PMT dark noise, the event quality cut is applied. The goodness of vertex reconstruction g_{vtx} and the goodness of direction reconstruction g_{dir} were used for the event quality cuts. The explanations of g_{vtx} and g_{dir} are described in Section 5.1. Both g_{vtx} and g_{dir} take values from zero to one. The larger g_{vtx} and the smaller g_{dir} are given for more reliable reconstruction results (i.e. hit pettern and timing distribution consistent with the Cherenkov light from charged particles). Therefore, $\Delta g^2 \equiv g_{\mathrm{vtx}}^2 - g_{\mathrm{dir}}^2$ takes a value from -1 to $+1$, with a larger value for higher event quality. In this analysis, an event satisfying $\Delta g^2 \geq 0.25$ was obtained as the prompt event candidate.

8.2.3 Energy Cut

Figure 8.3 shows the reconstructed total energy E_{rec} of the prompt events for the data after the fiducial volume cut is applied. The event rate increases at lower energy due to environmental radiations remaining in the fiducial volume. The prompt event candidates that satisfy $4.5\,\mathrm{MeV} \leq E_{\mathrm{rec}} < 14.5\,\mathrm{MeV}$ are selected in this analysis. In SK, triggers are issued for events with more than 34 hit-PMTs, and the data is recorded. This trigger threshold corresponds to the energy of $\sim$3.5 MeV, but because the number of hit-PMTs depends on the event vertex positions and has statistical fluctuation, the detection efficiency at 3.5 MeV is $\sim$50%. The lower energy threshold

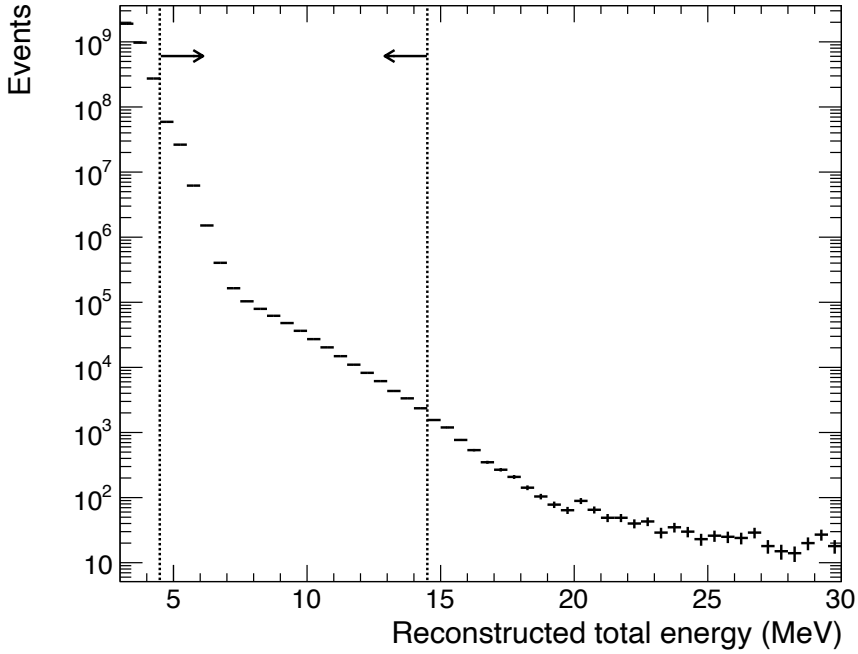

Figure 8.3: Reconstructed total energy of the prompt events for the data after the fiducial volume cut is applied. The events with the energy of 4.5–14.5 MeV are selected as the prompt event candidates in this analysis.

for this analysis is set to 4.5 MeV to ensure a detection efficiency of ∼100%. The upper limit is determined to be 14.5 MeV to cover the reconstructed β energy spectrum of the ^{9}Li $\beta + n$ decay generated from the MC simulation shown in Figure 8.4.

8.2.4 Neutron Tagging

A delayed event (n-Gd capture) was searched within 535 μs after the prompt event (electron). The selection criteria for delayed events are listed as follows.

(1) Event selections are applied using the distance between the vertex positions and the ID wall as follows (same as the prompt events):

- $d_{\mathrm{wall}} > 200$ cm
- $d_{\mathrm{eff}} > 650$ cm for $E_{\mathrm{rec}} < 5$ MeV
- $d_{\mathrm{eff}} > 400$ cm for $E_{\mathrm{rec}} \geq 5$ MeV.

(2) $35\,\mu\mathrm{s} \leq \Delta t_{\mathrm{pd}} \leq 535\,\mu\mathrm{s}$, where Δt_{pd} represents the time difference between the prompt and delayed events.

(3) $\Delta g^2 \geq 0.10$, where Δg^2 represents the event quality (Section 5.1). Δg^2 for MC and data are shown in Figure 8.5. This cut eliminates the background events due to PMT dark noise and mis-reconstructed events.

(4) $3.5\,\mathrm{MeV} \leq E_{\mathrm{rec}} < 10\,\mathrm{MeV}$, where E_{rec} represents reconstructed total energy. The range of the cut is defined to select a total 8 MeV γ rays emitted from neutron capture on Gd. E_{rec} distributions for the data and MC are shown in Figure 8.6. The peaks of the distributions are shifted from 8 MeV for the reasons explained below.

(5) $\Delta r < 350$ cm, where Δr is the distance between the prompt and delayed vertex (Figure 8.7). The upper limit was set to suppress the accidental coincidence of two background events while keeping the efficiency to ^{9}Li $\beta + n$ decays.

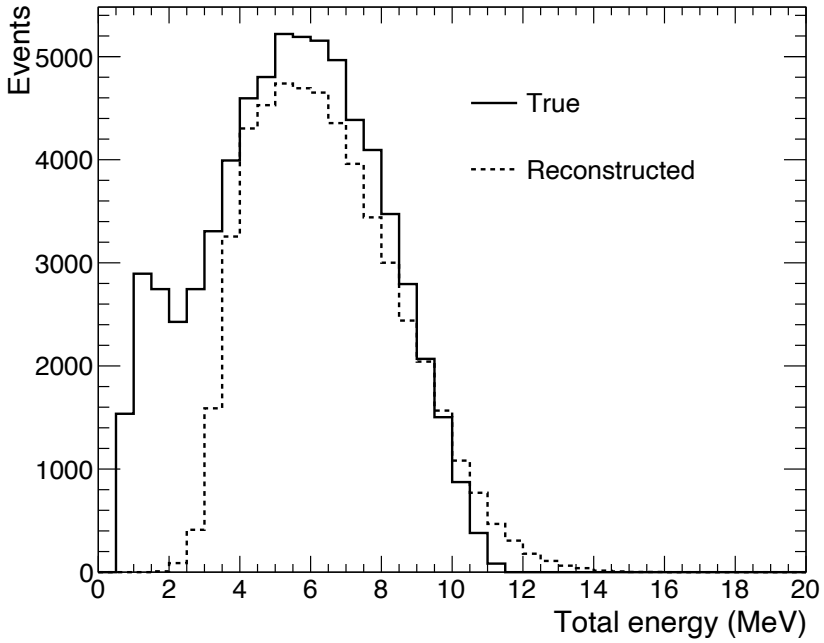

Figure 8.4: β energy spectrum of the ^{9}Li $\beta + n$ decay generated from the MC simulation. The solid line shows the true total energy and the dashed line shows the reconstructed total energy E_{rec}. The distribution of the reconstructed total energy drops off around $\sim$4 MeV because of the efficiency of SLE trigger which is $\sim$50% at 3.5 MeV and reaches $\sim$100% at round 4 MeV.

The range of the energy cut is extended with respect to the cut applied to the prompt event selection. In the prompt event selection, the lower limit is set to 4.5 MeV to measure the β spectrum with $\sim$100% trigger efficiency independent of the energy. While, the range is extended to the delayed events to increase the efficiency and avoid the cut around the peak of neutron capture on Gd. As the energy of the prompt and delayed events are not correlated, the inefficiency of the delayed events should not cause distortion of the energy spectrum of the prompt events.

The peak of the reconstructed energy of γ rays is lower than $\sim$8 MeV as shown in Figure 8.6 for the following reasons. When a neutron is captured on Gd, several γ rays totaling $\sim$8 MeV are emitted. These γ rays interact with electrons through the electromagnetic interactions; photoelectronic effect and Compton scattering, then the electrons travel in water and the Cherenkov photons are emitted. However, the amount of the Cherenkov photons is not proportional to the energy of the electron below a few MeV due to the Cherenkov threshold. The number of emitted photons per unit energy deposition (photons/MeV) is fewer for electrons with lower energy. In this analysis, since the energy is reconstructed from the number of detected photons (hit-PMTs) assuming all photons are emitted from an electron, reconstructed energy is underestimated for the total energy of multiple electrons as in the case of neutron capture on Gd.

If a delayed event that satisfied the criteria was found, the pair was selected as the ^{9}Li $\beta + n$ decay event candidate.

8.2.5 1 ms Veto After Muon

If there are muons within 1 ms before the prompt events, these prompt events are excluded from the analysis as these events are likely to be the muon-induced neutrons.

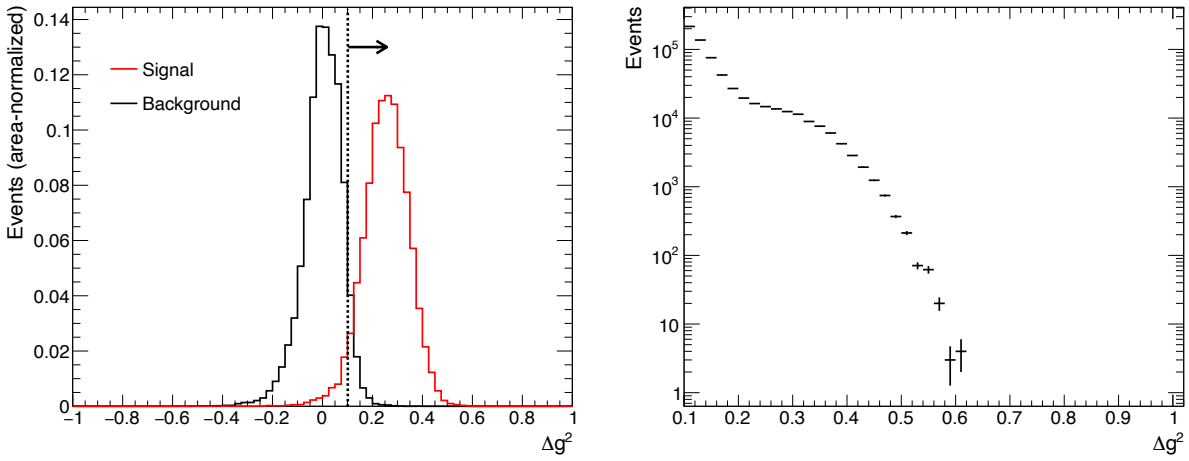

Figure 8.5: Distribution of Δg^2 for neutron capture on Gd for MC and data obtained with random triggers (left), and the delayed event candidates of the data before the selection criteria are applied (right). The selection $\Delta g^2 \geq 0.10$ (dashed line) has been applied for the SLE trigger events in the real-time process.

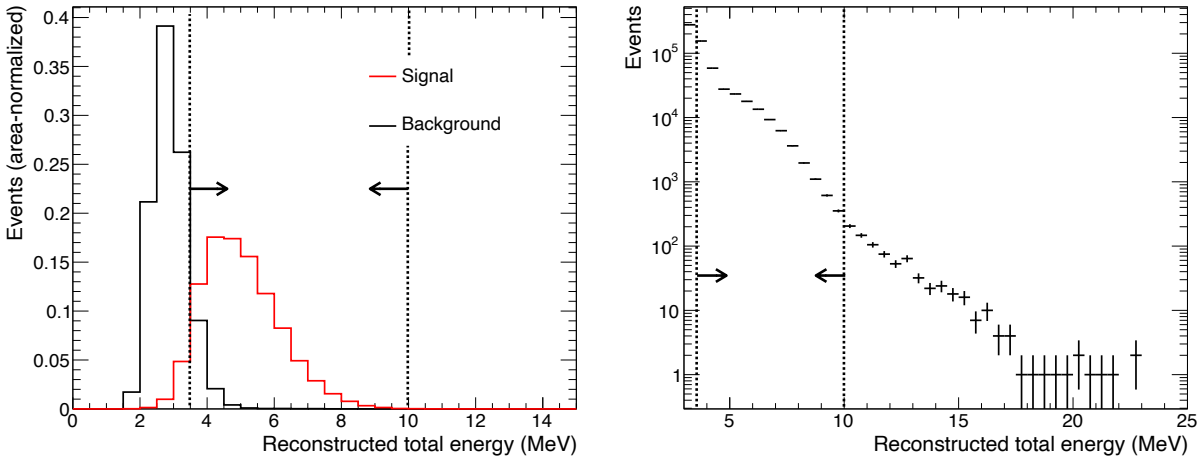

Figure 8.6: Distribution of reconstructed total energy E_{rec} for neutron capture on Gd for the MC and data taken with random triggers (left), and the delayed event candidates of data before the selection criteria are applied (right). The dashed lines represent the selection criterion $3.5\,\mathrm{MeV} \leq E_{\mathrm{rec}} < 10\,\mathrm{MeV}$. The selection $E_{\mathrm{rec}} \geq 3\,\mathrm{MeV}$ has been applied in the real-time process.

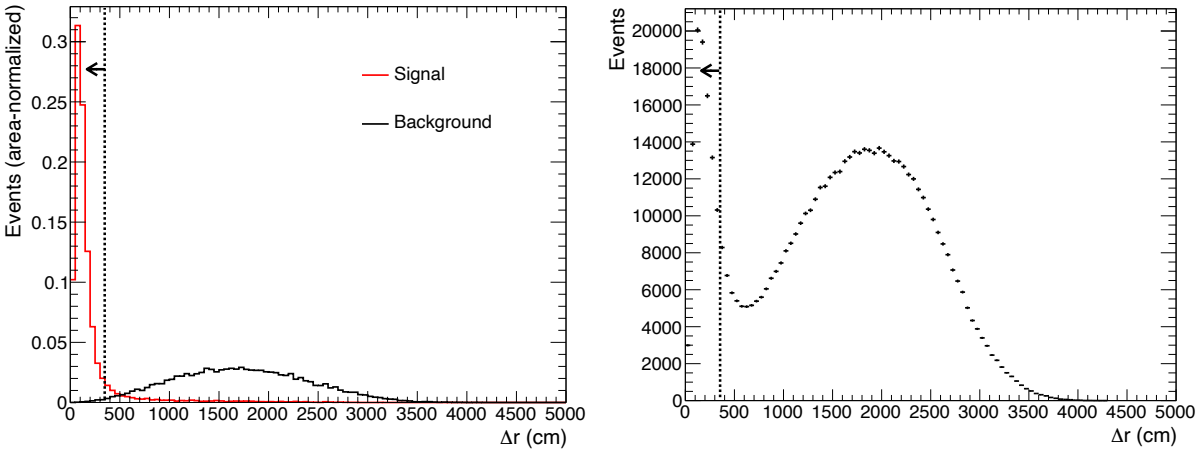

Figure 8.7: Distribution of the distance between the prompt and delayed vertex, Δr, for neutron capture on Gd for the MC and data taken with random triggers (left), and the delayed event candidates of data before the selection criteria are applied (right). The dashed lines represent the selection criterion $\Delta r < 350\,\mathrm{cm}$.

8.3 Selection of Muon Events

Once the pair of prompt and delayed events (prompt-delayed pair) is found, the parent muon event candidate is searched within the last 1 s. As the muon rate is $\sim 2\,\mathrm{s}^{-1}$ at SK, there are often more than one muon within 1 s. Among those, the parent muon of the ^{9}Li isotope is selected with the following five variables which represent the characteristics of energetic muons and spallation interactions.

- L_t: transverse distance from the the prompt event vertex position to the muon track (Figure 8.8). The positions of muon-induced isotopes decay should be near the muon track.
- L_{long}: longitudinal distance between the vertex position of the prompt event and the point in the muon track associated with the maximum dE/dx (Figure 8.8). The point with the maximum dE/dx is likely to be the point where the muons or induced showers interact with oxygen. Therefore, the muons which produce isotopes should have short L_{long}.
- Q_μ: total number of photons (photoelectrons) observed by the ID PMTs for the muon track. Muons that produce isotopes should deposit significantly large energy in the detector via the spallation interaction with oxygen.
- Q_{res}: difference between the observed number of photons (photoelectrons) and the expectation from the muon track length assuming a minimum ionization particle (MIP). The Q_{res} defined as

$$Q_{\mathrm{res}} \equiv Q_\mu - q \cdot L_\mu, \tag{8.1}$$

  where q and L_μ are the expected number of photoelectrons per unit length from the minimum ionization and the muon track length, respectively. The muon that produces isotopes not only loses energy continuously via ionization but also causes spallation interaction which breaks oxygen nuclei at a point along the track. Therefore, the energy loss of the muon-induced spallation interaction should be larger than the energy loss assuming the MIP throughout the trajectory in the detector.
- N_n: number of spallation neutron candidates following the muon. The muons which produce isotopes tend to induce electromagnetic and hadronic showers. Those showers interact with oxygen nuclei in a chain, producing many neutrons.

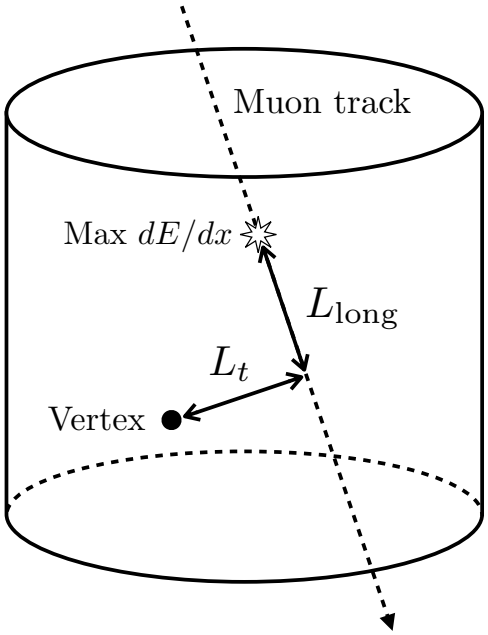

Figure 8.8: Schematic illustration of transverse distance L_t and longitudinal distance L_{long}. Max dE/dx is the point in the muon track associated with the maximum dE/dx.

First, the parent muon candidate is selected with the likelihood method using probability density functions (PDFs) for four variables L_{long}, Q_μ, Q_{res}, and N_n. Second, the triple coincidence of the prompt-delayed pair and the parent muon is selected as a ^{9}Li candidate if the L_t for the muon candidate is less than 500 cm.

As only $\sim 10^4$ ^{9}Li isotopes are expected to be produced in the SK detector within the data-taking period described in this study due to the small production rate, it is difficult to generate the PDF for each variable with high precision. Instead, PDFs are generated using another isotope ^{12}B. The production yield of ^{12}B is the largest among cosmogenic isotopes with lifetimes within 1 s [50]. ^{12}B has a lifetime of 0.029 s and emits an electron via β decay with a Q-value of 13.37 MeV. To generate PDFs for spallation variables, two different samples were prepared from the data. One is a "pre-sample" composed of prompt-delayed pairs and associated muons within 0.05 s before the prompt event candidate, and the other is a "post-sample" composed of prompt-delayed pairs and associated muons within 0.05 s after the prompt event candidate. The pre-sample and post-sample is schematically shown in Figure 8.9. The time width of 0.05 s is selected because ^{12}B isotopes are dominant within 0.05 s from muons. If an event with energy of several MeV is due to an electron emitted from an isotope (mostly ^{12}B) decays, the pre-sample should contain the muon that induced the event in addition to uncorrelated muons, while the post-sample should consist of only uncorrelated muons. Hence, the information (distribution of the variables described in the previous section) for decay events of muon-induced isotopes is extracted by subtracting the post-sample from the pre-sample.

The PDFs were generated for spallation samples and random samples, separately. The spallation sample was generated by subtracting the post-sample from the pre-sample, while the random sample was taken directly from the post-sample. The PDFs of the spallation sample ($\text{PDF}_i^{\text{spall}}$) and random sample ($\text{PDF}_i^{\text{rand}}$) are shown in Figure 8.10, where i represents the variable $i = L_{\text{long}}$, Q_μ, Q_{res}, and N_n. Using these PDFs for four variables, the spallation likelihood $\mathcal{L}$ is defined as

$$\mathcal{L} = \log\left(\prod_i \frac{\text{PDF}_i^{\text{spall}}}{\text{PDF}_i^{\text{rand}}}\right). \tag{8.2}$$

The likelihood $\mathcal{L}$ was calculated for each muon within 1 s before the prompt event candidate, and

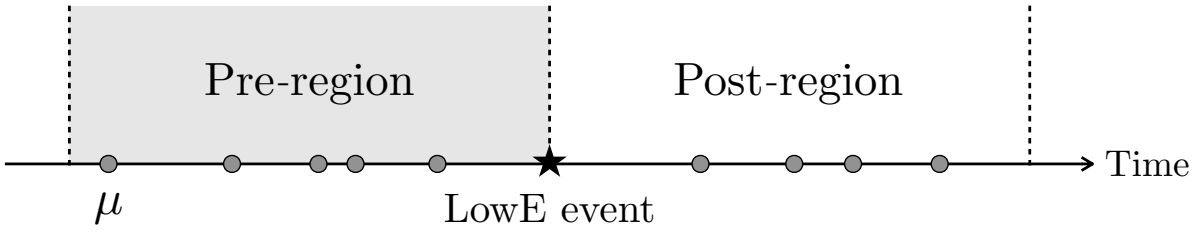

Figure 8.9: Definition of pre-sample and post-sample for the spallation variables. The "LowE event" (star) represents the event with several MeV from the decay of cosmogenic isotope. Muons around the LowE event are shown by circles. The parent muon induced the isotope (LowE event) should be in pre-region, and not in post-region.

Table 8.1: Reduction summary for ^{9}Li

$E_{\rm rec}$ (MeV)	4.5–5.5	5.5–6.5	6.5–7.5	7.5–8.5	8.5–9.5	9.5–14.5
Pre-selection	2,606,347	206,088	39,901	30,010	19,156	21,974
Event quality	154,737	35,638	25,923	26,847	18,235	21,512
Neutron tagging	14,671	14,445	5,726	720	219	304
1 ms cut	1,281	1,077	689	360	175	281
Muons	1,114	954	619	336	169	274
Transverse distance	188	223	210	147	101	186

the muon with the largest $\mathcal{L}$ was selected as the parent muon candidate. If the muon candidate satisfies $L_t < 500\,$cm, the prompt-delayed pair is selected as the ^{9}Li $\beta + n$ decay event. Otherwise, the prompt-delayed pair is rejected as there is no parent muon candidate. Figure 8.11 shows the distributions of L_t for pre-/post-sample and spallation sample.

8.4 Extraction of ^{9}Li Production Rates

Events that satisfy the triple coincidence of muon, prompt, and delayed event were obtained as ^{9}Li candidates. Table 8.1 summarized the number of observed events for each $E_{\rm rec}$ region. For the ^{9}Li candidates, following two types of time difference are obtained.

- $\Delta t_{\mu \rm p}$: time difference between the muon and prompt event
- $\Delta t_{\rm pd}$: time difference between the prompt and delayed event

$\Delta t_{\mu \rm p}$ is used to count the number of ^{9}Li while $\Delta t_{\rm pd}$ is used to confirm neutron capture events are selected.

The $\Delta t_{\mu \rm p}$ distributions are shown in Figure 8.12 for each $E_{\rm rec}$ region; $E_{\rm rec}$ = 4.5–5.5 MeV, 5.5–6.5 MeV, 6.5–7.5 MeV, 7.5–8.5 MeV, 8.5–9.5 MeV, and 9.5–14.5 MeV. The excesses in the short time difference regions are the contributions of ^{12}B. High-energy muons occasionally produce multiple ^{12}B's and other isotopes (X). Some of the isotopes have lifetimes of tens to hundreds of ms, which is much larger than the time scale of neutron capture but a small fraction still decays within the 535 μs time window. If those decays of the ^{12}B or the other isotopes occur twice in the same time window, they are recognized as a pair and become a fake signal of ^{9}Li $\beta + n$ decay events. Such a pair is denoted ^{12}B-^{12}B/X as at least one of them is decay of ^{12}B which is dominated in the time scale of this analysis. The pairs of ^{12}B-^{12}B/X remain even after the event reductions to fake ^{9}Li $\beta + n$ decay, therefore the $\Delta t_{\mu \rm p}$ distribution was fitted with a combination of two exponential functions including ^{9}Li and ^{12}B components:

$$f(\Delta t_{\mu \rm p}) = A \exp\left(-\frac{\Delta t_{\mu \rm p}}{\tau_{^{9}\rm Li}}\right) + B \exp\left(-\frac{\Delta t_{\mu \rm p}}{\tau_{^{12}\rm B}}\right) + C, \tag{8.3}$$

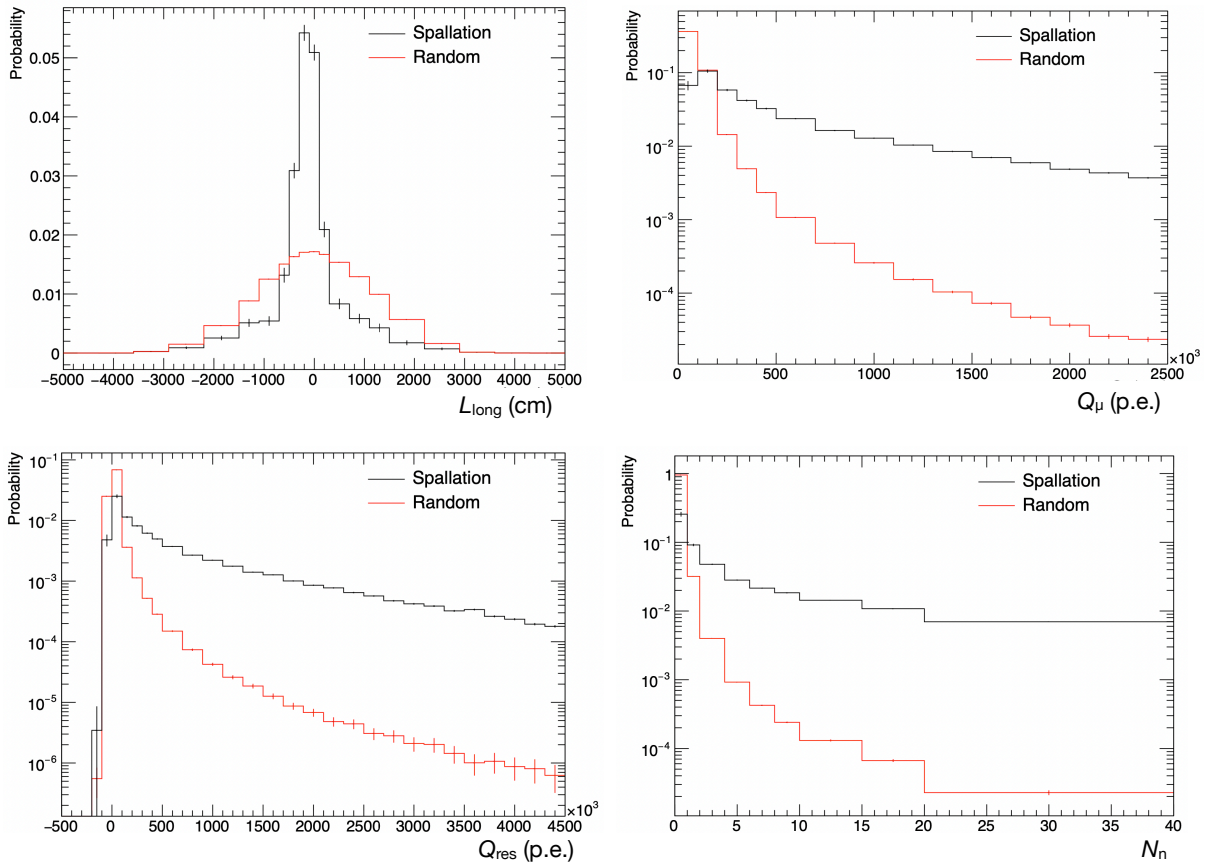

Figure 8.10: The PDFs of the spallation sample and random sample. PDFs for L_t (top left), Q_μ (top right), $Q_{\rm res}$ (bottom left), N_n (bottom right). The black and red line shows the spallation and random sample, respectively.

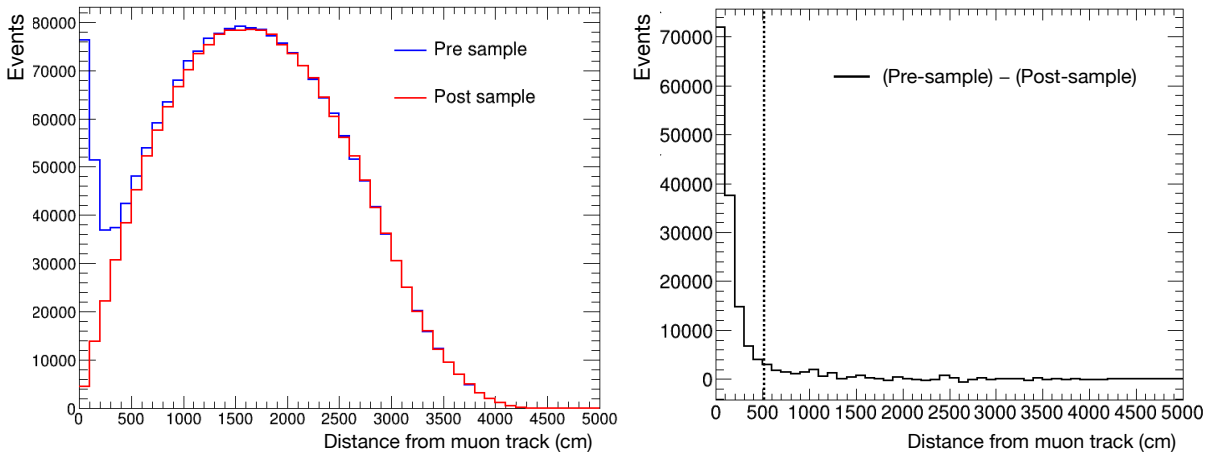

Figure 8.11: L_t distributions for pre-/post-sample (left) and spallation sample (right). The spallation sample is obtained by subtracting the post-sample from the pre-sample. The dotted line in the right figure represents the cut threshold.

Table 8.2: Summary of the fit results and $N_{^9\mathrm{Li}}$ for each E_{rec} region. A, B, and C correspond to the parameters in Eq. (8.4). The errors are statistical only.

E_{rec} (MeV)	A	B	C	χ^2/d.o.f	$N_{^9\mathrm{Li}}$
4.5–5.5	8.4 ± 3.3	181 ± 22	2.6 ± 0.7	29.13/17	42 ± 17
5.5–6.5	14.5 ± 3.5	230 ± 25	1.6 ± 0.6	11.81/17	73 ± 17
6.5–7.5	17.0 ± 3.6	183 ± 23	1.5 ± 0.6	30.09/17	86 ± 18
7.5–8.5	10.1 ± 3.1	128 ± 20	1.5 ± 0.6	18.70/17	51 ± 16
8.5–9.5	5.4 ± 2.1	115 ± 18	0.7 ± 0.4	25.13/17	27 ± 11
9.5–14.5	12.7 ± 2.6	220 ± 24	0.4 ± 0.4	23.05/17	64 ± 13

where $\tau_{^9\mathrm{Li}}$ and $\tau_{^{12}\mathrm{B}}$ are the lifetime of ^{9}Li and ^{12}B isotopes, which are 0.257 s and 0.029 s, respectively. These parameters are fixed to fit $\Delta t_{\mu\mathrm{p}}$. The parameters A and B represent the normalizations of ^{9}Li and ^{12}B events, and C is the background rate. The background is mainly due to radioactivities, such as the decay products of Rn from PMTs which have no correlation with muon. Therefore, the background component is set to a constant. The number of ^{9}Li candidates $N_{^9\mathrm{Li}}$ is calculated by integrating the fitting results for each E_{rec} as

$$N_{^9\mathrm{Li}} = \int_{1\,\mathrm{ms}}^{1\,\mathrm{s}} A \exp\left(-\frac{\Delta t_{\mu\mathrm{p}}}{\tau_{^9\mathrm{Li}}}\right) d(\Delta t_{\mu\mathrm{p}}). \tag{8.4}$$

The fit results and $N_{^9\mathrm{Li}}$ for each E_{rec} region are summarized in Table 8.2.

The Δt_{pd} distribution is shown in Figure 8.13. The Δt_{pd} distribution was fitted by the single exponential function

$$f(\Delta t_{\mathrm{pd}}) = A_n \exp\left(-\frac{\Delta t_{\mathrm{pd}}}{\tau_n}\right) + B_n, \tag{8.5}$$

where τ_n represents the time constant for neutron capture on Gd. A_n is the normalization of neutron capture events and B_n is the background rate. The parameter τ_n is determined from the fit as $\tau_n = 102.3 \pm 14.7\,\mu$s, which is consistent with the measurement result from the Am/Be, $116.5 \pm 0.2\,\mu$s (Section 4.4). The constant component in the distribution of Δt_{pd} is due to the background and ^{12}B-^{12}B/X pair. Although the time difference of the ^{12}B-^{12}B/X pairs should follow an exponential function with a time constant of more than a few ten ms, it is long enough for the time width of 535 μs to be considered a constant component here.

The β spectrum from the ^{9}Li $\beta + n$ decay was extracted using $N_{^9\mathrm{Li}}$ for each E_{rec} region. The result is shown in Figure 8.14 and compared with the MC. The result is normalized by the fiducial volume 22.5 kton and the livetime 454.2 days, while the correction for the efficiency is not applied.

8.5 Prospects for SRN Search

The energy spectrum of ^{9}Li produced by cosmic-ray muons was measured in SK with 0.01% Gd-loaded water in this study. The previous study [50] was performed using the data of 1,890 days in SK with ultra-pure water, where ^{9}Li events were searched above 8 MeV. In this study, taking advantage of the neutron detection efficiency and background rejection improved by the Gd loading to lower energy side, from 8 MeV to 4.5 MeV, using the data of 454.2 days with Gd-loaded water. Prospects for the SRN search and the relation to this study are described in this section.

The SRN flux depends mainly on the cosmic star formation rate (SFR) which is proportional to the core-collapse supernova rate. Since neutrinos emitted by old supernovae are affected by the redshift z due to the expansion of the universe, their energy is reduced by a factor of $(1+z)^{-1}$. Therefore, SRNs with lower energy of a few MeV provide information about the supernovae in the early stage of the universe as shown in Figure 8.15. Because the uncertainty on the SFR is large in the old universe, the prediction of the neutrino flux varies larger by the different models as the

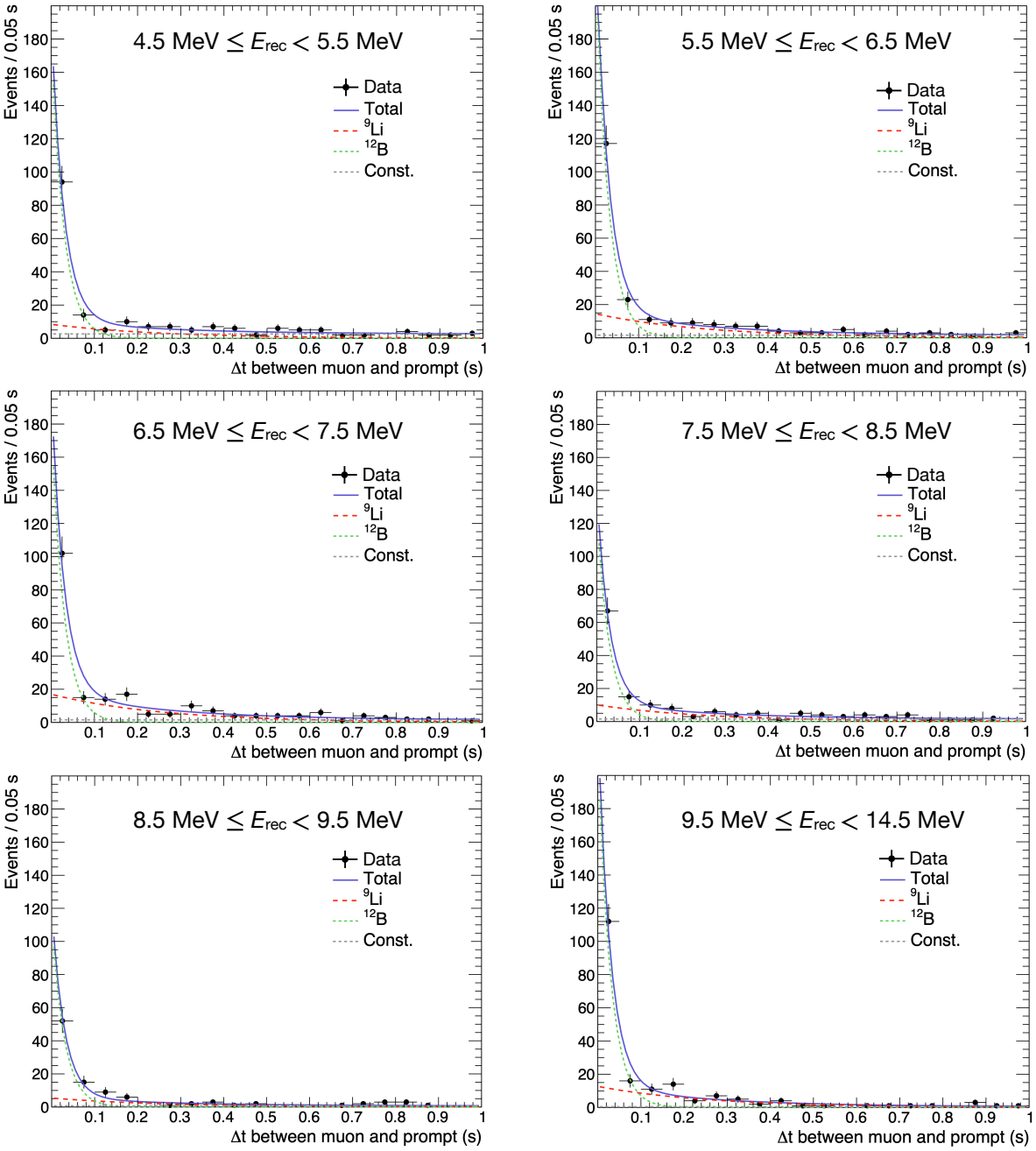

Figure 8.12: Distribution of time difference between muon and prompt event $\Delta t_{\mu p}$ for each reconstructed total energy $E_{\rm rec}$. The black circles represents the data and the solid blue line is the fit result. The dotted red, green, and gray lines are ^{9}Li, ^{12}B, and constant component in the fitting function Eq. (8.3), respectively.

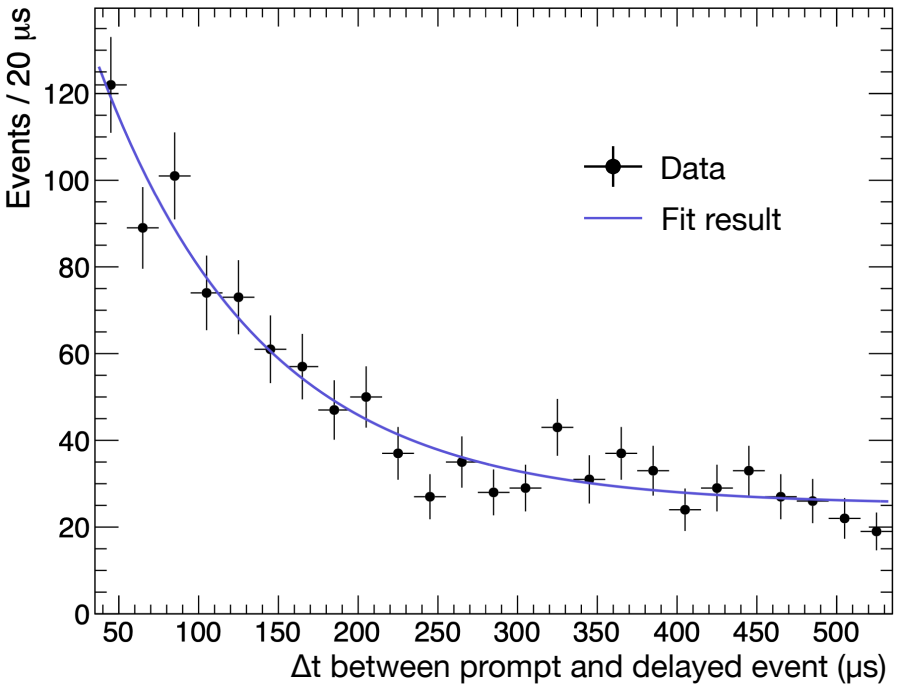

Figure 8.13: Distribution of time difference between prompt and delayed event Δt_{pd}. The black circles represents the data and the solid blue line is the fit result with Eq. (8.5).

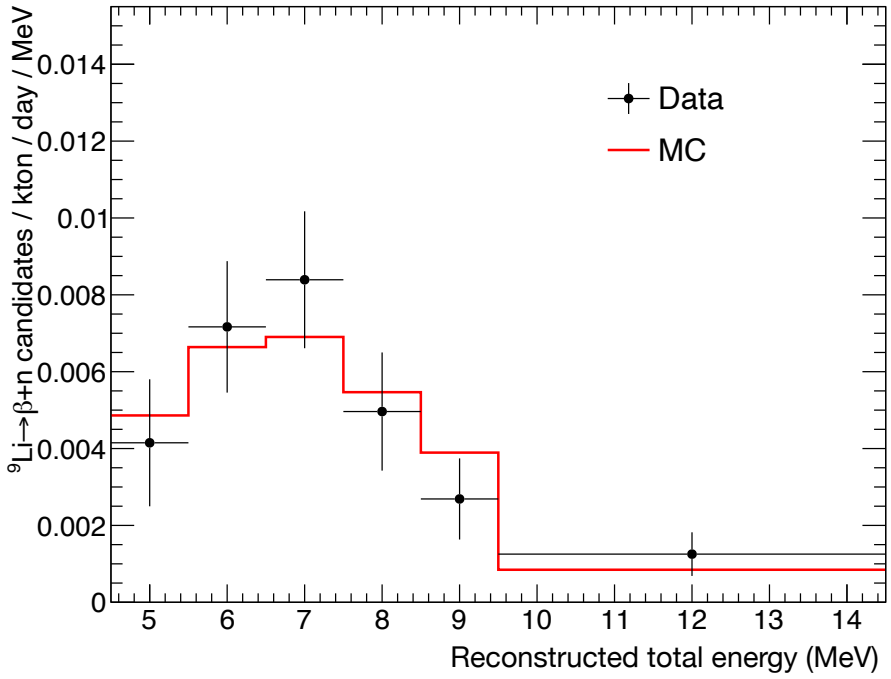

Figure 8.14: The β spectrum from the ^{9}Li $\beta + n$ decay.

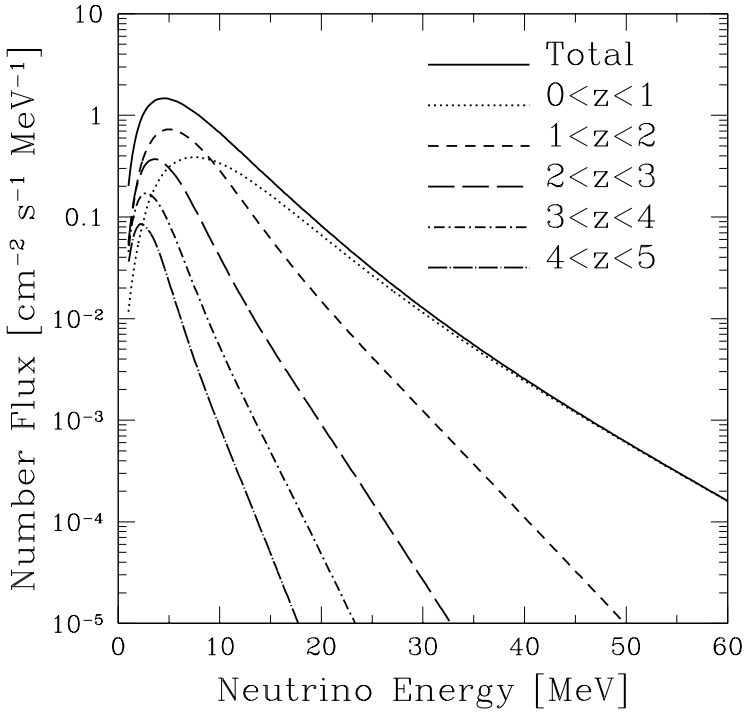

Figure 8.15: SRN flux from various redshift ranges assuming the supernova model of Ref. [72]. This figure is taken from Ref. [73].

redshift increases. Figure 8.16 shows the SRN event rates observed in SK for various SFR models. The differences between the models are particularly pronounced in the low-energy region. Current SRN search in SK is performed above 8 MeV while it is beneficial for the test of SFR models if the energy range of the search is extended to low energy region.

Since ^{9}Li is produced through the cosmic-ray muon spallation, events with a short distance from the muon track were selected as ^{9}Li events. While, the opposite event selection criteria are applied in the SRN search, i.e. events with a long distance from the muon track are selected. Therefore, the SRN analysis in the low-energy region is feasible if the analysis method developed in this study is reversed (Figure 8.17).

Here, the sensitivity of future SRN searches can be estimated. Figure 8.18 shows the expected energy spectrum for 10 years of observations with Gd concentration of 0.03%. In the actual SRN analysis, background is a major issue in the search at lower energy. In particular, the major background sources are ^{9}Li, atmospheric neutrinos, and electron antineutrinos from the reactor core (reactor neutrinos) although it depends on the condition of nuclear power plant operation. In this study, ^{9}Li and atmospheric neutrinos are assumed as the background sources. The component of ^{9}Li background is based on the result of this study and the atmospheric neutrino background is referred from Ref. [51]. So far, the ^{9}Li background for SRN search has been estimated by weighting the total ^{9}Li production rate measured above 8 MeV by the ^{9}Li energy spectrum obtained by MC with GEANT4. GEANT4 does not accurately model the deexcitation of ^{9}Be, the daughter nucleus of ^{9}Li, leaving some uncertainties due to the energy levels and branching ratios of ^{9}Be decay. Therefore, a more accurate estimation of the ^{9}Li background abundance can be obtained by using the measured spectrum instead of estimation from MC. Below 9.5 MeV, the background component is dominant, but the region is useful for constraining the background normalization. The advantage obtained by the results of this study is significant in the region 9.5–14.5 MeV. The systematic uncertainty on the atmospheric neutrino background in assumed based on Ref. [51] although the reduction of the rate and systematic uncertainty is investigated in the collaboration. The systematic uncertainty of ^{9}Li in that region is constrained by background normalization below

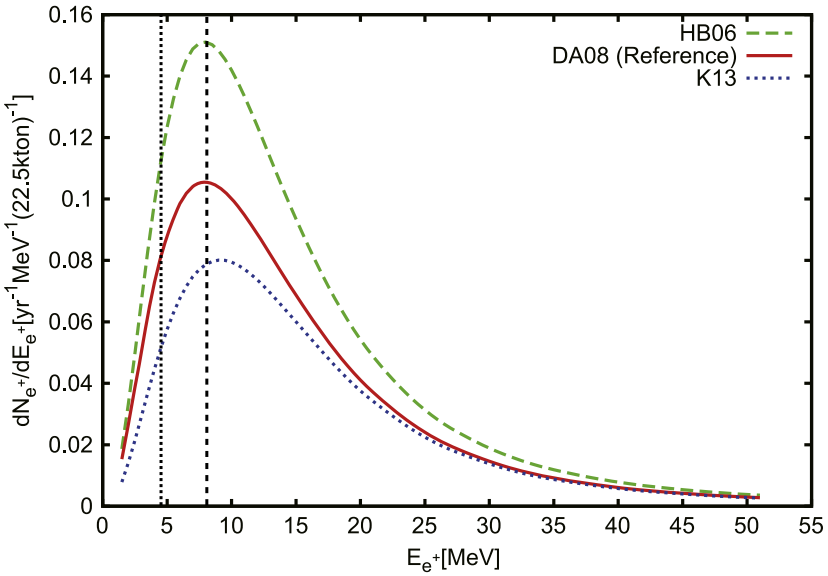

Figure 8.16: Event rates of the SRN observed in SK for various CSFRD models assuming the normal mass ordering. This figure is taken from Ref. [11]. The legends HB06, DA08, and K13 represent Ref. [74], [75], and [76], respectively. The vertical dotted and dashed lines are overwritten at 4.5 MeV and 8 MeV.

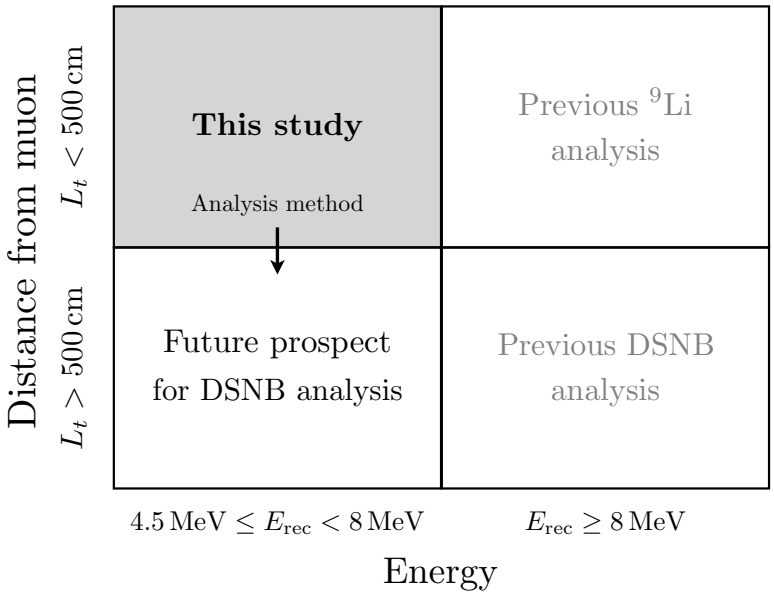

Figure 8.17: Schematic diagram of the correspondence between the SRN and ^{9}Li analysis.

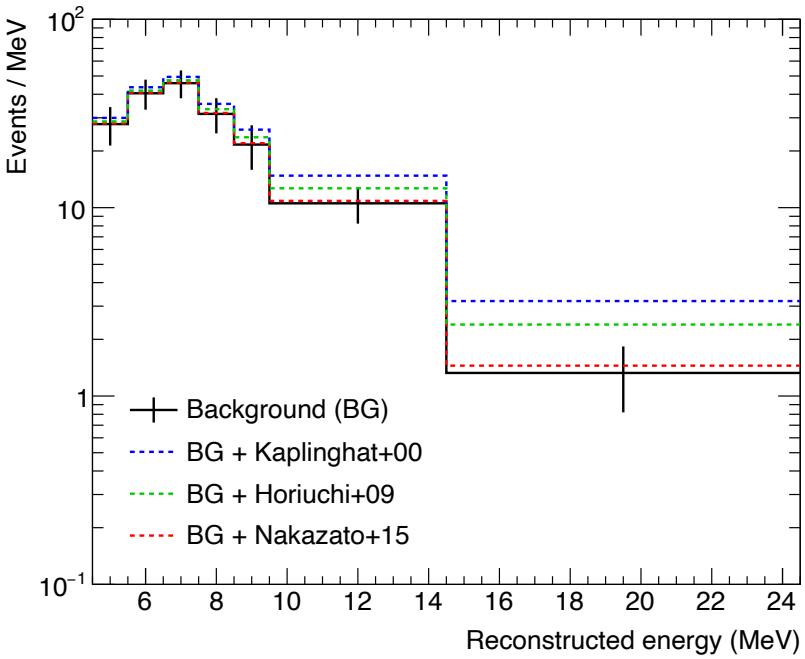

Figure 8.18: Expected energy spectrum for 4.5–24.5 MeV assuming ten years observation with 0.03% Gd concentration. The black points represent the expected background assuming ^{9}Li and atmospheric neutrinos. ^{9}Li component is based on the result of this study and the atmospheric neutrino background is referred from Ref. [51]. The dotted lines represent the expected number of SRN candidates, i.e. background plus expected SRN signals. The color represents the SRN flux model: blue is Kaplinghat+00 [18], green is Horiuchi+09 [13], and red is Nakazato+15 [11] assuming normal mass ordering.

9.5 MeV and β-spectrum shape measured by the data as shown in Figure 8.14. The systematic uncertainty of the ^{9}Li background rate is estimated to be 50% in the latest analysis [26], while the uncertainty could be suppressed to $\sim$20% in the next ten years by the additional constraints from the lower energy. This will lead to improve the sensitivity of SRN search especially in the 9.5–14.5 MeV region.

Chapter 9

Conclusion

The gadolinium (Gd) has been loaded into ultra-pure water in Super-Kamiokande (SK) in order to improve the neutron detection efficiency and the new observation phase (SK-Gd) has been started since August 2020. The major motivations for the upgrade are the first observation of neutrinos from past supernovae (supernova relic neutrinos, SRNs) and the suppression of the atmospheric neutrino background in the proton decay search. Neutrons are also produced via spallation interactions by cosmic-ray muons together with the other isotopes. These cosmogenic products are known as the background source in underground experiments, such as neutrino observations and dark matter searches. This thesis described the measurement of the cosmogenic products using the data from the SK-Gd experiment.

In order to realize the first observation of SRNs, it is necessary to continue the operation for a long time period, more than 10 years, with stable detector and water conditions. This thesis described a new method to monitor the stability and uniformity of neutron detection using neutrons produced in the detector by cosmic-ray muons. This method enables monitoring the neutron detection in the entire volume of the detector in parallel to the observation, and therefore is complementary to the calibration using the neutron source deployed in the detector. As a result, the measured Gd concentration was consistent with the expectation, and it was confirmed that the variation in time and positions are within $\pm 6.3\%$ (corresponds to $\pm 3.1\%$ of Gd capture fraction) during the data-taking period from September 2020 to May 2022. This variation is negligible compared to the other systematic uncertainties on the expected background rate in the SRN search. This method can be applied to secure stable operation, which leads to the first observation of SRNs in the future.

Extending the above study, the cosmogenic neutron production yield was measured using 283.2 days of data from September 2020 to September 2021 with 0.01% Gd-loaded water. The yield was measured to be $(2.76 \pm 0.02\,(\text{stat.}) \pm 0.19\,(\text{syst.})) \times 10^{-4}\,\mu^{-1}\text{g}^{-1}\text{cm}^2$ at an average muon energy of 259 GeV. This is the second case in which the neutron yield is measured with a water target, and the result provides information on the muon energy dependence. In addition, this study was performed at the same depth as the KamLAND detector with organic liquid scintillator, which is the first case that the neutron yields have been measured in different targets for the same muon energies. The result of this study is consistent with that of KamLAND, which shows no significant difference in neutron yield from oxygen and carbon spallation at this depth. These measurements provide the knowledge to systematically understand the neutron production and the secondary interactions, which leads to realizing the reliable simulations for the background estimations in the underground experiments.

In addition, the energy spectrum of electrons from β decay of ^{9}Li was also measured using 454.2 days of data from September 2020 to April 2022. Various radioactive isotopes are produced from the cosmic-ray muon spallation interactions. Among those, the β decay of ^{9}Li with an emission of neutron is one of the major background sources in SRN search at low energy region below 10 MeV, where the predicted SRN flux largely depends on the star formation models. ^{9}Li has been measured

above 8 MeV in the previous study with ultra-pure water, whereas the energy range was expanded down to 4.5 MeV in this study. Low energy bind together with the measured ^{9}Li spectrum will help to constrain contamination in the signal region and lead to improve the sensitivity of SRN search.

Bibliography

[1]F. Reines and C. L. Cowan, Phys. Rev. **92**, 830 (1953).

[2]G. Danby et al., Phys. Rev. Lett. **9**, 36 (1962).

[3]K. Kodama et al. (DONUT Collaboration), Phys. Rev. Lett. Sect. B Nucl. Elem. Part. High-Energy Phys. **504**, 218 (2001).

[4]Y. Fukuda et al. (Super-Kamiokande collaboration), Phys. Rev. Lett. **81**, 1562 (1998).

[5]H.-T. Janka, arXiv:1702.08713 (2017).

[6]K. Nakazato et al., The Astrophysical Journal Supplement Series **205**, 2 (2013).

[7]K. Hirata et al., Phys. Rev. Lett **58**, 1490 (1987).

[8]R. M. Bionta et al., Phys. Rev. Lett. **58**, 1494 (1987).

[9]E. N. Alekseev et al., Journal of Experimental and Theoretical Physics Letters **45**, 589 (1987).

[10]K. Hirata et al., Phys. Rev. D **38**, 2 (1988).

[11]K. Nakazato et al., The Astrophysical Journal **804**, 75 (2015).

[12]S. Galais et al., Phys. Rev. D **81**, 053002 (2010).

[13]S. Horiuchi et al., Phys. Rev. D **79**, 083013 (2009).

[14]S. Ando et al., Astroparticle Physics **18**, 307 (2003).

[15]D. H. Hartmann and S. E. Woosley, Astroparticle Physics **7**, 137 (1997).

[16]R. A. Malaney, Astroparticle Physics **7**, 125 (1997).

[17]T. Totani and K. Sato, Astroparticle Physics **3**, 367 (1995).

[18]M. Kaplinghat et al., Phys. Rev. D **62**, 043001 (2000).

[19]C. Lunardini, Phys. Rev. Lett. **102**, 231101 (2009).

[20]S. Horiuchi et al., Monthly Notices of the Royal Astronomical Society **475** (2018).

[21]D. Kresse et al., The Astrophysical Journal **909**, 2 (2021).

[22]S. Horiuchi et al., Phys. Rev. D **103**, 043003 (2021).

[23]Z. Tabrizi and S. Horiuchi, Journal of Cosmology and Astroparticle Physics **2021**, 05 (2021).

[24]K. Abe et al. (Super-Kamiokande Collaboration), Phys. Rev. D **104**, 122002 (2021).

[25]S. Horiuchi et al., Astrophysical Journal **738**, 154 (2011).

[26]M. Harada et al. (Super-Kamiokande Collaboration), The Astrophysical Journal Letters **951**, L27 (2023).

[27]S. Abe et al. (KamLAND Collaboration), The Astrophysical Journal **925**, 14 (2022).

[28]H. Kluck, "Production Yield of Muon-Induced Neutrons in Lead", PhD thesis (Karlsruhe Institute of Technology, 2015).

[29]T. K. Gaisser, R. Engel, and E. Resconi, *Cosmic Rays and Particle Physics* (2016).

[30]T. K. Gaisser and T. Stanev, Phys. Lett. B **592**, 228 (2004).

[31]A. Tang, G. Horton-Smith, V. A. Kudryavtsev, and A. Tonazzo, Phys. Rev. D **74**, 053007 (2006).

[32]K. Nakamura et al., JPG **37**, 075021 (2010).

[33]D. E. Groom, N. V. Mokhov, and S. I. Striganov, Atomic Data and Nuclear Data Tables **78**, 183 (2001).

[34]D.-M. Mei and A. Hime, Phys. Rev. D **73**, 053004 (2006).

[35]T. Luu and C. Hagmann, "Neutron Production by Muon Spallation I: Theory (UCRL-TR-226323)", (2006).

[36]A. Lindote et al., Astropart. Phys. **31**, 366–375 (2009).

[37]R. Hertenberger, M. Chen, and B. L. Dougherty, Phys. Rev. C **52**, 3449 (1995).

[38]L. B. Bezrukov et al., Sov. J. Nucl. Phys. **17**, 51 (1973).

[39]F. Boehm et al., Phys. Rev. D **62**, 092005 (2000).

[40]S. C. Blyth et al. (Aberdeen Tunnel Experiment Collaboration), Phys. Rev. D **93**, 072005 (2016).

[41]R. I. Enikeev et al., Sov. J. Nucl. Phys. **46**, 883 (1987).

[42]F. P. An et al. (Daya Bay Collaboration), Phys. Rev. D **97**, 052009 (2018).

[43]S. Abe et al. (KamLAND Collaboration), Phys. Rev. C **81**, 025807 (2010).

[44]M. Aglietta et al., eds. (AIP Conference Proceedings, 1999).

[45]G. Bellini et al. (Borexino Collaboration), J. Cosmol. Astropart. Phys. 08, 049–049 (2013).

[46]B. Aharmim et al. (SNO Collaboration), Phys. Rev. D **100**, 112005 (2019).

[47]Y.-F. Wang, V. Balic, G. Gratta, A. Fassò, S. Roesler, and A. Ferrari, Phys. Rev. D **64**, 013012 (2001).

[48]V. A. Kudryavtsev, N. J. C. Spooner, and J. E. McMillan, Nucl. Instrum. Meth. A **505**, 688 (2003).

[49]S. W. Li and J. F. Beacom, Phys. Rev. C **89**, 045801 (2014).

[50]Y. Zhang et al. (Super-Kamiokande Collaboration), Phys. Rev. D **93**, 012004 (2016).

[51]M. Harada, "Development of Neutron Tagging Algorithm and Search for Supernova Relic Neutrinos in Sk-Gd Experiment", PhD thesis (Okayama University, 2023).

[52]D. Tilley et al., Nuclear Physics A **745**, 155–362 (2004).

[53]M. Shinoki (Super-Kamiokande Collaboration), J. Phys.: Conf. Ser. **2156**, 012187 (2001).

[54]H. M. Araújo et al., Nucl. Instrum. Meth. A **545**, 398 (2005).

[55]M. Shinoki et al. (Super-Kamiokande Collaboration), Phys. Rev. D **107**, 092009 (2023).

[56]Y. Fukuda et al. (Super-Kamiokande Collaboration), Nucl. Instrum. Meth. A **501**, 418–462 (2003).

[57]Hamamatsu Photonics K.K., *Photomultiplier tubes and assemblies for scintillation couting & high energy physics* (2000).

[58]K. Abe et al. (Super-Kamiokande Collaboration), Nucl. Instrum. Meth. A **737**, 153 (2014).

[59]Y. Nakano et al., Nucl. Instrum. Methods Phys. Res., Sect. A **977**, 164297 (2020).

[60]K. Abe et al. (Super-Kamiokande Collaboration), Nucl. Instrum. Methods Phys. Res., Sect. A **1027**, 166248 (2022).

[61]R. M. Pope and E. S. Fry, Appl. Opt. **36**, 8710 (1997).

[62]N. Shigeta, *Evaluation of the detector responce using the Ni-Cf source in Super-Kamiokande*, 2023.

[63]M. Smy, Proceeding of the 30th International Cosmic Ray Conference **5**, 1279 (2008).

[64]Y. Nakano, "B-8 solar neutrino spectrum measurement using Super-Kamiokande IV", PhD thesis (University of Tokyo, 2016).

[65]Z. Conner, "A study of solar neutrinos using the Super-Kamiokande Detector", PhD thesis (Boston University, 2004).

[66]S. Desai, "High energy neutrino astrophysics with Super-Kamiokande", PhD thesis (Boston University, 2004).

[67]P. Antonioli, C. Ghetti, E. V. Korolkova, V. A. Kudryavtsev, and G. Sartorelli, Astropart. Phys. **7**, 357 (1997).

[68]"Geographical Survey Institute of Japan", unpublished, 1997.

[69]P. H. Barrett, L. M. Bollinger, G. Cocconi, Y. Eisenberg, and K. Greisen, Rev. Mod. Phys. **24**, 133 (1952).

[70]R. Burn et al., Report No. CERN-W5013 (1994).

[71]S. Agostinelli et al., Nucl. Instrum. Meth. A **506**, 250 (2003).

[72]T. Totani et al., The Astrophysical Journal **496**, 216 (1998).

[73]S. Ando, The Astrophysical Journal **607**, 20 (2004).

[74]A. M. Hopkins and J. F. Beacom, The Astrophysical Journal **651**, 142 (2006).

[75]N. Drory and M. Alvarez, The Astrophysical Journal **680**, 41 (2008).

[76]M. A. R. Kobayashi et al., The Astrophysical Journal **763**, 3 (2013).